# DEVELOPMENT OF A METHODOLOGY TO CHARACTERIZE THE DYNAMIC BIOMECHANICAL ENVIRONMENT OF THE HEART OUTFLOW TRACT OF CHICKEN EMBRYOS

By

Aiping Liu

A DISSERTATION

Presented to the Department of Biomedical Engineering
and the Oregon Health & Science University
School of Medicine
in partial fulfillment of
the requirements for the degree of

Doctor of Philosophy

June 2011

School of Medicine

Oregon Health & Science University

---

CERTIFICATE OF APPROVAL

---

This is to certify that the Ph.D. dissertation of

Aiping Liu

has been approved

---
Sandra Rugonyi, Ph.D.
Assistant Professor, Thesis Advisor

---
Kent L. Thornburg, Ph.D.
Professor

---
Ruikang Wang, Ph.D.
Professor, University of Washington

---
Monica Hinds, Ph.D.
Assistant Professor

---
Stephen R. Hanson, Ph.D.
Professor

*To my beloved parents, who always value education and encourage me to pursuit my dreams of life.*

# Table of Contents

# Acknowledgements

First and foremost I would like to express my sincere gratitude to my advisor, Dr. Sandra Rugonyi. Her patient guidance and persistent support have made this dissertation possible. By working closely with Dr. Rugonyi, I learned not only knowledge in biomechanics and computational fluid dynamics, but also basic scientific methodology, e.g., “the beauty of simplicity in scientific research” and “the difference between good and great lies in the details”. She exemplifies those indispensible qualities for scientific research, such as intelligence, enthusiasm, diligence, and integrity, which will have a long impact on my future career. Also, I greatly appreciate her efforts devoted to the numerous discussions, paper revisions, as well as to enhancing my communication skills.

I would like to thank my thesis committee members for their valuable suggestions and careful assessment of my work throughout my PhD training. To Dr. Kent Thornburg, for his foresight on the association of the biomechanical environment with embryonic heart development, the fundamental hypothesis of my thesis. I would also like to thank Dr Thornburg for encouraging me to think outside the box and providing so many valuable suggestions on my future career. To Dr. Ruikang Wang, for introducing me the state-of-the-art optical coherence tomography and its potential applications to embryonic heart research. To Dr. Monica Hinds, my first year mentor, for introducing me to the exciting field of biomedical engineering. Dr. Steven Hanson for carefully reviewing and commenting on my dissertation. My thanks extend to my previous student progress committee member, Dr. Sean J Kirkpatrick, now the chair of biomechanical engineering in Michigan Technological University, for his suggestions on fundamental biomechanical

concepts.

I would like to thank my previous advisors, Dr. Jinyang Zheng at Zhejiang University, China, and Dr. Ying Zhang and Dr. Jane Liu at Tennessee Technological University, for helping me build a solid foundation in Engineering and distilled me with passion for scientific research.

I am thankful to all of my colleagues and friends who made my years of PhD study a memorable and valuable experience. I would like to thank the people who ever worked in or collaborated with Dr. Rugonyi's group during my PhD program, including but not limited to: Dr. Vicente Grau, now a research fellow with Oxford University, for his guidance and contribution to developing segmentation algorithm; Dr. Xin Yin, for assistance on 4D image segmentation; Dr. Ian Sigal, now an assistant professor with Pittsburg University, for inspirational discussion on finite element modeling; Andrew Nickerson, for his excellent work on ultrasound measurement; Aaron Troyes and Dr. Liang Shi for their outstanding work on pressure measurement. I would like to give my special thanks to MS. Chuanmao Fan, MS. Lin An, Dr. Zhenhe Ma for the assistance in image acquisition with OCT system. Dr. Sandra Oster deserves my deepest appreciation on carefully editing my papers and teaching me effective, scientific communication skills.

I would like to acknowledge my funding sources: NIH R01HL094570 (S. Rugonyi, PI), AHA Beginning Grant in Aid (S. Rugonyi, PI), and AHA pre-doctoral fellowship 0910093G (A. Liu, PI).

Finally I thank my family for their years of support and encouragement. To my father,

Kangding, for teaching me hard work, humility, honesty, and integrity. He always encourage me not be afraid of taking risks and never cease to pursuit my dreams of life. To my mother, Ning, for teaching me love, curiosity, and beauty of life. To my sister, Aixia, for inspiring me to be strong and resolute when I was in doubt. Most of all to my husband, Yuming, whose endless love, valuable input, understanding, unwavering faith in me, help me to accomplish this milestone.

# List of Tables

# List of Figures

perpendicular to the cross section in (a); and when OFT walls are expanded: (c) center cross section and (d) longitudinal section. In (c) and (d), the dark areas in the lumen are due to a transient fading of signals when image acquisition rate is lower than the speed of blood flow. (e) An M-mode image generated from the cross-sectional image sequence along the dotted line in (a). M, myocardium; C, cardiac jelly; L, lumen. Scale bar = 100 μm.

**Figure 2.5** M-mode images extracted from cross-sectional image sequences of the OFT along the dotted line in Figure 2.4(a). Shown M-mode images were extracted from (a) the acquired OCT image sequence, (b) the same OCT image sequence pooled to one cycle using the cardiac period calculated by SLM ($T$ = 0.8146 s), and (c) the same sequence pooled to one cycle using the cardiac period calculated by FFT ($T$ = 0.7708 s). Note that (a) corresponds to one cardiac cycle of Figure 2.4(e).

**Figure 2.6** Lines chosen to perform sensitivity study in determining cardiac periods using SLM algorithm applied to M-mode (from the representative sequence shown in Figure 2.4). The panels show the positions of the lines when the OFT walls were most (a) constricted and (b) expanded.

**Figure 2.7** Lines chosen to perform sensitivity study in determining relative phase shifts using similarity algorithms applied to M-mode images (from the representative sequence shown in Figure 2.4). The panels show the positions of the lines when the OFT walls were most (a) constricted and (b) expanded.

**Figure 2.8** Comparison of M-mode images extracted from imaged and reconstructed longitudinal sections of the OFT. Lines selected to extract M-mode images are show in (a) and (b): close to the OFT inlet (I), middle OFT (M), and close to the outlet (O). (a)

Longitudinal sections acquired directly with OCT and (b) reconstructed from synchronized 4D image data. (c–e) M-mode images from a sequence acquired directly from OCT; (f–h) M-mode images from a reconstructed image sequence without phase lag adjustment; (i–k) M-mode images from the reconstructed image sequence with phase lag adjustment.

**Figure 2.9** OFT wall displacements close to the inlet and outlet. Wall displacements (showing the motion of the interface between the myocardium and cardiac jelly) were traced manually from the M-mode images shown in Figure 2.8: (a) from images acquired directly with OCT [Figures 2.8(c) and 2.8(e)]; (b) from reconstructed images without phase adjustment [Figures 2.8(f) and 2.8(h)]; and (c) from reconstructed images with phase adjustment [Figures 2.8(i) and 2.8(k)]. For ease of visualization, we present five cardiac cycles extracted directly from the acquired image sequence (a), and in (b) and (c) generated by circular repetition of the reconstructed pooled cardiac cycle.

**Figure 3.1** OCT images of the heart OFT of HH18 chick embryos. (A) Longitudinal section showing the regions where 50 OFT cross-sections were extracted from 4D image data. Purple lines showing the start (S), middle (M), and end (E) locations. The OFT middle cross-section at (B) its maximal expansion and (C) contraction states. M, myocardium; CJ, cardiac jelly; L, lumen; and O, the origin.

**Figure 3.2** Illustration of the definitions of negative and positive edges. The sign of an edge is determined by a dot operation between two vectors at a point on the edge, namely, the intensity gradient vector (g) and a directional vector (n) pointing from the center point (C) to the point on the edge. a and b are a point on the interior and exterior edges of the myocardium, respectively.

state. (A-F) show the exterior boundary (purple contour) and the interior boundary (green contour) of the myocardium, and the outline of the lumen (yellow contour) at selected cross-sections spanning evenly along the OFT, starting from the OFT inlet towards the OFT outlet demarked in Figure 3.1A. (G) shows the 3D surface reconstruction of the OFT from the segmented contours.

**Supplemental Figure 3.1** Comparisons between automatic (red contour) and manual (green contour) segmentations of (A) the exterior myocardium, (B) the interior myocardium, and (C) the lumen from a (2D+time) OCT image sequence of mid OFT cross-section. Examples depicted have the largest deviations from the manual segmentation (the ground truth).

**Supplemental Figure 3.2** Surface reconstruction of OFT contours segmented from a 2D+time OCT images, showing the large and heterogeneous deformation of an OFT middle cross-section over the cardiac cycle.

**Figure 4.1** Sections of HH18 chick heart OFT obtained from OCT images. The figure shows OCT images of the OFT during the cardiac cycle: (a) and (c) during ventricular systole, when the OFT is most expanded, (a) is a longitudinal section and (c) is a cross-section; (b) and (d) during ventricular diastole, when the OFT is most constricted, (b) is a longitudinal section and (d) is a cross-section. Point P marks the approximate location where velocities were acquired with Doppler OCT (see Fig 4.5.b). The white-dotted line corresponds to the direction of the incident light beam of Doppler OCT; the arrows indicate the direction of blood flow. Scale bar = 100 µm. L, Lumen, M, Myocardium; CJ, Cardiac jelly.

**Figure 4.2** Two FEMs of the OFT. Left: Cushion model: (a) reference cross-section and

(b) FEM discretization. Right: jelly model: (c) reference cross-section and d FEM discretization (Cylindrical model not shown). In (a) and (c), the inner part corresponds to the lumen and the outer part, to the wall. In (b) and (d), the lumen-wall interface is marked with a thick line. Dimensions are: R = 0.1875 mm, $L_1$ = 0.077665 mm, L = 0.5 mm, h = 0.025 mm, and r = 0.03 mm. Points A and B are representative points where WSS was analyzed in detail.

**Figure 4.3** Blood pressure and myocardium displacements prescribed as boundary conditions on the OFT models. Top temporal variations of ventricular pressure ($P_v$) prescribed at the inlet surface and pressure prescribed at the outlet surface ($P_a$). Bottom radial displacement prescribed on the external surface of the OFT models with amplitude $D_1$. Note the different scales for blood pressure (on left vertical axis) and radial displacements (on right vertical axis).

**Figure 4.4** Comparison of OFT lumen cross-sectional areas, obtained from our three models when (a) OFT is most expanded, and (b) OFT is most constricted.

**Figure 4.5** Blood velocities calculated and measured inside the OFT. (a) Calculated longitudinal velocities at the center of the mid-cross-section obtained from the cushion model with simultaneous and peristaltic wall motions, with prescribed wall motion amplitude D1 (70 μm). (b) Blood velocities measured with Doppler OCT at a fixed point located at the approximate center of the OFT lumen (see point P in Figure 4.1a) in the direction of incident OCT light beam (dotted line in Figure 4.1a).

**Figure 4.6** Volume flow rates (Q) at the mid-cross-section of the OFT obtained from the OFT models. For cylindrical, cushion, and jelly models, a simultaneous wall displacement of amplitude D1 was prescribed. For the cylindrical SA model (Sect. 4.2),

prescribed wall displacements were such that matched temporal variations of the lumen cross-sectional area calculated from the cushion model.

**Figure 4.7** Volume flow rates ($Q$) obtained from the cushion model. (a) Comparison between simulations of simultaneous and peristaltic OFT wall motions, calculated using a prescribed radial displacement amplitude $D_1$ = 70 µm. (b) Comparison between simulations of simultaneous OFT wall motion, calculated with prescribed radial displacement amplitudes $D_1$ = 70 $\mu$m and $D_2$ = 90 $\mu$m.

**Figure 4.8** Temporal variations of WSS in the cushion model at points A and B (Figure 4.2a) in the mid-cross-section of OFT. Results correspond to the case of simultaneous wall motion with prescribed wall displacement amplitude $D_1$ = 70 $\mu$m.

**Figure 4.9** Comparison of WSS obtained using the OFT models. WSS at (a) point A and (b) point B. The cushion and jelly models were simulated with simultaneous wall motion, with prescribed wall displacement amplitude $D_1$ = 70 µm; the wall motion of the cylindrical SA was prescribed such that temporal variations of cross-sectional area matched those of the cushion model.

**Figure 4.10** WSS obtained from the cushion model. Left: WSS at point A. (a) simultaneous versus peristaltic motion, and (b) prescribed wall displacement amplitude D1 (70 µm) versus D2 (90 µm). Right: WSS at point B. (c) simultaneous versus peristaltic motion, and (d) prescribed wall displacement amplitude D1 (70 µm) versus D2 (90 µm).

**Figure 5.1** Stage HH18 chick embryonic heart and its outflow tract (OFT). (A) Sketch of a chick embryonic heart with the OFT region marked by dotted black lines; the upper right inset shows a sketch of the OFT cross-section. Red arrows indicate the approximate

locations where blood pressures were measured: in the ventricle and aortic sac. The three purple dots indicate the approximate locations where blood flow was measured (near the OFT inlet, middle and outlet) using Doppler ultrasound. (B), (C) and (D) Optical coherence tomography (OCT) images of the HH18 chick heart, showing: (B) a transverse section of the OFT, (C) a cross-section of the OFT at the most constricted state, and (D) the same cross-section at the most expanded state. The dotted purple line in (B) indicates the location of the cross-section in (C) and (D). M, myocardium; C, cardiac jelly; L, lumen; A, atrium; V, ventricle; OFT, outflow tract; AS, aortic sac.

**Figure 5.2** OFT wall motion. (A) Transverse sectional OCT image of the OFT; the 5 lines show the locations where cross-sections were extracted from 4D OCT images. (B) The 5 extracted cross-sections at their most constricted state; the lines in image 1 show the major and minor semi-axes of the lumen, assuming an elliptical luminal area. (C) Calculated luminal areas (A1, A2, A3, A4, A5) for each of the 5 locations over the cardiac cycle. t, time; T, period of the cardiac cycle.

**Figure 5.3** 2D axisymmetric model of the chick embryonic heart OFT. The three white dots at the OFT centerline indicate the locations where centerline velocities were extracted to compare with those measured with Doppler ultrasound. $P_{as}$, aortic sac pressure; $P_v$, ventricular pressure; AS, aortic sac; Tr, transition region; OFT, outflow tract; V, ventricle.

**Figure 5.4** OFT lumen radius (R) over the cardiac cycle and along the OFT used in our 2D models. R was calculated and interpolated from the luminal areas obtained from the 5 cross-sections shown in Figure 5.2. $\lambda$, is the axial distance along the OFT centerline from the OFT inlet to the outlet.

**Figure 5.5** Pressure and wall motion phase lags. The figure shows representative pressures measured at the ventricle and aortic sac of stage HH18 chick embryos, as well as the luminal area at the OFT inlet (A1 from Figure 5.2C). It also shows hypothetical phase relationships among the pressures and OFT wall motion. $\Phi_p$, is the phase lag of the aortic sac pressure ($P_{as}$) with respect to the ventricular pressure ($P_V$); $\Phi_m$, is the phase lag of the ventricular pressure ($P_v$) with respect to the wall motion of the OFT inlet (A1).

**Figure 5.6** Temporal relationships among the representative luminal areas and the pressure drop along the OFT for different phase lag combinations ($\Phi_p$ and $\Phi_m$). A1, A3, and A5, are the luminal areas at the 3 cross-sections of the OFT (see Figure 5.2B); $\Delta P$, is the pressure difference between the ventricle and aortic sac ($\Delta P = P_v - P_{as}$).

**Figure 5.7** Geometric parameters used in 3D FE model of the OFT. (A) shape index (e = a/b) of the elliptical cross-section at the 5 selected cross-sections (see Figure 5.2) over a cardiac cycle. (B) Major semi-axis (a), and (C) minor semi -axis (b), of the OFT elliptical lumen cross-sections over a cardiac cycle and along the OFT. $\lambda$, is the axial distance along the OFT centerline from the OFT inlet to the outlet.

**Figure 5.8** Comparison of velocities measured using Doppler ultrasound and calculated using our 3D FE model of the OFT. The comparisons are shown at 3 locations in the OFT lumen (see Figures 5.1A and 5.11B): (A) near the OFT inlet (location I), (B) middle (location M), and (C) near the outlet of the OFT (location O). Measured centerline velocities were represented as the average velocity, $V_{US}$ (solid black line) ± standard deviations (dotted lines above and below the solid line). The grey line in (B) was obtained from the literature,[77] and measured the centerline blood velocity at about the middle region of a representative HH18 chick OFT using Doppler ultrasound.

**Figure 5.9** Averaged peak forward velocities (top) and peak backflow velocities (bottom) measured using Doppler ultrasound. Velocities were measured at about the 3 locations shown in Figure 5.1A: near the OFT inlet (I), middle (M) and outlet (O) of HH18 chick embryos (n = 10). Data are presented as mean and standard deviations.

**Figure 5.10** Centerline velocity profiles calculated using 2D FE models under different phase relationships between pressures and OFT wall motion. VI, VM, and VO, are centerline velocity profiles extracted at the centerline near the OFT inlet (I), middle (M) and outlet (O), respectively (see also Figure. 5.3).

**Figure 5.11** Blood flow patterns calculated using our 3D model of the cardiac OFT of HH18 chick embryos. (A) Centerline velocities over a normalized cardiac cycle, and (B) velocity profile along the major axis of the elliptical lumen cross-sections. Centerline velocities and velocities profiles are shown at the 3 locations shown in Figure 5.1A: near the OFT inlet (I), middle (M), and the outlet (O). The vertical lines in (A) indicate the cardiac phase of the velocities shown in (B). The three dots in (B) indicate the locations from where the centerline velocities in (A) were extracted.

**Figure 5.12** Distribution of wall shear stresses on the OFT wall at peak forward flow. The flow rate depicted was calculated from the flow at the middle cross-section of the OFT (Location M in Figure 5.1A).

**Supplemental Figure 5.1** The ventricular and aortic sac pressures used in a 2D dynamic FE model of the OFT (A) $P_v^{min}$ and $P_a^{min}$, and (B) $P_v^{max}$ and $P_a^{max}$.

**Supplemental Figure 5.2** Predicted centerline velocities near the OFT inlet, middle, and outlet, under pressure boundary conditions: (A) $P_v^{min}$ and $P_a^{min}$, and (B) $P_v^{max}$ and $P_a^{max}$, as shown in the Supplemental Figure 5.1. VI, VM, and VO are the centerline

blood velocity near the OFT inlet, middle, and outlet, respectively.

**Figure 6.1** OCT images of the OFT. Illustration of the OFT longitudinal and cross sections (A) when the OFT is constricted, and (B) when the OFT is expanded. OCT images of a OFT longitudinal section (A) when the OFT is constricted, overlaid lines showing the locations where 5 cross-sections were extracted from the 4D OCT images of the OFT; (D) when the OFT is fully expanded. (E-I) The 5 cross-sections at locations 1-5 at OFT maximal contracted state, and the same cross-sections (J-N) at OFT maximal expansion state. The yellow lines in (E, F, G, and I) showing the orientation of the opposing cardiac cushions in the OFT. M, myocardium; L, lumen; CJ, cardiac jelly; SPL, splanchnopleure membrane. Scar bar = 200 μm.

**Figure 6.2** Behaviors of the myocardium at 5 selected OFT cross-sections. (A) Temporal variations of radii, and (B) maximal expansion and contraction radial velocities of the myocardium at the 5 selected OFT cross-sections of the normal chick embryonic heart.

**Figure 6.3** Cyclic strains in the myocardium at 5 selected OFT cross-sections. (A) Temporal variation of circumferential strains in the myocardium, (B) temporal variation of radial strains, (C) peak circumferential strain in the myocardium compared with that in the endocardium, and (D) peak expansion and contraction circumferential strain rates.

**Figure 6.4** Behaviors of the cardiac jelly at 5 selected OFT cross-sections (L1-L5). (A) Temporal variation of areas of cardiac jelly over a cardiac cycle; and (B-F) temporal relationship between the areas of the OFT myocardium (MI), cardiac jelly (CJ), and lumen (L) along the OFT from L1 to L5, respectively.

**Figure 6.5** Behaviors of the heart OFT lumen of HH18 chick embryos. (A) A OCT image of the OFT cross-section, with segmented boundaries of the interior myocardium

(green contour), exterior myocardium (purple contour), and lumen outline (yellow contour) overlaid on the image; and (B) an M-mode OCT image extracted from the yellow line in (C) to illustrate the metrics defined for evaluating temporal behaviors of the lumen in (D). (C) Temporal variation of OFT luminal areas at 5 selected OFT cross-sections of a representative HH18 chick embryo; (B) time spans for luminal expansion ($T_e$), closing ($T_c$), and closure ($T_{closure}$) over a cardiac cycle at 5 selected OFT cross-sections of HH18 chick embryos.

**Figure 6.6** Temporal variations of wall stress over a cardiac cycle at (A) the OFT inlet and (B) outlet. WS, wall stress, P, intracardiac blood pressure, R, radius of the interior myocardium, h, wall thickness of the myocardium.

**Figure 6.7** Blood flow dynamics in the OFT. Temporal variation of blood velocity near OFT inlet (I), measured using Doppler OCT: (A) M-mode structural image, (B) M-phase image, (C) blood velocity trace over cardiac cycles, the velocity data were calculated using Eq 6.1 at the location of the horizontal dotted line overlaid on (A). Note that the perpendicular lines show the temporal relationship among the OFT wall motion, Doppler phase, and blood velocity, and the horizontal line overlaid on (C) indicates zero velocity. Spatial distribution of blood flow calculated using FE modeling: (D) blood flow profiles along the major axes of the elliptical cross-sections near the OFT inlet (I), middle (M) and outlet (O). Doppler flow data analysis was performed by Peng Lee.

**Figure 6.8** Temporal and spatial distribution of wall shear stress (WSS) magnitude on the OFT lumen surface. (A) Spatial distribution of maximal WSS magnitude on the OFT lumen surface when the OFT is fully expanded; (B) OFT lumen surface showing 4 selected locations (1-4) at three cross-sections near the OFT inlet (I), middle (M), and the

outlet (O). Points 1 and 3 are along the minor axis of the elliptical cross-section, representing the cushion region; points 2 and 4 are along major axis, represent the region without cushion. (C-E) Temporal variations of WSS at the 4 selected locations at cross-sections I, M, and O, respectively.

**Supplemental Figure 6.1** Temporal variation of circumferential strains in the endocardium at 5 selected OFT cross-sections.

**Supplemental Figure 6.2** Illustration of image processing on OCT images of the OFT. Segmented contours of the OFT lumen (yellow), the interior boundary (green) and the exterior boundary (purple) of the myocardium are overlaid on cross-sectional OCT images, when the OFT is fully (A) contracted and (B) expanded. An elliptical model (the green curve) that fit the lumen is overlaid on the OCT images of the same OFT cross-section, when the OFT is fully (C) contracted and (D) expanded.

**Supplemental Figure 6.3** Comparisons of predicted centerline velocity profiles between the assumptions of a transient flow and a quasi-steady flow in FE modeling of the OFT: (A) near the inlet, (B) middle, and (C) outlet. The locations correspond to L2, L3 and L4 in image analysis, respectively.

**Supplemental Figure 6.4** OCT image of a longitudinal section of the OFT, showing the locations of two cross-sections L1' and L2' to estimate the effects of longitudinal motion on image analysis. The two cross-sections are extracted from the 4D OCT image data that are perpendicular to the OFT axial centerline and move with the OFT longitudinally over the cardiac cycle.

**Supplemental Figure 6.5** Effects of phase relationship between $P_V$ and R on the wall stress in the myocardium at (A) the OFT inlet and (B) the outlet. 0T, 0.1T, 0.2T, 0.3T,

and 0.4T are conjectured phase lags of peak $P_V$ with respect to peak R. $P_V$, the ventricular pressure; R, effective radius of the myocardium; T, the cardiac cycle.

**Figure 7.1** OCT images of the heart OFT. (A) A longitudinal section of a normal OFT when the OFT is constricted, overlaid lines showing the locations where 5 cross-sections were extracted from the 4D OCT images of the OFT. (B) A longitudinal cross-section of a banded OFT, arrows showing the band. The cross-sections at locations 1-5 (C-G) at OFT maximal contracted state, and (H-L) at OFT maximal expansion state. The yellow lines in (C, D, E, and G) show the changes in the orientation of the OFT lumen along the OFT. M, myocardium; L, lumen; CJ, cardiac jelly; SPL, splanchnopleure membrane. Scar bar = 200 μm.

**Figure 7.2** Comparison of the maximal, minimal, and cyclic changes in the radium of the interior myocardium at the 5 selected OFT cross-sections between (A) normal and (B) OTB chick embryonic hearts. * indicates significantly different from normal ($p<0.05$).

**Figure 7.3** Maximal expansion and contraction radial velocities of the myocardium at the 5 selected OFT cross-sections of (A) normal and (B) OTB chick embryonic hearts. * indicates significantly different from normal ($p<0.05$).

**Figure 7.4** Temporal variation of the interior radium of the OFT myocardium over a cardiac cycle at 5 selected OFT cross-sections of (A) a representative normal and (B) a typical OTB chick embryo.

**Figure 7.5** Comparison of the maximal, minimal areas and cyclic area changes of the cardiac jelly at the 5 selected OFT cross-sections between (A) normal and (B) OTB chick embryonic hearts.

**Figure 7.6** Temporal variation in the areas of the cardiac jelly at the 5 selected OFT

cross-sections of (A) a representative normal and (B) a representative OTB chick embryonic heart.

**Figure 7.7** Comparison of the areas and area changes of the lumen at the 5 selected OFT cross-sections between (A) normal and (B) OTB chick embryonic hearts. * indicates significantly different from normal ($p<0.05$).

**Figure 7.8** Temporal variation of luminal areas at 5 selected OFT cross-sections of (A) a representative normal and (B) a representative OTB chick embryonic heart.

**Figure 7.9** Temporal behaviors of the lumen at the 5 selected OFT cross-sections of (A) normal and (B) OTB chick embryonic hearts. (C) A cross-sectional OCT image and (D) an M-mode OCT image extracted from the yellow line in (C) to illustrate the metrics for temporal behaviors of the lumen. $T_e$, time span for luminal expansion; $T_c$, time span for luminal closing, and $T_{closure}$, time span for luminal closure. * indicates significantly different from normal ($p<0.05$).

**Figure 7.10** Temporal variations of circumferential strains at the 5 selected OFT cross-sections in a representative normal and an OTB chick embryonic hearts. Circumferential strain in the myocardium: (A) normal and (B) OTB; circumferential strain in the endocardium: (C) normal and (D) OTB.

**Figure 7.11** Peak circumferential strains in the myocardium and the endocardium over a cardiac cycle at the 5 selected OFT cross-sections of (A) normal and (B) OTB chick embryonic hearts. * indicates significantly different from normal ($p<0.05$).

**Figure 7.12** Peak expansive and contractive circumferential strain rates in the myocardium over a cardiac cycle at the 5 selected OFT cross-sections of (A) normal and (B) OTB chick embryonic hearts. * indicates significantly different from normal

($p<0.05$).

**Figure 7.13** Comparison of radial strain in the myocardium between normal and OTB embryos. Time variations of the radial strains in (A) a representative normal and (B) a representative OTB embryo at the 5 selected locations along the OFT (L1-L5) over a cardiac cycle.

**Figure 7.14** Comparison of wall stress in the myocardium between normal and OTB chick embryos. Time variations of the wall stress (WS), ventricular pressure (P), wall thickness (h), and internal radium of the myocardium in: (A) a representative normal embryo and (B) a representative OTB embryo near the OFT inlet (prior to the band) over a cardiac cycle.

**Figure 7.15** Comparison of peak velocities near the OFT inlet, middle and outlet between normal and banded chick embryos.* indicates significantly different from normal ($p<0.05$). Doppler flow measurement was performed by Andrew Nickerson.

**Figure 7.16** Comparison of centerline velocities near the OFT inlet (I), middle (M), and outlet (O) between: (A-C) normal and (D-E) OTB chick embryos measured with Doppler Ultrasound. Note that the velocities were acquired sequentially at different OFT regions and were not synchronized in a normalized cardiac cycle. Vus, mean velocity measured using Doppler ultrasound; Vus±std, velocity varied with a standard deviation. Doppler flow measurement was performed by Andrew Nickerson.

**Supplemental Figure 7.1** OCT cross-sectional image of the OFT inlet of (A) a representative normal embryo and (B) a typical OTB embryo when the OFT is fully closed. Note those extensive branches of the endocardium (End) towards the myocardium in the OTB embryo.

**Supplemental Figure 7.2** Comparison of wall stress in the myocardium at the OFT inlet between (A) a normal chick embryo and (B) an OTB embryo under different combinations of phase relations between $P_V$ and R. 0T, 0.1T,0.2T, and 0.4T are conjectured phase lags of peak $P_V$ with respect to peak R at the OFT inlet. $P_V$, the ventricular pressure; R, effective radius of the myocardium; T, a cardiac cycle.

**Supplemental Figure 7.3** Temporal variation of the interior radius of the myocardium at 5 selected OFT cross-sections. This is another typical response to OTB, showing a slower peristaltic motion than normal HH18 chick embryos.

**Supplemental Figure 7.4** Temporal relationship between the areas of the OFT myocardium (MI), cardiac jelly (CJ), and lumen (L) at two locations: (A) L2 and (B) L4 in a typical OTB embryo. Large area of the cardiac jelly usually occurs during early myocardium relaxation and before fast increase of luminal area, or when the OFT is fully closed. The area of the cardiac jelly is small when the OFT is fully expanded or during fast myocardium contraction.

**Figure 8.1** Temporal variation of the OFT surfaces extracted from 4D OCT images of the OFT with a 4D segmentation algorithm. Blue and green surfaces are the external and the interior surfaces of the myocardium, respectively. Red surface is the OFT lumen. 4D segmentation on the OFT were performed by Dr. Xin Yin (Image courtesy of Dr. Yin Xin).

**Figure 8.2** Level and spatial distribution of gene expression of integrin-α4 in a normal HH24 chick embryo. (A-C) Examples of confocal microscopy images along the depth of the embryonic heart, with image intensity indicating the level of gene expression. (D) 3D voxel view of the gene expression of integrin-α4 (the red color), showing a strong express

in the compact ventricular myocardium, and a mild express in the OFT myocardium and trabeculae. The 3D voxel view was reconstructed from the confocal image dataset in (A-C) using Amira 5.2.2. Confocal imaging was performed by Dr. Carley Shaut.

# List of Videos

**Video 2.1** Voxel view of a beating chick-embryo OFT. The movie shows a frontal view of the OFT for the first cardiac cycle and then a 180-deg rotation of the OFT along the *Z*-axis for the second cardiac cycle. The dotted line (in the still image) encircles the OFT region that connects the ventricle proximally and aortic sac distally. M: myocardium, L: lumen (Quick-Time, 2 MB). [URL: http://dx.doi.org/10.1117/1.3184462.1]

**Supplemental Video 3.1** 4D surfaces of the heart OFT of a HH18 chick embryo. OFT surfaces were generated from the segmentation of 30 OFT volume datasets over the cardiac cycle, using the hybrid 3D segmentation algorithm that we developed.

**Supplemental Video 6.1** 4D geometry of the OFT of a HH18 chick embryo, reconstructed from the 4D OCT image data.

**Supplemental Video 6.2** Tempo-spatial distribution of blood flow field in the OFT of a HH18 chick embryo. The blood flow field was predicted with the 3D dynamic FE model of the OFT. For simplicity, blood flow profiles were depicted along the major axis of the elliptical cross-sections near the OFT inlet (I), middle (M), and the outlet (O).

**Supplemental Video 6.3** Tempo-spatial variation of wall shear stress (WSS) on the OFT endocardium of a HH18 chick embryo. WSS was predicted with the 3D dynamic FE model of the OFT.

**Supplemental Video 6.4** OCT images of a OFT longitudinal section of a HH18 chick embryo. A landmark point (red point) shows the longitudinal motion of the OFT over the cardiac cycle.

**Supplemental Video 6.5** OCT images of an OFT longitudinal section of a HH18 chick embryo, showing the wave-like motion of the cardiac jelly along the OFT.

**Supplemental Video 7.1** Longitudinal (A) and frontal views (B) of the OFT of a representative HH18 chick embryo. Frontal view depicts a curve plane approximately along the axial centerline of the OFT in (A). Note the wave-like motion of the cardiac jelly. MI, myocardium; L, lumen; CJ, cardiac jelly.

**Supplemental Video 7.2** Longitudinal (A) and frontal (B) views of the OFT of an OTB chick embryo. Frontal view depicts a curve plane approximately along the axial centerline of the OFT in (B). Note that the longitudinal motion of the OFT is dramatically reduced and that the wavelike-motion of the cardiac jelly is disrupted by OTB.

# List of Abbreviations

| | |
|---|---|
| CHD | congenital heart disease |
| CFD | computational fluid dynamics |
| CJ | cardiac jelly |
| FEM | finite element model |
| HH | Hamburg-Hamilton |
| L | lumen |
| ME | exterior boundary of the myocardium |
| MI | Interior boundary of the myocardium |
| OCT | optical coherence tomography |
| OFT | outflow tract |
| OPF | optical flow algorithm |
| OSI | oscillatory shear index |
| OTB | outflow track banding |
| WS | wall stress |
| WSS | wall shear stress |
| 2D | two dimensional |

| | |
|---|---|
| 3D | three dimensional |
| 4D | four dimensional (3D space + time) |

# Abstract

## Development of a Methodology to Characterize the Dynamic Biomechanical Environment of the Heart Outflow Tract of Chicken Embryos

Aiping Liu, M.S.

Doctor of Philosophy

Department of Biomedical Engineering

Oregon Health & Science University

School of Medicine

June 2011

Thesis Advisor: Sandra Rugonyi, Ph.D.

The biomechanical environment (e.g., stresses and strains) of embryonic cardiac cells plays an important role in regulating intrinsic genetic programming of these cells. Disturbances in the biomechanical environment have been associated with congenital heart diseases, which affect 36,000 newborns each year in the US. However, the underlying mechanisms by which the biomechanical environment affects heart development remain unclear, partly due to the lack of quantitative knowledge about the

biomechanical environment the cardiac cells experience in the living embryonic heart.

To study the role of the biomechanical environment in early heart development, Hamilton Hamburg (HH) stage 18 chick embryos were used as the animal model for early heart development in this thesis. An intervention procedure performed on chick embryos, outflow tract banding (OTB), was used to reproduce disturbances in the biomechanical environment that lead to heart defects. Specifically, we focused on the dynamic biomechanical environment in the chicken heart outflow tract (OFT), a distal heart region that undergoes intensive morphogenetic remodeling during heart development. At early developmental stages (e.g., HH18), morphogenesis of the OFT is very sensitive to mechanical disturbances that result in OFT malformations at later stages.

The objectives of this thesis were (1) to develop a methodology to quantify the dynamical biomechanical environment in the heart OFT of chick embryos *in vivo* and non-invasively; and (2) to characterize the physiological biomechanical environment and OTB-induced, acute changes in the biomechanical environment to which cardiac cells on the OFT wall are subjected *in vivo* in HH18 chick embryos.

First, we developed a methodology that integrates imaging, physiological measurements, and computational fluid dynamics (CFD) modeling to quantify the biomechanical environment in the chick heart OFT. Using optical coherence tomography (OCT) and the 4D imaging strategy developed in this thesis, we characterized the dynamics of the OFT wall over the cardiac cycle, from which cyclic cardiac wall strains were extracted. Using the dynamic geometry of the OFT wall from OCT imaging and *in*

*vivo* pressure measurements, we developed image-based CFD models of the OFT to quantify *in vivo* blood flow dynamics and flow-induced shear stresses on the OFT wall over the cardiac cycle.

Second, we characterized in detail the dynamic biomechanical environment in the OFT of HH18 chick embryos and OTB chick embryos using the integrative methodology. We showed that cardiac cells in the OFT wall were subjected to a distinct combination of biomechanical stresses and strains that varied at different spatial locations on the OFT wall and over the cardiac cycle. We also found that the biomechanical environment in the OFT altered acutely in response to OTB. The heterogeneous and dynamic biomechanical environment of the OFT are hypothesized to differentially regulate cardiac cell behaviors and gene expression critical for morphogenetic events that occur in later OFT development.

Collectively, the methodology we developed provides a way to elucidate the dynamic biomechanical environment in embryonic hearts. The knowledge of *in vivo* biomechanical environment as well as its changes will contribute towards understanding the mechanisms by which biomechanical factors affect heart development.

# Chapter 1: Introduction

In this thesis, a methodology is developed to characterize the dynamic biomechanical environment to which cardiac cells are subjected *in vivo* in living chicken embryonic hearts. In this chapter, I will provide some background on the cardiac morphogenesis, congenital heart diseases (CHD), the biomechanical environment in the embryonic heart, the chick embryonic heart, and the heart outflow tract (OFT). I will also briefly review the intervention model that we used to disturb normal biomechanical environment, the imaging technique that we used to image chick embryonic hearts, and computational fluid dynamics (CFD) that we used to quantify the blood flow dynamics.

## 1.1 Background

### 1.1 .1 Cardiac morphogenesis and congenital heart diseases

Mammalian and avian embryonic hearts undergo a similar complex morphogenetic process.[1] Details of cardiac morphogenesis and associated cellular and molecular events have been characterized in recent research.[2-5] Briefly, after cardiac differentiation, the functional heart begins as a straight tube with distinguishable heart segments, e.g., sinus venosus, primitive atrium, atrioventricular canal, primitive ventricle, and OFT connected in series; the tubular heart then loops in the middle and aligns the heart segments to their definitive positions. Endocardial cushions, septae, and valves form to divide primitive atria and primitive ventricles into a four-chambered mature heart. Cardiac morphogenesis is governed by genetic programs, which include essential genes that act during critical

steps of cardiac morphogenesis and determine cardiac phenotypes, and transcript genes that control the essential genes expressed in highly restricted temporal and spatial patterns.[2, 3, 6, 7]

Environmental factors, such as hyperthermia,[8] hypoxia,[9, 10] and disturbed intracardiac blood flow,[11-14] have been shown to modulate the genetic program of heart development. The biomechanical environment, such as strains and stresses that cardiac cells experience *in vivo*, has been recently recognized as an important environmental factor that affects heart development.[14-16] Intrinsic genetic programs and environmental factors, such as biomechanical stresses and strains, interact to ensure the fidelity of spatiotemporal genetic expression and thus normal cardiac morphogenesis.[4, 6, 14, 17, 18] Any perturbation in the biomechanical environment may disturb genetic expression patterns and eventually lead to hearts with various defects.

*Congenital heart diseases* (CHD) are structural abnormalities of the heart that arise during cardiac morphogenesis.[19] In the US, CHDs affect approximately 1% or 36,000 live babies, and are responsible for 37% of infant deaths from congenital defects each year.[19, 20] Evidence has shown that perturbed biomechanical environment alter the expression of genes that respond to biomechanical forces, leading to CHDs.[13, 21] However, to what extent and how biomechanical factors modify the genetic expression program that lead to CHDs are not known. One approach to reveal the mechanisms of biomechanical factors regulating genetic expression is to correlate patterns of genetic expression with distributions of biomechanical stresses or strains in the embryonic heart. This line of research has not been well studied *in vivo*, partly because the biomechanical

environment in the living embryonic heart are challenging to quantify in the tiny, beating heart (see Section 1.1.5).[22]

### 1.1.2 Biomechanical environment regulates cardiac morphogenesis

After the tubular heart starts to beat, intracardiac blood flow and wall motion create a dynamic biomechanical environment which cardiac cells experience *in vivo*. The biomechanical environment includes cyclic strains in the myocytes and endocardial cells exerted by blood pressures and myocardium contraction, wall stress developed in the myocardium in response to transmural blood pressures, and wall shear stress (WSS) exerted on the endocardium by the blood flow.

*Evidence for the regulation of cardiac morphogenesis*

Regulatory roles of biomechanical factors in cardiac morphogenesis are inferred from *in vivo* experiments in embryonic hearts of various species.[12, 13, 23] Hogers et al., in a venous clipped chick embryo model, have shown that altered intracardiac blood flow patterns result in heart malformations, especially in the OFT.[11, 13] Hove et al., have shown that significant reduction in WSS result in failed valvulogenesis in zebrafish embryonic hearts, suggesting that WSS is an essential epigenetic factor in cardiac morphogenesis.[14] Groenendijk et al. have revealed a correlation between the spatial distribution of WSS with expression levels of several shear stress-responsive genes in embryonic chick hearts.[21, 24] Increased intracardiac pressure achieved by banding the OFT accelerates the maturation of myocardium architectures in the ventricle, indicating that wall stress developed in the myocardium in response to the increased pressure modulates the maturation of myocytes.[15, 25] In addition, the alteration in diameter of banded OFT may

produce changes in laminar flow at and beyond the constriction region, which may be responsible for the dilation of the OFT downstream the band and may contribute to OFT abnormalities at later developmental stages.[12]

*Cellular level regulation*

Endothelial cells (ECs) in the endothelium are directly subjected to WSS induced by blood flow. ECs sense WSS through different mechanosensors, including integrins, vascular endothelial growth factors (VEGF) receptor-2 (Flk-1), ion channels, G-protain-coupled receptors (GPCRs) and trimetric G proteins, and adhesion molecules.[26, 27] The mechanosensors of ECs initiate intracellular signaling pathways by activating multiple signaling molecules, including protein kinase C (PKC), FAK, c-Src, Rho family GTPases, PI3K, and MAPKs.[28] Activated through the protein phosphorylation cascades, transcription factors (e.g., c-fos, c-jun, Egr-1, SP1 and NFkB) translocate into the nucleus to target cis-elements in biomechanically inducible genes, and then up- or down- regulate gene expression, thus modulating the EC behaviors and functions.[29, 30]

Evidence has shown that WSS regulate important signal pathways for two important functions of ECs in cardiac morphogenesis: (1) endothelial-mesenchymal transformation (EMT), a essential process for valve formation;[26, 27] and (2) secretion of signaling mediators (e.g. platelet-derived growth factor B-chain and NO[21, 31-34]) modulating cardiomyocyte proliferation, maturation, survival, and contraction.[28, 29, 35] *In vitro* studies suggest that ECs can sense and differentiate variations of WSS. ECs respond to different spatial and temporal features of WSS (magnitude, orientation, spatial and temporal

variations) by activating different downstream signaling pathways. ECs can detect WSS as low as 0.1 Pa[36] and respond as fast as milliseconds,[29, 35] which render ECs able to sense variations within a cardiac cycle. ECs are capable of sensing the stretch.[37] As a response to stretch, ECs remodel cell morphology and orientation,[38] regulate paracrine cytokine secretion[39] (endocardium-relaxing factors), and increase key tyrosine kinase receptors involved in vasculogenesis and anigiogenesis.[40] WSS and cyclic stretch has been reported to regulate EC morphology and cytoskeleton synergistically.[41]

Myocytes (MCs) are located in the myocardium and can sense wall stress and cyclic stretch of the OFT wall induced by transmural blood pressures. A physiological level of stretch has been shown necessary for maintaining physiological phenotypes of MCs including proliferation, differentiation, and contractile phenotypes.[42] Deviation from the physiological level of stretch leads to myocyte hyperplasia or hypoplasia that affects the maturation of myofiber architecture in the myocardium.[25, 43] Besides the level of stretch, MCs can also sense and respond to the amplitude and the rate of change in stretch , and alter cellular behaviors.[44, 45]

Current understanding of mechanotransduction of embryonic heart ECs and MCs was obtained mostly from *in vitro* studies on mature vascular ECs or MCs in a simplified environment, such as a flow chamber. In the living embryonic heart, cardiac cells are subjected to a combination of biomechanical stresses and strains, which vary dynamically over a cardiac cycle as the result of pulsatile blood flow and active contraction of the myocardium. The variations and combinations of biomechanical stimuli have not been fully characterized in embryonic hearts *in vivo*. Responses of MCs and ECs to the

biomechanical stimuli may be important for embryonic heart function and morphogenesis.[24, 46, 47] To understand the roles of biomechanical factors in heart development, we need to quantify the biomechanical environment that embryonic cardiac cells experience *in vivo*.

### 1.1.3 Chick embryonic heart and the outflow tract

The chick embryo is a popular animal model for cardiac development, because chick embryos: (1) share similar morphological and genomic patterns as mammals;[1] (2) grow externally, isolated from the influence of the mother's circulation, which allows easy measurement and microsurgery; (3) develop rapidly (about 21 days of incubation).[48, 49] According to Hamburg-Hamilton (HH) staging system, the development of a chick embryonic heart is divided into 46 stages (21 days of incubation); each stage is judged by the appearance of external features of chick embryos.[48, 49]

At HH18 (3 out of 21 days of incubation, and approximately corresponding to 28-day human embryo), the chick heart is a tiny s-shape looped tube (< 2mm) with no valves and a single primitive atrium and ventricle connected in a series (see Figure 1.1A).[50] The OFT is the distal region of the heart that connects the ventricle with the aortic sac in the primitive heart tube.[50] The chick heart beats at 2-2.5 Hz, and dynamically pumps blood to support embryo development. At this early developmental stage, contraction of the heart wall propagates along the heart wall towards the OFT to maintain unidirectional blood flow.[51, 52]

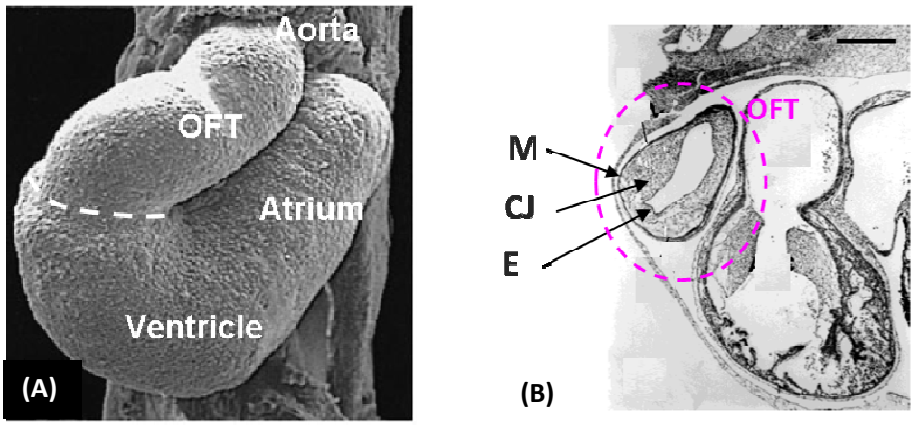


**Figure 1.1** S-shaped chicken embryonic heart and the outflow tract (OFT) at early stages: (A) Scanning electron microscopic image showing external structures of the OFT, reproduced from the literature [50] (with permission); (B) histological section showing internal structures of the OFT, reproduced from the literature[56] (with permission). E, endocardium; CJ, cardiac jelly; M, myocardium.

The OFT provides a good model system to study biomechanical factors in cardiac morphogenesis, mainly because: (1) the OFT, where portion of ventricular septa and semi-lunar valves form, undergoes extensive morphogenetic remodeling during development; (2) the morphogenesis of the OFT is particularly sensitive to biomechanical disturbances, especially during early stages (e.g., HH18);[11, 21] and (3) malformations of the OFT contribute to a large proportion of CHDs.[53]

At HH18, the OFT is a slightly curved tube (300-400 μm in diameter and 600-800 μm in length) with a three-layered wall consisting of endocardium, cardiac jelly, and myocardium (see Figure 1.1B).[50, 54-56] The endocardium is an EC monolayer lining the lumen of the OFT. The myocardium is an external muscle layer that provides active contraction. In between the myocardium and endocardium is the cardiac jelly, an amorphous extracellular matrix that contributes a large portion of the OFT wall. Cardiac

cushions in the OFT, which serve as primitive valves, are seen as localized protrusions of the cardiac jelly toward the lumen.[49, 56] Most knowledge of the OFT geometry was obtained from scanning electron microscopy and histological section slices,[50, 57] and therefore reconstructed 3D geometries are static and are subjected to errors from sample preparations. A 4D description of the OFT is critical to characterize the dynamic biomechanical environment and its roles in regulating the function and morphogenesis of the OFT, but is difficult due to the small size (<2 mm) and fast heart rate (2.5 Hz) of the chick embryonic heart at early stages.

### 1.1.4 Outflow tract banding model

To understand the roles of biomechanical factors in heart development, interventional experiments performed on animal models are designed to disturb hemodynamics or wall dynamics in order to reproduce human-like heart defects.[12, 13, 23, 58] OFT banding (OTB) is a common microsurgery procedure performed on chick embryonic hearts by constricting OFT lumen area with a 10-0 nylon suture. With OTB, ventricular pressure increases acutely and persistently with no significant changes in heart rates or cardiac outputs.[15, 59] In response to the persistent high blood pressure, the primitive ventricle remodels, and exhibits chamber dilation and elongation,[25] thickening of the compact myocardium,[25] and heart wall stiffening[16] at later stages. OTB eventually leads to a spectrum of structural defects in the chick heart, such as the double-outlet right ventricle, persistent truncus arteriosus, and ventricular septal defect; most of these heart defects are associated malformation of the OFT region.[12] However, other aspects of biomechanical changes, such as wall dynamics and blood flow dynamics, were under- characterized in OTB

embryos, although the important roles of blood flow dynamics[13, 14] and wall dynamics[58] have been well recognized in heart development. Alterations in the diameter of the banded OFT may produce a large change in laminar flow after the band, and contribute to OFT abnormalities at later stages.[12] From our preliminary study, we have observed changes in wall dynamics of the OFT in response to OTB.[60] These changes lead to the question of how OTB-induced alterations in the wall dynamics and blood flow dynamics of the OFT result in a biomechanical environment that eventfully leads to heart defects. Precise visualization and quantification of morphological changes, wall dynamics, and blood flow dynamics in the chick heart under normal or altered developmental environments is critical to determine the roles of the biomechanical environment on cardiac function and morphogenesis.

### 1.1.5 Optical coherence tomography to visualize the microstructure and blood flow of embryonic hearts

Optical coherence tomography (OCT) is a powerful imaging technique that offers high-resolution, non-invasive imaging of microstructures up to a depth of 2 mm in biological tissues.[61, 62] OCT is based on Michelson interferometry. OCT imaging is similar to that of ultrasound B-mode imaging except that OCT measures the echo time delay and intensity of coherently gated backscatter light instead of acoustic waves.[63, 64] The advantages of OCT over other widely used imaging modalities in developmental biology are: (1) compared to MRI and micro-CT, OCT provides real time, non-invasive imaging without touching the sample; and (2) compared to confocal microscopy[43, 65] and ultrasound biomicroscopy,[66] OCT combines the μm-scale high-resolution of confocal

microscopy with the mm-scale large depth-of -field in tissues of ultrasound. Thus OCT is especially suitable for imaging the dynamic structure of the embryonic heart at early developmental stages (<1 mm).[67, 68]

*Imaging the microstructure of embryonic hearts*

The potential of OCT in visualizing and quantifying the morphology and functional properties of the embryonic heart has been demonstrated in many model systems including Xenopus laevis,[69] chick,[60, 68, 70-72] and mouse embryos.[70] Current development of OCT allows studies of the dynamics of the chick embryonic heart in 2D.[60, 71, 72] Recently, Yelbuz et al. performed ex vivo 3D OCT imaging of fixed, nonviable chick embryonic hearts, showing the changes in 3D microstructures of abnormal chick embryonic hearts. [68] A first demonstration of direct 4D OCT imaging were performed on excised, electrically paced chick and mouse embryonic hearts.[70] However, 3D dynamic geometry of beating hearts in real time remains challenging for OCT (and most imaging systems) , because the current rate of image acquisition (up to 20 cardiac volumes per second) is not fast enough to study the dynamics of the beating embryonic hearts in 3D (typical heart rate at 2.5 Hz for HH18 chick embryos).[73] A strategy for 4D (3D+time) imaging is needed to extend the utility of OCT to better visualize and quantify the dynamics of embryonic hearts *in vivo*.

*Imaging blood flow in the embryonic heart*

Combined with laser Doppler flowmetry, OCT can simultaneously measure blood flow during structural imaging.[67, 68, 70] OCT and other flow-imaging techniques, such as Doppler ultrasound, and particle image velocimetry (PIV), have been used to measure

intracardiac blood flow in chick embryonic hearts.[60, 74-78] However, to my knowledge, none of these techniques provides sufficient temporal and spatial resolution of 3D blood flow field in the tiny, dynamically beating embryonic heart *in vivo*, especially near the moving heart wall, for accurately quantifying WSS (see Section 1.1.6).[22, 75, 79] To circumvent the challenges in intracardiac flow imaging, CFD modeling seems a more promising alternative for quantifying flow field in the embryonic heart.

### 1.1.6 Computational fluid dynamics to quantify hemodynamic forces in embryonic hearts

*Hemodynamic forces*, including WSS and transmural pressure, are blood-flow induced biophysical forces that act on the heart wall. Transmural pressure, the component of hemodynamic forces perpendicular to the wall, is equal to the difference of the intracardiac blood pressure and the pressure outside the heart wall. A servo-null micro-pressure measurement system, a well-established technique in developmental cardiovascular research, is used to measure blood pressures. (e.g.,[80-82]). WSS is the tangential component of hemodynamic forces to the wall that blood flow exerts on the endocardium. There is no direct way to measure WSS *in vivo*. WSS is calculated from intracardiac blood flow field using the equation:

$$\boldsymbol{\tau} = \mu \cdot d\mathbf{V}/d\mathbf{n} \tag{1.1}$$

where μ is the blood viscosity (μ is constant for a Newtonian fluid); **V** is the blood flow velocity vector; **n** is a unit vector normal to the lumen-wall surface; and $d\mathbf{V}/d\mathbf{n}$ is the directional derivative of the velocity in the normal direction to the lumen-wall surface.

CFD produces a detailed description of pressure and velocity fields by solving Navier-Stoke equations that governs blood flow in the embryonic heart. Finite element (FE) modeling is one common approach to solve CFD problems. The general procedure of FE modeling is shown in Figure 1.2. Using FE analysis, the complex geometry of the embryonic heart is discretized into many regular elements.[83] Partial differential governing equations, i.e., Navier-Stokes equations, are correspondingly discretized into a set of algebraic equations and are solved at the element level. To solve the partial differential equations, boundary conditions (i.e., flow velocities or pressures) are prescribed at the inlet and outlet boundaries of the OFT. To simulate the transient blood flow within a cardiac cycle, initial conditions (i.e., flow velocities and pressures) are prescribed over the entire OFT fluid domain at time zero.

An image-based FE model is generated from an anatomical detailed geometry of the OFT obtained from imaging. Given physiological boundary conditions, it can provide a realistic representation of cardiovascular flow dynamics.[84-87] Another advantage of image-based FE modeling is that it can be used to study the influence of hemodynamic parameters such as geometry, wall motion, and blood rheology on flow patterns.[88] Image-based FE modeling has been widely used to quantify the blood dynamics in the mature cardiovascular system.[86, 89, 90] Image-based FE models have also been applied to simulate the blood flow and WSS in early human and chick embryonic hearts.[21, 91] However, those FE models assumed that the blood flow was steady-state, which oversimplified the realistic blood flow in the embryonic heart. A dynamic image-based FE model is necessary to capture blood flow dynamics and temporal variations of WSS within the cardiac cycle in the embryonic heart.

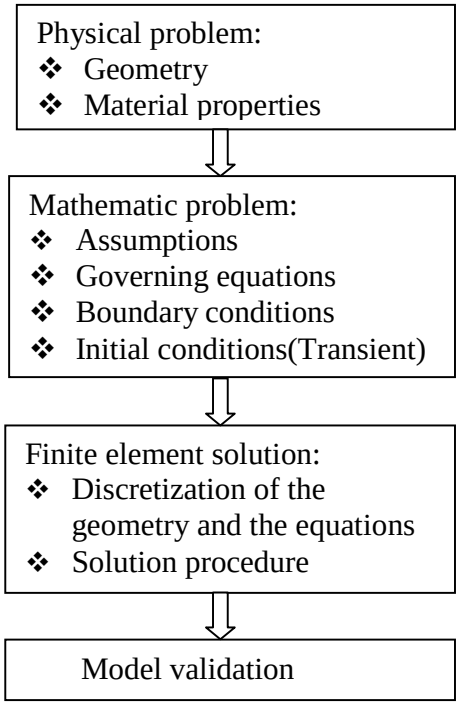


**Figure 1.2** Schematic procedures of Finite Element modeling.

## 1.2 Thesis objectives

The research in this thesis is part of a large collaborative research project in which the roles of biomechanical factors in the development of chick embryonic hearts are investigated in different aspects. The microstructure and blood flow of chick embryonic hearts are measured using the state-of-the art OCT system, which was built and optimized for imaging the chick embryonic heart by Dr. Ruikang Wang' lab. The physiological and genetic responses of chick embryonic hearts are characterized by Dr. Kent Thornburg's lab. The biomechanical behaviors of chick embryonic hearts including blood pressure, wall dynamics, and blood flow dynamics were characterized by Dr. Sandra Rugonyi's lab. My thesis research focused on the OFT of the chick embryonic heart at HH18.

The objectives of this thesis were (1) to develop a methodology that combines imaging, physiological data, and CFD to quantify the wall dynamics and flow dynamics of the OFT *in vivo*; (2) to characterize the biomechanical environment to which cardiac cells on the OFT wall are subjected within the cardiac cycle. The specific aims of this thesis were to

1. Develop a 4D imaging strategy to image *in vivo* the heart OFT in chick embryos using OCT;
2. Develop image analysis algorithms (image reconstruction and segmentation) to process 4D OCT image data of the OFT for better visualizing and quantifying the OFT wall dynamics;
3. Develop CFD models to quantify blood flow patterns in the OFT;
4. Characterize the biomechanical environment (strains and stresses) which cardiac cells on the OFT wall are subjected to within a cardiac cycle *in vivo*;
5. Characterize the acute responses in wall dynamics and hemodynamics in the OFT after one hour of OTB.

## 1.3 Thesis outline

Chapter 2 presents a non-gated 4D imaging strategy and a post-acquisition synchronization procedure for imaging the chicken embryonic heart using OCT. The 4D image strategy circumvents limitations on acquisition rate of current 4D imaging techniques for embryonic hearts. We demonstrated the efficiency and accuracy of the synchronization procedure by reconstructing the cardiac OFT of a chick embryo from

OCT images. We also showed that the reconstructed 4D images capture the dynamics of the OFT wall motion.

Chapter 3 presents a 3D image segmentation algorithm for delineating the OFT wall from OCT image sequences. The segmentation algorithm consists of the optical flow algorithm for rough segmentation of the OFT; and deformable models (active contour and active surface algorithms) for fine segmentation of the OFT. The performance of algorithm was evaluated with a 2D+time OCT image sequence and two 3D volume OCT images of the OFT. The segmented results were validated against manual segmentation. We applied the algorithm to a 4D OCT image dataset of the OFT to segment the dynamic 3D geometry of the OFT of a HH18 chick embryo.

Chapter 4 presents a simplified 3D FE model of the cardiac OFT of chick embryos at HH18. The geometrical parameters of the FE model were estimated from time series of OCT images of the OFT cross-section. Using this simple model, we investigated the effects of wall motion pattern (instantaneous vs. peristaltic motion), and cardiac cushion (geometric shape of cross-section) on the blood flow pattern and distribution of WSS in the OFT over the cardiac cycle. We found that the magnitude and pattern of wall motion affected blood flow dynamics in the OFT lumen. We also found that the presence of cardiac cushions altered the spatial distribution of blood flow velocities in the lumen of the OFT and resulted in an increase of WSS at cushion regions. The finding suggests that an image-based 3D dynamics FE model is necessary to capture the flow dynamics in the OFT *in vivo*.

Chapter 5 presents an image-based 3D dynamic FE model of the heart OFT of a

normal chick embryo at HH18. The FE model took into account physiologically pulsatile pressures imposed at the inlet and outlet of the OFT, and the dynamic wall motion obtained from 4D OCT images. We validated the model with flow measurement from Doppler ultrasound. The 3D dynamic FE model revealed a distinct blood flow field and a transient heterogeneous distribution of WSS over the cardiac cycle in a HH18 chick heart OFT.

In Chapter 6, we characterized the dynamic biomechanical environment of the OFT within a cardiac cycle *in vivo*. We employed a methodology that combined *in vivo* 4D imaging, image analysis, and FE modeling (developed in Chapters 2 to 5). From 4D OCT image datasets of the OFT of normal chick embryos, we characterized for the first time the wall dynamics of the OFT over the cardiac cycle, and analyzed the circumferential and radial strains that myocardium and/or endocardium experience *in vivo*. From the FE model of a representative chick OFT, we quantified the blood flow dynamics and flow-induced shear stress on the endocardium. Our results showed that cardiac cells in the OFT are subjected to a combination of biomechanical stimuli, and that the biomechanical environment to which the cardiac cells are subjected varies over the cardiac cycle and over spatial locations on the OFT wall. The unique biomechanical environment may be important for the extensive remodeling and morphogenetic events that occur later in the OFT.

In Chapter 7, we quantified the acute changes in the wall dynamics in the OFT after one hour of OTB. From 4D OCT image datasets of the OFT after OTB, we analyzed the wall dynamics and wall strains of the OFT. We found that the OFT has shown early signs

of compensational changes in the wall dynamics and blood flow dynamics after one hour banding. Consequently, the spatial distribution of the biomechanical stresses and strains was altered in the OFT wall, especially near the banding site. The changes in the biomechanical environment to which the cardiac cells on the OFT wall may predispose the functional and structural abnormalities in the OFT reported in OTB chick embryos at later developmental stages.

Chapter 8 summarizes our findings and contributions, and provides recommendations for future research.

# Chapter 2: Efficient post-acquisition synchronization of 4D nongated cardiac images obtained from optical coherence tomography: application to 4D reconstruction of the chick embryonic heart

Aiping Liu, Ruikang Wang, Kent L. Thornburg, Sandra Rugonyi

*This chapter was originally published by SPIE*

*in Journal of Biomedical Optics, 2009(4), 044020.*

*Reprinted with permission*

## 2.1 Introduction

During embryonic development, the heart undergoes a complex morphogenetic process that forms a primitive beating tubular heart, which ultimately becomes a four-chambered heart.[1, 5] Cardiac structure and function interact during this process to ensure normal cardiac development,[18] and disturbances can lead to congenital heart defects (e.g., [12, 14, 58]). Four-dimensional (4-D) imaging [imaging of three-dimensional (3-D) structures over time] of the embryonic heart at early stages of development, when the heart is an unseptated tube, is challenging due to the small dimensions of the heart (e.g., typically <2 mm.[50]) and the rapid cardiac motion (typically, more than two heartbeats per second[81]).

Optical coherence tomography (OCT) is a powerful imaging technique that can be applied to the visualization and quantification of morphological and functional properties of the heart during development. The technique offers high-resolution, noninvasive

imaging of microstructures up to a depth of 2–3 mm in biological tissues.[61-64] Compared to other non-invasive imaging modalities, such as confocal microscopy[43, 92] and high-frequency ultrasound,[66] OCT combines the high-resolution (at micrometer scale) capabilities of confocal microscopy with the large depth of field in tissue (at millimeter scale) of ultrasound. Thus OCT is especially suitable for imaging the embryonic heart at early developmental stages.[67, 68, 70] OCT has been used to image the embryonic hearts of frog,[93, 94] chick,[60, 68, 70, 71] and mouse.[70, 95]

OCT has been applied to 4–D imaging of *Xenopus laevi* and quail embryonic hearts;[73, 94] however, the current rate of image acquisition (up to 20 cardiac volumes per second) is not fast enough to study the dynamics of the beating embryonic hearts.[73] To circumvent limitations in the image acquisition rate, 4D cardiac images can be reconstructed by post-processing two-dimensional (2-D) image sequences (B-mode images) that together span the entire heart. This 4D cardiac imaging procedure requires synchronization of B-mode images to enable proper reconstruction of the 3-D geometry of the heart at sequential phases (time points) over the cardiac cycle. To synchronize 2-D image sequences, two approaches have been used:[96] (*i*) the prospective-gated (or hardware-gated) approach, in which acquisition of image sequences is triggered at a particular (known) phase of the cardiac cycle by a cardiac signal, and therefore, the acquired image sequences are synchronized (in phase), and (*ii*) the retrospective-gated (or nongated) approach, in which acquisition of image sequences is not triggered; hence, image sequences start at random phases of the cardiac cycle and image post-processing is required to synchronize them. Jenkins et al.[97] performed prospective-gated OCT imaging of the heart of an early developing chick embryo, triggering image acquisition with

signals obtained by a laser Doppler velocimeter from a vitelline vessel. Mariampillai et al.[98] performed retrospective-gated OCT imaging of a chick embryonic heart using Doppler velocities: during acquisition of B-mode structural images of the chick heart, they simultaneously collected Doppler signals from an aortic arch with a separate Doppler OCT system. Then, Doppler data were used to synchronize B-mode image sequences. The advantage of Mariampillai's imaging strategy was that imaging and image reconstruction were uncoupled. However, as with the prospective gated strategy, cardiac gating signals were needed to provide time stamps for post-acquisition synchronization. Therefore, errors introduced by weak gating signals—often encountered in the embryonic developing heart—affected the accuracy of 4D reconstruction. To eliminate the need of additional cardiac signals, Liebling et al.[65, 99] developed a retrospective-gated imaging strategy and image reconstruction procedure, and applied them to 4D imaging of the zebra-fish heart. In their approach, nongated B-mode images of the zebra fish heart were acquired using confocal microscopy at different depths, spanning the whole heart. Then, B-mode images were synchronized by invoking structural similarity between adjacent image sequences. To achieve computational efficiency of the synchronization algorithms, Liebling et al.[65, 99] used a subset of the wavelet series representation of the images for data reduction.

In this paper, we present an alternative nongated 4D imaging strategy combined with a simple and efficient post-acquisition synchronization procedure to reconstruct 4D images of the *in vivo* embryonic heart. B-mode images of transverse sections of the heart are acquired without gating. To achieve computational efficiency, our post-acquisition synchronization procedure uses M-mode images (line scans over time),[100] extracted from

the B-mode images; synchronization of adjacent image sequences is then achieved by applying structural similarity along a line. In our procedure, we found that synchronization of image data based on similarity of local structures alone does not fully recover the peristaltic-like motion of the embryonic heart wall, which introduces phase lags in cardiac wall motion. Our synchronization procedure accounts for this phase lag by adjusting the phase of each image sequence after synchronization based on structural similarity was performed. We applied the nongated 4D imaging strategy and post-processing synchronization procedure to OCT images of the cardiac outflow tract (OFT) of a chick embryo. We studied the chick embryo because at early stages, cardiac development in the chicken is similar to that in humans;[1] the chick embryonic heart is also easy to access and develops faster than most other animal models.[101] OCT images of the OFT were acquired *in vivo* at an early developmental stage, Hamburger–Hamilton (HH) 18 (3 days of incubation).[48] At this early stage of development, the chick heart is tubular and has no valves; the OFT is the distal region of the embryonic heart—connecting the ventricle with the arterial system—and functions as a primitive valve by contracting to limit blood flow regurgitation. The OFT is a crucial cardiac segment to study because a large portion of congenital heart defects originate in the OFT.[53] The OFT is also a good region for testing the capability of our reconstruction procedure to capture peristaltic-like motions of the heart wall.

Section 2 of this chapter presents the 4D imaging strategy and image post-acquisition synchronization procedure. Section 3 presents the application of the presented procedure to images of the chick embryonic OFT and tests of its accuracy. Finally, Section 4 presents a brief discussion, and Section 5 gives the conclusions to the paper.

## 2.2 Imaging Strategy and 4D Image Reconstruction Procedure

### 2.2.1 Nongated 4D Imaging Strategy

The nongated 4D imaging strategy used (illustrated in Figure 2.1) is similar to that used by Liebling et al.[99]

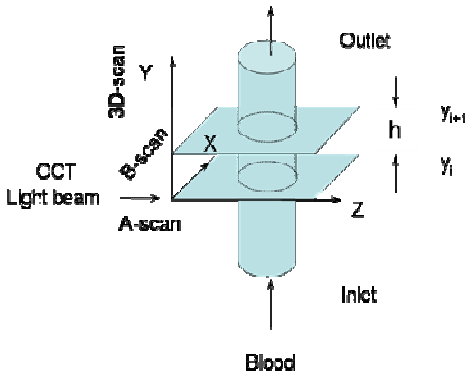


**Figure 2.1** Schematic representation of nongated 4-D image acquisition.

B-mode image sequences are collected at successive imaging planes (*X*-*Z* planes along the *Y* direction in Figure 2.1): starting at $y_1$=0, OCT acquires a sequence of 2-D cross-sectional images (*X*-*Z* plane) for approximately five cardiac cycles, and then the imaging plane moves longitudinally an increment *h* to the next cross section. Image acquisition is then repeated until the whole region of interest is spanned and $y_L$ is reached. The value of the distance *h* between adjacent image planes is kept small so that structural imaging data at adjacent locations are similar. An image sequence of a longitudinal cardiac section (*Y*-*Z* plane in Figure 2.1) is also acquired to adjust phase lags later. Therefore, a 4D image data set consists of *L* sets of B-mode cross-sectional image sequences acquired along the *Y* direction and a B-mode image sequence of a longitudinal

section. Because OCT image acquisition is nongated, acquired image sequences are out of phase. To reconstruct 4D images of the heart, image sequences need to be synchronized; that is, the phase relationship between imaging sequences needs to be determined.

### 2.2.2 Post-acquisition Synchronization Procedure

Our synchronization procedure assumes that (*i*) motion and deformation of the heart are periodic and (*ii*) changes in cardiac structural features are continuous (structural data in B-mode images acquired at adjacent locations are similar).

To synchronize the acquired image sequences, the following steps are performed:

1. determination of the cardiac period for each image sequence,
2. determination of relative phase shifts between neighboring image sequences,
3. determination of absolute phase shifts of image sequences relative to the first image sequence,
4. estimation and adjustment of phase lags between image sequences introduced by peristaltic-like motions of the heart wall,
5. synchronization of image sequences and 4D image reconstruction.

Compared to Liebling's synchronization procedure,[99] our procedure has three major differences. First, to achieve computational efficiency, rather than using a subset of the image wavelet series, our synchronization procedure analyzes M-mode images that are extracted from the image sequences (see Figure 2.2). Representing a B-mode image sequence at a location $y_i$ by the intensity function $I_{y_i} = (x, z, t)$, an M-mode image

extracted along a vertical line $x = x_k$ of the B-mode sequence is $I'_{y_i} = I_{y_i}(x, z, t)$. Second, to improve the accuracy of the synchronization procedure, instead of keeping image frames in a sequence in the order they were acquired and cropping image data to a whole number of cardiac cycles (to apply the synchronization algorithm), data from image sequences (spanning approximately five cardiac cycles) are pooled into one normalized cardiac cycle. Third, to accurately recover the dynamic motion of the heart, we provide a procedure to estimate and adjust phase lags between adjacent image sequences introduced by peristaltic-like contractions of the heart wall. This later step may not be necessary, however, if imaging is performed at non-transversal planes of the heart (such as longitudinal planes). In Sections 2.2.2.1–2.2.2.5, we describe each step of the synchronization procedure.

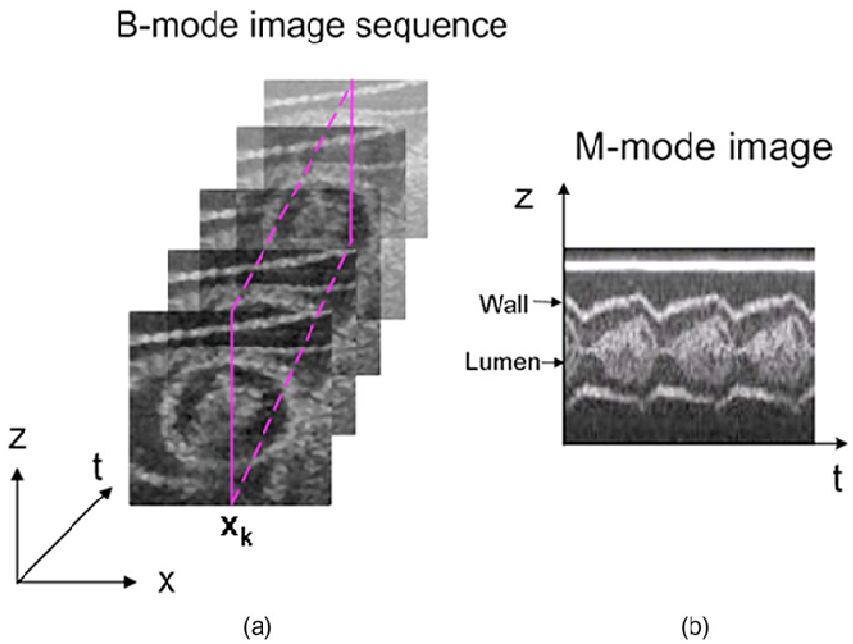


**Figure 2.2** Illustration of M-mode image extraction from a B-mode image sequence: (a) B-mode image sequence and (b) M-mode image extracted along a line ($x = x_k$) from (a).

#### 2.2.2.1 Determination of cardiac period

Because our synchronization procedure relies on the periodicity of the cardiac cycle, the cardiac period must be known to ensure proper synchronization of image sequences and to pool data from image sequences to a normalized cardiac cycle. To adjust for small variations in period that occur during imaging (mostly due to temperature fluctuations), we calculate the cardiac period, $T(y_i)$, of each of the $L$ image sequences at locations $y_i$. To calculate $T(y_i)$, we use a string-length method (SLM).[102, 103] SLM is particularly well suited for determining periods in cases of relatively few observations (a few cycles) when conventional methods, such as the Fourier transform, fail to provide reliable results.[104] SLM assumes that periodic signals, discretely sampled over several cycles, are continuous. Then, if the period of the signal is known, the phase (time position within the cycle) of each data point can be determined, and "strings" (line segments) that join successive data points (arranged by their phases) have the shortest total length. Hence, the period minimizes the total length of strings. In our implementation of the SLM algorithm, the cardiac period, *T*, of each image sequence is determined from the M-mode image extracted from that sequence. Each vertical line in the M mode consists of *M* pixels, and the horizontal line of *N* pixels, where *N* is the number of images in a sequence (each acquired at a distinct time $t_n$). Each pixel in the M-mode image ($M \times N$ pixels in total) is a data point, and the magnitude of each point is the intensity, denoted as $I'_{y_i}(z_m, t_n)$. Giving a candidate period $T'$, the phase, $p_n$, of each data point is

$$p_n = t_n - \lfloor t_n/T' \rfloor T' \ (n = 1, \dots, N) \tag{2.1}$$

where $\lfloor . \rfloor$ denotes integer part. Using $p_n$, vertical lines in the M-mode image are

resequenced by their phases such that $p_{n-1} \leq p_n \leq p_{n+1}$. The total length, *D*, of the strings is

$$D^2(y_i, T') = \sum_{m=1}^{M} \sum_{n=2}^{N} \left[ \left| I'_{y_i}(z_m, p_n) - I'_{y_i}(z_m, p_{n-1}) \right|^2 + |p_n - p_{n-1}|^2 / T'^2 \right] \quad (2.2)$$

The right-hand side terms in Eq. (2.2) are the differences in magnitudes and in phases of two consecutive pixels in the re-sequenced M-mode image and are functions of $T'$. To give equal weights to both terms,[103] $I'_{y_i}$ and $p_n$ are normalized, such that their values lie into the range $[0, 1]$.

The cardiac period $T(y_i)$, is found by minimizing the string length$D(y_i, T')$

$$T(y_i) = \min_{T'} D^2(y_i, T'), \qquad T' \subseteq [T_{min}, T_{max}] \quad (2.3)$$

The string length $D(y_i, T')$ is a nonconvex function of $T'$with several local minima. Thus, searching algorithms based on gradient methods might be trapped in local extremes,[105] and direct searching for *T* was used here within a range $[T_{min}, T_{max}]$.

#### 2.2.2.2 Determination of relative phase shift between adjacent image sequences

To synchronize nongated image sequences, we determine the temporal relation (or phase shift) between adjacent sequences assuming structural similarity. We find the phase shift by maximizing the similarity of M-mode images—extracted along the same line $(x = x_k)$ from two adjacent B-mode image sequences. Thus, we performed structural similarity along a line of the image sequences.

To improve the accuracy of the synchronization, which is limited by image acquisition rate, we pooled M-mode image data (from several cycles) into one cardiac cycle,

rearranging vertical lines by their phases. The algorithms to determine phase shifts (described below) require M-mode images with the same number of vertical lines, equally spaced in time. To accomplish this, we normalized the cardiac cycle and re-sampled each M-mode image with the same number (*K*) of evenly phase-distributed vertical lines. Re-sampling was performed using cubic spline interpolation, which offers the best cost-performance tradeoff among available interpolation methods.[106, 107]

Structural similarity between two re-sampled M-mode images, $I'_{y_i}(z, p^*)$ and $I'_{y_{i+1}}(z, p^*)$, extracted from adjacent image sequences was calculated using a correlation coefficient $C_{i,i+1}$ between the M-mode images as the similarity index,

$$C_{i,i+1}(s) = \sum_{m=1}^{N} \sum_{n=1}^{K} I'_{y_i}(z_m, p_n^*) I'_{y_{i+1}}(z_m, p_n^* - s) \tag{2.4}$$

where *s* is a candidate phase shift and *p** is the phase in the normalized cardiac cycle. The phase shift, $S_{i,i+1}$, between the two adjacent image sequences is then found by maximizing the similarity index $C_{i,i+1}(s)$,

$$S_{i,i+1} = \max_{s} C_{i,i+1}(s), \quad s \subseteq [0,1] \tag{2.5}$$

#### 2.2.2.3 Determination of absolute phase shift with respect to a reference sequence

The next step is to synchronize the image sequences with respect to a common reference sequence. Taking the first image sequence$(y_1 = 0)$ as the reference, the absolute phase shift $S_i$ —the phase shift between a sequence at $y_i$ and the reference—is the accumulated sum of relative phase shifts (between adjacent image sequences),

$$S_i = \sum_{j=1}^{i-1} S_{j,(j+1)} \text{ , with } i = 1,2,\dots,L \text{ and } S_1 = 0 \quad (2.6)$$

### 2.2.2.4 Estimation and adjustment of phase lag for all image sequences

During early developmental stages, contractile cardiac waves travel from the heart atrium to the OFT,[51] producing a peristaltic-like motion of the heart wall and introducing phase lags among different regions of the heart. To estimate these phase lags $(p_{lag})$ between adjacent image sequences, we use data from the acquired image sequence showing the longitudinal section of the heart. Two M-mode images are extracted at two locations a distance *d* apart along the longitudinal cardiac section (see Figure 2.3).

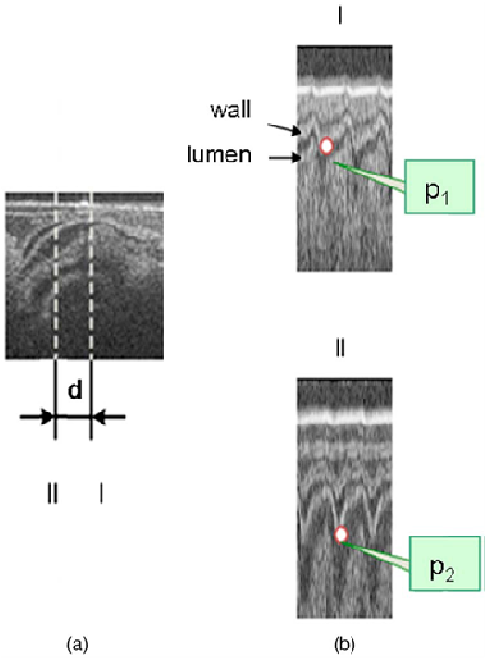


**Figure 2.3** Illustration of how phase lags in OFT wall motion are estimated: (a) OCT image of a longitudinal section of the OFT and (b) M-mode images extracted from the longitudinal section at the locations I (close to the OFT inlet) and II (close to the OFT outlet) in (a). Note that M-mode images were magnified and cropped for better visualization. *d* is the distance between locations I and II; $p_1$ and $p_2$ are the phases of maximal OFT wall contraction identified from the M-mode images extracted along lines I and II, respectively.

The phases of maximal cardiac contraction, $p_1$ and $p_2$, are then identified from the M-mode images, and the phase lag, $\Delta p$, between these two locations is calculated. To minimize errors in the estimation of $\Delta p$, we average $\Delta p$ over several cycles, i.e.,

$$\Delta p = \frac{1}{q}\sum_{i=1}^{q}(p_1^i - p_2^i) \tag{2.7}$$

where *i* represents the *i*th cardiac cycle and *q* is the number of sampled cardiac cycles. Assuming that the velocity of the contractile wave, *v*, is constant in the cardiac region under consideration,

$$v = d / \Delta p \tag{2.8}$$

The phase lag between two adjacent image sequences a distance *h* apart is then estimated by

$$p_{lag} = h/v \tag{2.9}$$

The adjusted absolute time shifts, $S_i'$, are then calculated by

$$S_i' = S_i + (i-1)p_{lag} \tag{2.10}$$

The assumption of constant *v* holds approximately true in relatively small regions of the heart (such as the OFT), and hence to achieve accurate reconstruction, phase lags should be evaluated at each individual region.

**2.2.2.5 Reconstruction of 4D images**

To reconstruct 4D cardiac images from a nongated data set, images in image sequences are shifted in time according to adjusted phase shifts $(S_i')$. We then pooled the images to a normalized cardiac cycle and resampled images at *P* selected equally spaced phases over the cardiac cycle, using linear interpolation between images. We then assembled 2-D images into 3-D image datasets at the *P* phases and reconstructed 4-D images of the heart.

## 2.3 Application to 4D Images of the Chick Heart OFT

Our imaging strategy and synchronization procedure were used in imaging the heart OFT of chick embryos at stage HH18 (approximately three days of incubation). OFT images were acquired with OCT, and the algorithms to calculate cardiac period and phase shifts were tested for accuracy and sensitivity to the line chosen to extract M-mode images.

### 2.3.1 Embryo Preparation

Fertilized white leghorn eggs were incubated blunt-end up at 38 °C and 85% humidity in a horizontal rotation incubator to stage HH18.[48] To expose the embryonic heart, the egg shell was opened and the membrane overlaying the embryo was removed. During egg manipulation and imaging, temperature of the embryo was allowed to drop below its normal physiological temperature (38 °C), which allowed the heart rate to drop.

### 2.3.2 Image Acquisition with OCT

A spectral domain OCT system was used to acquire images of the OFT of a chick embryo at HH18. OCT acquired 40 B-scans (2-D image frames, see Figure 2.1) per second; with each B-scan composed of 250 A-scans (line scans). The OCT system employed has 10 µm axial (*Z* in Figure 2.1) and 16 µm lateral (*X* and *Y* in Figure 2.1) spatial resolutions and a light penetration depth of 2.0 mm in tissue (assuming a refractive index of 1.35). Because at the early developmental stages under study the chick tissue is almost transparent, light penetration depth is further limited only by blood, such that the practical penetration depth when imaging the OFT is 1 mm (enough to image the OFT at HH18).

We used the nongated image acquisition strategy described in Sec. 2.1 to obtain a 4D image data set of the OFT. A total of 65 B-mode image sequences of OFT cross sections were taken along the OFT, 12.5 μm apart, spanning the entire OFT region (800 μm in length). Each image was 250×430 pixels, and each image sequence consisted of 185 frames (more than five cardiac cycles). A B-mode image sequence, corresponding to a longitudinal OFT section approximately perpendicular to the center cross section of the OFT, was also acquired to adjust phase lags due to peristaltic-like wall motion in the OFT.

Figures 2.4(a)–(d) show representative OCT images of the OFT. The structure of the OFT wall—the lumen interface, cardiac jelly, and myocardium—is clearly demarcated. We extracted an M-mode image from the dotted line in Figure 2.4(a). The M-mode image [Figure 2.4(e)] traces the periodic displacements of the OFT wall over the acquired cardiac cycles.

### 2.3.3 Testing the Synchronization Procedure

Using the OFT images acquired with OCT, we tested the accuracy of the synchronization procedure and the sensitivity of the procedure to the line chosen to extract M-mode images. We performed the tests on a representative image sequence of the OFT acquired approximately at the center cross section of the OFT [see Figures 2.4(a) and 2.4(c)].

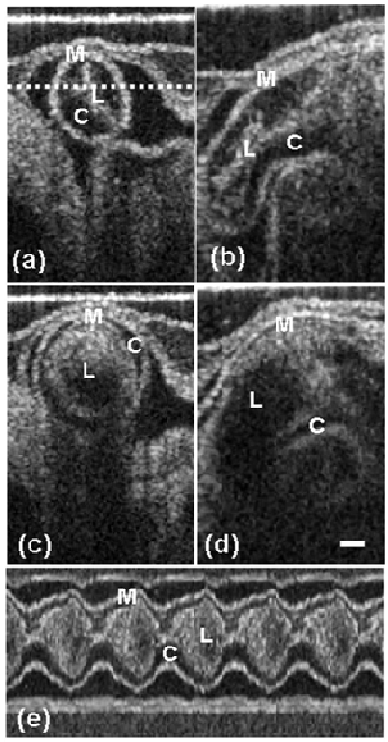


**Figure 2.4** Representative OCT images (in B and M modes) of the heart OFT from an HH18 chick embryo. Images show the OFT when its walls are constricted: (a) cross section of the OFT at about its center and (b) longitudinal section approximately perpendicular to the cross section in (a); and when OFT walls are expanded: (c) center cross section and (d) longitudinal section. In (c) and (d), the dark areas in the lumen are due to a transient fading of signals when image acquisition rate is lower than the speed of blood flow. (e) An M-mode image generated from the cross-sectional image sequence along the dotted line in (a). M, myocardium; C, cardiac jelly; L, lumen. Scale bar=100 μm.

#### 2.3.3.1 Determination of cardiac period

We used the SLM algorithm, applied to M-mode images, to determine the cardiac period, *T*, of the chick embryonic heart from each acquired image sequence (see Sec. 2.2.1). Because during imaging embryo temperature was lower than physiological temperature (see Sec. 3.1), calculated *T* (0.8 s, see below) was higher than normal (usually <0.5 s for an HH18 embryo8). To quantify *T* we used Eq. (2.3), with a search range of cardiac periods from 0.7 to 0.9 s and searching step size of $10^{-4}$ s.

*Accuracy*. To study the accuracy of the SLM algorithm applied to M mode, we compared cardiac periods calculated using SLM applied to M- and B-mode images, as well as calculated using fast Fourier transform[108] (FFT) (FFT was performed on a curve showing the correlation of the images in a sequence with respect to a reference image). To this end,

we used the representative OCT image sequence of the OFT (Sec. 3.3). The cardiac period calculated using FFT ($T$ = 0.7708 s) was not expected to be accurate due to the small data sampling size (only approximately five cycles). The SLM algorithm, in contrast, was accurate and predicted approximately the same solution ($T$ = 0.8146 s) regardless of whether M- or B-mode images were used (the difference was less than the searching step). SLM applied to M-mode images, however, was >200 times faster than SLM applied to B-mode images.

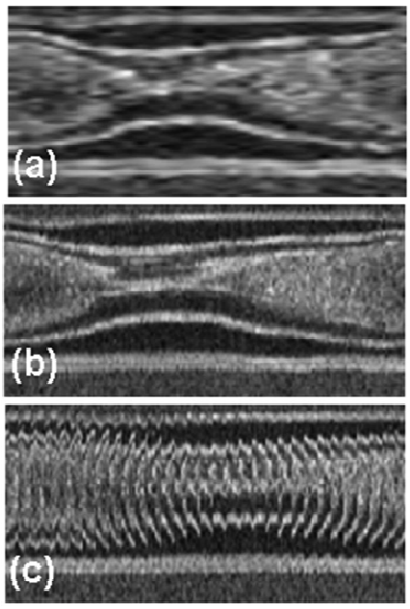


**Figure 2.5** M-mode images extracted from cross-sectional image sequences of the OFT along the dotted line in Figure 2.4(a). Shown M-mode images were extracted from (a) the acquired OCT image sequence, (b) the same OCT image sequence pooled to one cycle using the cardiac period calculated by SLM ($T$ = 0.8146 s), and (c) the same sequence pooled to one cycle using the cardiac period calculated by FFT ($T$ = 0.7708 s). Note that (a) corresponds to one cardiac cycle of Figure 2.4(e).

To verify the accuracy of the calculated $T$, we pooled all the images in the sequence into one cardiac cycle, arranging them by phase according to the calculated $T$. From these pooled sequences, we generated M-mode images along the dotted line shown in Figure 2.4(a). Figure 2.5 shows a comparison of M-mode images extracted from an acquired image sequence [Figure 2.5(a)] and from pooled images [Figures 5(b) and 5(c)]. The M-mode image from the acquired image sequence [Figure 2.5(a)] shows a pixelated view

due to the low image acquisition rate (40 fps). The M-mode image obtained from pooled images arranged according to the *T* calculated from FFT [Figure 2.5(c)] shows that if *T* is inaccurate, the M-mode image looks discontinuous. The M-mode image obtained from pooled images arranged according to the *T* calculated using the SLM [Figure 2.5(b)] is smooth looking and resembles Figure 2.5(a), indicating that the *T* calculated using SLM is accurate.

*Sensitivity to M-mode line*. To test the sensitivity of the SLM algorithm to the line selected to extract the M-mode image from the 2-D image sequences, we extracted M-mode images along horizontal and vertical lines (lines were 130-μm apart, see Figure 2.6) from the representative OCT image sequence. Lines were grouped according to the following criteria: (*i*) lines that overlay the OFT region over the cardiac cycle (H3–H5 and V3–V5); (*ii*) lines that overlay the OFT region only for a time interval during the cardiac cycle (V2, H2, V6, and H6); and (*iii*) lines that lie outside the OFT region (H1, V1, H7, and V7). We calculated *T* using the SLM algorithm applied to these M-mode images (see Table 2.1). We found that SLM was, in general, robust, as long as the lines from which M-mode images were extracted overlaid the OFT during the cardiac cycle (i.e., H3–H5 and V3–V5); the maximum deviation from *T* occurred at V4 and was within 0.1%. The deviation at V4, however, was mainly due to transient fading of signals during imaging (wash-out phenomenon),[109] which occurs when blood flow velocity is much faster than image acquisition rates, resulting in interference signals that average out and appear as a dark region in the lumen [see Figures 4(c) and 4(d)]. Better reproducibility of results was achieved when SLM was applied to M-mode images extracted from horizontal rather than vertical lines. The inferior performance of the M-mode images

from vertical lines was due to both attenuation of signals along the tissue depth and transient fading of signals.

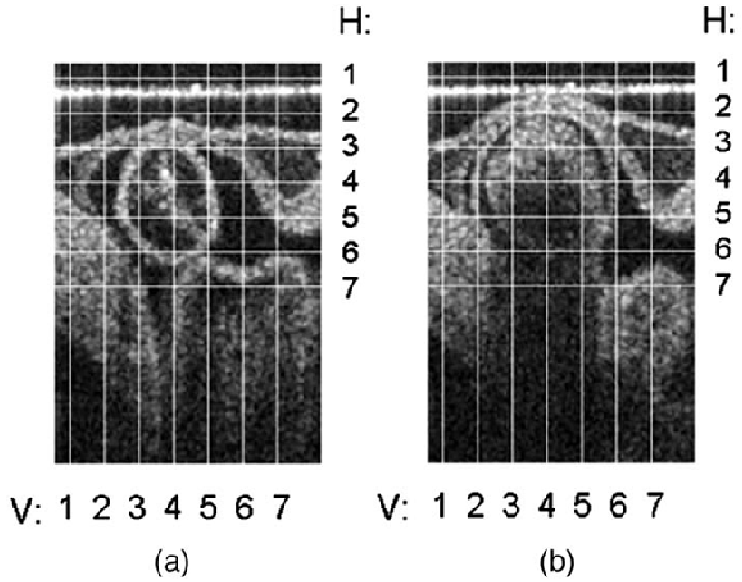


**Figure 2.6** Lines chosen to perform sensitivity study in determining cardiac periods using SLM algorithm applied to M-mode (from the representative sequence shown in Figure 2.4). The panels show the positions of the lines when the OFT walls were most (a) constricted and (b) expanded.

**Table 2.1** Cardiac periods (in seconds) calculated from M-mode images extracted from different lines (see Figure 2.6).

| | 1 | 2 | 3 | 4 | 5 | 6 | 7 |
|---|---|---|---|---|---|---|---|
| H | 0.8180 | **0.8146** | **0.8146** | **0.8146** | **0.8146** | 0.8206 | **0.8146** |
| V | 0.8206 | **0.8146** | **0.8146** | 0.8153 | **0.8146** | **0.8146** | 0.8125 |

Bold numbers show calculated periods that are within 0.01% accuracy with respect to the centerline [shown in Figure 2.4(a)] used to determine the accuracy of SLM.

### 2.3.3.2 Determination of relative phase shift

To calculate phase shifts, $Si,i+1$, between adjacent image sequences, we used a similarity

algorithm that searched for $S_{i,i+1}$ by maximizing the correlation between M-mode images [Eq. (2.5)]. Because each image sequence consisted of 185 frames, $S_{i,i+1}$ was expected to be at least accurate within one frame in a pooled sequence (or $0.005T$).

*Accuracy*. To study the accuracy of the similarity algorithm applied to M-mode images, we first tested the algorithm using synthetically generated image sequences with known relative phase shifts. To obtain the image sequences, we chose the representative image sequence [see Figure 2.4(a) and 4(c)] and, using linear interpolation between frames, we then generated 10 image sequences that were shifted in phase from the representative sequence. Phase shifts were randomly chosen from 0 to $T$. Using these sequences, we compared the performance of the similarity algorithms applied to B- and M-mode images [extracted along the line shown in Figure 2.4(a)] in terms of accuracy and computational efficiency.

We found small errors—with respect to known shifts (maximum 0.3%)—when phase shifts were calculated using similarity on either B- or M-mode images. Calculation of the phase shift using M-mode images, however, was 400 times faster than when using B-mode images.

*Sensitivity to M-mode line*. To study the sensitivity of calculated phase shifts to the line selected to extract the M-mode images, we used the representative image sequence [see Figure 2.4(a) and 4(c)] together with its adjacent image sequence, and applied the similarity algorithm to M-mode images extracted from the two image sequences. According to Sec. 3.3.1, $T$ was more accurate when lines that overlaid the OFT over the cardiac cycle were used to extract M-mode images; therefore, we focused on M-mode

images extracted from these lines. We generated 16 M-mode images extracted from horizontal and vertical lines (50-μm apart, see Figure 2.7), and found the phase shift between the sequences by applying similarity, Eq. (5), to these M-mode images. Calculated phase shifts, $S_{i,i+1} = (0.25 \pm 0.005)T$, for all M-mode lines were within the expected accuracy.

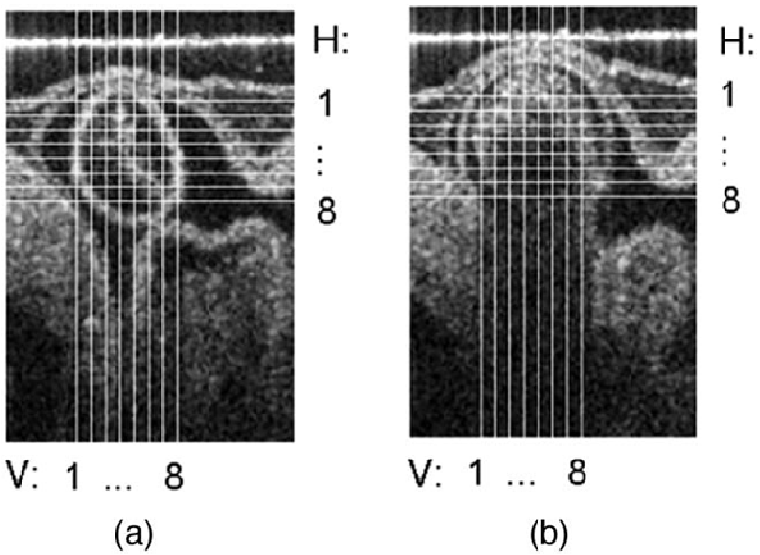


**Figure 2.7** Lines chosen to perform sensitivity study in determining relative phase shifts using similarity algorithms applied to M-mode images (from the representative sequence shown in Figure 2.4). The panels show the positions of the lines when the OFT walls were most (a) constricted and (b) expanded.

#### 2.3.3.3 Reconstruction of 4D images of the OFT

To reconstruct 4D images of the OFT, we used the 4D data set obtained as described in Sec. 3.2. For each OFT cross sectional image sequence, we generated an M-mode image from a horizontal line within the center region of the OFT cross section (e.g., line H4 in Figure 2.6). Then, using the SLM algorithm [Eqs. (2.2) and (2.3)], we determined *T* for each image sequence. Once *T* was determined, we used similarity [Eqs.(2.4) and (2.5)], to determine the relative phase shift between each adjacent image sequence pair. Finally, we

estimated the phase lag among image sequences due to the peristaltic-like motion of the OFT wall [Eqs. (2.8) and (2.9)] from the acquired sequence of OFT longitudinal section images. This phase lag was found to be 0.32*T* from the inlet to the outlet of the OFT, and thus was non-negligible. After calculating absolute phase shifts with respect to a reference sequence [Eq.(2.6)], we corrected for this phase lag [Eq. (2.10)], and then synchronized image sequences according to the adjusted absolute phase shifts. We then reassembled the 2-D images of the OFT into 3-D image data sets at 180 phases of the cardiac cycle, and thus reconstructed 4D images of the OFT. To better visualize the structure and motion of the OFT walls and their interaction with blood flow over the cardiac cycle, 4D images were further analyzed using the image software Amira 3.1 (see Video 2.1).

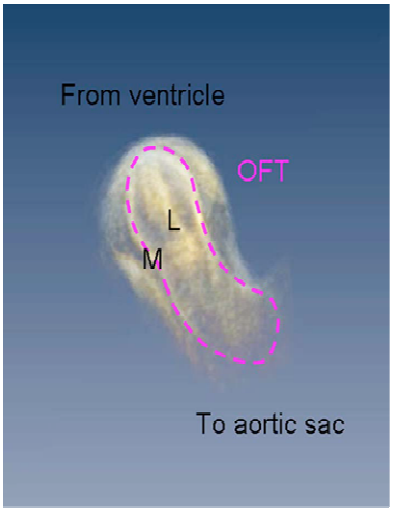


**Video 2.1** Voxel view of a beating chick-embryo OFT. The movie shows a frontal view of the OFT for the first cardiac cycle and then a 180-deg rotation of the OFT along the *Z*-axis for the second cardiac cycle. The dotted line (in the still image) encircles the OFT region that connects the ventricle proximally and aortic sac distally. M: myocardium, L: lumen (Quick-Time, 2 MB). [URL: http://dx.doi.org/10.1117/1.3184462.1]

*Accuracy*. To test the accuracy of the 4D reconstruction, we extracted image sequences showing an OFT longitudinal section over the cardiac cycle from the reconstructed 4D images with and without phase-lag adjustment. By visual inspection, the plane at which OFT longitudinal sections were extracted from reconstructed images was close to the

plane where the OFT longitudinal image sequence was acquired directly with OCT. We then extracted M-mode images from three lines of the reconstructed and imaged OFT longitudinal sections (see Figure 2.8): (*i*) line I, which was close to the ventricle (the OFT inlet); (*ii*) line M, approximately at the middle of the OFT; and (*iii*) line O, which was close to the aortic sac (the OFT outlet). The extracted M-mode images showed very similar wall-motion patterns. To better visualize differences in wall-motion phase relations, we manually traced the upper interface between the myocardium and the cardiac jelly from the M-mode images and plotted the displacement of this interface over time (see Figure 2.9). We found that when the OFT is reconstructed without phase-lag adjustment, phase relations between lines I and O—$(0.02 \pm 0.02)T$—did not resemble those observed from direct OCT imaging—$(0.11 \pm 0.02)T$. When phase-lag adjustment was introduced in the reconstruction, however, the phase relations between lines I and O were recovered. Thus, our results indicate that phase-lag adjustment is needed to properly capture the dynamics of the OFT wall motion.

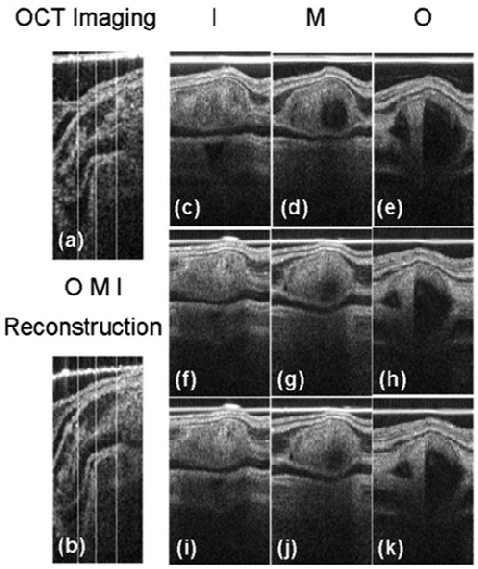


**Figure 2.8** Comparison of M-mode images extracted from imaged and reconstructed longitudinal sections of the OFT. Lines selected to extract M-mode images are show in (a) and (b): close to the OFT inlet (I), middle OFT (M), and close to the outlet (O). (a) Longitudinal sections acquired directly with OCT and (b) reconstructed from synchronized 4D image data. (c–e) M-mode images from a sequence acquired directly from OCT; (f–h) M-mode images from a reconstructed image sequence without phase lag adjustment; (i–k) M-mode images from the reconstructed image sequence with phase lag adjustment.

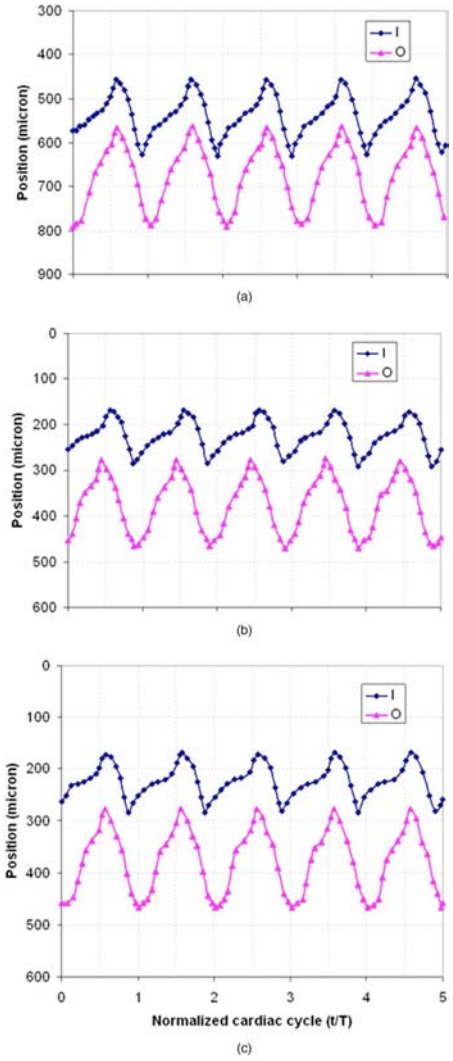


**Figure 2.9** OFT wall displacements close to the inlet and outlet. Wall displacements (showing the motion of the interface between the myocardium and cardiac jelly) were traced manually from the M-mode images shown in Figure 2.8: (a) from images acquired directly with OCT [Figures 2.8(c) and 2.8(e)]; (b) from reconstructed images without phase adjustment [Figures 2.8(f) and 2.8(h)]; and (c) from reconstructed images with phase adjustment [Figures 2.8(i) and 2.8(k)]. For ease of visualization, we present five cardiac cycles extracted directly from the acquired image sequence (a), and in (b) and (c) generated by circular repetition of the reconstructed pooled cardiac cycle.

## 2.4 Discussion

In this paper, we present an imaging strategy together with an accurate and efficient post-acquisition synchronization procedure to assemble nongated 2-D cardiac image sequences (B-mode images) into a synchronized 4D image data set. Phase shifts between adjacent image sequences are calculated by maximizing the similarity of M-mode images extracted from B-mode images. In the proposed procedure, the M-mode images function as an optical cardiogram, providing gating data used for post-acquisition

synchronization.[98] Furthermore, our synchronization procedure provides a means of estimating phase lags in the motion of cardiac walls, introduced for instance by peristaltic-like wall contractions, and adjusting phase lags for proper image reconstruction. Because synchronization of image sequences is performed using line scans (M-mode images), computational efficiency is achieved.

### 2.4.1 Application Realm of the Synchronization Procedure

Application of our procedure to 4D image reconstruction is subjected to two underlying assumptions. The first assumption is the periodicity of cardiac motion and deformation. For chick embryos at early developmental stages, the central neural system, which regulates heart rate, has not yet developed and the heart rate is only a function of embryo temperature. Although during our imaging acquisition the temperature of the embryo was lower than physiological, temperature was stable within 1 °C and temperature-induced variations in the heart rate were small (<9% among image sequences). Thus, during imaging, motion of the OFT wall was approximately periodic. The second assumption is structural similarity of image sequences acquired at adjacent locations. To ensure structural similarity, the distance $h$ (12.5 µm) between acquired cross-sectional image sequences was less than the lateral spatial resolution of our OCT system (16 µm), and much smaller than the length of the OFT (~800 µm). Our nongated 4-D imaging strategy and synchronization procedure can be generalized to applications involving other animal models or organ systems, as well as other imaging modalities.

### 2.4.2 Accuracy of the Synchronization Procedure

The accuracy of our synchronization procedure depends on the line chosen to extract M-mode images from B-mode images. We found that calculations of period and relative phase shift from M-mode images are not too sensitive to the locations or orientations of the lines as long as the lines overlaid the region of interest (e.g., the OFT) over the entire cardiac cycle. For OCT images, however, attenuation of the imaging signal along the tissue depth and the transient fading of signal due to fast motion of blood flow affect the accuracy of calculations. Therefore, lines containing points within the same depth in tissue (horizontal lines in Figures 2.6 and 2.7) and within the center region of the OFT are preferred.

OCT images of the OFT (B- and M-modes) contain periodic data from the OFT (our region of interest), but also data from other parts of the heart and surrounding organs, such as the head. To estimate the percentage of the image that contains OFT (useful) data, we can use the average surface of the image occupied by the OFT over total surface area for B-mode images, and the average OFT length over total line length for M-mode images. For cross-sectional images, we can assume that the OFT external layer is a circle with radius $R$, and that the image is a square with side length $L$ (with $R<L$). Then, the ratio of OFT data to total imaging data goes as $(R/L)^2$ for 2-D images and $R/L$ for line scans. Because $R/L>(R/L)^2$, using properly chosen lines for M-mode extraction, the algorithms to calculate period and phase shift could achieve higher accuracy when applied to M-mode rather than B-mode images.

We compared the performance of the algorithms used to calculate cardiac period and

relative phase shifts applied to B- and M-mode images obtained from a horizontal line within the center region of the OFT (see Figures 2.6 and 2.7). We found that, regardless of whether the algorithms were applied to B- or M-mode images, similar accuracy was achieved (see Sections. 2.3.3.1 and 2.3.3.2). Moreover, calculations were significantly faster (~400 times faster) when performed using M-mode rather than B-mode images. Employing M-mode images dramatically improved the efficiency of the synchronization procedure without compromising accuracy.

Other factors that affect accuracy of our synchronization procedure are the number of frames per cardiac cycle that the system can acquire and the total number of cardiac cycles acquired in a sequence. Our reconstruction is based on ~30 frames per cycle and 5 cardiac cycles, thus about 150 frames in total to accurately reconstruct a cardiac cycle (as all the images are pooled to one cycle). We verified that this number of frames is sufficient for correct reconstruction. We also checked the accuracy of the reconstruction if more or less frames were considered (results not shown in the manuscript) and our results suggest that 150 frames in an image sequence are probably close to optimal. Thus, for other systems and faster cardiac rates, image acquisition should be such that at least 150 frames are acquired. A caveat, however, is that if the number of frames acquired per cardiac cycle is $\ll 30$, then each image frame might not be considered "instantaneous" (because it takes time for the system to scan the frame) and this would introduce inaccuracies. Our results indicate that acquiring OCT images at a rate of ~30 frames/cardiac cycle for about five cardiac cycles is sufficient to predict cardiac cycle and time shifts with reasonable accuracy.

### 2.4.3 4D Reconstruction (Phase-Lag Correction)

We found that synchronization of images based on structural similarity alone is not sufficient to capture the peristaltic-like motion of the heart walls of chick embryos at early developmental stages. During early development, the embryonic heart does not have valves and, to maintain unidirectional blood flow, contractile waves travel along the heart.[51] These traveling waves produce peristaltic-like wall motion and thus introduce phase lags between different regions of the heart. In our synchronization procedure, to correctly recover the dynamics of the OFT wall, we adjusted the phases of image sequences from those obtained by structural similarity.

Because contractile waves travel from the inlet to the outlet of the heart, the need to correct for the phase lag in our procedure largely depends on our choice of imaging cross-sectional (transverse) planes. For our procedure, we acquired cross-sectional images because they ensure similarity between adjacent image sequences (i.e., the OFT always shows in the image frame, no matter whether the OFT is expanded or contracted), whereas with longitudinal images, there are imaging planes from which the OFT "disappears" when its walls contract and "reappears" when its walls expand, making similarity algorithms more difficult to implement and more prone to inaccuracies.

Currently, there is controversy about the nature of cardiac motion at early stages of development, with some authors arguing that heart wall motion is peristaltic,[110, 111] whereas others argue that the heart acts as a suction pump.[112] We certainly found that in reconstructing the OFT motion from the nongated OCT images we acquired, phase-lags in wall motion between the inlet and outlet of the OFT (not accounted for by structural

similarity) need to be considered. In other regions of the heart, and/or at later stages, this phase lag might be negligible. Application of our synchronization procedure, however, will certainly aid in the characterization of cardiac mechanics during early development.

## 2.5 Conclusions

In this paper, we have presented a 4D nongated imaging strategy and post-acquisition synchronization procedure to reconstruct 4D images of the embryonic heart. We have demonstrated the efficiency and accuracy of the procedures by reconstructing the cardiac OFT of a chick embryo from OCT images. Our nongated 4D imaging strategy and synchronization procedure can be generalized to applications involving other animal models or organ systems, as well as other imaging modalities, providing that the two underlying assumptions, periodicity of the motion and similarity of adjacent image sequences, are satisfied. The synchronization procedure presented is especially useful for 4D imaging when: (*i*) reliable physiological gating signals are difficult to acquire, (*ii*) the acquisition rate of the imaging system employed is limited, and (*iii*) phase lags are non-negligible.

# Chapter 3: A robust 3D hybrid optical flow and deformable model segmentation algorithm for 4D OCT images of the chicken heart outflow tract

## 3.1 Introduction

Chapter 2 has demonstrated that OCT is a powerful non-invasive image technique that is capable of visualizing *in vivo* the early chick embryonic heart development. The 4D (3D space + time) imaging and post-acquisition reconstruction strategy that we developed further extends the functional capability of OCT to capture the dynamics of the beating heart within a cardiac cycle, which is important for early diagnosis and prevention because function abnormalities usually precede gross structural malformation of the heart[11, 13, 113] To extract structural and dynamic information of the chick embryonic heart from the OCT images, segmentation, a process of partitioning the anatomical structures from images, is a critical step towards reliable quantification of the wall dynamics of the embryonic heart.

In this thesis, our region of interest is the outflow tract (OFT), a distal region of the heart that connects the primitive ventricle to the aortic sac, of stage HH18 chick embryos. The OFT is a slightly curved tube that has a three-layered wall (Figure 3.1): (1) the myocardium, an external muscle layer; (2) cardiac jelly, the extracellular matrix shown as the dark region in-between the myocardium and lumen in OCT images; and (3) a thin layer of endocardium (<10 μm), enclosing the OFT lumen. In the OCT images, the

endocardium layer cannot be distinguished from the lumen because the blood within the lumen and the endocardium have similar refractive index. Here the endocardium is defined as the outline of the lumen. To quantify the dynamic structure of the OFT wall as well as its interaction with blood flow within the OFT, we need to segment the OFT from the OCT images over cardiac cycles. As a first step towards 4D segmentation, our objective was to construct a 3D segmentation scheme that partitions the OFT myocardium and the lumen contours over the cardiac cycle from a 2D+time OCT image sequence or surfaces at any given cardiac phase from a 3D volume OCT image dataset.

Segmentation of OCT images generally faces two major problems.[114] First, the image intensity decreases with the increase of imaging depth, and the intensity inhomogeneities exclude those segmentation methods based on image intensity. Second, OCT images are subjected to speckle noises, which decrease the image quality. These typical drawbacks with OCT images result in discontinuities and spurious edges, making the segmentation task a challenging problem. Challenges associated with OCT image sequences of the OFT further complicate the task of automatic segmentation (Figure 3.1). First, the OFT undergoes large deformation during the cardiac cycle, in particular, the lumen has large shape change. Second, there is a transient fading of signals (washout effect[115]) in the OFT lumen when the velocity of blood flow in the OFT is large, which usually occurs at maximal blood ejection from the ventricle (shown as the center dark region in the lumen in Figure 3.1). Third, it is difficult to distinguish the edges of interest (OFT wall layers) from other surrounding tissues, which are in close proximity and have similar intensities as the OFT wall in OCT images.

Deformable models (also referred to as active contours in a 2D problem[116] or active surfaces in a 3D problem[117]) offer a reasonable approach to handle these problems, due to their major advantages: (1) ease of incorporating smoothness constraint on the object shape, which offers robustness to both image noises and boundary gaps common in medical images, and (2) capability of accommodating the significant variability of biological structures over time and across different objects. Deformable models have been a rigorous research area in medical image analysis and covered by many excellent reviews.[118-121] Briefly, deformable models are closed parametric curves or surfaces defined in an image domain that can move under the influence of internal constraints and external forces. The internal constraints are defined within the curve or surface to keep the model continuous and smooth during deformation, and external forces are computed from the image data to drive the model towards the desired object boundaries. One major disadvantage of the deformable models is its performance of segmentation is sensitive to its initial contour location because the deformable model is usually formulated into a minimization problem, and thus deformation of contours is easily tracked into local minimums.

To address the sensitivity of initial contour location, Mikic and colleagues proposed to incorporate the optical flow algorithm to guide the active contours in segmenting echocardiographic sequences.[122] The optical flow is a 2D displacement field computed from two consecutive image frames that traces the motion of an object over time, based on the assumption that the intensity pattern of a moving object is time invariant.[123] Given the 2D displacement field, the position of the object can be predicted in the subsequent image frame without human supervision. Thus, the optical flow algorithm enables us to

track and segment fast-moving objects such as the cardiac structures in an image sequence.

In this Chapter, we have constructed a hybrid 3D image segmentation scheme that consists of the optical flow algorithm for coarse segmentation[124] and the deformable model algorithms (active contour and active surface algorithms) for fine segmentation.[125] In order to achieve robust segmentation of OCT images of the OFT, we also introduced a number of enhancements and modifications to the formulations of deformable models. By applying our algorithm to a 2D + time OCT image sequence and 3D datasets of the OFT, we have shown that our hybrid algorithm of optical flow and active contour/surface renders a robust segmentation scheme for segmenting the 3D OCT images of the OFT. The algorithm will be used to quantify the wall dynamics of the OFT in normal chick embryos in Chapter 6, as well as to quantify the changes in the wall dynamics of the OFT in OTB chick embryos in Chapter 7.

## 3.2 Methods

### 3.2.1 Optical flow algorithm

The optical flow algorithm calculates a displacement field ($u$, $v$) that describes the motion of a feature point at ($x$, $y$, $t$) in an image, I, to a new position ($x+ u$, $y + v$, $t+1$) in the next frame. Using the displacement field, we can trace object boundaries frame-by-frame in a 3D dataset. To determine the displacement field ($u$, $v$) at each image point, we minimized an energy function $E$, defined as follows: [124]

$$E(u,v) = \iint_{\Omega} \left[K_{\rho}\left(I_x u + I_y v + I_t\right)^2 + \omega(|\nabla u|^2 + |\nabla v|^2)dxdy\right] \qquad (3.1)$$

where $I_x$, $I_y$, and $I_t$ are the derivatives of I (image intensity) with respective to x, y, and t, respectively; *K* is a Gaussian kernel of standard deviation $\rho$; $\alpha$ is a weight parameter. The first term is a data term that assumes the brightness within some neighborhood of size $\rho$ is constant over time. A large $\rho$ has better tolerance for noises, whereas small values of $\rho$ better preserve the flow discontinuities at edges. The second term is a regularization term that imposes a smoothness constraint on the displacement field. Larger values for the weight parameter ω lead to a smoother flow field. Since the spatial and temporal image derivatives ($I_x$, $I_y$, and $I_t$) are sensitive to image noises, it is common to smooth the image sequence prior to differentiation by convoluting a Gaussian kernel with standard deviation σ to remove image noises.

The flow field $(u, v)$ that minimizes the energy function $E$ satisfies the Euler-Lagrange equations: [124]

$$\Delta u - \frac{1}{\alpha}\left[k_\rho(I_x)^2 u + k_\rho\left(I_x I_y\right)v + k_\rho(I_x I_t)\right] = 0 \tag{3.2}$$

$$\Delta v - \frac{1}{\alpha}\left[k_\rho\left(I_x I_y\right)u + k_\rho\left(I_y\right)^2 v + + k_\rho\left(I_y I_t\right)\right] = 0 \tag{3.3}$$

where $\Delta := \partial_{xx} + \partial_{yy}$ denotes the spatial Laplace operator. The equations were implemented using a finite difference scheme by Dr. Vicente Grau in Matlab platform, following the procedures described in [124, 126].

### 3.2.2 Active contour algorithm

Active contour is a parametric contour $C(s)$ (0 < s < 1, where s is the arc-length parameterization of the curve) that deforms and converges to the desired object boundaries driving by the forces defined within the image data under the internal

constraint of smoothness and continuity.[116] A deformable active contour $C(s,t)$ is to stabilize the equation: [120]

$$-\frac{\partial}{\partial s}\left(\alpha\frac{\partial C}{\partial s}\right)+\frac{\partial^2}{\partial s^2}\left(\beta\frac{\partial^2 C}{\partial s^2}\right)+\gamma F(C)=\frac{\partial C}{\partial t} \tag{3.4}$$

where t is time; $\alpha, \beta,$ and $\gamma$ are weighting parameters. The first two terms are inner force terms that control the elasticity and rigidity of the contour, respectively; the third term is the external force term that is derived from the image data and attracts the contour to the desired object boundaries. Here, the external force term is expressed as a superposition of several different forces to incorporate constraints from the prior knowledge on the OFT and to improve the robustness of the segmentation, as follows:

$$F=\gamma_d F_d+\gamma_p F_p+\gamma_s F_s+\gamma_v F_v \tag{3.5}$$

where $F_d$ , $F_p$, $F_s$, and $F_v$ are distance force, pressure force, spring force, and volcano force, respectively; $\gamma_d, \gamma_p, \gamma_s$, and $\gamma_v$ are their weighting parameters.

*Distance force*

The distance force converges the contour to edges which have the lowest distance potential. Distance force is defined as follows[120, 125]

$$F_d(x,y)=-\nabla P_d(x,y) \tag{3.6}$$

where $P_d$ is the distance potential and $\nabla=\frac{\partial}{\partial x}+\frac{\partial}{\partial y}$ denotes partial differential operator. The distance potential is a function of the Euclidean distance between each pixel in the image and the closest edges that the edges have the lowest distance potential. Minimization of the distance potential drives the initial contour to the closest edges. The

definition of distance potential follows that in [120, 125];

$$P_d(x,y) = -\gamma_d exp[-d(x,y)^2], \tag{3.7}$$

where $d$ is the distance to the closed edges and is determined by an Euclidean distance transformation of the edges detected by a Canny edge detector. [127]

*Pressure force*

To increase the attraction range of the active contour and reduce the sensitivity to initialization, we used a pressure force defined as:[125]

$$F_p(C) = \gamma_p N(C), \tag{3.8}$$

where $N(C)$ is a outward unit normal vector of the contour. The inflation and deflation of the contour is determined by the sign of $\gamma_p$, which varies based upon whether C is inside or outside the desired object.

*Interactive forces incorporating geometric constraints*

Deformation of two contours such as the interior and exterior boundaries of the myocardium has to satisfy certain geometric relation. In the case of the OFT, the thickness of myocardium is within certain range$[h_{min}, h_{max}]$. To avoid distraction of surrounding tissues and overlapping of interior and exterior myocardium boundaries, we constrained the deformation of the exterior myocardium within the range $[h_{min}, h_{max}]$ using a "spring force" Fs(C) and a "volcano force" Fv(C), defined as follows:

$$F_s(C) = \begin{cases} N(C)(h_{max}/d - 1), & if\ d > h_{max} \\ 0, & otherwise \end{cases} \tag{3.9}$$

$$F_v(C) = \begin{cases} N(C)(h_{min}/d - 1), & if\ d < h_{min} \\ 0, & otherwise \end{cases} \quad (3.10)$$

where d is the distance between corresponding points on the contours of interior and exterior boundaries of the myocardium. The two interactive forces, namely the spring force and the volcano force, pull or push a contour toward or away from each other where the distance between the contours is outside of the defined range.

### 3.2.3 Active surface algorithm

Active surface is a generalization of active contours in a 3D image domain. A deformable parametric surface S (s,r) (0 < s < 1, 0 < r< 1 where s and r are two spatial variables of the surface) is defined as follows:[125]

$$\frac{\partial S}{\partial t} = \frac{\partial}{\partial s}\left(\alpha_1 \frac{\partial S}{\partial s}\right) + \frac{\partial}{\partial r}\left(\alpha_2 \frac{\partial S}{\partial r}\right) - 2\ \frac{\partial^2}{\partial s \partial r}\left(\beta_1 \frac{\partial^2 S}{\partial s \partial r}\right) - \frac{\partial^2}{\partial s^2}\left(\beta_2 \frac{\partial^2 S}{\partial s^2}\right) - \frac{\partial^2}{\partial r^2}\left(\beta_3 \frac{\partial^2 S}{\partial r^2}\right) + F(S) \quad (3.11)$$

where $\alpha_i\ (i = 1, 2)$ and $\beta_j (j = 1, 2, 3)$ are weighting factors of internal forces, which determine the relative importance of the elasticity ($\alpha_1$ and $\alpha_2$), the rigidity ($\beta_1$ and $\beta_2$) and resistance ($\beta_3$) on the shape of the surface; the external force F(S) is defined as a superposition of pressure force and distance force on the active surface. The active contours and surfaces were implemented using the finite element methods, similar to.[125, 128]

### 3.2.4 Segmentation scheme for the heart OFT

When applying our algorithm, we also incorporated several strategies to achieve a successful segmentation of the OFT. First we elaborate on the major strategies and then

summarize our procedures in a flow chart.

### 3.2.4.1. Extracting OFT cross-section

One issue associated with OFT segmentation is that the OFT is a curved tube, whereas the imaging plane was fixed in space when we acquired the OCT images f the OFT. A 2D cross-sectional image may not necessarily reflect the cross-section of the OFT, and the deviation between the imaging plane and OFT cross-section increases towards the distal OFT (refer to Figure 3.1A). To segment the OFT cross-section, from the 4D OCT image data of the OFT we extracted a longitudinal section of the OFT that runs roughly through the centerline. From a static longitudinal section when the OFT was fully contracted, we approximated the axial centerline of the OFT with an arc shape and estimated the radius and origin of the arc. Through the origin of the arc, we defined 50 locations with 1 degree apart on the longitudinal section and extracted cross-sections of the OFT from the 4D OCT image data (see the starting and ending locations in Figure 3.1A). Our segmentation were then applied to the 50 time series of the OFT cross-sections (see an example of an extracted OFT cross-section in Figures 3.1.B and C).

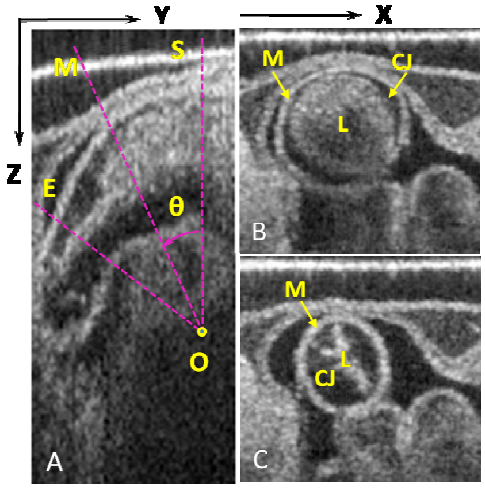


**Figure 3.1** OCT images of the heart OFT of HH18 chick embryos. (A) Longitudinal section showing the regions where 50 OFT cross-sections were extracted from 4D image data. Purple lines showing the start (S), middle (M), and end (E) locations. The OFT middle cross-section at (B) its maximal expansion and (C) contraction states. M, myocardium; CJ, cardiac jelly; L, lumen; and O, the origin.

### 3.2.4.2. Edge enhancement

The conformity of the active contour to the desire boundaries heavily depends on the quality of the edge map (see Section 3.2.2). To improve the quality of the edge map, we employed the following strategies:

*(1) Distinguish internal and external edges of an objective*

To discriminate internal and external edges of an object, we used the directional information of the edge [129, 130] 131132(Figure 3.2). A directional vector $n = P(x, y) - P_c$ was defined as a unit vector that points from a specified point Pc within the OFT lumen to a point $P(x, y)$ on a given edge. The gradient vector $g(x, y) = \nabla I(x, y)$ was calculated at point $P(x, y)$. By comparing the direction of the gradient vector with the directional vector at each point on edges, we grouped edges into positive edges and negative edges, as follows.

Positive edge map:

$$f_p(x, y) = \begin{cases} 1, & if \quad n \cdot g(x, y) > 0 \\ 0, & otherwise \end{cases} . \tag{3.12}$$

Negative edge map:

$$f_n(x, y) = \begin{cases} 1, & if \quad n \cdot g(x, y) < 0 \\ 0, & otherwise \end{cases} . \tag{3.13}$$

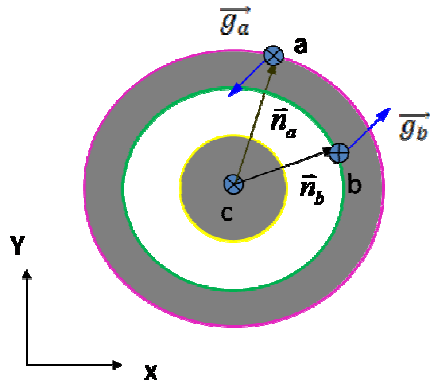


**Figure 3.2** Illustration of the definitions of negative and positive edges. The sign of an edge is determined by a dot operation between two vectors at a point on the edge, namely, the intensity gradient vector (g) and a directional vector (n) pointing from the center point (C) to the point on the edge. a and b are a point on the interior and exterior edges of the myocardium, respectively.

According to this criterion, the interior edge of the myocardium was classified into $f_p$ and the exterior and the outline of the lumen were classified into $f_n$. The segmentation was then based on the edge map of $f_p$ or $f_n$. The interferences between the neighboring edges of the myocardium were avoided.

*(2) Threshold by the length of the edge*

To avoid the undesired effects of noises, we discarded the edges that were shorter than certain length. Empirically, we chose 4 pixels as the threshold.

*(3) Mask the edge map*

To avoid segmentation to converge to the edges of neighboring tissues, before segmenting the lumen and external myocardium, we created a binary mask from the segmented contour of interior myocardium; the mask has a value of 1 at image pixels within the region enclosed by the contour and a value of zero at pixels outside the contour. To remove the edges that lie outside or inside of the interior myocardium, the edges maps of the exterior myocardium $f_{ext}$ and the lumen $f_{lumen}$ were generated by

applying the mask to the negative edge map $f_n$, as follows:

$$f_{ext} = f_n \cdot Mask, \tag{3.14}$$

$$f_{Lumen} = f_n \cdot {\sim}Mask, \tag{3.15}$$

where ~ is the logic negation operator; and ~Mask has a value of zero at image pixels within the region enclosed by the contour and a value of one outside the contour. The segmentation of the exterior myocardium and then lumen was then based on the masked edge maps of $f_{ext}$ and $f_{lumen}$.

### 3.2.4.3. Adaptive parameters

The shape of the lumen changes during the cardiac cycle, deforming from a xxx. Accordingly, we adapted weighting parameters of internal (α and β) and external forces (γ) of the active contour to the phase of the cardiac cycle. The larger the values of α and β, the smoother the active contour and thus more robust to image noises; the smaller the values of α and β the more compliant the active contour and thus better accommodate the irregular shape of the lumen but easily distracted by image noise. The weight parameter γ determine the strength of image force to attach the active contour to the edge. A proper choice of weighting parameters is important for the active contour to converge to the desired edges in noisy medical images.

We estimated the phase of the cardiac cycle using the area (A) of the segmented interior myocardium.

$$\alpha = w_1\alpha_{exp} + w_2\alpha_{con} \tag{3.16}$$

$$\beta = w_1\beta_{exp} + w_2\beta_{con} \tag{3.17}$$

$$\gamma = w_1\gamma_{exp} + w_2\gamma_{con} \tag{3.18}$$

where $w_1 = \frac{A - A_{con}}{A_{exp} - A_{con}}$ and $w_2 = 1 - w_1$; the subscripts "con" and "exp" indicate the most constricted state and expanded states of the OFT, respectively.

#### 3.2.4.4 3D surface reconstruction

Our segmentation provides series of contours that have the coordinates defined in each 2D image domain or a 2D local coordinate system $(x, y)$ (refer to Figure 3.2). Given the knowledge of the origin O (Yo, Zo) and angle ($\theta$) of the plane where the cross-sections were extracted (refer to Figure 3.1A), the contours were reconstructed into 3D global coordinate system $(X, Y, Z)$(refer to Figure 3.1), using the following transformation equations:

$$X = x \tag{3.19}$$

$$Y = y\cos\theta \tag{3.20}$$

$$Z = -aX - bY + c \tag{3.21}$$

where a, b and c are the parameters of a given cross-section plane, determined by three known points on the plane in the global coordinate system.

#### 3.2.4.5 Flow chart

The scheme flow for segmenting the OFT is as follows (also summarized in a flow chart, see Figure 3.3)

1. Extract 50 cross-sections that are approximately perpendicular to the axial centerline of the OFT from 4D image data.

2. Normalize the image sequences of cross-sections into one cardiac cycle to improve the temporal resolution of OCT images. This procedure reduces the maximal displacement of the OFT wall between consecutive image frames to the capture range of optical flow algorithm (4 pixels in the image) which is important for optical flow algorithm to accurately follow the deformation of a beating OFT.

3. Apply a Gaussian filter with a standard deviation $\sigma$ to reduce speckle noises of the OCT images.

4. Semi-automatically trace the outlines of the myocardium and lumen using the live-wire algorithm implemented in Amira 5.2.2. These traces are used as initial contours in the optical flow algorithm. To avoid accumulating errors in computing optical flow, we used three additional re-initiation contours that evenly span over the cardiac cycle when segmenting a image sequence, and used two re-initiation contours that span along the OFT when segmenting a 3D volume dataset.

5. Apply optical flow algorithm on an image sequence frame-by-frame to compute the 2D displacement field between two consecutive image frames at each pixel in the image domain. Based on the displacement fields, the locations of initial contours are updated and follow the motion of OFT boundaries over time or over space. In this way, the OFT wall is roughly segmented.

6. Enhance the edge map by distinguishing internal and external edges of the OFT wall layers (see Eqs. 3.12-3.13) and thresholding the noisy edges.

7. Apply 2D active contour algorithm frame-by-frame on an image sequence using the segmentation solution from the optical flow algorithm as initial contours. Due to

different properties of the OFT layers, the 2D algorithms applied to the interior and the exterior boundaries of the myocardium, and the lumen were slightly modified in terms of the formulation of external forces and proper parameters. Since the interior edge of the myocardium is well defined, we first applied the 2D algorithm to segment the interior boundary of the myocardium. Usually the pressure force and distance force are sufficient for the segmentation of interior myocardium boundary. With the knowledge of interior myocardium boundary, we further enhanced the edge maps for the lumen and exterior boundary of the myocardium (see Eqs. 3.14-3.15). In segmenting exterior myocardium boundary, additional geometry constraint on the wall thickness was incorporated into the 2D algorithm as the spring and volcano forces (see Eqs. 3.9-3.10). For the lumen, adaptive parameters were used to accommodate large shape changes (see Eqs. 3.16-3.18).

8. Apply 3D active surface algorithm on a set of contours extracted from 2D active contour algorithm.

9. Transform the 2D local coordinate system of contours into 3D global Cartesian coordinate system if segmenting 3D volume data of the OFT (see Eqs. 3.19-3.21). The contours were then lofted and interpolated into surfaces using Rhinoceros 4.0.

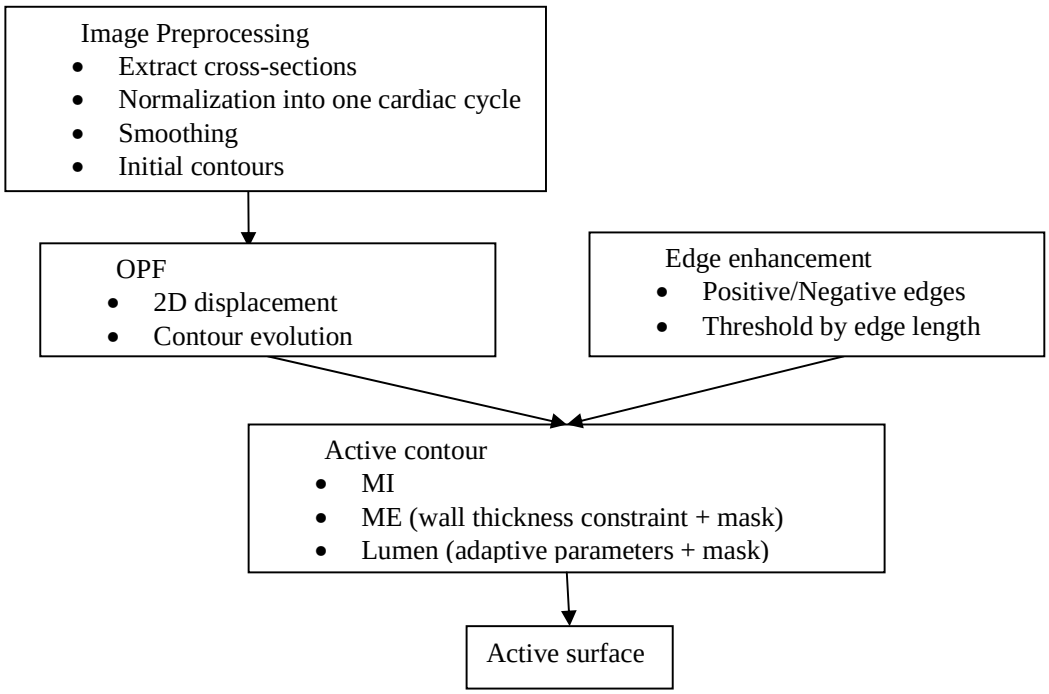


**Figure 3.3** Flow chart in segmentation of the OFT.

### 3.2.5 Algorithm validation

The evaluation of the segmentation is based on two quantitative measures (Figure. 3.4): namely, similarity index (SI), and maximal or mean absolute distance (AD_max or AD_mean). SI measures the degree of overlapping in areas enclosed by two contours and provides an indicator of the overall goodness of segmentation against the ground truth (usually manual segmentation). SI is defined as: [131, 132]

$$SI = 2\frac{|A \cap B|}{|A|+|B|} \tag{3.22}$$

where A and B are the areas from two segmentations with manual and automatic segmentation, respectively.

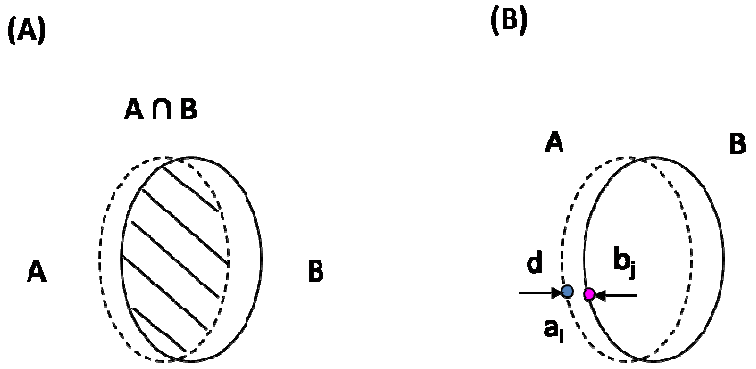


**Figure 3.4** Illustration of the evaluation measures of the segmentation. (A) The similarity measure evaluates the degree of overlapping in areas enclosed by two segmented contours A and B; (B) maximal or mean absolute deviation between two contours measures the maximal or mean distance (d) between corresponding points (such as $a_i$ and $b_j$) at two contours A and B.

Maximal or mean absolute distance (AD_max or AD_mean) measure the maximum or mean Euclidean distance between the target boundary (usually through manual tracing) and the contour extracted from algorithm, and thus provides a local measure for segmentation performance. AD_mean and AD_max between two contours A and B are defined as:[122, 133]

$$AD\_mean = (A,B) = \frac{1}{2}\left\{\frac{1}{n}\sum_{j=1}^{n} d(\alpha_j, B) + \frac{1}{m}\sum_{i=1}^{m} d(b_i, A)\right\} \quad (3.23)$$

$$AD\_\max(A,B) = \max\left\{d(a_j, B), d(b_i, A)\right\} \quad (i = 1,2,..,m, j = 1,2,\dots,n) \quad (3.24)$$

where $A = \{a_1, a_2, \dots, a_n\}$ and $B = \{b_1, b_2, \dots, b_m\}$ represent coordinates of points which define the contours from manual tracing and algorithm extraction, respectively. $d(a_i, B) = min\|b_j - a_i\|$ finds the distance between a point $a_i$ on the contour A and its closest point on the contour B.

## 3.3 Results and discussions

We tested our algorithm on a 2D + time image sequence of a middle OFT cross-section and two 3D volume image sequences from a 4D OCT image dataset of a HH18 chick heart OFT. In our implementation, we empirically chose $\sigma = 0.5, \rho = 3, and\ \omega = 50$ for the optical flow algorithm. The parameters used for active contour and surface algorithms are shown in Table 3.1 and Table 3.2, respectively. Performance of different segmentation algorithms was compared in Table 3.3.

**Table 3.1** Parameters in 2D active contour algorithm

| Region | Parameters |
|---|---|
| Lumen | $\alpha_{exp} = 2(1/n)^2$;$\alpha_{con}=0.5(1/n)^2$ |
| | $\beta_{exp} =2(1/n)^4$; $\beta_{con}=0.5(1/n)^4$ |
| | $\gamma_{d\ exp}=30$; $\gamma_{d\ con}=40$ |
| | $\gamma_{p\ exp} =0.005$; $\gamma_{p\ con}=0.001$ |
| Myo I | $\alpha = 5(1/n)^2$;$\beta =5(1/n)^4$;$\gamma_d =20$; $\gamma_p =0.002$ |
| Myo E | $\alpha= 8(1/n)^2$ ; $\beta =10(1/n)^4$; $\gamma_d =10$; $\gamma_p=0.005$; $\gamma_s= \gamma_v =0.5$; |

n is the number of points in the contour. The choice of parameters is referred to [125].

**Table 3.2** Parameters in 3D active surface algorithm

| Region | Parameters |
|---|---|
| Lumen | $\alpha_{exp} = 200/[n \times (m-1)]^2$; $\alpha_{con}=20/[n \times (m-1)]^2$ |
| | $\beta_{exp} =200/[n \times (m-1)]^3$; $\beta_{con}=20/[n \times (m-1)]^3$ |
| | $\gamma_{d\ exp} =1$; $\gamma_{d\ con}=2$ |
| | $\gamma_{p\ exp} =0.02$; $\gamma_{p\ con}=0.01$ |
| Myo I (or MyoE) | $\alpha_1 =\alpha_2= 200/[n \times (m-1)]^2$ |
| | $\beta_1 =\beta_2 =\beta_3=200/[n \times (m-1)]^3$ |
| | $\gamma_d =1$; $\gamma_p =0.1$ |

n is the number of points in a contour, and m is the number of frames in an image sequence. The choice of parameters is referred to [125].

### 3.3.1 Segmentation evaluation

To evaluate our hybrid algorithm, we selected 5 images from the middle OFT cross-sections that evenly span over the cardiac cycle; and we applied 4 segmentation algorithms, namely, the optical flow algorithm, a combined algorithm of active contours and active surfaces, a combined algorithm of optical flow and active contours algorithms, and our hybrid algorithm that consists of optical flow, active contour and active surface algorithms to segment the interior and exterior myocardium and the outline of the lumen. Segmentations from different algorithms were qualitatively compared (see examples shown in Figure 3.5). We further evaluated quantitatively the performance of the segmentation using SI, AD_max and AD_mean against manual segmentation, the ground truth (Table 3.3).

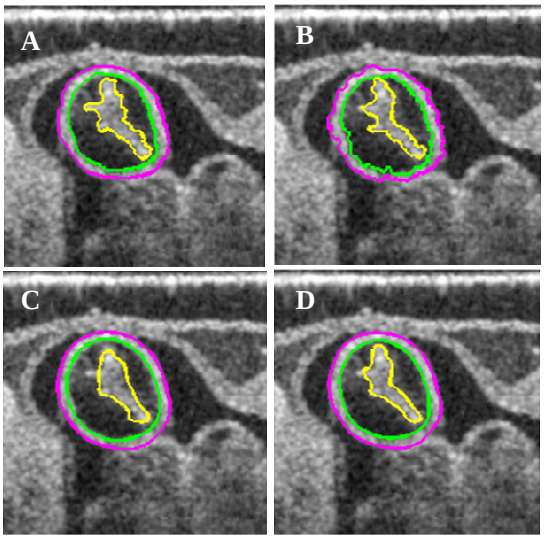


**Figure 3.5** Comparison of the performance of different segmentation methods: (A) manual segmentation, (B) optical flow algorithm, (C) combined active contour and active surface algorithms, and (D) our hybrid algorithm consisting of optical flow + active contour + active surface algorithms. Performance of segmentation algorithms is illustrated with the interior myocardium (green), exterior myocardium (purple), and the lumen (yellow) overlaid on an OCT image of the fully contracted OFT.

**Table 3.3** Comparison of different segmentation methods

| Method | AD_mean | | | AD_max | | | SI | | |
|---|---|---|---|---|---|---|---|---|---|
| | Lumen | Myo I | Myo E | Lumen | Myo I | Myo E | Lumen | Myo I | Myo E |
| OPF | 0.98 | 0.68 | 0.80 | 7.32 | 4.35 | 5.58 | 0.86 | 0.96 | 0.96 |
| | (0.30) | (0.06) | (0.17) | (1.94) | (0.63) | (1.60) | (0.03) | (0.006) | (0.005) |
| AC+AS | 1.32 | **0.39** | **0.61** | 8.49 | 2.78 | 3.42 | 0.88 | 0.98 | 0.98 |
| | (0.52) | (0.07) | (0.11) | (3.26) | (0.32) | (0.60) | (0.08) | (0.008) | (0.001) |
| OPF+AC | **0.97** | 0.96 | 0.70 | **5.64** | 3.56 | 3.26 | **0.90** | 0.96 | 0.98 |
| | (0.14) | (0.19) | (0.17) | (1.50) | (0.36) | (0.44) | (0.05) | (0.003) | (0.005) |
| OPF+AC +AS | 1.20 | 0.69 | 0.63 | 5.72 | **2.59** | **3.16** | 0.89 | 0.98 | 0.98 |
| | (0.13) | (0.16) | (0.09) | (1.35) | (0.32) | (0.49) | (0.06) | (0.004) | (0.002) |

Data are presented as mean (standard deviation). AC, active contour algorithm; AS, active surface algorithm; OPF, optical flow algorithm. The best segmentations are bold; the worst are underlined. AD_mean, mean absolute deviation; AD_max, maximal absolute deviation; SI, similarity index.

Our general observations are:

1. Segmentations using the optical flow algorithm were not smooth (Figure 3.5B), and had the largest deviations from the manual segmentation, in particular the exterior myocardium (see Table 3.3). The contours of exterior myocardium using the optical flow algorithm were likely attracted by surrounding tissues.
2. The combined active contour and surface algorithms had a comparable performance as our hybrid algorithm in segmenting the myocardium, which mainly attributed to the geometric constraint on the myocardium thickness. However, the segmentation of the lumen was poor, mainly because of the difficulties of algorithms in dealing with the irregular shape of the lumen; the contour of the lumen was easily distracted by spurious edges near the lumen (Figure 3.5C).
3. The combined optical flow and active contours algorithms showed a superior performance on segmenting the lumen, which demonstrated the utility of the optical flow algorithm in tracing the large deformation during the cardiac cycle. By comparing the performance between the combined algorithm (optical flow + active contour) and our hybrid algorithm, we found that the active surface algorithm reduced the instability induced by image noises and edge ambiguities, and improved the segmentation on the myocardium by imposing the smoothness constraint over time. However, the smoothness constraint over time compromised the segmentation of the lumen which had large shape changes over time.
4. Our hybrid algorithm provided the best overall performance on segmenting the OFT wall layers (Figure 3.5D and Table 3.3). By comparing the performance of our hybrid algorithm on different layers of the OFT, we found that the segmentation of the lumen was less accurate than that of the myocardium in terms of SI, AD_max, and

AD_mean. The largest deviation (AD_max) in the lumen was up to 7 pixels (or 35 μm) when the OFT was constricted; the contour could not fully capture the branches towards the myocardium (Supplemental Figure 3.1). The averaged deviations of all three contours were about 1 pixel or less, and are within manual segmentation errors.

To quantify the performance of our hybrid algorithm on 3D volume data, we evaluated 3 segmentations that span the OFT when the OFT was most expanded and when the OFT was contracted respectively (Table 3.4). We found that the performance on the 3D volume datasets was consistent with that on time series. The largest error occurred at the lumen when the OFT was most constricted.

**Table 3.4** Evaluation of segmentation over 3D volume images

| Region | AD_mean | AD_max | SI |
|---|---|---|---|
| Lumen | 1.1(0.3) | 5.2(1.8) | 0.91(0.06) |
| Myo I | 0.5(0.1) | 2.5(0.4) | 0.98(0.004) |
| Myo E | 0.6(0.2) | 3.8(1.6) | 0.98(0.01 ) |

Data are presented as mean (standard deviation).

### 3.3.2 Application to 2D + time OCT images of the OFT

Figure 3.6 shows the segmentation of the exterior myocardium (purple), interior myocardium (green), and lumen (yellow) at middle cross-section of the OFT over the cardiac cycle. The edges are superimposed on the original OCT images. The contours followed the edges closely over time. The differentiation of the positive and negative edge prevents the interaction between the two proximal edges of the myocardium, and

ensures the successful segmentation of the interior myocardium edge. The adaptive parameters accommodate the large shape change of the lumen. The enforcement of wall thickness constraint on the external myocardium prevents the contours to be attracted by the neighboring membrane or tissues.

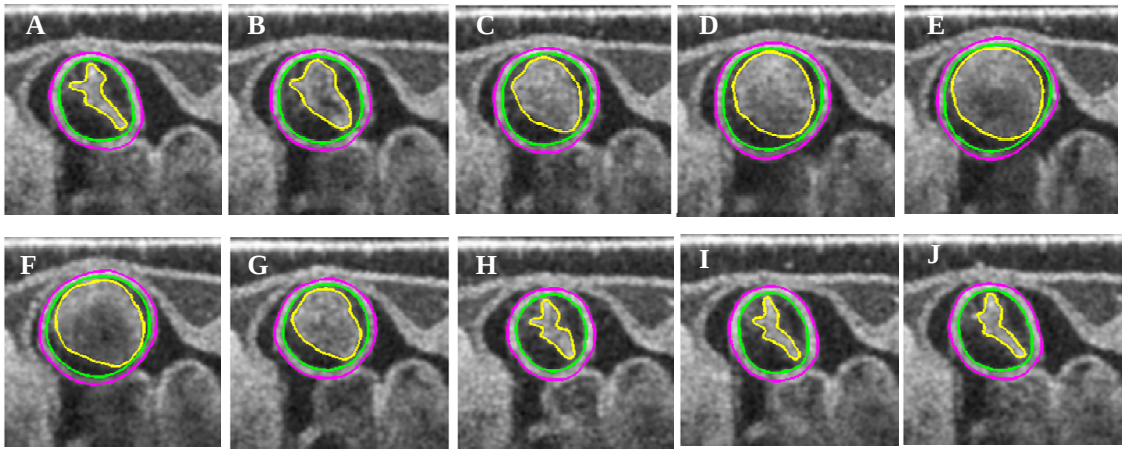


**Figure 3.6** Segmentation of a (2D+time) OCT image sequence of the middle OFT cross-section. (A-J) show the exterior boundary (purple contour) and the interior boundary (green contour) of the myocardium, and the outline of the lumen (yellow contour) at selected cardiac phases spanning evenly over the cardiac cycle.

From the segmentation, we can observe the dynamic structure of the OFT wall more clearly. The lumen underwent large shape changes from an elongated slit-like shape during fully contraction to an expanded circular shape during maximal blood ejection. Some irregular branches were seen to extend from the lumen during OFT contraction, which are presumably the endocardium folds.[134] The large shape change and uneven deformation is best illustrated when rendering the contours into 3D surface (see Supplemental Figure 3.2). The myocardium remained relatively circular over the cardiac cycle. At maximal expansion, due to external constraints, the shape of the myocardium deviated from a circle. Moreover, the segmentations enable us to quantify physiological

dimensions as well as the dynamics of the OFT wall motion. Quantification of wall thickness of the myocardium and dynamic changes in areas of the myocardium, the cardiac jelly, and the lumen is presented in Chapter 6 and Chapter 7.

### 3.3.3 Application to 3D OCT images of the OFT

We applied the algorithm to 3D image datasets of the OFT. Figures 3.7 and 3.8 show the 3D segmentation of the OFT when the OFT at the most expanded and contracted states, respectively.

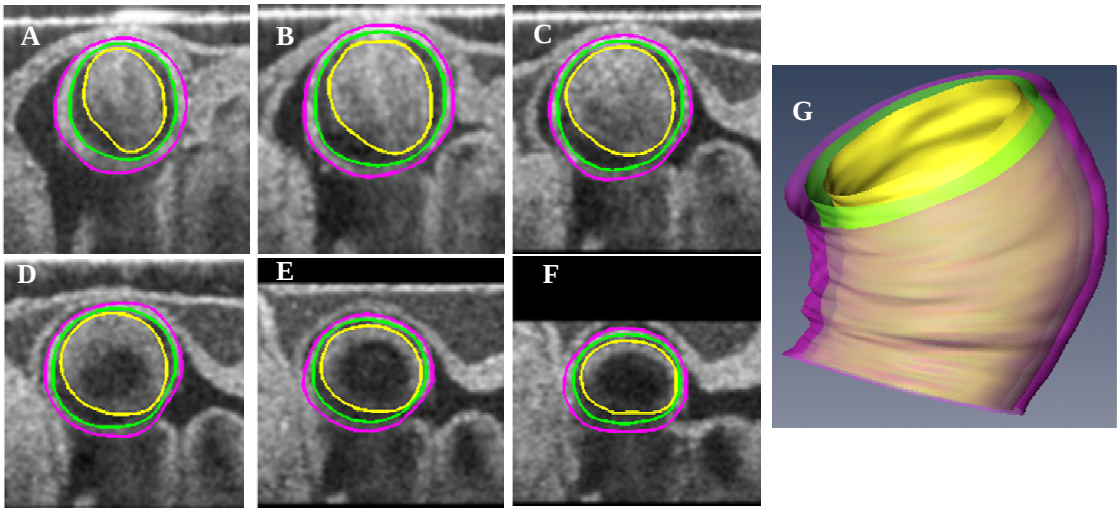


**Figure 3.7** Segmentation of a 3D volume OCT image dataset of the OFT at its expansive state. (A-F) show the exterior boundary (purple contour) and the interior boundary (green contour) of the myocardium, and the outline of the lumen (yellow contour) at selected cross-sections spanning evenly along the OFT, starting from the OFT inlet towards the OFT outlet demarked in Figure 3.1A. (G) shows the 3D surface reconstruction of the OFT from the segmented contours.

When the OFT was most expanded, the bottom edge of the myocardium became blurred as the OFT lumen filled with blood, and washout effect in the lumen (seen as the dark region) became prominent towards the distal OFT (refer to Figure 3.7). Despite the degradation of image quality towards the distal OFT, segmentation performance is superb

as the algorithm makes the best estimate of the edges by imposing smoothness and incorporating information from neighboring images. When the OFT was most constricted, the shape of lumen varied along the OFT (refer to Figure 3.8). With the same weighting parameters, the contour followed the shape of the lumen along the OFT well, indicating the robustness of the active contour and active surface algorithms.

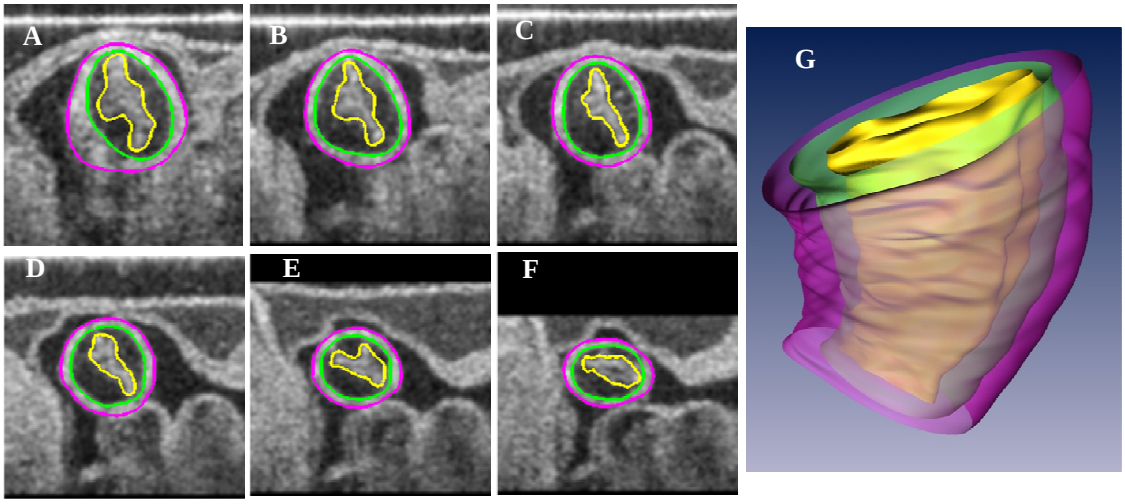


**Figure 3.8** Segmentation of a 3D volume OCT image dataset of the OFT at its contracted state. (A-F) show the exterior boundary (purple contour) and the interior boundary (green contour) of the myocardium, and the outline of the lumen (yellow contour) at selected cross-sections spanning evenly along the OFT, starting from the OFT inlet towards the OFT outlet demarked in Figure 3.1A. (G) shows the 3D surface reconstruction of the OFT from the segmented contours.

By reconstructing the segmented contours into surfaces, we revealed the surfaces of the 3D curved OFT tube. While the myocardium remained proximally circular along the OFT, the lumen varied its shape as well as its orientation along the OFT, especially when the OFT was constricted, indicating a spiral distribution of cardiac jelly along the OFT (in-between the interior myocardium surface and the lumen surface). From the 3D reconstruction, we can measure physiological parameters of the OFT in 3D such as the curvature of the axial OFT centerline, the cyclic volume changes of the lumen and the myocardium.

### 3.3.4 Application to a 4D OCT image dataset of the OFT

As a first attempt to 4D segmentation, we applied the 3D algorithm to 30 volume image datasets of the OFT that span over a cardiac cycle. We used the solutions of 3 (2D+time) image sequences at 3 locations that evenly space along the OFT as initial contours. We then applied the algorithms to 30 volume image data over the cardiac cycle and reconstructed the segmented contours into 3D surfaces. From the 4D surfaces (see Supplemental Video 3.1), we observed the peristaltic motion of the OFT wall over the cardiac cycle, which may be important for regulating blood flow in the OFT when the embryonic heart has no valves. 4D segmentation allows us to study the dynamic interaction of the wall and blood flow within the OFT.

## 3.4 Conclusions

We constructed a 3D hybrid segmentation algorithm that combines the advantages of optical flow and active contour/surface algorithms. We also developed a set of strategies to successfully delineate the heart OFT walls of chick embryos from OCT images. Our segmentation algorithm allows better visualization of the dynamic geometry and quantifying the wall dynamics of the OFT in the tiny and beating embryonic heart over the cardiac cycle for the first time (see Chapters 6 and 7). In addition, the segmentation allows us to generate image-based computational models to quantify the blood flow dynamics in the OFT (see Chapters 4 and 5).

## 3.5 Data supplemental

*Supplemental Video:*

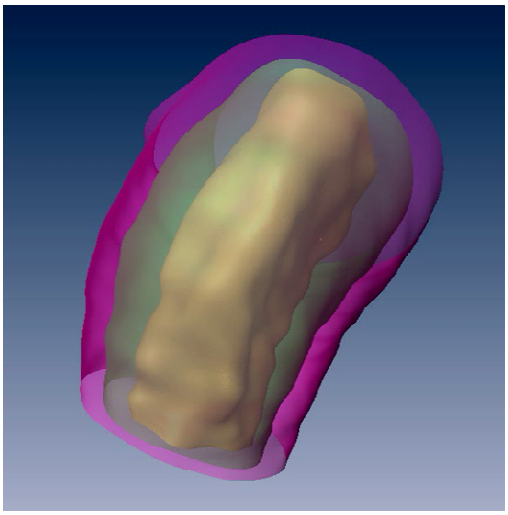

**Supplemental Video 3.1** 4D surfaces of the heart OFT of a HH18 chick embryo. OFT surfaces were generated from the segmentation of 30 OFT volume datasets over the cardiac cycle, using the hybrid 3D segmentation algorithm that we developed.

*Supplemental Figures:*

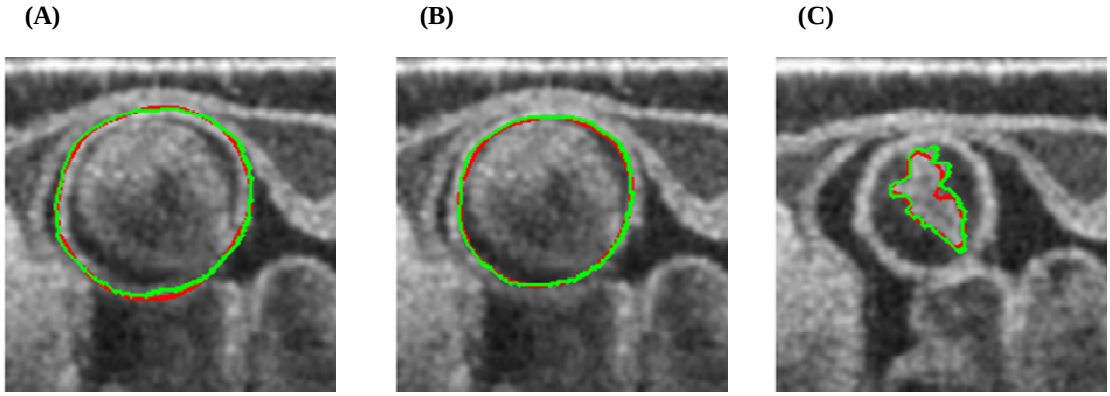


**Supplemental Figure 3.1** Comparisons between automatic (red contour) and manual (green contour) segmentations of (A) the exterior myocardium, (B) the interior myocardium, and (C) the lumen from a (2D+time) OCT image sequence of mid OFT cross-section. Examples depicted have the largest deviations from the manual segmentation (the ground truth).

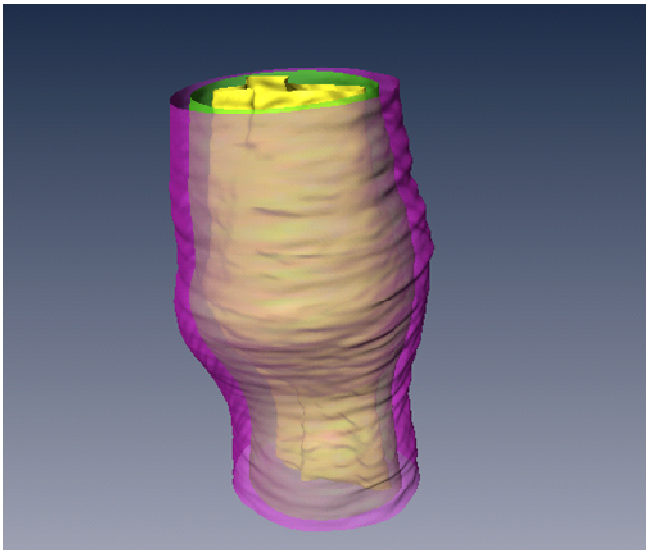

**Supplemental Figure 3.2** Surface reconstruction of OFT contours segmented from a 2D+time OCT images, showing the large and heterogeneous deformation of an OFT middle cross-section over the cardiac cycle.

# Chapter 4: Dynamic variation of hemodynamic shear stress on the walls of developing chick hearts: computational models of the heart outflow tract

Aiping Liu, Ruikang Wang, Kent Thornburg, Sandra Rugonyi

*This chapter was originally published by Springer*

*in Engineering with Computers, 2009(1), 73-86.*

*Reprinted with permission*

## 4.1 Introduction

The morphogenesis and growth of the developing heart are influenced by hemodynamic forces, which are exerted on the heart walls by the flow of blood.[18] Experiments on embryos from chicks, zebra fish, and mice during early development have shown that deviations from normal blood flow in the embryo heart lead to malformations[11, 13, 14, 135] that resemble heart defects in human with congenital heart diseases (CHD). CHDs affect about 1% of all human live babies in the United States .[19, 136]

Both *in vitro* and *in vivo* studies have shown that the cells that form the walls of the heart (and blood vessels) respond to alterations in hemodynamic forces by generating a cascade of signaling and gene expression events that ultimately lead to changes in heart morphology and growth.[15, 21, 25, 28, 29, 45, 137] Hemodynamic forces can be divided into: (1)

blood pressure, which acts perpendicularly to the wall, and (2) wall shear stress, which acts tangentially to the wall. Wall shear stress originates from viscous (friction) forces due to blood movement near the wall and is proportional to the gradient of blood velocities in the direction normal to the wall. In order to predict the effect of abnormal blood flow on heart development, a better understanding of the mechanisms by which hemodynamic forces affect heart development is needed. A step towards achieving this goal is to characterize the dynamic distribution of hemodynamic forces (blood pressure and wall shear stress) acting on the walls of the developing heart over the cardiac cycle.

Inside the developing chick heart, blood pressure can be measured *in vivo* (e.g.,[82, 138]), and wall shear stress can be calculated from blood velocity profiles measured *in vivo* near the heart wall. Blood velocities in the hearts of chick embryos[75] and zebra fish[14] have been measured using micro-particle imaging techniques. However, such measurements present several challenges due to a combination of the small length-scales of the developing heart (2 mm) and the continuous movement of the heart walls. Such difficulties, and their effect on the accuracy of the measurements, affect the calculation of wall shear stress in embryonic hearts.[22] Finite element models (FEM) have also been used to predict wall shear stress on the chick embryonic heart.[21, 91, 139] However, these previous FEMs were static, neglecting the dynamic effects of the heart wall motion and pulsatile blood pressure on wall shear stress.

Our objective is to determine how changes in the heart geometry and wall motion affect wall shear stress during the cardiac cycle, focusing on models of the outflow tract (OFT) of the chick heart during an early developmental stage (Hamburger Hamilton stage

18;[48] HH18). To this end, we used dynamic FEMs, which differ in the geometries of the OFT, and that incorporated the effects of dynamic wall motion and pulsatile blood pressure on blood flow. Geometric parameters and motion patterns of the chick OFT walls used in the FEMs were estimated from high-resolution optical coherence tomography (OCT) images. We chose the chick for our animal model because (1) chick embryos are easy to access for imaging and measuring; and (2) in early stages of development, the chick heart resembles the human heart.[140] We chose to focus on the OFT of the chick heart at HH18 because at this stage the OFT has a relatively simple geometry suitable for biomechanical modeling[49, 55] and because the OFT is very sensitive to changes in hemodynamic conditions.[13] Quantification of the changes in wall shear stress over a cardiac cycle in the OFT provides a step towards elucidating the role of hemodynamic forces on heart development.

## 4.2 Biological problem

During development, the morphology of the chick embryonic heart changes from a tubular structure into a four-chambered heart.[49] The chick heart starts beating at HH10 (36 h of incubation).[49, 141] At HH18 (68 h incubation), the heart of the chick embryo consists of a looped tube that pumps blood presumably via a peristaltic-like contraction motion.[51, 138] Heart septation and chamber formation start after HH21 (84 h of incubation).

At HH18, the chick heart consists of contiguous segments: the sinus venosus (inflow tract), the primitive atrium, the atrioventricular (AV) canal, the primitive ventricle, and the OFT.[49, 50] Although the heart has no valves at HH18, the AV canal and the OFT have

cardiac cushions, which are protrusions of the heart walls toward the lumen (domain where the blood flows) that are located where heart valves will form.[49, 55, 56] These cardiac cushions presumably increase the pumping efficiency of the developing heart. At HH18, the OFT is a slightly curved tube with an average external diameter of 430 μm[54] and an approximate length of 600 μm[50]. Typical heart rates of chick embryos at HH18 are 2.2–2.4 beats per second;[81, 138] thus, the period of the cardiac cycle, T is 0.45 s. During ventricular systole (about 1/3 of the cardiac cycle[138]), when the ventricle is contracting and ejecting blood into the chick arterial system, the OFT is fully open, allowing the flow of blood from the ventricle to the aortic sac (Figures 4.1a and 4.1c). However, during ventricular diastole (about 2/3 of the cardiac cycle), when the ventricle is filling with blood mainly from the atrium, the OFT walls contract (Figures 4.1b and 4.1d), limiting reverse blood flow (backflow).

The walls of the OFT are composed of three concentric layers:[55] endothelium, cardiac jelly, and myocardium. The endothelium, a single layer of endothelial cells (ECs), lines the internal part of the OFT wall and thus, it is in direct contact with blood flow. The cardiac jelly is comprised of an amorphous extracellular matrix that constitutes the bulk of the wall, including the cardiac cushions. The myocardium, consisting of a layer of primitive myocardial cells (MCs), is in the outer part of the OFT and actively contracts to limit backflow during ventricular diastole (note that in contrast to the OFT myocardium, the myocardium in the ventricle contracts to eject blood during ventricular systole). Previous research suggested that MCs respond mainly to changes in blood pressure,[15, 25, 45] whereas ECs respond mainly to changes in wall shear stress.[21, 28, 29, 137] *In vitro* studies of ECs further suggested that the response of ECs depends on both changes in wall shear

stress that occur over time (temporal variation) and the spatial distributions of wall shear stress.[28, 29, 137, 142, 143] To better understand the response of ECs to blood flow *in vivo*, we need a more comprehensive characterization of wall shear stress acting on the cardiac walls of the chick heart.

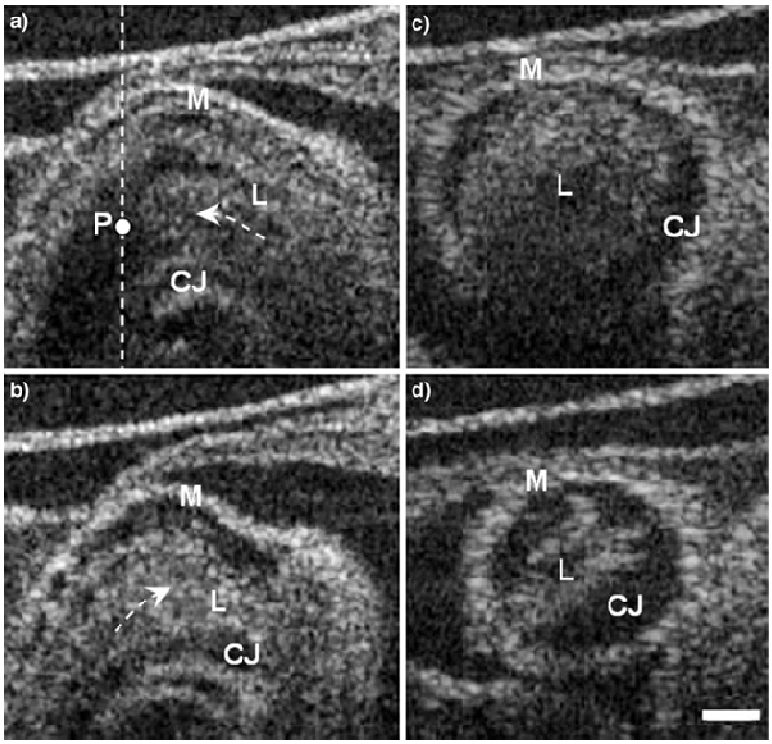


**Figure 4.1** Sections of HH18 chick heart OFT obtained from OCT images. The figure shows OCT images of the OFT during the cardiac cycle: (a) and (c) during ventricular systole, when the OFT is most expanded, (a) is a longitudinal section and (c) is a cross-section; (b) and (d) during ventricular diastole, when the OFT is most constricted, (b) is a longitudinal section and (d) is a cross-section. Point P marks the approximate location where velocities were acquired with Doppler OCT (see Fig 4.5.b). The white-dotted line corresponds to the direction of the incident light beam of Doppler OCT; the arrows indicate the direction of blood flow. Scale bar = 100 µm. L, Lumen, M, Myocardium; CJ, Cardiac jelly.

## 4.3 Methods

To determine the influence of wall geometry and motion on wall shear stress in the

developing chick heart, we used dynamic FEMs of the chick OFT at HH18. Our OFT models were based on *in vivo* 2D images of the chick heart that captured the motion of the OFT during the cardiac cycle. Simulations of these models gave the temporal variations and spatial distributions of wall shear stress on the OFT during the cardiac cycle.

Previously, we developed a dynamic, 3D image-based FEM of the OFT based on the assumption that the OFT has circular lumen cross-sections.[144] However, at HH18 the OFT has cardiac cushions that render the lumen cross-section non-circular[56] (see Figures 4.1c and 4.1d). To study the effect of cardiac cushions on the distribution of wall shear stress, we developed FEMs of the OFT with and without cardiac cushions.

### 4.3.1 Heart morphology and blood flow imaging

An OCT imaging system with a spatial resolution of 10 µm was used to acquire 2D morphological images of the OFT of chick embryos at HH18 (n = 4). Details of the OCT system, which was based on a spectral domain configuration, were reported previously.[145-147]

To image the OFT of the chick heart, fertilized white leghorn eggs were incubated with blunt end up at 102$^{o}$F and 85 to 87% humidity, in a horizontal rotation incubator (No. 1536E GQF Mfg. Co., Savannah, GA) for 3 days. To access the embryonic heart, the egg shell was opened, and the membrane that overlays the chick heart was removed. The egg was then placed on a custom-made stage under the OCT probe and the embryo was gently positioned so that the OFT could be easily imaged. For each embryo, OCT acquired 2D images of longitudinal and transverse cross-sections of the OFT (Figure 4.1)

over a period of 5 s, at a rate of 20 images per second. Thus, we captured 10 frames per cardiac cycle. The images revealed the contraction and expansion of the OFT wall during the cardiac cycle and the presence of the cardiac cushions, which greatly reduced the cross-sectional area of the lumen during contraction.

In addition, velocity of blood flow inside the OFT was measured by the OCT system configured in Doppler mode.[146] Velocity data were acquired at a point located at the approximate center of the OFT (point P in Figure 4.1a) with a time resolution of 0.1 ms. Measured velocity data corresponded to the projection of the 3D blood velocity vector in the direction of the incident OCT light beam (dotted line in Figure 4.1a). Although measured velocity data did not provide an accurate description of the 3D velocity field inside the OFT, they revealed temporal variations of blood flow velocity over the cardiac cycle.

### 4.3.2 Mathematical model and finite element discretization

#### 4.3.2.1 Mathematical model

Blood flow inside the chick OFT was modeled as an incompressible Newtonian flow (i.e., using the Navier–Stokes equations). Because the OFT walls contract and expand during the cardiac cycle, the lumen geometry (fluid domain) changes continuously with time. Dynamic changes in the geometry of the OFT lumen affect blood velocities and therefore need to be incorporated into the equations of blood flow. This was done through an arbitrary Lagrangian–Eulerian (ALE) formulation of motion (e.g.,[148, 149]), in which equations are expressed in terms of a moving reference frame (in the finite element implementation, the moving reference frame is the deforming finite element mesh).

Using the ALE formulation, the Navier–Stokes equations (in Cartesian coordinates and using indicial notation) are

$$\rho\left[\delta v_i/\delta_t + \left(v_j + \widehat{v_j}\right)\right] = \tau^F_{ij,j} \tag{4.1}$$

$$v_{i,j} = 0 \tag{4.2}$$

where the indices $i$ and $j$ indicate components (in the *x*, *y* and *z* directions) and ‘‘,’’ indicates differentiation; $\rho$ is density; $v_i$ indicates the (i)th component of the fluid velocity vector (with respect to a frame fixed in space); $\tau^F_{ij}$ is the (*i*, *j*)th component of the fluid stress tensor; $\delta v_i/\delta_t$ is the time derivative of $v_i$ with respect to the moving reference frame (as measured by an observer moving with the frame); and $\widehat{v_i}$ is the (*i*)th component of the velocity of the moving reference frame (with respect to a frame fixed in space).

The constitutive relations for a Newtonian fluid are

$$\tau^F_{ij} = -p\delta_{ij} + 2\mu e_{ij} \tag{4.3}$$

$$e_{ij} = \frac{1}{2}\left(v_{i,j} + v_{j,i}\right) \tag{4.4}$$

where $p$ is hydrostatic pressure, $\mu$ is viscosity, and $\delta_{ij}$ is the Kronecker delta.

In this study, the walls of the OFT were only included in the models to simulate the deformations of the lumen cross-section with time. Wall motion was assumed to be quasi-static (transient terms were neglected), with governing equations of motion given by:

$$\tau^S_{ij,j} = 0 \tag{4.5}$$

where $\tau_{ij}^{S}$ is the ($i$, $j$)th component of the wall Cauchy stress tensor. The OFT walls were assumed to be elastic. For an elastic material, the constitutive relations are:

$$\tau_{ij}^{S} = \frac{Ev}{(1+v)(1-2v)}\varepsilon_{kk}\delta_{ij} + \frac{E}{1+v}\varepsilon_{ij} \tag{4.6}$$

$$\varepsilon_{ij} = \frac{1}{2}\left(u_{i,j} + u_{j,i}\right) \tag{4.7}$$

where $E$ is the material Young's modulus (elastic modulus), $v$ is Poisson's ratio, and $u_{\,i}$ is the ($i$)th component of the wall displacement vector.

The coupling between the blood flow and wall equations was accomplished by satisfying two conditions (e.g., [150]):

i) equilibrium of forces at the interface,

$$\tau_{ij}^{F} n_j^{I} = \tau_{ij}^{S} n_j^{I} \tag{4.8}$$

and

ii) compatibility

$$\hat{u}_i^{I} = u_i^{I} \tag{4.9}$$

In Eqs. (4.8) and (4.9), the superscript $I$ indicates interface, $n_j^{I}$ is a unit vector normal to the wall that points towards the lumen, $\hat{u}_i^{I}$ is the displacement of the lumen boundary, and $u_i^{I}$ is the displacement of the wall at the interface with the lumen.

In addition, a no-slip condition was imposed at the interface between the lumen and the wall,

$$v_i^{I} = \dot{u}_i^{I} \tag{4.10}$$

The no-slip condition ensured that blood particles in contact with the wall moved with the wall (at the same velocity).

The force per unit interfacial area exerted by the flow of blood on the walls of the OFT, the stress vector $t_i$, was obtained from the fluid stress tensor ($\tau_{ij}^F$) evaluated at the lumen-wall interface (e.g., [150]):

$$t_i = \tau_{ij}^F n_j^I \tag{4.11}$$

where $\tau_{ij}^F$ is evaluated at the interface. $t_i$ can be decomposed into a normal vector and a vector tangential to the wall. The normal stress vector $t_{ni}$, is the projection of $t_i$ into $n_j^I$, and its magnitude is approximately equal to the hydrostatic pressure, $p$; hence, the normal vector is:

$$t_{ni} = \left(t_j n_j^I\right) n_i^I \approx -p n_i^I \tag{4.12}$$

The tangential stress vector or ‘‘wall shear stress vector’’, $\tau_{w_i}$, is the projection of $t_i$ into the plane of the lumen-wall interface,

$$\tau_{w_i} = t_i - t_{n_i} \tag{4.13}$$

Volume flow rate, Q, is the volume of blood flow that passes through a lumen cross-section per unit time. If $n_i^A$ is a unit vector normal to the plane of the cross section (pointing towards the OFT outlet), and A is the area of the lumen cross-section, then

$$Q = \int_A v_i n_i^A dA \tag{4.14}$$

$Q$ is positive when blood flows from the ventricle to the aortic sac and negative during backflow.

#### 4.3.2.2 Geometry of OFT models

To investigate the influence of cardiac cushions on the wall shear stress vector $\tau_{w_i}$ (eq. 4.13), we generated three models of the OFT: (1) a ‘‘cylindrical model’’, in which the lumen was modeled as a straight circular cylinder (the walls were not explicitly modeled); (2) a ‘‘cushion model’’ (Figures 4.2a and 4.2b) that included the OFT lumen and cardiac cushions, and (3) a ‘‘jelly model’’ (Figures 4.2c and 4.2d) that included the OFT lumen, cardiac cushions, and an additional layer of wall (to simulate additional cardiac jelly material in contact with the myocardium).

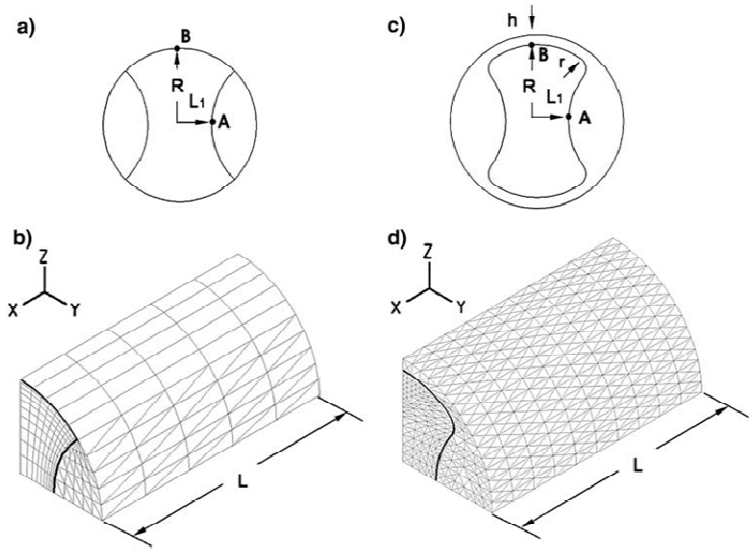


**Figure 4.2** Two FEMs of the OFT. Left: Cushion model: (a) reference cross-section and (b) FEM discretization. Right: jelly model: (c) reference cross-section and d FEM discretization. (Cylindrical model not shown.) In (a) and (c), the inner part corresponds to the lumen and the outer part, to the wall. In (b) and (d), the lumen-wall interface is marked with a thick line. Dimensions are: R = 0.1875 mm, $L_1$ = 0.077665 mm, L = 0.5 mm, h = 0.025 mm, and r = 0.03 mm. Points A and B are representative points where WSS was analyzed in detail.

In all three models, the external surface of the OFT was modeled as a straight circular cylinder. The cylindrical model, given its symmetry, was simulated using a 2D

axisymmetric FEM of blood flow. The symmetry of the cushion and jelly models allowed us to represent only one quadrant of each model, which were simulated using a 3D fluid structure interaction procedure (see Figure 4.2). The cylindrical, cushion, and jelly models differed in the geometry of the lumen cross-section, and therefore simulations of these three FEMs were used to determine differences in wall shear stress due to OFT lumen geometry.

In analyzing wall shear stress on the OFT using the cushion and jelly models, we focused on two points (see Figures 4.2a and 4.2c): A and B. Because of the symmetry of these models, $\tau_{w_i}$ at points A and B has always the same direction (relative to the ‘‘cell’’ position) but changes in magnitude during the cardiac cycle. For the cylindrical model, points A and B cannot be distinguished, and wall shear stress is uniform at the lumen-wall interface. We assumed that the ‘‘magnitude’’ of the wall shear stress vector $\tau_{w_i}$; WSS was positive during forward flow and negative during backflow.

#### 4.3.2.3 Boundary conditions on the OFT models

*4.3.2.3.1 Motion of the OFT wall* To simulate the passive distension and active contraction of the OFT myocardium during the cardiac cycle, a radial displacement (see Figure 4.3) was prescribed on the OFT external surface, which had cylindrical symmetry for all three models. The temporal variation and amplitude of the prescribed radial displacement were estimated from the OFT cross-sectional images acquired with OCT over time (e.g., Figures 4.1c and 4.1d) and simplified as shown in Figure 4.3. The amplitude of the prescribed radial displacement, $D_1$ was 70 μm (see also[54]). The reference geometry of the cushion and jelly models (when prescribed radial displacement was zero)

is shown in Figure 4.2. Maximum OFT expansion corresponds to a radial displacement of 0.5 $D_1$, and maximum OFT contraction corresponds to a radial displacement of -0.5 $D_1$. A different amplitude, $D_2$ = 90 μm, was also used to assess the effect of wall motion amplitude on blood flow and WSS.

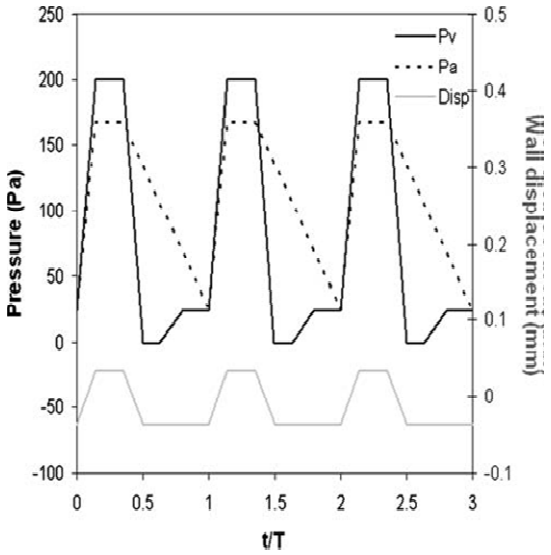


**Figure 4.3** Blood pressure and myocardium displacements prescribed as boundary conditions on the OFT models. Top temporal variations of ventricular pressure ($P_v$) prescribed at the inlet surface and pressure prescribed at the outlet surface ($P_a$). Bottom radial displacement prescribed on the external surface of the OFT models with amplitude $D_1$. Note the different scales for blood pressure (on left vertical axis) and radial displacements (on right vertical axis).

To further study the influence of wall motion on blood flow dynamics, we simulated two types of wall motion: (1) Simultaneous motion, in which prescribed radial displacements were the same along the OFT longitudinal direction; that is, all points on the OFT external surface moved the same amount in the radial direction, at the same time. Simultaneous motion was applied to all three FEMs. (2) Peristaltic motion, in which prescribed radial displacements were modeled as a displacement wave traveling along the OFT longitudinal direction, at a velocity of 7 mm/s.[51] In other words, peristaltic motion involves time lags in the wall motions of contiguous OFT cross-sections. Peristaltic

motion was applied to the cushion model. The simulated wall motions were used to determine the effect of wall motion on Q and WSS.

In our three OFT models, the walls were not allowed to expand or contract in the longitudinal direction. This was accomplished by restricting the longitudinal motion of the OFT ends.

*4.3.2.3.2 OFT lumen inlet and outlet conditions* For the boundary conditions on the OFT lumen inlet, we used published ventricular blood pressure data.[138] We prescribed a simplified pulsatile pressure wave (see Figure 4.3) on the lumen inlet surface of the OFT models, as a normal stress vector or normal traction.

Since there were no available data for blood pressure at the outlet of our OFT models (close to the aortic sac), we used blood pressure data in the chick dorsal aorta[82] to estimate blood pressure at the outlet. Because the location of the dorsal aorta is relatively far downstream from the outlet of our OFT models, using dorsal aorta pressure directly would have resulted in an over-estimation of the pressure difference between inlet and outlet, $\Delta P$. To overcome this difficulty, we prescribed a simplified pulsatile pressure on the surface of the lumen outlet that preserved the temporal variation of blood pressure in the dorsal aorta, but in which maximum and minimum pressure values were increased to reduce $\Delta P$. The increase in maximum and minimum pressure values (from dorsal aorta measurements) was determined by assuming $\Delta P$ to be equal to 0 at the start of ventricular ejection, and 33 Pa at ventricular systole, about the same mean $\Delta P$ measured in the AV canal during ventricular filling.[138] This later assumption was made because the AV canal and OFT apparently have similar roles in regulating blood flow through the

developing heart.[81, 141] Outlet blood pressures were prescribed as normal tractions.

Blood pressures at the inlet and outlet surfaces of our OFT model were the same for all FEMs. Therefore the temporal variation of $\Delta P$ was the same for all OFT models.

#### 4.3.2.4 FEM implementation

In our OFT models, embryonic chick blood was assumed to be a viscous, incompressible Newtonian fluid with a density of $\rho = 1{,}060\ kg/m^3$ and a viscosity of $\mu = 3 \times 10^{-3}\ kg/m\ s$,[91, 144] and the flow of blood was assumed to be laminar.[151] The OFT walls in the cushion and jelly models were assumed to be an almost incompressible elastic material with a Poisson's ratio of $v = 0.49$ and a Young's modulus of E = 1,000 Pa.

The lumen of our models was discretized using flow condition-based interpolation (FCBI) elements,[152] with the mesh near the wall slightly refined to better capture velocity variations near the wall and therefore, to calculate wall shear stress with greater accuracy. Using FCBI elements to discretize our models is equivalent to using control volume methods to calculate blood flow.[153] The specific FEM discretization used for each of our OFT models are summarized in Table 4.1.

**Table 4.1** Finite element discretization of the OFT models

| Model | OFT lumen | OFT wall |
|---|---|---|
| Cylindrical | 100 4-node FCBI axisymmetric 2D fluid elements | Imposed wall displacement. |
| Cushion | 1000 8-node FCBI 3D fluid elements | Imposed wall displacement and 675 4-node 3D solid elements (cardiac cushions). |
| Jelly | 19660 4-node FCBI fluid elements | Imposed wall displacement and 10200 11-node 3D solid elements. |

Blood flow was assumed to be initially at rest and three cardiac cycles were simulated. Each cardiac cycle (T = 0.45 s) was discretized using 100 time steps, with each time step equal to $4.5 \times 10^{-3} s$. All of our OFT models were simulated using the FEM software ADINA (Watertown, MA).[152]

#### 4.3.2.5 Convergence study

To ensure the accuracy of the results obtained, we performed a convergence study. We focused on the convergence of the blood-flow solution since, in this study; we were primarily interested in calculating WSS. The walls of the chick OFT were simulated to account for the approximate deformation of the lumen cross-section over a cardiac cycle, but not to calculate strains and stresses in the wall accurately. For the blood flow convergence study, we compared volume flow rate Q and WSS at representative points (points A and B in Figures 4.2a and 4.2c). Reported values correspond to those obtained at the mid-cross-section of the OFT models.

Convergence of the cylindrical model was assessed by comparing the FEM solution—using simultaneous wall motions and quasi-static conditions (in which transient terms in the fluid equations are neglected)—with the solution of the Hagen–Poiseuille flow under identical $\Delta P$ and model radius, R. Using the Hagen–Poiseuille solution,[154] derived for a fully developed flow in a circular tube, volume flow rate ($Q$) is equal to:

$$Q = \frac{\pi}{8\mu}\frac{\Delta P}{L}R^4 \tag{4.15}$$

and wall shear stress (WSS) is:

$$WSS = \frac{\Delta P}{2L}R \tag{4.16}$$

where $L$ is the length of the cylinder in the longitudinal direction. The maximum differences between the Hagen-Poiseuille solution and the results of the cylindrical model were 0.05% for $Q$ and 2.5% for *WSS*, suggesting that the FEM mesh that was used for the cylindrical model captured the behavior of the blood flow with accuracy.

To test the convergence of the cushion and jelly models, the results obtained with the fluid mesh specified in Table 4.1 and a mesh with ~eight times more fluid elements were compared for the cases in which the OFT had the maximum expansion and contraction (see Figure 4.4). Maximal differences found between the meshes were 2.7% for $Q$ and 3.2% for *WSS*, suggesting that the meshes shown in Table 4.1 and that were used in this study were sufficiently dense.

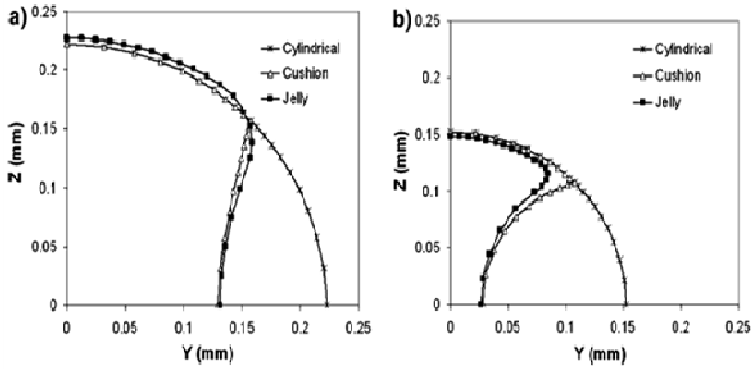


**Figure 4.4** Comparison of OFT lumen cross-sectional areas, obtained from our three models when a OFT is most expanded, and b OFT is most constricted.

We also simulated the transient behavior of the cushion and jelly models using the mesh specified in Table 4.1 but decreasing the time-step to $2.25 \times 10^{-3}\, s$ (from $4.5 \times 10^{-3} s$ used in the simulations). Maximal differences between solutions obtained with the two time steps were 0.5% for Q and 3% for WSS. Therefore, the time step employed was sufficient to provide accurate solutions.

## 4.4 Results

We report results as a function of a non-dimensional time t/T, where t is time and T is the period of the cardiac cycle (T = 0.45 s in our simulations). For reference, in our models ventricular systole is between t/T = 0 and t/T = 0.38, and ventricular diastole from t/T = 0.38 to t/T = 1. We chose the cushion model as our basic OFT model, against which we compared the cylindrical and jelly models.

### 4.4.1 Importance of inertial effects on blood flow

Blood flow in the chick heart is characterized by low Reynolds (Re) and Womersley (Wo)

numbers.[75, 144] Re—a measure of the ratio between inertial and viscous forces[154] --is defined as: $Re = \rho VR/\mu$, where $\rho$ is the fluid density, $V$ is a characteristic velocity, $R$ is radius (or a characteristic length), and $\mu$ is the fluid viscosity. A small *Re* therefore implies that flow inertial forces are negligible. Wo—a measure of viscous effects in oscillating flows[154]—is defined as: $Wo = \rho\Omega R^2/\mu$, where $\Omega$ is a characteristic frequency (in our case the frequency of the cardiac cycle—about 2 Hz). A small $Wo$ indicates that velocity is in phase with the pressure gradient. Flow with small Re and $Wo$ numbers is laminar (not turbulent).

For the cylindrical model, we compared the results of simulations under quasi-static conditions with those of a transient analysis. These comparisons showed that the temporal variation of the center velocity, *Q* and *WSS*, were very similar for both cases (results not shown). The maximal differences occurred during contraction of the OFT wall, when the transient solutions presented a small time lag of about 0.003 s (less than a time step). Differences between the solutions obtained with the two approaches when the OFT was most constricted (t/T = 0.5) were 4% for the center velocity, 3.5% for Q and 2.8% for WSS. These small differences were in agreement with the small Re (maximum ~27) and $Wo$ (maximum ~0.24) obtained from the transient solution.

Small Re and Wo numbers were obtained in all our simulations of OFT models. Maximal Re = 17.9 and maximal $Wo = 0.26$—for the cushion and jelly models, the ‘‘radius’’ R in the definition of Re and Wo numbers was assumed to be the distance between the center of the model cross-section and point B (see Figures 4.2a and 4.2c). Obtained Re and $Wo$ from our OFT models were consistent with previous reports[75, 144],

and confirmed that inside the OFT inertial effects are negligible.

### 4.4.2 Blood velocity and volume flow rate

Figure 4.5a shows the axial velocity of blood flow at the center of the OFT cross-section during the cardiac cycle calculated from the cushion model (with simultaneous and peristaltic wall motions), and Figure 4.5b shows the velocity measured using Doppler OCT at point P in Figure 4.1a. Since the measured velocity is the projection of the blood velocity vector in the direction of the incident light beam (the dotted line in Figure 4.1a), we could compare only the shape of the velocity profiles over time but not the absolute values of measured and calculated velocities. The calculated velocity (especially for the cushion model with peristaltic wall motion) resembled the temporal features of the measured velocity. Both calculated and measured velocities showed a peak during ventricular systole and significant backflow during ventricular diastole. However, the ratio between the absolute values of the peak positive and negative velocities was smaller for the calculated velocity (~1.4 for simultaneous and ~2.0 for peristaltic wall motion) than that of the measured velocity (~3.5), suggesting that our models overestimated backflow. In our OFT models, blood velocity just before ventricular systole was negative, whereas the measured Doppler OCT data showed some oscillations above zero. Discrepancies between calculated and measured velocities can be attributed to the simplifying assumptions of the cushion OFT model and to experimental uncertainties during velocity measurement, e.g., point P was fixed in space and therefore its relative position inside the OFT changed due to rigid body motions of the beating chick heart; the same is true for the angle between blood flow and the direction of the incident light beam.

Given that our objective was to determine the influence of wall geometry and motion on WSS, the discrepancies between calculated and measured velocities were not crucial for our analysis.

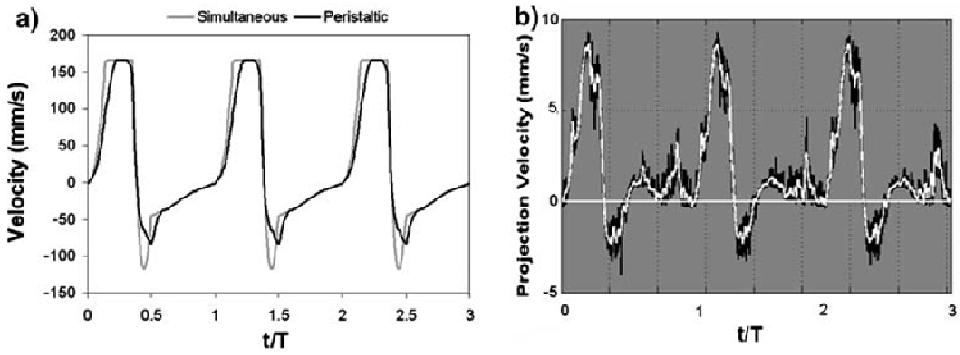


**Figure 4.5** Blood velocities calculated and measured inside the OFT. (a) Calculated longitudinal velocities at the center of the mid-cross-section obtained from the cushion model with simultaneous and peristaltic wall motions, with prescribed wall motion amplitude D1 (70 µm). (b) Blood velocities measured with Doppler OCT at a fixed point located at the approximate center of the OFT lumen (see point P in Figure 4.1a) in the direction of incident OCT light beam (dotted line in Figure 4.1a).

Figure 4.6 shows *Q* obtained from simulations of the cylindrical, cushion and jelly models. The temporal variation of *Q* obtained from the cushion model was very similar to that from the jelly model (see also Table 4.2). In contrast, the magnitude of *Q* obtained from simulations of the cylindrical model was about two times larger than *Q* from the cushion model during ventricular systole and about four times larger during peak backflow. Differences in *Q* among the models, might be due to differences in the lumen cross-sectional areas of the OFT models. Simulations of the cylindrical, cushion, and jelly models resulted in variations in lumen cross-sectional areas during the cardiac cycle (see Figure 4.4). Differences in the lumen cross-sectional areas between the cushion and jelly models were relatively small (about 5% difference when the OFT was most expanded). The cylindrical model, because of the absence of cardiac cushions, had a

significantly larger lumen cross-sectional area than the cushion and jelly models (about 33% difference from the cushion model when the OFT was most expanded).

To determine whether the geometry of the OFT lumen also affects *Q*, we varied the radius of the cylindrical model over time so that its cross-sectional area matched the cross-sectional area of the cushion model (we called this resulting model the cylindrical ‘‘same area’’ (SA) model). Simulations of the cylindrical SA model showed that *Q* was greatly reduced, when compared to the original cylindrical model (see Figure 4.6). However, absolute maximum and minimum values of *Q* obtained from the cylindrical SA model were still larger than those from the cushion and jelly models (see also Table 4.2). These results suggest that cardiac cushions minimize backflow primarily by reducing the OFT lumen cross-sectional area but also by changing the geometry of the lumen.

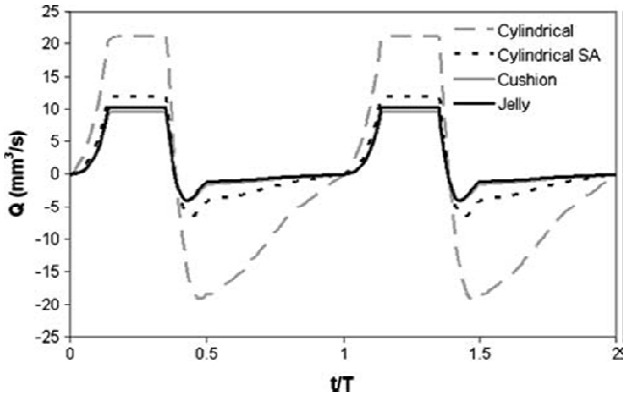


**Figure 4.6** Volume flow rates (Q) at the mid-cross-section of the OFT obtained from the OFT models. For cylindrical, cushion, and jelly models, a simultaneous wall displacement of amplitude D1 was prescribed. For the cylindrical SA model (Sect. 4.2), prescribed wall displacements were such that matched temporal variations of the lumen cross-sectional area calculated from the cushion model.

**Table 4.2** Volume flow rates (Q) and wall shear stress (WSS) obtained from simulations of the OFT models

| Wall motion | | Simultaneous | | | | | Peristaltic |
|---|---|---|---|---|---|---|---|
| Model | | Cylindrical | | Cushion | | Jelly | Cushion |
| Wall displacement | | *D*1 | SA | *D*1 | *D*2 | *D*1 | *D*1 |
| Mean Q ($mm^3/s$) | | -0.59 | 1.53 | 1.78 | 2.77 | 2.10 | 1.53 |
| Max Q ($mm^3/s$) | | 21.11 | 11.79 | 9.61 | 12.65 | 10.34 | 9.61 |
| Min Q ($mm^3/s$) | | -19.15 | -6.55 | -4.10 | -4.04 | -4.01 | -2.26 |
| Mean WSS (Pa) | A | -4.05 | -2.51 | -1.17 | 0.31 | -0.75 | -1.18 |
| | B | | | -1.60 | -1.06 | -1.53 | -1.61 |
| Max WSS (Pa) | A | 7.09 | 6.13 | 8.19 | 8.67 | 8.23 | 8.18 |
| | B | | | 5.55 | 5.98 | 5.76 | 5.54 |
| Min WSS (Pa) | A | -19.34 | -13.28 | -12.15 | -10.78 | -11.62 | -12.82 |
| | B | | | -9.65 | -8.21 | -9.63 | -11.29 |
| OSI | A | 0.25 | 0.29 | 0.40 | 0.46 | 0.43 | 0.39 |
| | B | | | 0.33 | 0.38 | 0.34 | 0.31 |

Changes in the motion of the OFT wall also resulted in different temporal variations of $Q$. Figure 4.7a shows differences in $Q$ obtained from the cushion model when the prescribed wall motion was simultaneous and peristaltic. Peristaltic motion reduced the absolute value of $Q$ during backflow (see Table 4.2) and smoothed the abrupt variations of $Q$ (produced by the non-smooth $\Delta P$ prescribed). Increasing the amplitude of OFT

prescribed displacement from $D_1$ (70 µm) to $D_2$ (90 µm), affected $Q$ (Figure 4.7b). During ventricular systole, $Q$ was larger when the amplitude of the wall motion was $D_2$ than when it was $D_1$ (see Table 4.2) because of an increase in the area of the OFT lumen. During backflow, however, the differences in $Q$ between simulations of the two displacement amplitudes were smaller than during forward-flow.

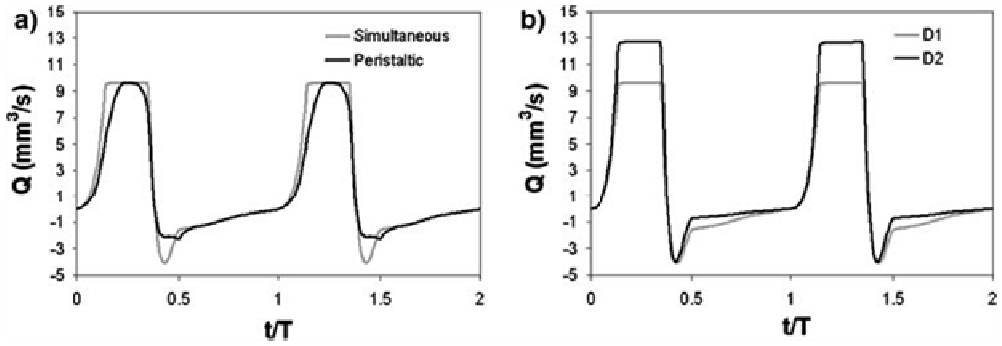


**Figure 4.7** Volume flow rates ($Q$) obtained from the cushion model. (a) Comparison between simulations of simultaneous and peristaltic OFT wall motions, calculated using a prescribed radial displacement amplitude $D_1$ = 70 µm. (b) Comparison between simulations of simultaneous OFT wall motion, calculated with prescribed radial displacement amplitudes $D_1$ = 70 $\mu$m and $D_2$ = 90 $\mu$m.

### 4.4.3 Wall shear stress

Variations in WSS were influenced by the geometry of the OFT models. While our cylindrical models, due to their symmetry, presented a uniform WSS along the perimeter of the lumen cross-section (and even along the OFT if we assume a fully developed blood flow profile), our cushion and jelly models showed a non-uniform distribution of WSS, with maximal WSS at the cardiac cushion (Figure 4.8).

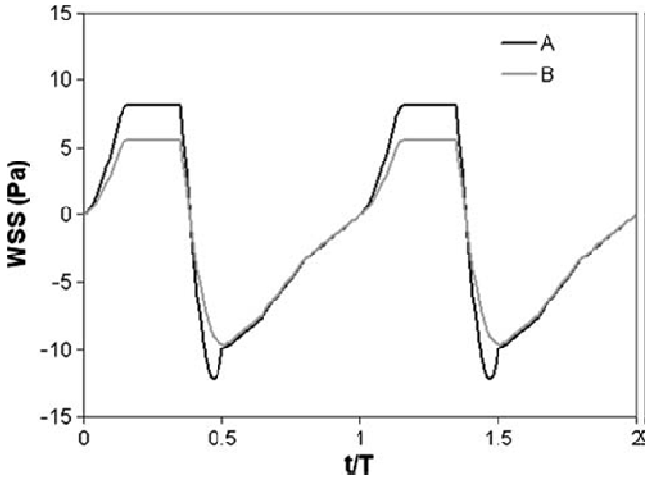


**Figure 4.8** Temporal variations of WSS in the cushion model at points A and B (Figure 4.2a) in the mid-cross-section of OFT. Results correspond to the case of simultaneous wall motion with prescribed wall displacement amplitude $D_1$ = 70 $\mu$m.

To evaluate differences in WSS, for the cushion and jelly models two points were considered: (1) point A, located at the center of the cardiac cushion, at the lumen wall interface; and (2) point B, located at the center of the lumen-wall interface where there is no cardiac cushion (Figures 4.2a and 4.2c). The temporal variations of WSS for the cushion and jelly models at points A and B were very similar (see Figure 4.9). Temporal variations of WSS in the cylindrical SA model differed from those in the cushion and jelly models at points A and B, see Figure 4.9. These results showed that the geometry of the OFT affected the temporal variation and spatial distribution of WSS.

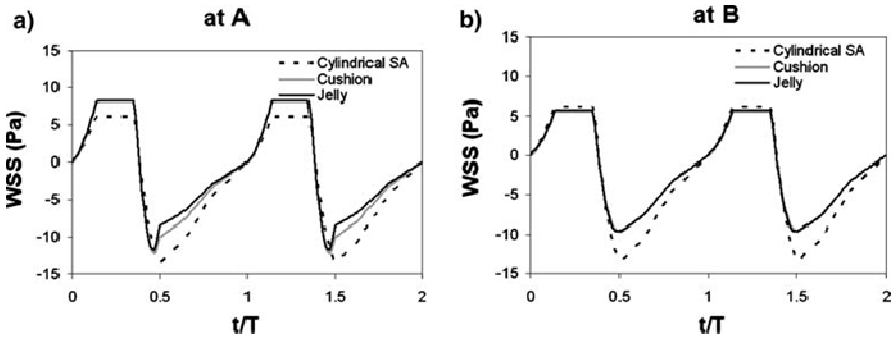


**Figure 4.9** Comparison of WSS obtained using the OFT models. WSS at (a) point A and (b) point B. The cushion and jelly models were simulated with simultaneous wall motion, with prescribed wall displacement amplitude $D_1$ = 70 µm; the wall motion of the cylindrical SA was prescribed such that temporal variations of cross-sectional area matched those of the cushion model.

Changes in OFT wall motion also resulted in variations of WSS. Peristaltic wall motion in the cushion model smoothed the temporal variation of WSS at points A and B and introduced slight changes in the amplitude of oscillation of WSS compared to simultaneous wall motion applied to the cushion model (see Figures 4.10a and 4.10c; and Table 4.2). Increasing the amplitude of the prescribed radial displacement from $D_1$ to $D_2$, using simultaneous wall motion, changed the magnitude of WSS at points A and B (Figures 4.10b and 4.10d; and Table 4.2) with a larger change observed at point A during ventricular diastole. Maximal WSS during systole and minimal WSS during diastole; however, did not change significantly, even though $Q$ changed significantly with changes in wall motion amplitude (see Figure 4.7b and Table 4.2). These results suggest that changes in geometry affect the temporal variation and spatial distribution of WSS more than do variations in wall motion.

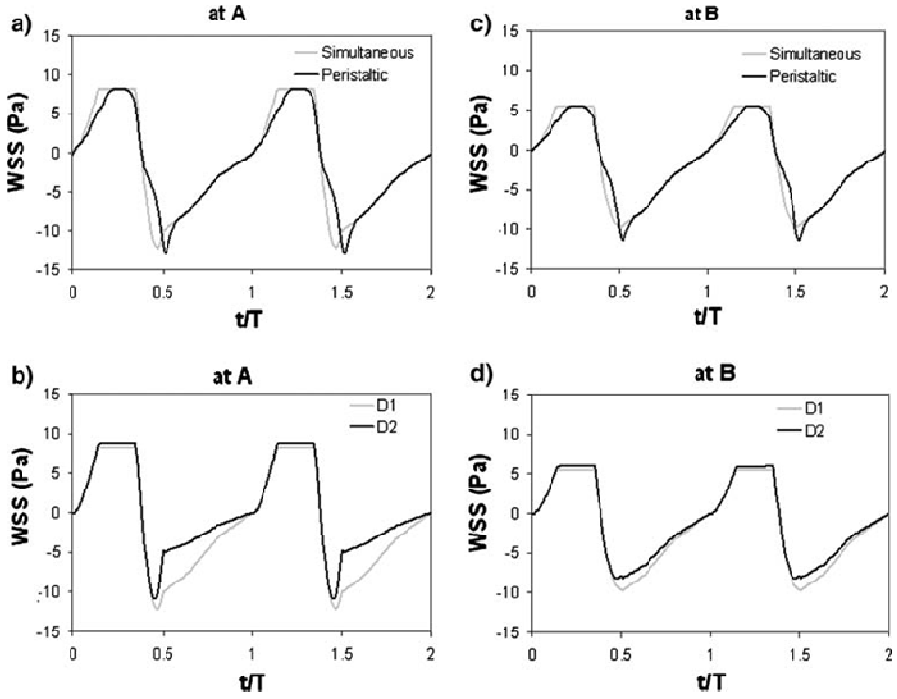


**Figure 4.10** WSS obtained from the cushion model. Left: WSS at point A. (a) simultaneous versus peristaltic motion, and (b) prescribed wall displacement amplitude D1 (70 µm) versus D2 (90µm). Right: WSS at point B. (c) simultaneous versus peristaltic motion, and (d) prescribed wall displacement amplitude D1 (70 µm) versus D2 (90 µm).

### 4.4.4 Oscillatory shear index

The oscillatory shear index (OSI), following Ku et al.,[155] estimates the change in direction of the wall shear stress vector, $\tau_{w_i}$ (defined by Eq. 4.13) with respect to a ‘‘mean’’ direction. This change in direction occurs due to changes in the direction of blood flow. Due to the symmetry of our OFT models, blood flow at points A and B is either forward or backward (no cross-flow can occur). Thus, OSI was defined as:

$$OSI = \frac{\int_0^T WWS^* dt}{\int_0^T |WSS| dt} \tag{4.17}$$

With

$$WWS^{*} = \begin{cases} 0\,, & if\ sign(WSS) = sgn\left(\int_0^T WSSdt\right) \\ |WSS|\ \ , & if\ sign(WSS) \neq sgn\left(\int_0^T WSSdt\right) \end{cases}$$

where $T$ is the period of the cardiac cycle. Positive WSS corresponds to forward flow of blood and negative to backflow. OSI then is the fraction of the integral of |WSS| in which WSS has a sign (+ or -) opposite to the sign of the mean. Note that if WSS is constant, then OSI = 0, and when WSS oscillates in a sinusoidal fashion, $OSI \rightarrow 0.5$.

In all cases (except for the cushion model with prescribed radial displacement amplitude $D_2$), mean WSS was negative (Table 4.2). Therefore, OSI gave the ratio of the integral in time of positive WSS (during forward flow) and the integral in time of |WSS| in a cardiac cycle. It also provided a means to estimate the ratio between the integral of |WSS| during forward and reverse flow. We found that (see Table 4.2): (1) OSI was smaller in the cylindrical model compared to the cushion and jelly models; (2) OSI was larger at point A (i.e. at the cushion) than at point B (cushion and jelly models); and (3) peristaltic motion had almost no influence on OSI.

## 4.5 Discussion

The cylindrical, cushion, and jelly models of the HH18 chick heart OFT presented here were developed to determine the influence of OFT geometry and wall motion on WSS. The OFT in the cylindrical model had a circular lumen cross-section, and the cushion and jelly models (Figure 4.2) had non-circular OFT lumen cross-sections because of the presence of cardiac cushions. For each model, radial displacements were prescribed on the external surface of the models, to simulate myocardium contraction/distension and

wall motion during the cardiac cycle. Also for each model, a drop in blood pressure, $\Delta P$, that changed over time was prescribed between the inlet and outlet surfaces of the OFT lumen (by applying ‘‘pressure’’ boundary conditions to the inlet and outlet surfaces, Figure 4.3) to simulate the driving force for blood flow within the OFT.

Our OFT models were mainly based on three assumptions: (1) the pressure prescribed at the lumen outlet was estimated: since measured pressure data at the aortic sac (the outlet of our models) was not available, the prescribed outlet pressure was estimated from measurements downstream of the OFT; (2) the geometry of the FEMs was simplified: the OFT was modeled as a straight tube (instead of a bended tube), with either circular cross-sections (cylindrical model) or with a pair of identical and symmetric cardiac cushions (cushion and jelly models); and (3) the motion of the OFT wall was simulated by prescribing a radial displacement: the external surface of our models remained circular at all times and the temporal variation of radial displacements was estimated (from ten sequential OCT images). Given these assumptions, our models of the OFT neglected several aspects of actual blood flow inside the OFT.

Regarding Assumption 1, the estimation of prescribed outlet pressure affected $\Delta P$; and since $\Delta P$ provides an important driving force for blood flow through the OFT, calculated $Q$ and WSS were also affected. Therefore, our models provided only estimates of $Q$ and WSS. Furthermore, in our OFT models, pressure boundary conditions were prescribed and hence uncoupled from the OFT dynamics. In living chick embryos, because cardiovascular circulation forms a closed system, $\Delta P$ and the geometry of the OFT lumen and wall motions are coupled. Uncoupling these variables, however, allowed

for less complex calculations and interpretation of results. Regarding Assumption 2, the FEMs neglected the influence of the OFT curvature on blood flow, which affects the local variation of WSS. In addition, actual cardiac cushions are not as symmetric as in our models (Figure 4.1), and therefore our models neglected non-symmetric distributions of WSS. Regarding Assumption 3, the motion of the OFT wall was assumed to go from an open to a close state (Figures. 4.3 and 4.4), which is likely an oversimplification of the actual wall motion. In addition, the external surface of our OFT models was assumed to remain circular at all times, and therefore the effects of the non-symmetric motion of the myocardium layer, observed in the OCT images, were neglected in our simulations. Given these assumptions, our OFT models represent a starting point to estimate variations in $Q$ and WSS during the cardiac cycle and to determine how wall geometry and motion change WSS in the chick developing heart.

Our results showed that volume flow rate, Q, was generally in phase with the imposed $\Delta P$, but was also influenced by the motion of the OFT wall. Small phase shifts between $Q$ and $\Delta P$ occurred due to wall motion, especially when the OFT was quickly expanding or contracting. Given the small length scales of the developing heart (<2 mm), blood flow inside the heart is strongly affected by viscous forces. This is reflected by the small Re (<30) and $Wo$ (<1) numbers obtained from the simulations. Thus, $Q$ was expected to generally be in phase with the imposed $\Delta P$, but with amplitude modulations and small time shifts due to the effect of OFT wall motion on blood flow. We found that the amplitude of the wall motion contributed to the amplitude of oscillation of $Q$ (Figure 4.7b), as expected, and that peristaltic motion (due to the time lags in the motion of

contiguous cross-sections) altered the temporal variation of $Q$ with respect to that of simultaneous wall motion (Figure 4.7a). The simulations performed, indicated that a peristaltic motion prevents backflow more efficiently than a simultaneous motion. In our models this is because for the simulated peristaltic motion the inlet of the OFT started contracting 0.036 s (0.08 T) before contraction started in the simulated simultaneous wall motion case.

Since WSS is affected by $Q$ inside the heart, WSS depends on $\Delta P$ and the motion of the OFT wall. Changes of WSS over time were influenced by the amplitude of the wall motion ($D_1$ or $D_2$) (see Figures 4.10b and 4.10d). We found, however, that wall motion had a larger influence on $Q$ than on WSS (compare Figure. 4.7b with Figures 4.10b and 4.10d). For a cylindrical model, the Hagen–Poiseuille solution (Eqs. 4.15 and 4.16) predicts that WSS is proportional to $Q^{1/4}$. Thus, while variations in $Q$ affect WSS, changes in WSS are relatively smaller than changes in $Q$. This is consistent with results from our models (although the proportionality with $Q^{1/4}$ is no longer valid for the cushion and jelly models).

Our results showed that cardiac cushions limit backflow in the OFT by constricting the lumen area and affecting the distribution of blood flow velocities in the lumen of the OFT. When the OFT myocardium contracts and pressure inside the OFT decreases, the cardiac cushions bulge towards the OFT lumen (see Figure 4.4), reducing the area of the OFT lumen cross-section. This decrease in area significantly reduces $Q$ during backflow—a reduction that is evident when comparing the calculated Q in the cushion and jelly models with the calculated $Q$ in the cylindrical model (Figure 4.6). The presence of

cardiac cushions also changes the geometry of the OFT lumen cross-section, which we found to play a role in reducing backflow. Simulations of the cylindrical model, in which the cross-sectional area changed over time like the cushion model (cylindrical SA) showed that the magnitude of $Q$ in models with cardiac cushion was smaller than in the cylindrical SA model, especially during backflow (Figure 4.6). These results indicate that $Q$ is influenced not only by the cross-sectional area of the OFT lumen but also by the geometry of the lumen cross-section. Differences in $Q$ between models with and without cardiac cushions were consistent with the increase in the area of the lumen-wall interface in models with cardiac cushions (relative to cylindrical SA models). A larger interface increases the viscous resistance to blood flow (on the walls of the OFT), and therefore for the same applied $\Delta P$ and cross-sectional area, models with larger interfacial area result in lower $Q$. Hence, the geometry of cardiac cushions is effective in reducing backflow by reducing cross-sectional area and increasing the resistance to blood flow.

The presence of cardiac cushions also affects the temporal variation and spatial distribution of WSS at the lumen-wall interface. Because cardiac cushions change the geometry of the lumen cross-section (from that of a cylindrical tube), they affect $Q$ and the distribution of blood velocities within the lumen and hence WSS (see Figures 4.8 and 4.9). The smaller OSI found for the cylindrical SA model compared to that of the cardiac and jelly models, indicates that the cardiac cushions increase the ratio between the time integral of |WSS| during forward and backflow (mean WSS in our models was generally negative). We also found that for models with cardiac cushions, at point A (cardiac cushion) the ratio of the integral of |WSS| during forward and backflow is smaller than at point B (OSI at point A is larger than at point B). Whether endocardial cells (ECs) can

differentiate a positive from a negative WSS, or whether ECs respond to the magnitude of WSS, the integral of WSS over time or some other related variable is not yet known. However, it is clear that the ECs that line the cardiac cushion (where valves will later form) are subjected to different mechanical stimuli than cells outside the cardiac cushions. The biological implications of these spatial variations in mechanical stimuli are not yet fully understood, but WSS likely plays an essential role on valve formation.

## 4.6 Conclusions

We developed OFT models of HH18 chick embryos to characterize patterns of WSS over the cardiac cycle and to determine whether these patterns are affected by OFT geometry and wall motion (simultaneous and peristaltic wall motions were considered and two amplitudes of wall motion were simulated). Our OFT models showed that even though backflow through the OFT is limited by the presence of cardiac cushions, WSS during backflow can have a larger absolute value than WSS during forward flow. WSS showed significant oscillation over time and was asymmetrically distributed, with larger absolute values at the cushions. Therefore, ECs located at the cardiac cushions are subjected to different WSS than are ECs located elsewhere. These differences in WSS may affect valve formation.

# Chapter 5: Quantifying blood flow and wall shear stresses in the outflow tract of chick embryonic hearts

Aiping Liu, Andrew Nickerson, Aaron Tryoer, Xin Yin, Robert Cary, Kent Thornburg, Ruikang Wang, Sandra Rugonyi

*This chapter was originally published by Elsevier*

*in Computers & Structures, 2011(11-12), 855-867.*

*Reprinted with permission*

## 5.1 Introduction

Stresses exerted by blood flow on cardiac walls modulate growth and development of the heart in such a way that altered blood flow patterns could lead to cardiac defects, which affect 1% of newborns in the US each year.[136] Underlying mechanisms by which blood flow affects cardiac development remain elusive, partly due to a lack of methodologies to accurately quantify wall stresses in the beating embryonic heart. In particular, wall shear stresses (WSS) are known to regulate the response of endocardial cells (EC), which line the lumen of the heart.[14, 21, 24, 156] *In vitro* studies have shown that ECs sense and respond to WSS by activating signaling pathways that modulate EC function.[156, 157] To understand the role of WSS in heart development, quantification of spatial and temporal distributions of WSS as the heart beats are needed. Here, we used the chick embryonic heart as our animal model of cardiac development, focusing on the chick heart outflow tract (OFT), and quantified the distribution of WSS on the wall of the OFT during the cardiac cycle using a combination of physiological data, imaging, and finite element (FE)

modeling.

The chick embryo is frequently used to study cardiac development because of structural and functional similarities between chick and human embryonic hearts at early developmental stages[1, 158] and easy access of chick embryos inside the egg-shell.[1, 157] At the early chicken developmental stage (i.e., Hamburger-Hamilton stage HH18 [48, 49]) that we studied here, the chick embryonic heart is an s-shape tube, with no valves or chambers, but with distinguishable heart segments: the sinus venosus, primitive atrium, primitive ventricle, and OFT.[48, 50] The OFT is the distal region of the heart, which connects the ventricle to the aortic sac, from where arterial branches bifurcate (see Figure 5.1A). The OFT wall has 3-layers: (i) myocardium, an external muscle layer that actively contracts; (ii) endocardium, a monolayer of ECs lining the heart wall; and (iii) cardiac jelly, an extracellular matrix that interposes between the myocardium and endocardium. In the OFT, the cardiac jelly forms cardiac cushions, which are protrusions of the cardiac wall toward the lumen (see Figures 5.1B and 5.1C) and which distribute spirally along the OFT.[159] During myocardial contraction, the cardiac cushions deform to close the OFT lumen, acting as primitive valves to regulate blood flow through the OFT.[160, 161] At HH18, the OFT, which will eventually develop into valves and septa of the heart, is very sensitive to changes in blood flow dynamics.

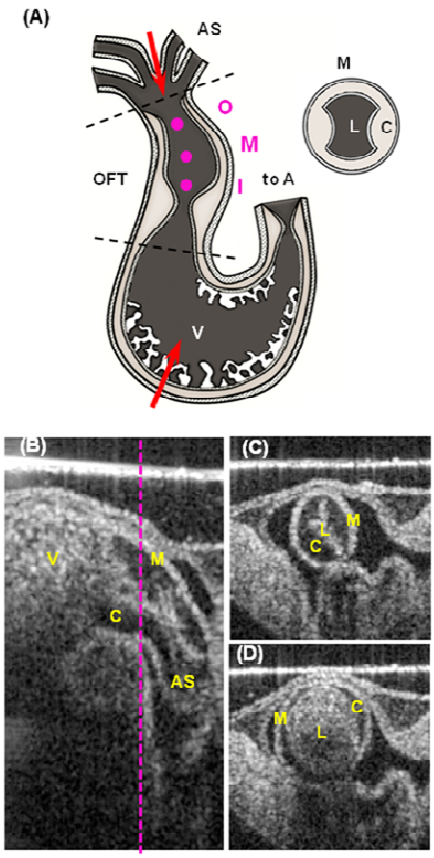


**Figure 5.1** Stage HH18 chick embryonic heart and its outflow tract (OFT). (A) Sketch of a chick embryonic heart with the OFT region marked by dotted black lines; the upper right inset shows a sketch of the OFT cross-section. Red arrows indicate the approximate locations where blood pressures were measured: in the ventricle and aortic sac. The three purple dots indicate the approximate locations where blood flow was measured (near the OFT inlet, middle and outlet) using Doppler ultrasound. (B), (C) and (D) Optical coherence tomography (OCT) images of the HH18 chick heart, showing: (B) a transverse section of the OFT, (C) a cross-section of the OFT at the most constricted state, and (D) the same cross-section at the most expanded state. The dotted purple line in (B) indicates the location of the cross-section in (C) and (D). M, myocardium; C, cardiac jelly; L, lumen; A, atrium; V, ventricle; OFT, outflow tract; AS, aortic sac.

To understand how the blood flow dynamics affect the morphogenesis of the OFT, it is important to quantify the distribution of WSS on the OFT wall. WSS is a hemodynamic force that blood flow imposes tangentially on the surface of the heart wall. It cannot be measured directly in the OFT *in vivo*, but can be derived from the flow velocity field:

$$\boldsymbol{\tau} = \mu \cdot d\mathbf{V}/d\mathbf{n} \tag{5.1}$$

where $\mu$ is the blood viscosity; $\mathbf{V}$ is the blood flow velocity vector; $\mathbf{n}$ is a unit vector normal to the lumen-wall surface; and $d\mathbf{V}/d\mathbf{n}$ is the directional derivative of the velocity in the direction normal to the lumen-wall surface.

Accurately quantifying the blood velocity field is critical for estimating WSS. Several

flow-imaging techniques, such as Doppler ultrasound, and particle image velocimetry (PIV), have been used to measure intracardiac blood flow in the chick embryonic heart.[60, 74-78] However, none of these techniques gives sufficient temporal and spatial resolution of 3D velocity fields in the tiny dynamic beating embryonic heart for accurately quantifying WSS.

Computational fluid dynamic (CFD) models have been developed to compute blood flow in human and chick embryonic hearts.[21, 91, 111, 139, 162] Early CFD models of embryonic hearts assumed a steady-state flow and a rigid, simplified geometry.[139, 162] These simplified models suggested that blood flow dynamics is affected by the heart morphology, which varies significantly as the heart develops. Therefore, realistic models of the embryonic heart at specific developmental stages are needed to understand how blood flow dynamics affect heart development. To take the complex geometry of the embryonic heart into account, DeGroff and colleagues[91] pioneered the use of image-based FE models to simulate the blood flow in stages 10 and 11 human embryonic hearts, followed by Groenendijk and colleagues[21] who generated a FE model of an HH14 chick embryonic heart.[21, 91] Both image-based FE models showed 3D spatial distribution of WSS in early human and chick embryonic hearts; high WSS were identified at narrow lumen regions and the inner curvature of the lumen surface. However, the calculated WSS corresponded to a static geometry of the embryonic heart. To study the effects of the cardiac wall dynamics on the blood flow, Taber and colleagues generated a simplified 2D dynamic model of the chick embryonic heart.[111] The model indicated that the presence of cardiac cushions and peristaltic motion of the heart wall in early developing hearts renders pulsatile cardiac blood flow.

In our previous study, we generated dynamic models of the OFT, which included pulsatile pressures and dynamic wall motion.[144, 163] Our previous models have complementarily showed that the 3D curvature of the OFT, the shape of the luminal cross-section, and the peristaltic wall motion of the OFT affect the distribution of WSS on the OFT wall. However, these models simplified the geometry of the OFT, and thus, they did not fully characterize blood flow dynamics and WSS in the OFT. In this study, we present a methodology to quantify the temporal and spatial distribution of WSS using image-based FE models of the developing heart OFT, combined with physiological data.

## 5.2 Experimental methods

To develop image-based FE models of the OFT, we imaged the OFT of an HH18 chick embryo *in vivo* using optical coherence tomography (OCT) and developed image analysis algorithms to extract the cardiac OFT wall geometry and motion. To provide proper boundary conditions to our OFT model, we measured blood pressures in the chick embryonic heart ventricle and aortic sac, which are the heart sections that are immediately upstream and downstream of the OFT, respectively (see Figure 5.1A). Finally, to validate the blood flow velocity field predicted by our FE models, we measured blood flow at representative locations in the OFT using Doppler ultrasound.

### 5.2.1 4D imaging and reconstruction of the OFT

The OFT of chick embryos at HH18 was imaged *in vivo* using OCT. Current state-of-the-art OCT and 4D imaging techniques allow studying heart dynamics in 4D.[70, 73, 97, 164] OCT is a high resolution (2-20 μm) non-invasive (and non-contact) tomographic

imaging technique that can image up to a 2-mm depth in biological tissues.[62] Therefore, OCT is well suited for imaging the chick embryonic heart during early development (<2 mm in size) .[62, 67] For this study, we imaged the chick OFT *in ovo* using a spectral OCT[60] with axial spatial resolution of 10 μm, lateral spatial resolution of 20 μm, and image acquisition rate of 140 frames per second.

Prior to imaging, fertilized White Leghorn eggs were incubated to HH18 (~3 days of incubation).[48] A small window was opened on the egg shell and the overlying membrane was removed to expose the embryonic heart and its OFT. During imaging, the temperature of the chick embryo was maintained at 37.5 ± 0.5°C within a warming chamber, since temperature affects cardiac function. 2D image sequences of the OFT were obtained over a 2-second time interval, which spanned 4-5 cardiac cycles. These 2D image sequences were acquired at contiguous OFT cross-sections 10-μm apart, spanning the entire OFT. Since image acquisition gating was not used (i.e., the beginning of image sequence acquisition was not triggered at the same phase during each cardiac cycle) the image sequences were out of phase. To synchronize these imaging sequences and reconstruct 4D images of the OFT (the OFT 3D structure over time), we employed our developed image-based, post-acquisition synchronization procedure,[164] which uses similarity of adjacent image sequences and a phase correction that accounts for peristaltic-like wall motion. Reconstructed 4D images were used to extract the geometry of the OFT lumen over time and generate FE models of the chick heart OFT.

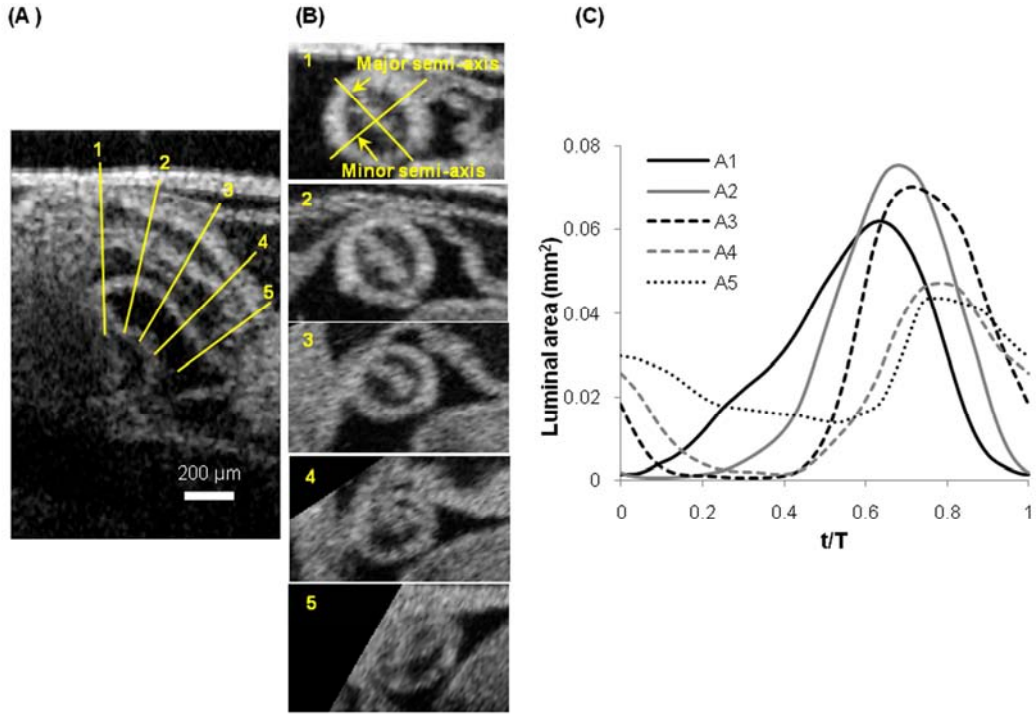


**Figure 5.2** OFT wall motion. (A) Transverse sectional OCT image of the OFT; the 5 lines show the locations where cross-sections were extracted from 4D OCT images. (B) The 5 extracted cross-sections at their most constricted state; the lines in image 1 show the major and minor semi-axes of the lumen, assuming an elliptical luminal area. (C) Calculated luminal areas (A1, A2, A3, A4, A5) for each of the 5 locations over the cardiac cycle. t, time; T, period of the cardiac cycle.

We developed a set of image-analysis algorithms in order to extract the dynamic geometry of the OFT from the 4D OCT image data sets. We first chose a 3D image dataset corresponding to a phase in the cardiac cycle in which the OFT was most constricted, and using our algorithms we segmented (delineated) the OFT lumen-wall surface and myocardium from the 3D image, and calculated the OFT centerline. To characterize the wall dynamics of the OFT, we used the 4D image reconstructions to extract image sequences from 5 equally spaced cross-sections perpendicular to the OFT centerline: (1) OFT inlet, (2) middle upstream, (3) middle, (4) middle downstream, and

(5) outlet (see Figure 5.2A and Figure 5.2B). Segmentations of the OFT lumen-wall interface over time in these 5 cross-sections were used to build the geometry of our FE models of the OFT lumen (see Sections 5.3.1.1 and 5.3.2.1).

### 5.2.2 Measuring intracardiac pressures

We used a servo-null micro-pressure system (Model 5A-LN, Instrumentation for Physiology and Medicine, San Diego, CA) to measure blood pressures in the ventricle, and in the aortic sac of normal chick embryos at HH18 (see Figure 5.1A). Pressure data were collected following standard procedures:[165] while maintaining the chick embryos at 37.5 ± 0.5°C, real-time pressure traces were sampled at 100 Hz in the ventricle, and in the aortic sac of normal chick embryos (n = 26 and n = 9, respectively) over at least 10 cardiac cycles. Representative intracardiac pressures that had peak values closest to measured averages were used as boundary conditions in our FE models of the OFT.

### 5.2.3 Measuring blood flow in the OFT

We used a Vevo 2100 ultrasound imaging system with an MS-550S transducer (VisualSonics, Inc., Toronto, Canada) to measure blood flow in the OFT of normal chick embryos at HH18 (n=10). In pulsed wave Doppler mode, we measured blood flow centerline velocities over time near the inlet, middle, and outlet of the OFT of chick embryonic hearts (Figure 5.1A, dots along the OFT centerline). During data acquisition, embryos were submerged in pre-warmed chick Ringer's solution, and temperature was maintained with a heat lamp and temperature controller. The Doppler angle, the angle between the sound wave and the blood flow direction, was adjusted within 30° by tilting

the angle of the transducer with respect to the embryo. The acquired blood flow velocities were corrected for the Doppler angle, approximately determined from a static image of the embryonic heart.

At each selected location of the OFT (inlet, middle, outlet; I, M, O in Figure 5.1A), centerline velocities were obtained by tracing the Doppler ultrasound images. After normalizing in time and aligning these velocity traces at their peak within a cardiac cycle, we calculated the average velocity trace and its standard deviation over three cardiac cycles and among 10 chick embryos. The average velocity traces that represented the blood flow at the OFT inlet, middle and outlet were compared with the centerline velocities predicted by our FE models of the OFT at corresponding locations.

## 5.3 Finite element models

We developed two FE models of the chick embryonic heart OFT at HH18: a 2D axisymmetric model and a 3D model. Both models included the dynamics of blood flow over the cardiac cycle, and featured OFT wall motions that were extracted from 4D OCT images of the OFT (Section 5.2.1). Because OCT images of the OFT, and pressure measurements in the ventricle and the aortic sac, could not be acquired simultaneously nor in the same embryos (due to technical difficulties), the 2D models were used as an initial approximation of the blood flow in the embryonic OFT, to aid in the determination of proper time phases among the measured OFT wall motion, OFT inlet pressure (ventricular pressure) and OFT outlet pressure (aortic sac pressure). A 3D model of the chick heart OFT was then developed to more accurately quantify blood flow dynamics in the OFT of living embryos. 2D and 3D models were implemented using the FE software

Adina (ADINA R & D, Inc. Watertown, MA).[152]

### 5.3.1 2D dynamic models of the OFT

#### 5.3.1.1 Model geometry

In our 2D FE models, the OFT was modeled as a straight tube with circular cross-sections (see Figure 5.3). The geometrical parameters of the OFT model were obtained from OCT images. Specifically, to extract geometrical parameters, we used the 5 representative cross-sections perpendicular to the OFT centerline (see Figures 5.2A and 5.2B). After segmenting the lumen-wall interface of each cross-section over time, we calculated the lumen area A'. Since it was difficult to distinguish blood and the thin layer of the endocardium in OCT images due to their similar reflective index, our segmentation included the endocardium, and thus A' overestimated the OFT luminal area. To correct for the thickness of the endocardium, we approximated the area of the endocardium as the minimal A' assuming that the OFT lumen is closed (zero luminal area) when the OFT is fully constricted; thus we subtracted the minimal area from A' (see Figure 5.2C). Since the OFT at location 5 does not close completely, we estimated for this position the area of endocardium from locations 1 to 4. Further, to avoid a transient zero luminal area, which would cause numerical difficulties in FE analysis, we artificially added a very small area (0.0003 $mm^2$). From the corrected luminal area, $A$, we calculated a model radius $R$ as follows,

$$R(t,\lambda_i) = [A(t,\lambda_i)/\pi]^{1/2} \; (\; i = 1,2,3,4,5) \tag{5.2}$$

where $t = [0,T]$ is time, and $T$ is the cardiac period; the subindex $i$ represents each of the 5

representative cross-section, with $\lambda_i$ indicating the axial location of each cross-section. To remove discontinuities in wall motion, we smoothed the radii over time and space with a moving average filter (see Figure 5.4).

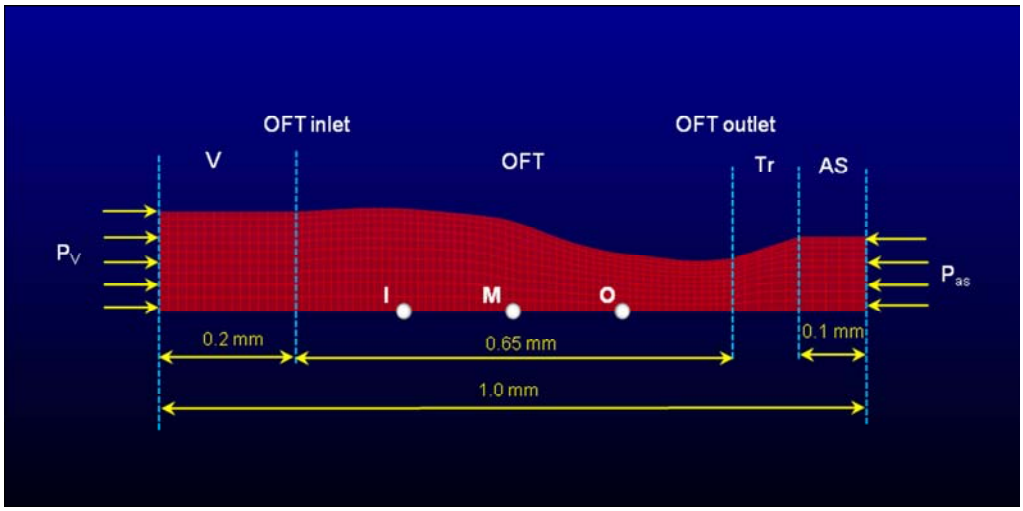


**Figure 5.3** 2D axisymmetric model of the chick embryonic heart OFT. The three white dots at the OFT centerline indicate the locations where centerline velocities were extracted to compare with those measured with Doppler ultrasound. $P_{as}$, aortic sac pressure; $P_v$, ventricular pressure; AS, aortic sac; Tr, transition region; OFT, outflow tract; V, ventricle.

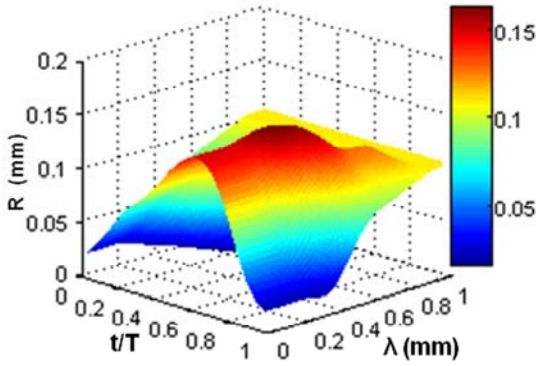


**Figure 5.4** OFT lumen radius (R) over the cardiac cycle and along the OFT used in our 2D models. R was calculated and interpolated from the luminal areas obtained from the 5 cross-sections shown in Figure 5.2. λ, is the axial distance along the OFT centerline from the OFT inlet to the outlet.

To correctly impose measured pressure boundary conditions, we extended the axial

dimensions of our 2D FE models of the OFT to a total length of 1.0 mm (see Figure 5.3). The pressure boundary conditions were measured outside the range of the imaged OFT with an axial distance of ~1.0 mm, while the axial length of the imaged OFT was ~0.6 mm (see Figure 5.1A). To account for this discrepancy, we extended the model 0.2 mm before the OFT inlet and ~0.2 mm after the OFT outlet. We assumed that the extended 'inlet region', which was the distal region of the ventricle, had the same motion as the OFT inlet ($\lambda_1$). Because the aortic sac does not actively contract during the cardiac cycle, in the extended 'outlet region' we modeled a rigid aortic sac and a transition region from the aortic sac to the moving OFT (Figure 5.3). We approximated the radius of the aortic sac as the average of the mean and largest radius of the OFT outlet over the cardiac cycle, as observed from our CCD images of the chick heart.

#### 5.3.1.2 Model boundary and initial conditions

We chose representative pressure traces measured at the ventricle and aortic sac as boundary conditions of the 2D FE models of the OFT (see Figure 5.5). The measured pressures were imposed on the extended inlet and outlet of the 2D FE models as normal tractions. The wall motion of the OFT (moving boundary) was imposed as a displacement (D) in the radial direction of the model, with respect to the initial configuration,

$$D(t,\lambda) = R(t,\lambda) - R(0,\lambda) \ . \tag{5.3}$$

A non-slip condition was applied at the moving boundary representing the lumen-wall interface. An arbitrary Lagrangian-Eulerian formulation was used to account for the effects of wall motion on blood flow dynamics in the OFT models.

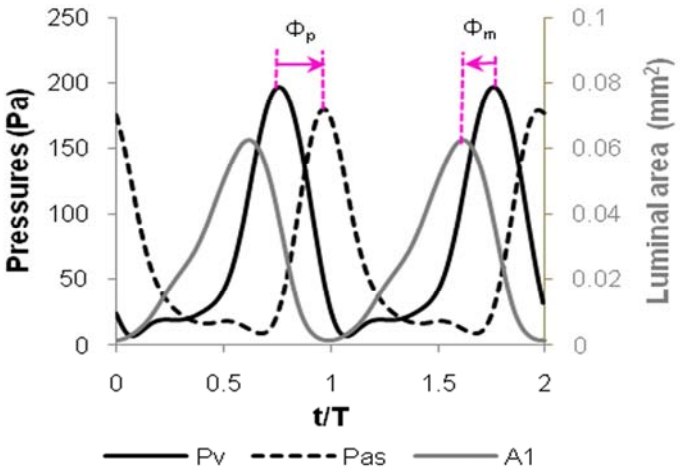


**Figure 5.5** Pressure and wall motion phase lags. The figure shows representative pressures measured at the ventricle and aortic sac of stage HH18 chick embryos, as well as the luminal area at the OFT inlet (A1 from Figure 5.2C). It also shows hypothetical phase relationships among the pressures and OFT wall motion. $\Phi_p$, is the phase lag of the aortic sac pressure ($P_{as}$) with respect to the ventricular pressure ($P_V$); $\Phi_m$, is the phase lag of the ventricular pressure ($P_v$) with respect to the wall motion of the OFT inlet (A1).

In our 2D FE models of the OFT, resulting blood flow velocities depended on the blood pressures imposed at the OFT inlet and outlet, and the prescribed OFT wall motion. Due to measurement procedures we were uncertain of the phase lag between imposed inlet and outlet pressure, as well as the phase lag between the ventricular (inlet) pressure and the wall motion of the OFT. We used the 2D models to test the effects of applying different phase lags among pressure boundary conditions and wall displacements. To quantify phase lags for comparison, we defined $\Phi_p$ as the phase lag between the peak aortic sac pressure and the peak ventricular pressure, and defined $\Phi_m$ as the phase lag between the peak ventricular pressure and the peak inlet cross-sectional area of the OFT (see Figure 5.5). We assumed $\Phi_p$ = 0 to 0.2T, and $\Phi_m$ = 0 to 0.2T, which we will discuss in Section 5.5.2. Figure 5.6 shows different combinations of the two phase relationships. We assumed that the OFT was initially (reference configuration) at its

most constricted state with zero blood flow velocity.

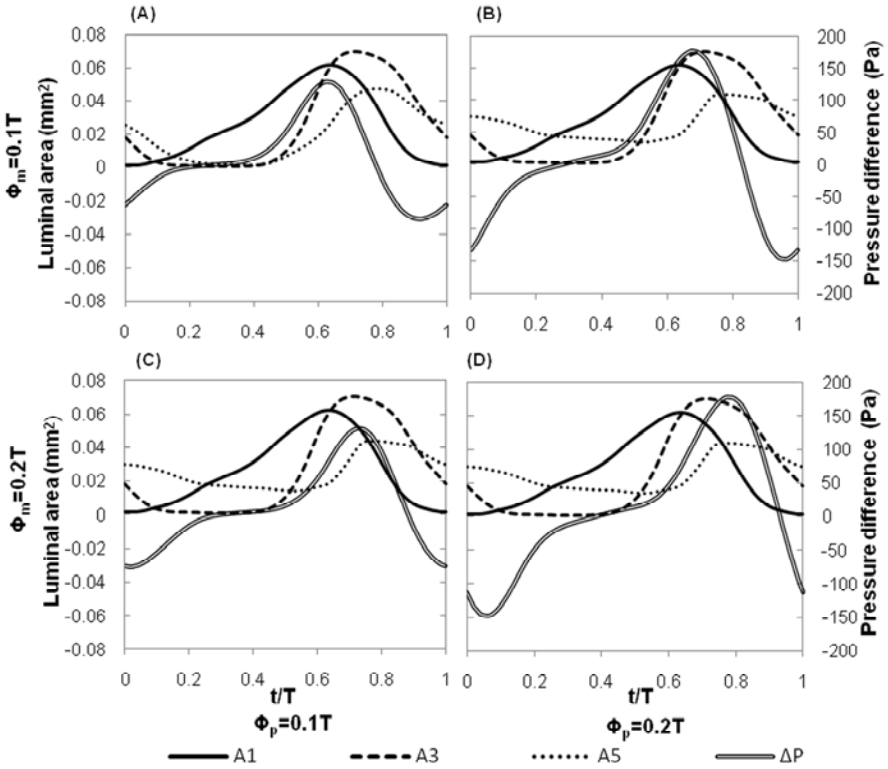


**Figure 5.6** Temporal relationships among the representative luminal areas and the pressure drop along the OFT for different phase lag combinations ($\Phi_p$ and $\Phi_m$). A1, A3, and A5, are the luminal areas at the 3 cross-sections of the OFT (see Figure 5.2B); ΔP, is the pressure difference between the ventricle and aortic sac ($\Delta P = P_v - P_{as}$).

### 5.3.1.3 Material properties

The blood of chick embryos was modeled as a continuous, incompressible Newtonian fluid with a density $\rho = 1060\ kg/m^3$and a viscosity $\mu = 3 \times 10^{-3}\ kg/(m\ s)$[144]. The non-Newtonian behavior of blood increases with the blood hematocrit, and at 0% hematocrit blood presents a Newtonian behavior. The assumption of Newtonian fluid is justified for embryonic chick blood, because it has low hematocrit (20 % for embryonic blood vs. 45% for mature whole blood). [166, 167] The embryonic blood flow was modeled as a laminar (Re<< 2000), transient, and incompressible flow.

#### 5.3.1.4 Finite element discretization

The 2D blood flow model of the OFT was discretized with axisymmetric 2D 4-node quadratic flow-condition-based-interpolation (FCBI) elements.[152, 153] Mesh-independent solutions were obtained with a mesh consisting of 946 nodes and 850 elements. Time independent dynamic solutions were achieved with 200 time steps per cardiac cycle (T = 400 msec, $\Delta t$ = 2 msec). To fully damp initial transient effects, we simulated two cardiac cycles in the 2D FE models and used the second cycle as our results.

Blood flow velocities calculated with our 2D OFT models were analyzed and compared to measured blood flow velocity data. We used these comparisons (see Section 4.4) to approximate the phase lags $\Phi_p$ and $\Phi_m$ to impose as boundary conditions in more accurate 3D models of the developing heart OFT.

### 5.3.2 3D dynamic model of the OFT

To more accurately quantify the blood flow dynamics in the cardiac OFT of chick embryos at HH18 and the distribution of WSS on the OFT walls, we developed a 3D FE model of the OFT. This model included the 3D curvature and non-circular cross-sections of the OFT lumen, as well as the heart wall motion and pulsatile pressures.

#### 5.3.2.1 Model geometry

In our 3D models of the OFT, the OFT lumen (blood flow domain) was modeled as a 3D curved tube with elliptical cross-sections, with geometrical parameters extracted from 4D OCT images (Section 5.2.1). Specifically, to construct the 3D models of the OFT, we used the OFT centerline and image sequences from the 5 representative locations (see

Figure 5.2). Elliptical cross-sections were chosen to represent the geometry of the lumen-wall interface, as they approximately represent the shape of the lumen as observed with OCT (see Figures 5.1C, 5.1D and 5.2B). To follow the motion of the OFT lumen-wall surface over the cardiac cycle, the length of the ellipse major semi-axis, $a$, and minor semi-axis, $b$, were allowed to change with time.

To determine the ellipse parameters from imaging data, we used the segmented OFT lumen-wall interface over time from the 5 representative cross-section image sequences (see also Section 5.3.1.1). Using the segmented curves, we calculated and corrected the area of the lumen, $A(t, \lambda_i)$, over time as explained in Section 5.3.1.1.The orientation of the ellipse major and minor semi-axes in 3D were calculated (at a phase when the OFT was most constricted), and initial values of the major and minor semi-axes, $a'(t, \lambda_i)$ and $b'(t, \lambda_i)$, over time, were determined by fitting the segmented lumen curve to an ellipse. However, $a'(t, \lambda_i)$ and $b'(t, \lambda_i)$ did not preserve the lumen area. To enforce the lumen area, we first calculated e(t, $\lambda_i$), the ratio between $a'$ and $b'$ that describes the shape of the ellipse at each $\lambda_i$ as it changes from a fully open OFT configuration (e ≅ 1, close to a circle), to a contracted OFT configuration (e ≅ 2.5) over the cardiac cycle (see Figure 5.7A). We then calculated the ellipse model parameters as follows,

$$a(t, \lambda_i) = \sqrt{A(t, \lambda_i)e(t, \lambda_i)/\pi} \quad (i = 1,2,3,4,5), \tag{5.4}$$

$$b(t, \lambda_i) = a(t, \lambda_i)/e(\mathrm{t}, \lambda_\mathrm{i}) \quad (i = 1,2,3,4,5), \tag{5.5}$$

where $a(t, \lambda_i)$ and $b(t, \lambda_i)$ are the major semi-axis and minor semi-axis at $\lambda_i$ used in our model. $a(t, \lambda)$ and $b(t, \lambda)$ were then smoothed in time and space to remove

discontinuities (see Figures 5.7B and 5.7C).

The 3D geometrical model of the OFT was constructed starting from the OFT centerline. We first divided the centerline into 61 equally spaced points (the 5 representative cross-sections were uniformly located at center points i = 1, 16, 31, 46, 61). Then, at each of these points we generated cross-sections that were perpendicular to the centerline. To describe the elliptical shape of a cross-section, at a point ($X_c$, $Y_c$, $Z_c$) in the centerline, we built a local Cartesian coordinate system based on the direction of the major semi-axis (denoted as a unit vector **L**), the direction of the minor semi-axis (denoted as a unit vector **S**), and the tangential direction of the centerline (denoted as a unit vector **N**) at this point. In the local coordinate system (*x*, *y*), the elliptical cross-section was described using a general formulation of a 2D elliptical curve:

$$x(t) = \mathrm{a(t)}\cos(\theta)$$

$$y(t) = b(t)\,sin(\theta) \tag{5.6}$$

where $\theta = [0, 2\pi]$ indicates a closed curve. To implement the 3D curvature of the OFT in a global Cartesian coordinate system, we calculated the coordinates of the elliptical cross-sections in a global coordinate system (*X*, *Y*, *Z*),

$$[X, Y, Z]^T = \mathbf{R} \cdot [x + X_c, y + Y_c, Z_c]^{\mathrm{T}} \tag{5.7}$$

where $\mathbf{R} = [\mathbf{L}, \mathbf{S}, \mathbf{N}]^T$ is the transformation matrix between the local and global coordinate systems at any given centerline point ($X_c$, $Y_c$, $Z_c$). The 3D OFT lumen surface at any given time was then generated from the 61 elliptical contours which were lofted and interpolated between adjacent elliptical contours in 3D space using Rhinoceros 4.0 (Robert

McNeel & Associates, Seattle, WA).

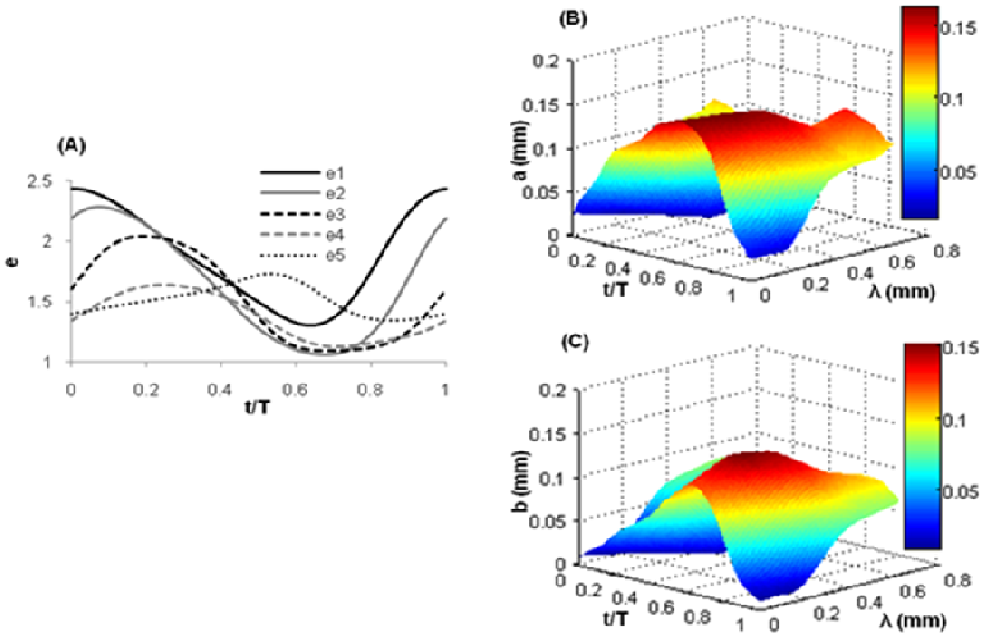


**Figure 5.7** Geometric parameters used in 3D FE model of the OFT. (A) shape index (e = a/b) of the elliptical cross-section at the 5 selected cross-sections (see Figure 5.2) over a cardiac cycle. (B) Major semi-axis (a), and (C) minor semi -axis (b), of the OFT elliptical lumen cross-sections over a cardiac cycle and along the OFT. λ, is the axial distance along the OFT centerline from the OFT inlet to the outlet.

### 5.3.2.2 Boundary and initial conditions

We used pressures and wall motion as boundary conditions in our 3D model of the OFT. The wall motion of the OFT was modeled by imposing displacements on the lumen-wall surface. We assumed that the displacement in the axial direction was negligible. For each elliptical cross-section, the displacement was calculated in the local coordinate system using:

$$D_x(t,\lambda) = x(t,\lambda) - x(0,\lambda)$$

$$D_y(t,\lambda) = y(t,\lambda) - y(0,\lambda)$$

$$D_z(t, \lambda) = 0 \tag{5.8}$$

Displacements were prescribed on the lumen surface in the local coordinate system (i.e., skew system in Adina [152]). To account for the motion of the wall and moving mesh within the blood fluid domain, an arbitrary Lagrangian-Eulerian formulation was employed.

The phase relationships between the pressures and wall motion ($\Phi_p$ and $\Phi_m$) used in the 3D FE model were determined from the 2D models and physical arguments (see Section 5.4.4). To account for the discrepancy in axial distance of pressure measurement and imaged OFT axial length (see Section 5.3.1.1 and Figure 5.3), we extracted pressures at both OFT inlet and outlet from the 2D model with the same $\Phi_p$ and $\Phi_m$; and imposed the pressures uniformly at the inlet and outlet of the 3D FE model as normal tractions. Similar to our 2D models, we assumed that initially the OFT was at its most constricted state with no blood flow.

#### 5.3.2.3 Material properties

In our 3D FE model, we used the same material properties for the embryonic blood as in the 2D models and assumed incompressible, Newtonian, laminar flow (see Section 5.3.1.3).

#### 5.3.2.4 Finite element discretization

The flow domain of the 3D FE model was discretized with 3D 4-node tetrahedral FCBI elements. Mesh-independent solutions were obtained using 66400 nodes and 353000 elements. To calculate WSS, we defined a very thin boundary layer (a built-in function in

Adina[152]) at the OFT wall in the fluid model. The thickness of the boundary layer was specified as 0.0004 mm, which was less than 1/5 of the element size in the fluid model. We simulated two cardiac cycles and used 200 time steps per cardiac cycle (T = 400 msec; $\Delta t$ = 2 msec). For further analysis, we extracted results at 3 cross-sections: near the OFT inlet about 0.16 mm away from the inlet, at the middle, and near the outlet about 0.16 mm away from the outlet (see Figure 5.11B).

## 5.4 Results

To quantify blood flow dynamics and WSS in the chick embryonic heart OFT, we generated 2D and 3D FE models of the OFT. Boundary conditions were obtained from pressure measurement and 4D OCT imaging of the OFT *in vivo*. Our 2D models characterized the effects of different phase relationships among the pressures and wall motion. We then used our 3D FE model to more accurately quantify the blood flow field and distribution of WSS in the OFT.

### 5.4.1 Wall motion of the OFT

Figure 5.2C shows the temporal variations of the luminal areas of the 5 representative cross-sections of the OFT over the cardiac cycle; the 5 cross-sections were extracted about evenly spaced along the OFT from the 4D OCT images (see Figures 5.2A and 5.2B). Using the OFT luminal area as an indicator of the OFT wall motion, we found that the motion of the OFT wall changes from the inlet to the outlet. Towards the inlet (A1), the OFT wall motion showed a gradual expansion and steep contraction; in contrast, toward the outlet (A5), the OFT wall motion showed a relatively steep expansion and gradual contraction. The middle region of the OFT had the greatest wall motion and the

OFT outlet had the smallest wall motion. The traces of the luminal areas at the 5 locations suggested that the entire OFT wall opened and closed peristaltically, with a phase lag with respect to the OFT inlet.

From each of the 5 cross-sections that we extracted along the OFT, we found the OFT lumen underwent eccentric deformation, deforming from an almost circular shape when the OFT was fully expanded, to a slit-like shape when the OFT was fully constricted (e.g., Figures 5.1C and 5.1D). The lumen shape can therefore be approximately represented by an ellipse. Due to the presence of the cardiac cushions, the OFT lumen was fully closed (slit-like shape in Figure 5.2B) at locations 1 to 4 during OFT contraction, but not at location 5 (the OFT outlet). The orientation of the major axis was also observed to change counter-clockwise from the OFT inlet to the outlet (see Figure 5.2B), indicating helical distribution of the cardiac cushions along the OFT.

### 5.4.2 Blood pressure measurements

Figure 5.5 shows representative ventricular and aortic sac pressures used in our 2D models. We found that the ventricular pressure and aortic sac pressure were very similar in shape and magnitude. Both pressure waveforms were pulsatile and showed a peak.

### 5.4.3 Centerline velocity profiles

Figure 5.8 shows the blood flow average velocity traces and their variation ranges measured with Doppler ultrasound near the OFT inlet, middle and outlet, from 10 chick embryos (Section 5.2.3).

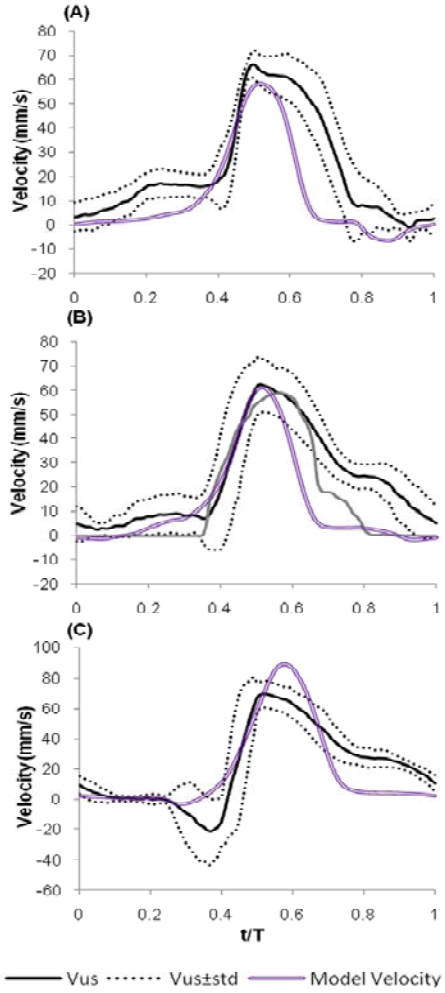


**Figure 5.8** Comparison of velocities measured using Doppler ultrasound and calculated using our 3D FE model of the OFT. The comparisons are shown at 3 locations in the OFT lumen (see Figures 5.1A and 5.11B): (A) near the OFT inlet (location I), (B) middle (location M), and (C) near the outlet of the OFT (location O). Measured centerline velocities were represented as the average velocity, $V_{US}$ (solid black line) ± standard deviations (dotted lines above and below the solid line). The grey line in (B) was obtained from the literature,[77] and measured the centerline blood velocity at about the middle region of a representative HH18 chick OFT using Doppler ultrasound.

We termed blood flow as *positive* when blood flowed from the inlet toward the outlet (also referred to as *forward flow*) and *negative* when blood flowed back towards the inlet (*backflow*). At the OFT inlet (Figure 5.8A), the velocity profile exhibited a slow increase (i.e., *a shoulder*) followed by a fast increase in velocity to a peak, then a gradual decrease in velocity. At the OFT middle (Figure 5.8B), the velocity profile first exhibited a sharp increase in velocity and then a gradual decrease after the velocity peak. At the OFT outlet (Figure 5.8C), a backflow was observed *before* the velocity peak and a shoulder followed the peak velocity. Deviations from these general trends were observed in our Doppler

ultrasound flow measurements due to the biological variations of chick embryos and operator's uncertainties (i.e., reproducible selection of measurement locations and determination of Doppler angles).

Figure 5.9 gives the average peak forward velocity and peak backward velocity measured near the OFT inlet, middle and outlet for 10 chick embryos. Although the peak velocities were not significantly different, the average magnitude of the peak forward flow tended to be higher near the OFT outlet (70±10 mm/s) than near the inlet (60±10 mm/s), this is consistent with the tapering of the OFT lumen towards the outlet. The magnitude of the peak backflow exhibited the same trend.

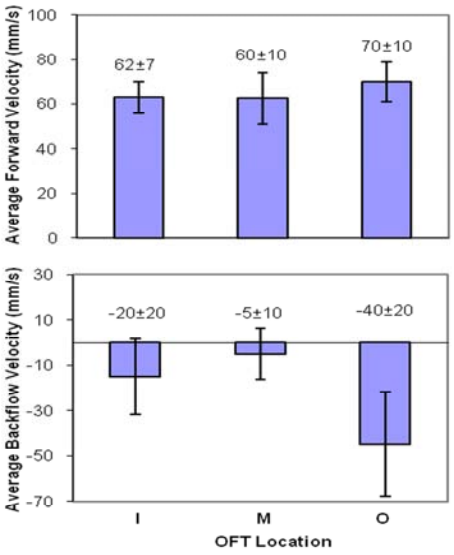


**Figure 5.9** Averaged peak forward velocities (top) and peak backflow velocities (bottom) measured using Doppler ultrasound. Velocities were measured at about the 3 locations shown in Figure 1A: near the OFT inlet (I), middle (M) and outlet (O) of HH18 chick embryos (n = 10). Data are presented as mean and standard deviations.

### 5.4.4 2D FE models of the OFT

Our 2D FE models were generated to study blood flow velocities under different combinations of phase relationships within the range of 0 to 0.2T between the representative ventricular pressure and aortic sac pressure ($\Phi_p$), and between the ventricular pressure and wall motion of the OFT inlet ( $\Phi_m$), see also Figure 5.5.

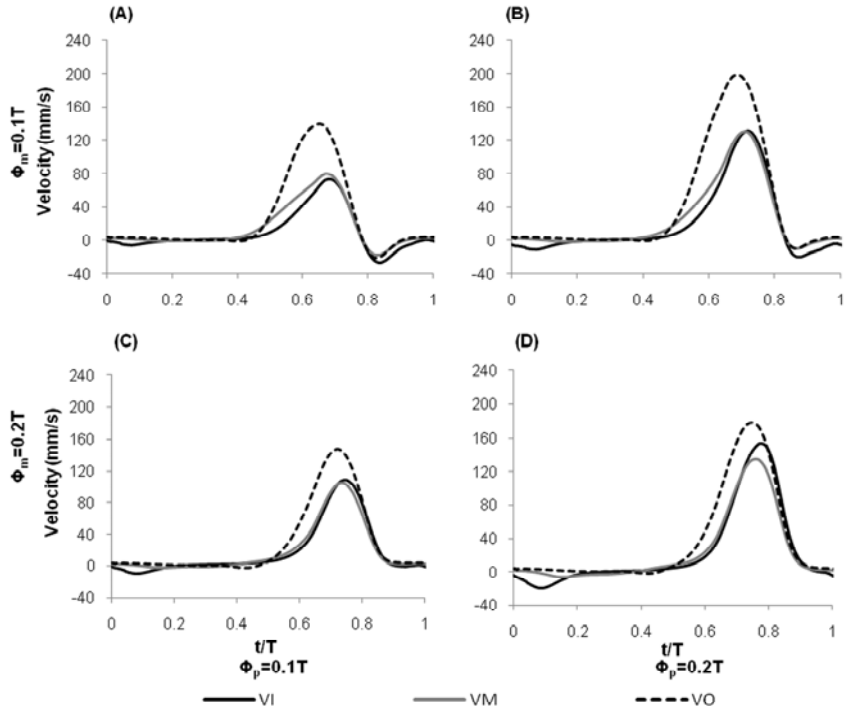


**Figure 5.10** Centerline velocity profiles calculated using 2D FE models under different phase relationships between pressures and OFT wall motion. VI, VM, and VO, are centerline velocity profiles extracted at the centerline near the OFT inlet (I), middle (M) and outlet (O), respectively (see also Figure. 5.3).

Figure 5.10 shows examples of the velocities predicted from our 2D models for different phase relationships within the ranges: $\Phi_p$= 0.1 to 0.2T and $\Phi_m$= 0.1 to 0.2T (see Figure 5.6). For all combinations of $\Phi_p$ = 0 (data not shown), the magnitudes of the predicted velocities were lower than those of the velocities that we measured using Doppler ultrasound. For all combinations of $\Phi_m$ = 0 (data not shown), the 2D FE models predicted a dramatic backflow that was not observed in the velocity profile measurements (Figure 5.8). For the particular cases depicted here, when $\Phi_m$ is constant, as $\Phi_p$ increases $\Delta P$ increases, and thus centerline velocities increase. When $\Phi_p$ is constant, the peak $\Delta P$ moves towards larger t/T as $\Phi_m$ increases, and the differences in the peak flow among the inlet, middle and outlet reduce because the differences in luminal areas at the peak $\Delta P$

reduce (see Figure 5.6).

### 5.4.5 3D dynamic model of the OFT

We chose the cases (1) $\Phi_p = 0.1T$ and $\Phi_m = 0.15T$, and (2) $\Phi_p = 0.1T$ and $\Phi_m = 0.2T$, and applied these phase lags in boundary conditions to more accurate but time consuming 3D models of the OFT. We found that the case of boundary conditions $\Phi_p = 0.1T$ and $\Phi_m = 0.2T$, yielded velocity profiles that better resemble those of ultrasound flow measurement.

Figure 5.8 shows a comparison of blood flow velocity profiles between our 3D FE model prediction ($\Phi_p = 0.1T$ and $\Phi_m = 0.2T$) and Doppler ultrasound flow measurement. The centerline velocities predicted from our 3D FE model captured some characteristics of the velocity traces measured from Doppler ultrasound. Near the OFT inlet and middle region, the predicted peak forward and backward centerline velocities were within the ranges of our Doppler ultrasound measurements, but near the OFT outlet the predicted peak forward flow was higher than the measurements (see Figures 5.9 and 5.10).

As shown in Figure 5.11, the 3D FE model predicted a skewed distribution of velocity profile at the OFT inlet towards OFT inner curvature; the effects of the 3D curvature on velocity profiles diminished towards the OFT middle region. In-plane flow near the OFT wall was also observed, reflecting the effects of the wall motion and helical orientation of the elliptical cross-sections. No noticeable vortex was observed.

Figure 5.12 shows the heterogeneous distribution of WSS magnitude on the OFT wall at peak forward flow. When the OFT was expanding, a high level of WSS magnitude transiently located at the outlet; the maximal WSS (~11 Pa) occurred at the outlet of the

OFT where the peak blood velocity was highest (see Figure 5.8). A low level of WSS was found at the middle region of the OFT, which had a large lumen area. At each OFT cross-section, WSS were higher at the cushion side (the minor axis of the elliptical lumen) than the region without the cushion (the major axis). Near the OFT inlet, WSS was higher towards the inner curvature than the outer curvature, a result of the skewed velocity towards the inner curvature.

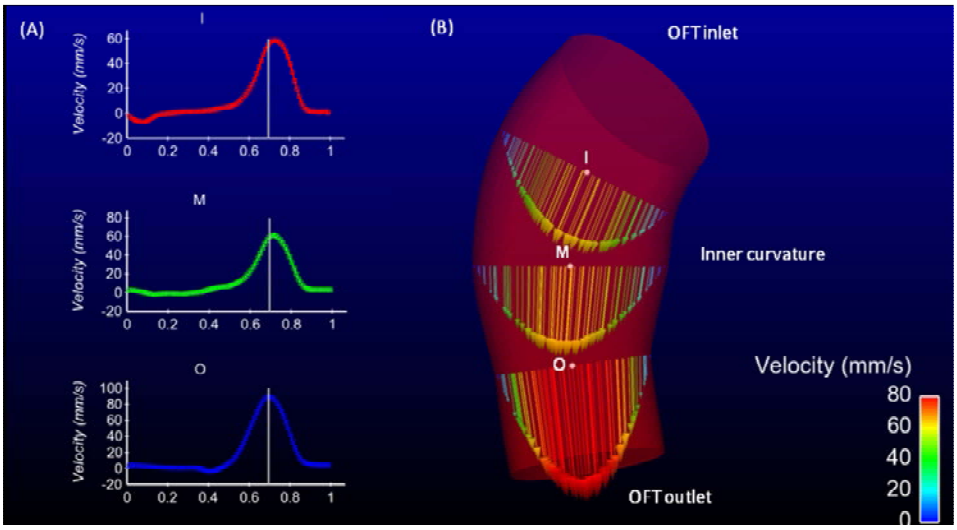


**Figure 5.11** Blood flow patterns calculated using our 3D model of the cardiac OFT of HH18 chick embryos. (A) Centerline velocities over a normalized cardiac cycle, and (B) velocity profile along the major axis of the elliptical lumen cross-sections. Centerline velocities and velocities profiles are shown at the 3 locations shown in figure 1A: near the OFT inlet (I), middle (M), and the outlet (O). The vertical lines in (A) indicate the cardiac phase of the velocities shown in (B). The three dots in (B) indicate the locations from where the centerline velocities in (A) were extracted.

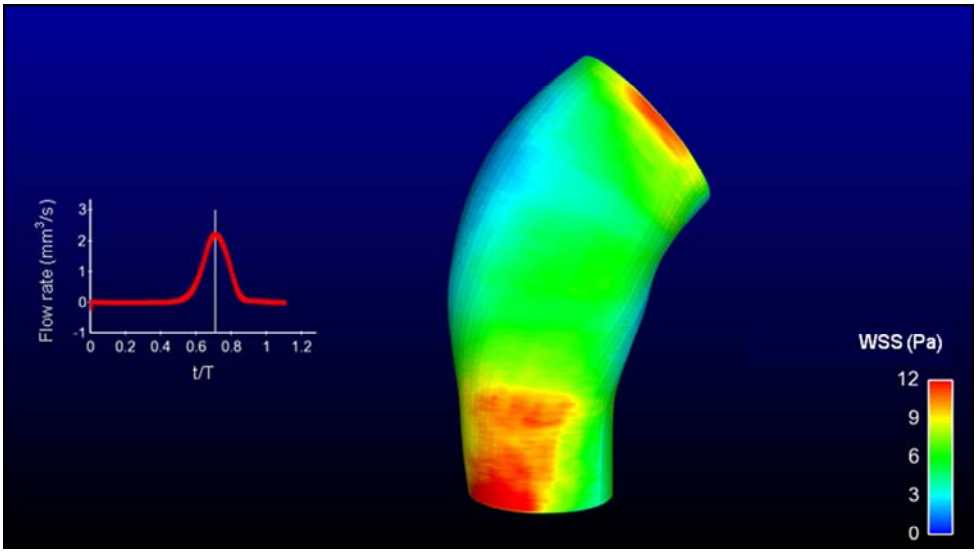


**Figure 5.12** Distribution of wall shear stresses on the OFT wall at peak forward flow. The flow rate depicted was calculated from the flow at the middle cross-section of the OFT (Location M in Figure 5.1A).

## 5.5 Discussion

In this paper, we present image-based 2D and 3D dynamic FE models of the heart OFT of normal chick embryos at HH18; these models were generated based on our 4D OCT images of the OFT and *in vivo* pressure measurements. Our 2D FE models of the OFT were used to characterize the effects of phase relationships in boundary conditions (pressures and wall motion). Our 3D dynamic FE model took into account the 3D curvature of the OFT, cardiac cushions, dynamic wall motion, and pulsatile pressures imposed at the OFT inlet and outlet. Within the scope of the model assumptions, the 3D FE dynamic model quantified the distinct blood flow field and tempo-spatial distribution of WSS in the normal chick OFT at HH18. Thus we expect that our 3D models of the cardiac OFT will contribute to understanding the role of hemodynamics in heart development.

### 5.5.1 Assumptions and limitations of the 3D FE Model

In our 3D FE model of the OFT, we simplified the OFT geometry. To model the effects of cardiac cushions, we assumed that the cross-section of the OFT lumen was elliptical. The shape of the OFT luminal cross-section does not strictly resemble an ellipse because the cardiac cushions are not evenly distributed around the OFT cross-section; and the effects of the cardiac cushions become more noticeable when the OFT contracts (see Figures 5.1C and 5.2B). To minimize the effects of the assumed elliptical shape of OFT lumen on blood flow simulations, while we modeled the segmented lumen using ellipses, the areas of the ellipses were kept the same as those of the segmented lumens. In addition, the shape of the ellipses (see Figure 5.7A) was allowed to vary during the cardiac cycle and along the OFT to better model the dynamic deformation of the OFT lumen. Therefore, we expected that the elliptical cross-section might locally and transiently affect the distribution of the blood flow within the cross-section during OFT contraction, but not the general pattern of blood flow.

We also simplified the wall motion of the OFT. To model the OFT wall motion, we obtained wall dynamics from the 4D OCT image data of the OFT. Full implementation of the wall motion demands a 4D segmentation algorithm for the 4D image data of the OFT, which is still under development. Therefore, we estimated the wall motion from 5 representative OFT locations and captured the heterogeneous wall motion along the OFT at those points. We expected that our 3D FE model qualitatively predicted the effects of the heterogeneous wall motion on the blood flow pattern and distribution of WSS in the OFT.

To prevent numerical difficulties in FE analysis, in our 3D FE models we simulated the closure of the OFT lumen using a very small area. This procedure might result in blood flow (though low in magnitude) driven by the pressure difference between the OFT inlet and outlet when the OFT was closed. Since the OFT wall contracted sequentially along the OFT from 0 to 0.5T, calculated blood flow and thus WSS during this time period is not accurate.

In studying the effects of the 3D curvature of the OFT on blood flow distribution, we assumed that the OFT was a curved tube and that the OFT centerline was static. However, the curvature of the centerline changes during the cardiac cycle. To evaluate the changes in the curvature of the OFT centerline during the cardiac cycle, we extracted and compared two OFT centerlines: one centerline when the OFT was fully contracted and one, when fully expanded. We found that the maximal curvature of the OFT centerline changes slightly (<15%). Therefore, we expected that the changes in 3D curvature only modestly affected the skewed distribution of the velocity profile, and thus heterogeneous distribution of WSS during the cardiac cycle.

In our FE models, we used blood pressures as both inlet and outlet boundary conditions, rather than commonly used blood flow as inlet boundary condition. This was based on the following two reasons: (1) detailed and accurate blood flow velocity data are not available due to challenges of measuring the blood flow in the tiny beating embryonic heart (dimension $\cong$1 mm and heart rate at 2 to 2.5 Hz) and a lack of flow measurement techniques with sufficient spatial and/or temporal resolution; (2) the assumption of Poiseulle- or Womersley-type blood flow, which is a common and good inflow condition

for simulating vessels, may not be valid for the inflow to the OFT ejecting from the primitive ventricle. At this time, we consider that our pressure data are more accurate. Our underlying assumption of using blood pressure as boundary conditions is that the blood pressures reflect the effects of both upstream ventricle and downstream aortic sac on the OFT inlet and outlet, respectively. However, besides increasing the ventricular pressure, the contraction of the ventricle provides momentum driving the blood flow to the OFT. The limitation might affect the magnitude of the velocities at the shoulder region during ventricular contraction transiently. Considering that the predicted velocities captured the flow features observed from measurement, we expected our 3D models were qualitatively valid.

### 5.5.2 Phase relationships between blood pressure and wall motion of the OFT

For the chick OFT, which is essentially a curved tube, blood flow is regulated by two factors: (1) the pressure difference between the OFT inlet and outlet; and (2) the motion of the OFT wall. However, we were uncertain of the phase relationship between the ventricular pressure and aortic sac pressure ($\Phi_p$), and the phase relationship between the ventricular pressure and wall motion ($\Phi_m$) due to technical difficulties.

To determine a suitable range of values for $\Phi_p$ and $\Phi_m$, we used physical arguments. Since during the cardiac motion blood pressure waves travel from the ventricle to the aortic sac, the peak pressure at the aortic sac (outlet) has to occur later than the peak ventricular pressure (inlet). The magnitude of the pressure wave speed is on the same order of the propagating speed of contractile wave of the OFT wall. Inspections of Figure 5.2C shows that the phase lag between the maximal lumen areas in the OFT inlet and

outlet is about 0.2T; this finding is consistent with the reported impulse conductance speed of the OFT wall (~7 mm/s[51]) that travels along the OFT (~1 mm), inducing sequential contraction of the OFT wall from the OFT inlet to the OFT outlet. From these arguments, a reasonable range of $\Phi_p$ is 0 to 0.2T.

We assumed that the peak radius of the OFT inlet occurred earlier in cardiac phase than the peak ventricular pressure within the range of $\Phi_m$ = 0 to 0.2T. The assumption was reasonable based on the following arguments. First, the peak ventricular pressure has been reported to occur during ventricular contraction, in other words, the largest ventricular area occurs before the peak ventricular pressure.[165] Since the conducting speed of depolarizing impulse, which induces consecutive contraction of the embryonic heart tube, is fast in the ventricle (V = ~40 mm/s for HH18 chick embryos [51]), the electric impulse reaches the OFT inlet and induces the contraction of the OFT inlet almost synchronized to that of the ventricle. Therefore we assumed that the peak area of the OFT inlet occurs before the peak ventricular pressure, and with approximately the same phase lag as that of the ventricular walls. Second, we approximated the pressure-area (P-A) loops using the ventricular pressure and area of the OFT inlet with different phase relationships $\Phi_m$ varying between [0 $2\pi$], and compared them to the published P-A loop for HH18 chick embryos.[165] We were aware that the areas used by Keller and colleadges[165] were different from ours: the areas by Keller and colleadges[165] were measured by tracing the epicardial border of the ventricle from light microscopic images, while ours were measured by tracing the interior boundary of the myocardium of the OFT inlet cross-section in the OCT images. We expected, however, that their temporal relationship with the ventricular pressure were similar over the cardiac cycle. We found

that only P-A loops within $\Phi_m$ = 0.1 to 0.2T were comparable to the reported P-A loops. Therefore we considered that $\Phi_m$ = 0 to 0.2T was a reasonable range for the phase relationship between the ventricular pressure and wall motion at the OFT inlet.

Given the assumed ranges for $\Phi_p$ and $\Phi_m$, we generated 2D FE models of the OFT to study the effects of different combinations of phase relationships among the imposed pressures and wall motion on blood flow. We compared qualitatively the centerline velocities predicted from 2D models with those measured using Doppler ultrasound. We expected the general patterns of the velocity profiles to be similar between the 2D and 3D models since the luminal areas were the same in both models. We also expected that the magnitudes of centerline velocities predicted from 2D models would be higher than those from our more accurate 3D models. This is because under the same pressure conditions blood flow in our 3D models with an elliptical lumen, spiral distribution of cardiac cushions, and 3D curvature of the OFT tube would have larger momentum loss than that in the 2D models that were essentially consisted of a straight tube with circular cross-section. We found that the phase relationships of $\Phi_p$ = 0.1T and $\Phi_m$ = 0.2T best reproduced our flow measurement with Doppler ultrasound (see Fig 5.8), based on 2 selective criteria: (1) the shape of the centerline velocities and (2) relative ratio among peak velocities at three locations. We considered that the phase relationships ($\Phi_p$ = 0.1T and $\Phi_m$ = 0.2T) approximated well the coupled relationships between the pressures and wall motion of the OFT for normal chick embryos at HH18.

### 5.5.3 Comparison of blood flow velocity between model and experimental data

Blood flow dynamics regulate the morphogenesis of the OFT.[11] To quantify blood flow dynamics in HH18 chick heart OFT, we generated 3D FE models of the OFT based on in *vivo* pressure measurements and the dynamic geometry derived from the 4D OCT imaging data. Our FE models reproduced qualitatively some trends and values (within the same order of magnitude) of the centerline velocity profiles over the cardiac cycle measured from our Doppler ultrasound (see Figure 5.8) and Oosterbaan's Doppler ultrasound,[77] despite some discrepancies that we will discuss in the following paragraph. Our 3D FE model also qualitatively reproduced the skewed blood flow towards the inner curvature of the OFT, which was previously observed using PIV,[75] and using Doppler OCT.[76] In addition, our 3D dynamic FE model of the OFT revealed a heterogeneous flow field in the OFT, which is important for estimating WSS distribution on the OFT wall.

Discrepancies between Doppler ultrasound velocity measurements and modeled velocities (see Figure 5.8) could be due to experimental errors in flow measurements, simplifying geometrical assumptions of our FE models, and uncertainties in the phase relationships between pressures and wall motion. Experimental errors in flow measurements are mainly due to three factors. First, Doppler ultrasound acquires the component of blood flow velocity in the direction of the incident sound wave within a small sample volume (30µm x 30µm x 30µm) that is fixed in space (rather than moving with the heart); thus velocity data measured with Doppler ultrasound images reflect the

flow within the small volume that is manually selected from a static image. Second, to obtain the absolute velocity, measured velocity data needs to be corrected for the Doppler angle, which is difficult to determine *in vivo* since the OFT is a curved tube. The Doppler angle is also manually estimated from a static image. The Doppler angle was especially difficult to determine accurately towards the OFT outlet where the OFT changes its orientation sharply (refer to Figure 5.1A); this difficulty may partly explain discrepancies with the model results (see Figure 5.8C). Third, it is difficult to choose reproducible locations along the OFT *in vivo* (center lumen point near the OFT inlet, middle and the outlet). Variations in flow measurements, as well as the biological variations of the chick embryos, may artificially broaden the average blood flow traces (see Figure 5.8).

The simplifying geometrical assumptions and uncertainties in the boundary conditions of our 3D FE models also contributed to the discrepancies observed. Our models did not properly consider the contractile effects of the ventricular wall as well as the influence of the curvature of the upstream ventricle on the inflow. The simplified OFT wall motion may also affect blood flow. These limitations of the models may partly explain the discrepancy between the model prediction and flow measurement, especially, the shoulder region after the peak flow. Considering the errors in blood flow measurements, model limitations, and biological variations of chick embryonic hearts, we did not expect modeled and measured velocity traces to match exactly but to qualitatively capture the characteristics of the flow.

### 5.5.4 Blood flow in the OFT

The blood flow in the OFT is characterized by three dimensionless numbers: Reynolds (Re), Womersley (Wo), and Dean (De) numbers. Re is a measure of the ratio between inertia forces and viscous forces. Wo is a measure of the ratio between pulsatile flow frequency and viscous forces. De is a measure of curvature effects (centrifugal forces) with respect to flow viscous forces. Calculated from our 3D model of the OFT, the maximum De (max De=~3.0) of the blood flow in the OFT occurred near the OFT inlet where the OFT centerline had the largest curvature. There the blood flow profile slightly skewed toward the inner curvature, which is consistent with *in vivo* flow measurements.[75, 168] The estimated Re (max Re= ~5.0) and Wo (max Wo=~0.4) of the blood flow in the OFT were low, which is consistent with the estimates from previous flow measurements[78] and computational models of chick embryonic hearts.[144, 163] Low Re and Wo imply that blood flow in the OFT is laminar, with viscous forces dominating the blood flow.

The effects of initial or boundary conditions in our FE models only locally and temporally affected the accuracy of the calculated flow field. Boundary effects were limited to 0.1 mm, so the hemodynamic parameters that we extracted about 0.16 mm away from the OFT inlet or outlet in our 3D FE model were not affected by boundary effects. Initial transient effects were estimated to last for less than 0.03 cardiac cycles (0.03T).

In our models, the blood flow pattern in the OFT is mainly regulated by the pressure difference imposed on the OFT from the ventricle and aortic sac, and heterogeneous wall

motion. We found that along the OFT the effects of the pressure difference and wall motion varied. At the inlet, the centerline velocity profile followed closely the shape of the pressure difference (see Figures 5.6, 5.8, and 5.9A), indicating that the pressure difference dominated the velocity profiles near the OFT inlet. Towards the outlet of the OFT, the effects of the heterogeneous wall motion on the blood flow increased. Other factors such as the 3D curvature, elliptical cross-sections, and orientation of the elliptical sections also locally affected the flow field in the OFT, including the skewed flow towards the inner curvature and in-plane flow, which may be important for the WSS distribution on the OFT wall. These local and global effects affect the distribution of WSS on the OFT wall.

### 5.5.5 WSS on the wall of the OFT

To understand the role of WSS in the morphogenesis of the OFT, it is necessary to quantify the spatial distribution of the WSS on the OFT wall over the cardiac cycle. Compared to rigid wall, steady state models,[21, 91, 139, 162] the WSS distribution predicted by our current 3D model was more realistic because the geometry and motion of the 3D model were obtained from the 4D OCT images of the OFT, and the pressures imposed at the inlet and outlet were measured *in vivo* at the ventricle and aortic sac.

From the 3D FE model of the OFT, we found the maximal WSS (~11 Pa) occurred near the outlet when the OFT was expanded (0.16 mm away from the outlet). Note that the high level of the WSS at the inlet and outlet (<0.1 mm from the inlet/outlet surface) may be due to the boundary effects and thus is not analyzed. The magnitude of calculated WSS was consistent with WSS derived from the blood flow field measured using PIV [75,

[78] and Doppler OCT.[169] Our predicted distribution of the WSS was also consistent with the literature:[21, 91, 144, 163] the high level of WSS was located at the narrower lumen regions, inner curvature of the OFT wall, and at the cardiac cushions. In addition, our 3D FE model of the OFT predicted a transient variation of WSS along the OFT. The transient heterogeneous distribution of WSS implies that ECs are subject to differential biomechanical stimuli, which may modulate differential growth and morphogenesis in the OFT.

## 5.6 Conclusions

This paper provides a methodology to quantify subject-specific distributions of WSS in the living embryonic heart. We developed image-based dynamic FE models of the cardiac OFT of normal chick embryos at stage HH18. The FE models took into account physiologically pulsatile pressures imposed at the inlet and outlet of the OFT, and the dynamic wall motion obtained from the 4D OCT imaging. The 2D FE models of the OFT, integrated with Doppler ultrasound and OCT imaging techniques, aided in the determination of the phase relationships between the pressures and wall motion, which provided the boundary conditions for our 3D FE model. The 3D FE model of the OFT revealed a distinct blood flow field and transient heterogeneous distribution of WSS in the OFT over the cardiac cycle. We found that on the OFT wall the high level shear stress was located at the outlet towards the inner curvature and at the cardiac cushions, and low level shear stress was located at the middle region and towards the outer curvature. In the future, correlation of WSS and shear-response gene expressions (e.g., [21, 24]) will lead to a better understanding of the role of WSS in cardiac development.

## 5.7 Data supplement (unpublished)

*Sensitivity study on the uncertainties in blood pressures*

The blood pressures imposed from the ventricle ($P_v$) and aortic sac ($P_a$) on the OFT inlet and outlet create a pressure gradient in the OFT that drives the blood flow through the OFT from the ventricle to the artery system. In our FE models of the OFT, we used $P_v$ and $P_a$ as our boundary conditions to predict the blood flow in the OFT. However, due to technical difficulties, the pressure measurements in the ventricle and in the aortic sac were performed in different chick embryos. The uncertainties in combinations of $P_v$ and $P_a$ would affect the pressure gradient in the OFT, and thus the accuracy of blood flow prediction using FE modeling.

To study the effects of the uncertainties in pressure data on the predicted blood flow, we used a 2D dynamic FE model of the OFT (refer to Figure 5.3) and analyzed the sensitivity of the centerline velocities to different choices of pressure data as boundary conditions. Here, we choose two sets of extreme pressure data: (1) $P_v^{min}$ and $P_a^{min}$, and (2) $P_v^{max}$ and $P_a^{max}$ from our pressure measurements (see Supplemental Figure 5.1). The phase relationship between $P_v$ and $P_a$ ($\Phi p$), and the phase relationship between $P_v$ and the effective radius of the OFT inlet ($\Phi m$) were kept the same as the 3D dynamic FE model in Chapter 5, that is, $\Phi p=0.1T$ and $\Phi m=0.2T$ (refer to Figure 5.5).

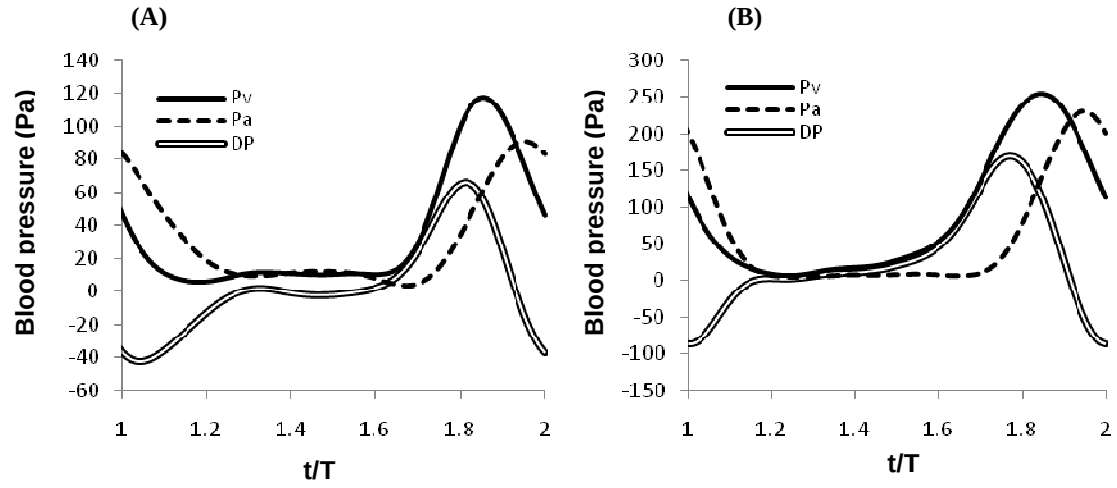


**Supplemental Figure 5.1** The ventricular and aortic sac pressures used in a 2D dynamic FE model of the OFT (A) $P_v^{min}$ and $P_a^{min}$, and (B) $P_v^{max}$ and $P_a^{max}$.

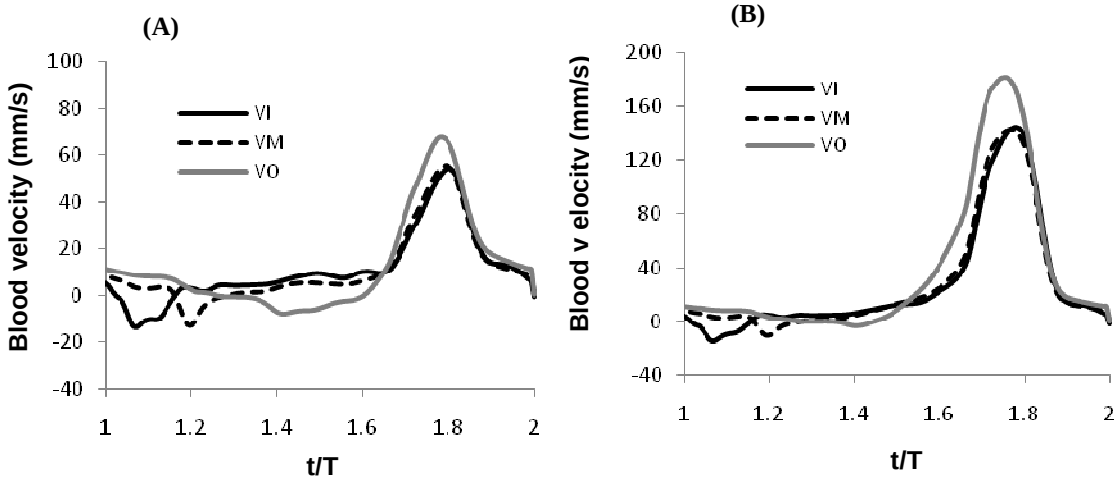


**Supplemental Figure 5.2** Predicted centerline velocities near the OFT inlet, middle, and outlet, under pressure boundary conditions: (A) $P_v^{min}$ and $P_a^{min}$, and (B) $P_v^{max}$ and $P_a^{max}$, as shown in the Supplemental Figure 5.1. VI, VM, and VO are the centerline blood velocity near the OFT inlet, middle, and outlet, respectively.

Supplemental Figure 5.2 compares centerline velocities, extracted near the OFT inlet, middle, and outlet (refer to Figure 5.3), between the two extreme blood pressure scenarios (Supplemental Figure 5.1). We found that a large difference in the values of

peak blood flow velocities, which was mainly due to the pressure difference imposed between the OFT, the major driving force for the blood flow in the OFT. We also found that predicted centerline velocity profiles in the two extreme cases of blood pressure conditions shows similar spatial and temporal variations. Near the OFT inlet, the velocity profile exhibited a transient backflow (~15 mm/s) followed by a shoulder; then the blood flow rose fast to the peak and followed by a shoulder after the peak. The velocity profile at the OFT middle region was similar to that near the OFT inlet, except that the transient backflow occurred 0.1T later at the middle OFT. Near the OFT outlet, the centerline velocity profile had a transient backflow immediately before the fast rise of velocity, after the peak a shoulder region followed. The maximal peak blood velocity occurred near the OFT outlet.

Our results suggest that the magnitude of the blood flow velocity is sensitive to the uncertainties in pressure data. Validation of the FE prediction with *in vivo* flow measurement is essential to ensure the magnitude of the flow velocity within the physiological range in the OFT. Our results also suggest that the predicted trend (spatial and temporal variations) of the blood flow velocity is consistent with different choices of pressure data.

In the FE models in Chapter 5, we used representative pressures that were closest to the averages of the group, and we compared the model predicted velocities with Doppler ultrasound flow measurements at corresponding locations. Further, the sensitivity study on the pressure data ensures us that the conclusions drawn from the FE models in Chapter 5 are reasonably accurate.

# Chapter 6: Quantifying the dynamic biomechanical environment in the heart outflow tract in HH18 chick embryos

*(Paper in preparation to be submitted to Circulation)*

## 6.1 Introduction

During early developmental stages, blood flow is essential for normal cardiac development,[14, 170] and perturbations in blood flow dynamics lead to structural defects in the heart.[11-14] Congenital heart defects occur in about 1% live births, and are responsible for about 10% stillbirths, and possibly up to 20% of spontaneous miscarriages.[136] A big portion of the defects is likely due to abnormal blood flow conditions during the first weeks of development. Up to now, however, technological difficulties prevented progress in the field.

The interaction between blood flow and cardiac tissue determines the biomechanical environment (strains and stresses) to which cardiac cells are subjected. This biomechanical environment affects cardiac cellular responses, and thus further cardiac development. Experimental difficulties in quantifying the biomechanical environment to which cells are subjected to i*n vivo* have hindered progress in the field. In this manuscript, we used an integrative approach to determine the biomechanical environment to which cardiac cells are subjected during early embryonic developmental stages.

We used the chicken embryo heart as our model system because at early developmental stages chicken and human hearts are very similar and developmental

processes are highly conserve among vertebrate species.[1] Further, we focused here on the heart outflow tract (OFT), the distal part of the heart connecting the primitive ventricle to the arterial system. The OFT has a wall composed of: (i) a myocardium layer, which actively contracts; (ii) endocardium layer, a monolayer of endothelial cells in direct contact with blood flow; and (iii) a cardiac jelly layer, composed of extra-cellular matrix, in between the myocardium and endocardium. At the very early stage of development that we are studying, HH18 (~3 days of incubation), the heart is an s-shape tube that have no valves.[48, 49] The cardiac cushions in the OFT, the localized protrusions of cardiac jelly act as primitive valves to regulate blood flow from the ventricular to the arterial system .[171] At later stage, the OFT undergoes extensive morphogenesis, giving rise to cardiac semilunar valves and septa, and eventually developing into aortic and pulmonary outlets.[55, 56] OFT morphogenesis is sensitive to the hemodynamic environment,[11, 21] and thus biomechanical stimuli, and heart defects associated with the OFT contribute to a large number of congenital heart defects. [53]

To quantify the biomechanical environment of the developing heart, we used a combination of imaging, physiological measurements (blood pressure and blood flow velocities) and computational fluid dynamics (CFD) modeling. Current state-of-the-art optical coherence tomography (OCT) and 4D imaging techniques allow studying heart dynamics in 4D.[70, 73, 97, 164] OCT is a high resolution (2-20 μm) non-invasive (non-contact) tomographic imaging technique that can image up to a 2-mm depth in biological tissues.[62] Therefore, OCT is well suited for imaging small embryonic hearts during early development (<2 mm in size).[62, 67] Using OCT imaging of the chick OFT, we first characterized the *in vivo* motion of the OFT wall over the cardiac cycle, and

cardiac wall strains. Using the dynamic geometry of the OFT wall, obtained from OCT, we then developed image-based (subject-specific) CFD models of the developing heart OFT to quantify *in vivo* blood flow patterns and wall shear stresses over the cardiac cycle.[84-87] The combination of OCT imaging and CFD modeling allowed us to characterize, in more details than ever before, the *in vivo* dynamic biomechanical environment to which cardiac cells are exposed during the cardiac cycle on the OFT of chicken embryos.

## 6.2 Materials and Methods

### 6.2.1 Chick embryo preparation

Fertilized white Leghorn eggs (n = 7) were incubated at 38 ℃ and 80% humidity to stage HH18 (approximately 72 hours). Embryo staging followed standard procedures.[48] Before imaging or pressure measurement, a small window was opened on the egg shell and the underlying membrane was removed to expose the embryo heart. Since temperature affects cardiac function, during data acquisition the temperature of the chick embryo was maintained at $37.5 \pm 0.5$ ℃ within a warming chamber using a temperature controller.

### 6.2.2 4D imaging using OCT

We used a spectral-domain OCT customized to image the structure and blood flow of the chick OFT in *ovo.*[60] The system used a superluminescent diode broadband light source with full-width-half-maximum of 56 nm centered at 1310 nm (Denselight, Singapore), which yielded an axial spatial resolution of 10 μm and a lateral spatial resolution of 16 μm. With a 1024 element infrared InGaAs line-scan camera with 14 bit digital depth and

a maximal line-scan rate of 47 kHz, the OCT system allows us to acquire images of 512 x 256 pixels (256 A-scans) at 140 frames per second.

To capture the dynamics of the fast beating embryonic heart (typical heart rate is 2.5 Hz at HH18) from OCT images, we used our previously developed 4D imaging and reconstruction procedures.[164] Briefly, 2D image sequences (B-mode images) of the OFT were acquired over 4-5 cardiac cycles at sequential cross-sections that were 7.5-μm apart, until the entire OFT was imaged. From the acquired image sequences, 4D images of the heart OFT (3D geometry over time) was then reconstructed using our developed post-acquisition synchronization algorithm.[164]

The unique advantage of spectrum domain OCT is that during structural imaging the flow information within the OFT is also obtained. Phase images were obtained by calculating the phase differences $\Delta\varphi$ between two adjacent A-scans in a B-scan, this phase difference is introduced by the movement of tissue and cells, such as the myocardial wall and blood. Phase images can be easily converted to Doppler velocity images,[60]

$$V_z = \frac{\lambda_0}{4\pi n\tau}\Delta\varphi \tag{6.1}$$

where $V_z$ is the Doppler velocity, $\lambda_0$ is the central wavelength; $n$ is the refractive index of tissue (~1.3); $\tau$ is the time difference between the two adjacent A-scans (~21 μs).

### 6.2.3 Image processing

To extract the dynamic geometry of the OFT wall and blood flow in the OFT from the OCT images, we developed a set of image-analysis algorithms using Matlab2009a (The

MathWorks, Inc. Natick, MA).

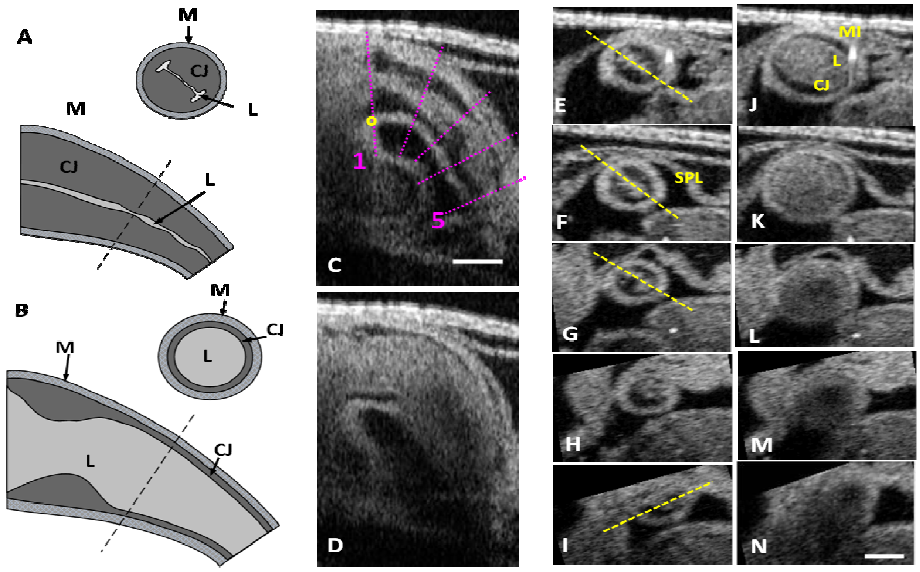


**Figure 6.1** OCT images of the OFT. Illustration of the OFT longitudinal and cross sections (A) when the OFT is constricted, and (B) when the OFT is expanded. OCT images of a OFT longitudinal section (A) when the OFT is constricted, overlaid lines showing the locations where 5 cross-sections were extracted from the 4D OCT images of the OFT; (D) when the OFT is fully expanded. (E-I) The 5 cross-sections at locations 1-5 at OFT maximal contracted state, and the same cross-sections (J-N) at OFT maximal expansion state. The yellow lines in (E, F, G, and I) showing the orientation of the opposing cardiac cushions in the OFT. M, myocardium; L, lumen; CJ, cardiac jelly; SPL, splanchnopleure membrane. Scar bar = 200 µm.

*Geometry and wall motion*

To characterize the geometry and motion of the OFT wall, we used segmentation algorithms (see Chapter 3) to delineate the layers of the heart OFT. For each embryo image set, we first segmented the myocardium of the OFT from a reconstructed 3D-image dataset, at the phase when the OFT was most constricted, and calculated the centerline along the axis of the OFT. We then extracted 2D image sequences at 5 evenly spaced cross-sections perpendicular to the axial centerline of the OFT (L1-L5, see Figure 6.1C) from the 4D reconstructed images. L1-L3 approximately represented the OFT proximal region (also referred to as conus[172]); L4 and L5 represented the OFT distal

region (or the truncus). From the extracted image sequences, we delineated the boundaries of the OFT myocardium and lumen (e.g. Figure 6.1E and refer to Figure 6.5A) frame-by-frame over the cardiac cycle, and calculated the boundary perimeters, and the areas enclosed by these boundaries for further analysis.

*Wall strains*

Using the image segmentation, we characterized circumferential strains in the myocardium and the endocardium over the cardiac cycle. Circumferential strains were estimated by:

$$\varepsilon_\theta = (C - C_{max})/C_{max} \tag{6.2}$$

where C is the perimeter of either the interior boundary of the myocardium or the cushion-endocardium interface, calculated from image segmentation.

Similarly, radial strains of the myocardium were estimated by:

$$\varepsilon_r = (h - h_{max})/h_{max} \tag{6.3}$$

where h is the average thickness of myocardium at the OFT cross-section considered, calculated from the segmented inner and outer myocardium boundaries from the images.

*Luminal behavior*

To further quantify the behavior of the OFT, from the OFT cross-sectional image sequences (L1 to L5, Figure 6.1C), we also extracted M-mode images along a line perpendicular to the cushion surface (see Figure 6.5A). M-mode images show the structure of the OFT (image gray scale) along the line over time, and thus can be used to visualize the dynamic motion of the structure over cardiac cycles. From these M-mode

images, we quantified the time spans in a cardiac cycle in which (i) the lumen was closed, $T_{closed}$, (ii) luminal area was increasing, $T_e$, and (iii) luminal area was decreasing, $T_c$ (see Figure 6.5 D).

*Interaction between blood flow and wall motion*

To characterize the interaction between cardiac wall motion and blood flow dynamics within the OFT, we analyzed together structural and Doppler velocity images from the acquired 2D image sequences. From the structural image sequences, we then extracted M-mode images along a vertical line that approximately cut the OFT in two halves. From corresponding phase images, we also extracted M-phase images (showing phase in the vertical direction over time in the horizontal direction). We then chose a line from the M-mode images that remains in the lumen at all times (except when the OFT is fully closed) and extracted the Doppler velocity, $V_z$, along that line over time. $V_z$ provides an estimation of the component of blood flow centerline velocity along the OCT beam direction.

### 6.2.4 Pressure measurements

We used a servo-null micro-pressure system (Model 5A-LN, Instrumentation for Physiology and Medicine, San Diego, CA) to measure blood pressures in normal chick embryonic hearts at HH18. Pressure data were collected in the ventricle and in the aortic sac, immediately upstream and downstream the OFT, following standard procedures. [165] Pressure traces were sampled at 100 Hz over at least 10 cardiac cycles in the ventricle (n = 29) and in the aortic sac (n = 8).

To evaluate wall stress in the myocardium, we assumed that the OFT myocardium was a thin wall cylinder with uniform wall thickness, and used the Laplace law to approximate the circumferential wall stress, $\sigma_\theta$, in the myocardium:

$$\sigma_\theta = PR/h \tag{6.4}$$

where P is the intracardiac blood pressure, R is interior radius of the myocardium, and h is the average wall thickness of the myocardium at the OFT cross-section considered.

### 6.2.5 Computational fluid dynamics modeling of the OFT

To quantify the 3D blood flow dynamics within the heart OFT over the cardiac cycle, we used a subject-specific CFD model of the chick OFT developed using the finite element software Adina (ADINA R & D, Inc. Watertown, MA). The lumen geometry and wall motion of the CFD model were obtained from the OCT image data of a representative HH18 embryo, with OFT dimensions and motions closest to the measured average of the imaging group (n=7). A detailed description of the CFD model and assumptions is given elsewhere.[173] For the CFD model, we assumed that the lumen of the OFT was a 3D curved tube with elliptical cross-sections. Blood flow was modeled as a continuous, transient and incompressible Newtonian fluid (density $\rho = 1060\ \mathrm{kg/m^3}$ and viscosity $\mu = 3 \times 10^{-3}\ \mathrm{kg/(m\ s)}$) since embryonic chick blood has low hematocrit (20% Ht). [166, 167] The OFT lumen was discretized using 4-node tetrahedral fluid-condition-based-interpolation (FCBI) elements.[153] A time-varying displacement was imposed on the model surface representing the lumen-wall interface, to simulate the motion of the cardiac OFT wall as quantified from OCT images. Representative ventricular and aortic sac pressures, which had peak values closest to measured averages, were imposed

uniformly at the inlet and outlet of the OFT model as normal traction boundary conditions. We assumed that initially the OFT was at its most constricted state with no blood flow. Mesh and time-step independent results were obtained.

## 6.3 Results

### 6.3.1 Characterization of OFT wall dynamics

OCT images distinctly showed the microstructure of the OFT wall (Figure 6.1). The myocardium and cardiac jelly layers (shown as the dark region in-between the myocardium and lumen) of the OFT wall were readily distinguished in OCT images. The endocardium layer, however, was not distinguishable from the lumen blood due to their similar refractive index. Since the endocardium is a thin monolayer of endothelial cells that enclose the lumen surface, the endocardium was approximated by the cardiac jelly-lumen interface.

Visualization of the 4D image reconstruction of the HH18 cardiac OFT from 4D OCT images (e.g., Supplemental Video 6.1), showed a characteristic peristaltic-like dynamic motion of the OFT wall. The OFT wall opened to allow blood ejecting from the ventricle to flow to the arterial circulation. After blood ejection, the OFT myocardium contracted, and the cardiac cushions became in contact with each other closing the lumen sequentially along the OFT to prevent backflow. Through the distinct dynamics of the OFT wall, the OFT acts as a primitive valve regulating blood flow from the ventricle to the aorta in the early developing heart.

To characterize OFT wall dynamics, we selected 5 OFT cross-sections evenly

distributed along the axis of the OFT (Figure 6.1C, L1 to L5), and quantified motions of the myocardium, cardiac jelly, and endocardium, as well as their effects on the lumen area over the cardiac cycle.

#### 6.3.1.1 Myocardium

At each of the 5 cross-sections, the myocardium had a slight ellipse-like shape (Figures 6.1 E-6.1N). The ratio of the length of the major and minor axis, the shape factor λ, was between 1 (circular shape), when the OFT myocardium was most expanded, and 1.3, when the myocardium was most constricted (see Table 6.1). The minor axis of the ellipse was found to be along the direction of maximal cardiac cushion thickness (refer to Figures 6.1E-I and 6.4C). [72] External constraints, such as the splanchnopleure membrane that wraps and pushes against the heart tube, were observed to slightly restrict myocardial motion and altered deformation patterns of the myocardium (refer to Figure 6.1L).

Since the myocardium remained approximately circular during the cardiac cycle, for simplicity and to ease interpretation of data, myocardial dimensional changes were characterized by an effective myocardial radius, $R = \sqrt{A_{MI}/\pi}$, where $A_{MI}$ was the area enveloped by the segmented internal contour of the myocardium (refer to Figure. 6.4C). At each of the 5 selected OFT cross-sections, R varied cyclically over the cardiac cycle (see Figure 6.2A). The peristaltic myocardial wall motion was manifested as a sequential appearance of $R_{max}$ followed by a sequential contraction from the OFT inlet (L1) to the outlet (L5). We found that the OFT wall exhibited different behaviors at its proximal and distal regions (Figure 6.2A): proximally (L1), the myocardium exhibited a relatively long period of expansion (relaxation) followed by a short contraction; while distally (L5), the

myocardium exhibited a relatively short expansion period followed by a long contraction period. Further, while proximally contraction of the myocardium resulted in lumen closure, distally the contraction of the OFT wall was frequently (6/7 embryos) not enough to completely close the lumen (refer to Figure 6.2A). The amplitude of the radial myocardium motion (ΔR) decreased from L1 to L5.

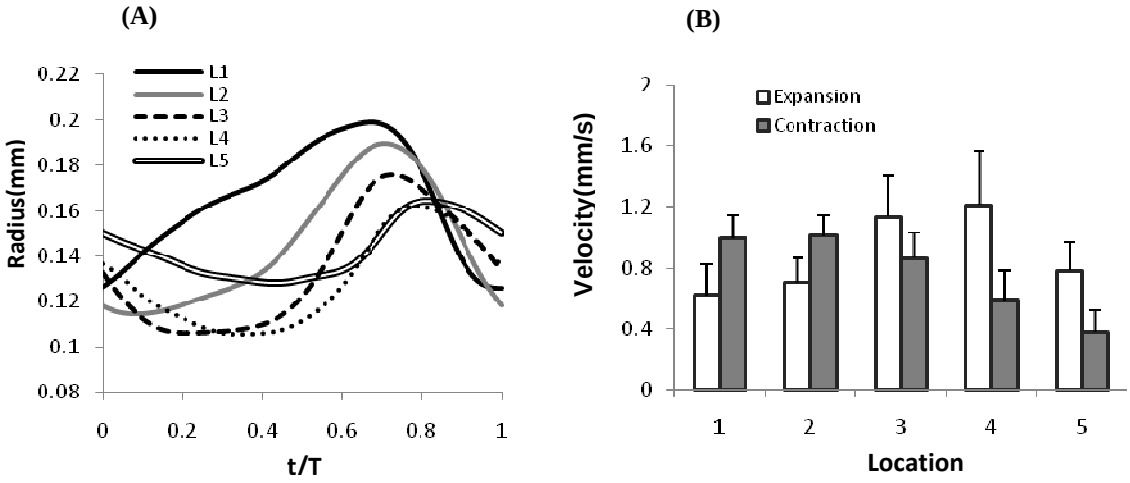


**Figure 6.2** Behaviors of the myocardium at 5 selected OFT cross-sections. (A) Temporal variations of radii, and (B) maximal expansion and contraction radial velocities of the myocardium at the 5 selected OFT cross-sections of the normal chick embryonic heart.

To further quantify myocardial wall motion, we calculated the rate of change of R, dR/dt, which represents radial cardiac wall velocities. Comparing the maximum rates of myocardial expansion and contraction along the OFT (Figure 6.2B), we found that from L1 to L5 rates of expansion seem to first increase and then decrease, while rates of contraction decreased. Interestingly, while proximally rates of contraction were larger than rates of expansion, this behavior was reversed distally of the OFT (Figure 6.2B).

**Table 6.1** Summary of OFT dimensions at 5 selected cross-sections (L1-L5)

| Variables | L1 | L2 | L3 | L4 | L5 |
|---|---|---|---|---|---|
| Myocardium | | | | | |
| $\lambda_{max}$ | 1.27(0.06) | 1.21(0.08) | 1.2 (0.1) | 1.26(0.07) | 1.19(0.09) |
| $R_{max}$ | 0.21(0.02) | 0.20(0.02) | 0.19(0.02) | 0.17(0.03) | 0.15(0.01) |
| $R_{min}$ | 0.14(0.01) | 0.13(0.01) | 0.12(0.02) | 0.11(0.01) | 0.12(0.01) |
| $\Delta R_{max}$ | 0.07(0.01) | 0.07(0.01) | 0.073(0.009) | 0.06(0.01) | 0.035(0.008) |
| ASF | 0.55(0.06) | 0.60(0.05) | 0.63(0.03) | 0.59(0.04) | 0.41(0.08) |
| Lumen | | | | | |
| $\lambda_{max}$ | 2.7(0.4) | 2.5(0.4) | 2.1(0.4) | 1.7 (0.3) | 1.6(0.2) |
| $A_{max}$ | 0.09(0.01) | 0.09(0.02) | 0.09(0.02) | 0.07(0.02) | 0.05(0.01) |
| $A_{min}$ | 0.022(0.004) | 0.019(0.004) | 0.017(0.004) | 0.014(0.005) | 0.022(0.005) |
| $\Delta A_{max}$ | 0.07(0.01) | 0.07(0.02) | 0.07(0.02) | 0.06(0.02) | 0.03(0.01) |
| ASF | 0.75(0.05) | 0.79(0.04) | 0.81(0.03) | 0.79(0.03) | 0.60(0.08) |
| Cardiac jelly | | | | | |
| $A_{max}$ | 0.06(0.02) | 0.05(0.01) | 0.03(0.01) | 0.027(0.008) | 0.026(0.006) |
| $A_{min}$ | 0.039(0.008) | 0.028(0.008) | 0.021(0.007) | 0.013(0.005) | 0.014(0.004) |
| $\Delta A_{max}$ | 0.021(0.009) | 0.014(0.006) | 0.010(0.005) | 0.009(0.005) | 0.009(0.004) |
| ASF | 0.33(0.07) | 0.31(0.07) | 0.29(0.09) | 0.3 (0.1) | 0.4(0.1) |

Data are presented as mean (standard deviation). λ, the shape factor; R, radius (mm); ΔR, radius change over the cardiac cycle; A, area ($mm^2$); ΔA, area change over the cardiac cycle (mm2); ASF, area shortening factor.

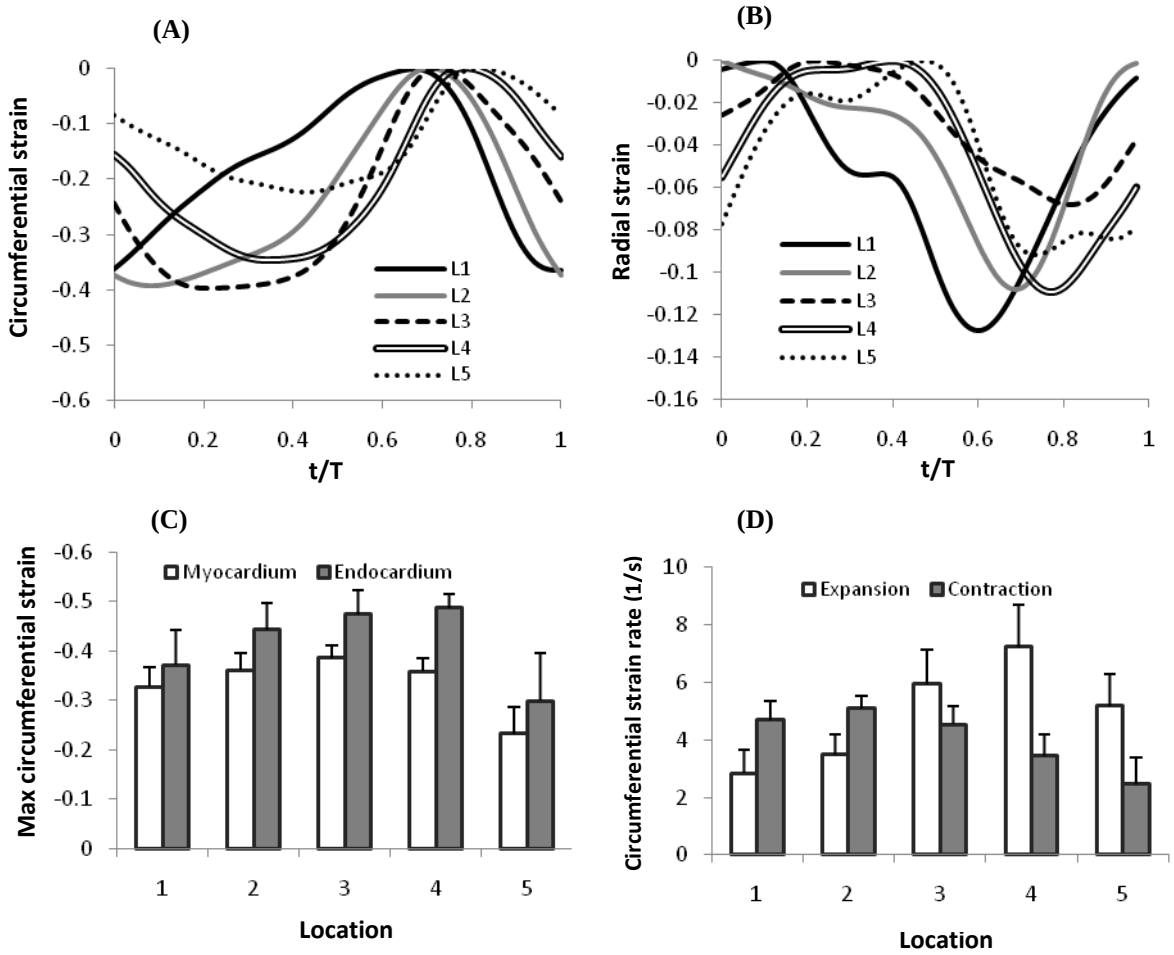


**Figure 6.3** Cyclic strains in the myocardium at 5 selected OFT cross-sections. (A) Temporal variation of circumferential strains in the myocardium, (B) temporal variation of radial strains, (C) peak circumferential strain in the myocardium compared with that in the endocardium, and (D) peak expansion and contraction circumferential strain rates.

Circumferential strains over the cardiac cycle, measured relative to the maximal expansion state of the OFT for each cross-section (Eq. 6.2), showed the cyclic contraction of the OFT myocardium, as expected (Figure 6.3A). We found that absolute maximum values of circumferential strain decreased from L1 to L5, with peak contraction strains higher at L1 to L4, and dropping significantly at L5 (Figure 6.3A). Thickening and thinning of the myocardium layer over the cardiac cycle were analyzed by radial strains,

measured relative to the maximal myocardial thickness, Eq (6.3), which corresponded to maximum OFT contraction for each cross-section. Similar to the circumferential strain, the radial strain varied over the cardiac cycle and along the OFT (Figure 6.3.B). Compression strains (negative strains) increased during OFT expansion (myocardium thinning) and decreased during OFT contraction (myocardium thickening). Peak compression radial strains were larger at both ends of the OFT with the maximal at the OFT inlet (L1) and the smallest peak radial strain at the middle region (L3) (see Figure 6.3B).

#### 6.3.1.2 Cardiac jelly

The cardiac jelly was unevenly distributed across the OFT cross-section, and divided into two opposing cardiac cushions (see Figures 6.1E-I). If we follow the line that separates the cardiac cushions when the OFT cross-section is most constricted, the orientation of the line changes along the OFT, especially between L3 and L5. The orientation at L4 is ambiguous since the lumen has a star appearance at contraction (in 5/7 embryos, refer to Figure 6.1H). These findings that two pairs of spirally distributed cardiac cushions with the proximal cushion pair extending from L1 towards L4 and a distal cushion pair starting at L4 and extending towards L5were consistent within the HH18 embryos and similar as the cushions observed in the OFT of HH21 chick embryos. [56]

The area of the cardiac jelly, calculated as the difference between the area enclosed by the inner myocardium boundary and the lumen area at each cross-section, decreased towards the OFT outlet (Table 6.1). Further, over time, the maximal area of the cardiac jelly along the OFT, occurred sequentially from the OFT inlet to the outlet, describing a

peristaltic-like change in areas (see Figure 6.4A). The area change of the cardiac jelly was not in phase with the peristaltic motion of the myocardium (Figure 6.4B-F). In general, at each cross-section, cardiac jelly area was relatively large when the myocardium was contracted, and the OFT lumen closed; the jelly area reached its maximum when the myocardium started to relax. Minimal cardiac jelly areas were observed when the myocardium was most expanded. Changes in cardiac jelly area over the cardiac cycle were about 30% for all cross-sections (see Table 6.1).

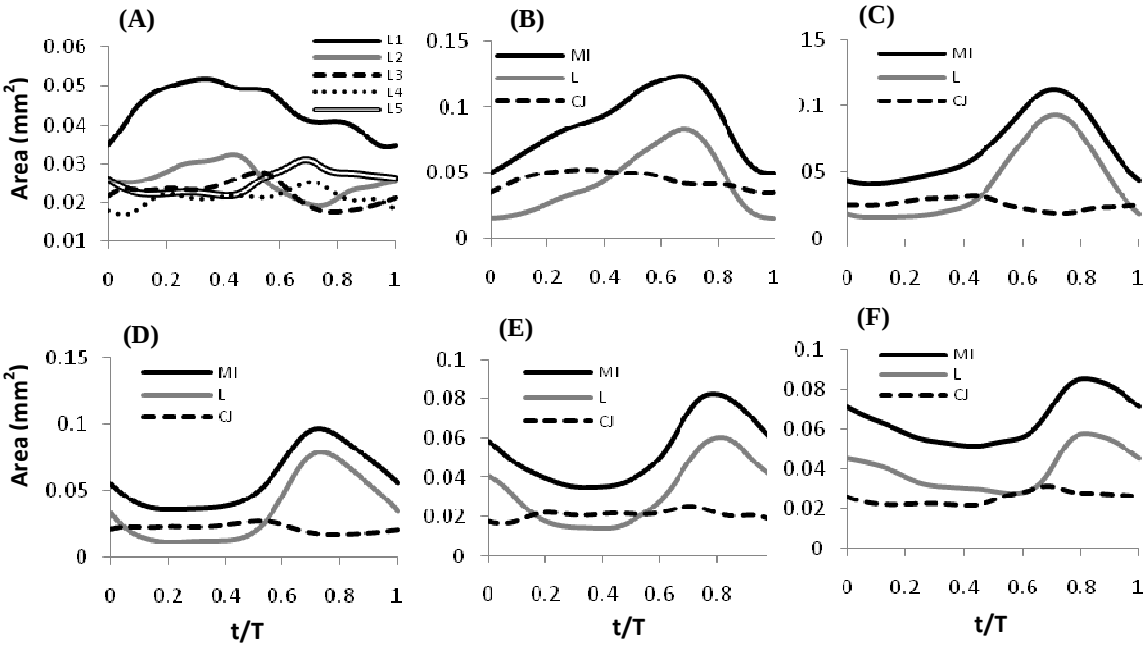


**Figure 6.4** Behaviors of the cardiac jelly at 5 selected OFT cross-sections (L1-L5). (A) Temporal variation of areas of cardiac jelly over a cardiac cycle; and (B-F) temporal relationship between the areas of the OFT myocardium (MI), cardiac jelly (CJ), and lumen (L) along the OFT from L1 to L5, respectively.

### 6.3.1.3 Endocardium

Because the endocardium and the lumen cannot be distinguished from OCT images, we will analyze the endocardium and lumen together (refer to Figure 6.5A). The

endocardium layer exhibited large shape changes during cardiac cycle: from a slit-like shape during contraction (where observed slit 'branches' were likely known endocardial folds[134]), to an almost circular shape during myocardial expansion.

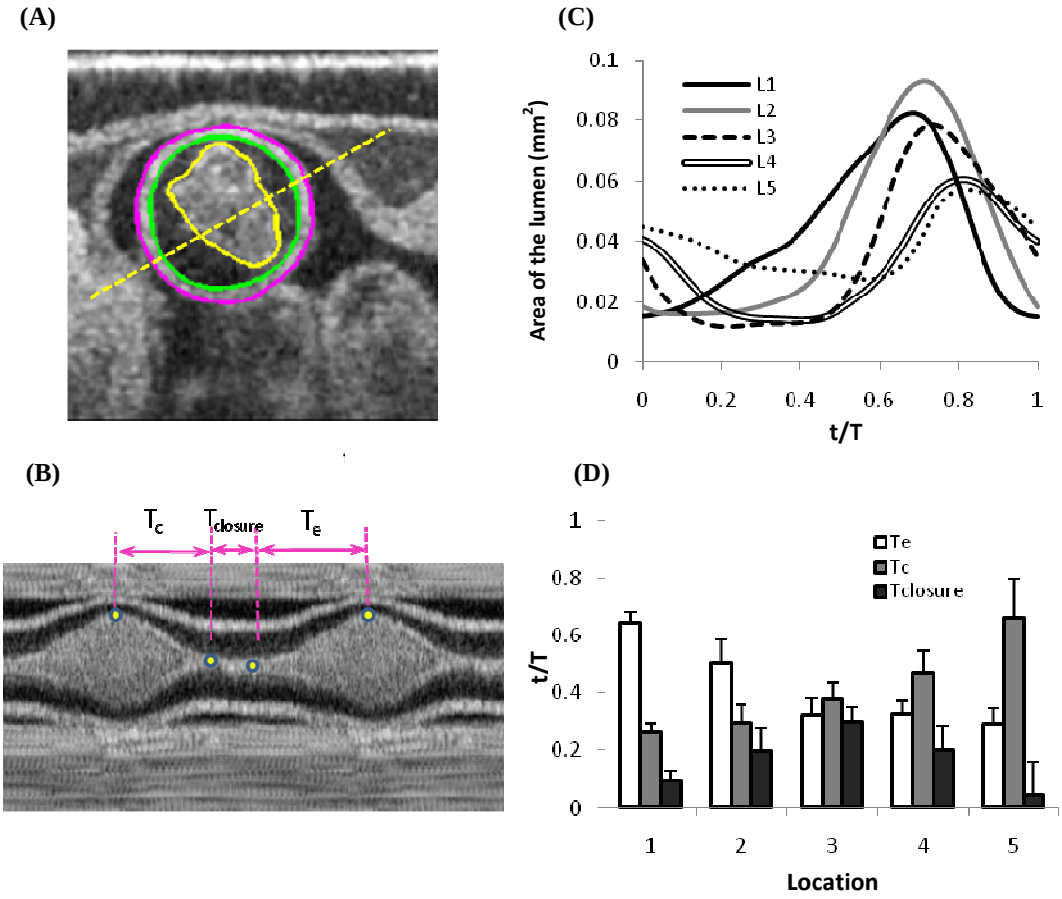


**Figure 6.5** Behaviors of the heart OFT lumen of HH18 chick embryos. (A) A OCT image of the OFT cross-section, with segmented boundaries of the interior myocardium (green contour), exterior myocardium (purple contour), and lumen outline (yellow contour) overlaid on the image; and (B) an M-mode OCT image extracted from the yellow line in (C) to illustrate the metrics defined for evaluating temporal behaviors of the lumen in (D). (C) Temporal variation of OFT luminal areas at 5 selected OFT cross-sections of a representative HH18 chick embryo; (B) time spans for luminal expansion ($T_e$), closing ($T_c$), and closure ($T_{closure}$) over a cardiac cycle at 5 selected OFT cross-sections of HH18 chick embryos.

Using the length of the segmented endocardium boundary, we quantified changes in endocardium strain, measured as differences in length with respect to the maximum length of the segmented curve, Eq (6.2). We observed that, over the cardiac cycle, the

temporal variations of endocardial strains were similar to circumferential myocardial strains (see Supplemental Figure 6.1), but the values of the endocardial strains were larger (Figure 6.3C), indicating that changes in segmented length were larger in the endocardium than inner myocardium boundary.

#### 6.3.1.4 Lumen

Due to the irregular shape of the OFT lumen and the large changes in luminal shape observed during the cardiac cycle, we used the area to describe the cyclic changes of the OFT lumen (see Figure 6.5C, and Table 6.1). The maximal lumen area, and changes in lumen area, were significantly larger at the proximal region of the OFT (L1-L3) than at its distal region (L5). During myocardium contraction, the lumen area was minimal. Since the endocardium and the lumen cannot be distinguished from OCT images, we conjectured that during OFT contraction the lumen is fully closed, and the calculated area corresponds to the area occupied by the endocardium. The lumen however closed at all selected cross-sections, except the L5 cross-section, in which the lumen did not fully close (in 6/7 embryos).

To further characterize and quantify the lumen shape, and the lumen shape change, we assumed an ellipse-like shape for the lumen with the major axis of the ellipse aligning with the opposing cardiac cushion and minor axis perpendicular to the cushions (see Supplemental Figure 6.2). This is approximately true for most of the cardiac cycle, except when the lumen is closed and ‘folds’ of the endocardium are visualized. We then calculated the shape factor of the ellipse that better fitted the lumen boundary and its area (see Table 6.1). As expected, at any given cross-section, the lumen shape factor increased

during OFT contraction, and reduced during OFT expansion. Shape factors also changed along the OFT: maximal shape factor was found at L1 (~2.7) and decreased towards L5 (~1.6). This elliptical fitted lumen shapes, were also used in the CFD model of the OFT.

To better characterize the valvular behavior of the OFT at HH18, we analyzed temporal behaviors of the OFT lumen from M-mode images extracted along a line that approximately aligned with the minor axis of the elliptical lumen (see Figures 6.4C and 6.4D, refer to Supplemental Figure 6.2C). M-mode images revealed that $T_e$ increased towards the distal end of the OFT, while $T_c$ decreased towards the distal end of the OFT (Figure 6.5D). The time span, over which the OFT lumen is presumably closed ($T_{closure}$), was highest at L3 and decreased proximally and distally of L3. At L5, only 1/7 embryos showed lumen closure. Since the OFT lumen along the 5 selected cross-sections was closed sequentially at different phases of the cardiac cycle (see Figure 6.5C), overall the OFT lumen was closed for ~0.5 T.

### 6.3.2 Changes in the intracardiac pressures and myocardial wall stresses

Ventricular pressures (n = 29) and aortic sac pressures (n = 6) were measured in the ventricle and aortic sac that are immediately upstream and downstream of the OFT, respectively. Obtained ventricular pressure data was consistent with previously reported blood pressures at HH18 embryos.[138 174 113] We found that the aortic sac pressure was similar to the ventricular pressure in shape, both has distinct systolic and diastolic components (see Figure 6.6). The peak ventricular pressure was higher than the peak aortic sac pressure (196 ± 37 Pa vs. 180 ± 35 Pa).

To evaluate wall stress in the myocardium, we used representative ventricular pressure

and aortic sac pressure to approximate the pressures at the OFT inlet and outlet (L1 and L5, respectively). We then estimated myocardial wall stress at L1 and L5 of a representative embryo using Laplace law (Figure 6.6). Our results showed that at L1 (OFT inlet), wall stress in the myocardium was low during myocardium relaxation (0.1 to 0.6 T). Wall stress then significantly increased and reached a peak during OFT wall contraction. Similar behavior was observed at L5 (OFT outlet), but the peak wall stress occurred later in the cardiac cycle. The peak WS at L5 was larger than that at L1.

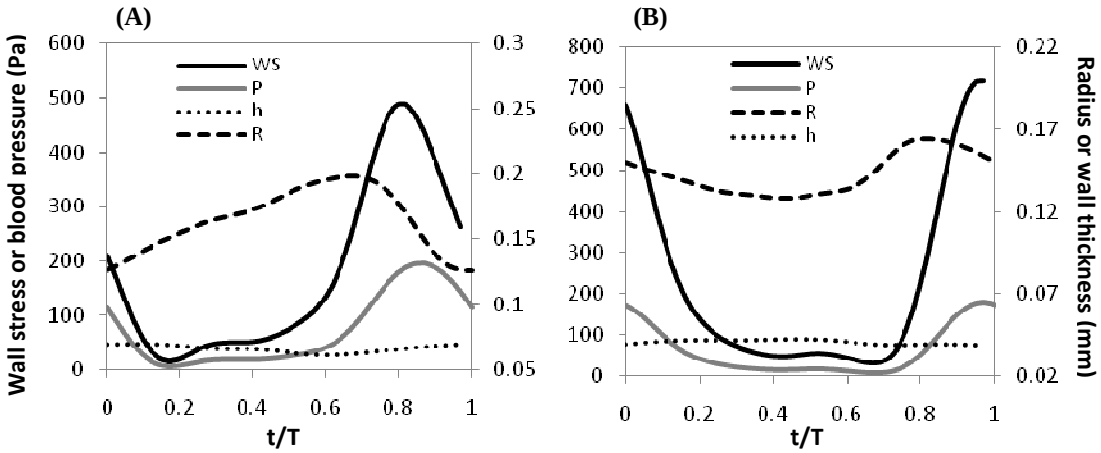


**Figure 6.6** Temporal variations of wall stress over a cardiac cycle at (A) the OFT inlet and (B) outlet. WS, wall stress, P, intracardiac blood pressure, R, radius of the interior myocardium, h, wall thickness of the myocardium.

## 6.3.3 Characterization of blood flow dynamics

### 6.3.3.1 Doppler OCT

Doppler OCT data revealed the timing of blood flowing through the OFT with respect to the OFT wall motion. From the representative embryo studied, we identified a cross-sectional image sequence from the acquired OCT data, which approximately corresponded to the cross-section L2 (except that the plane for this image sequence was

vertical, whereas the plane for the L2 sequence was rotated about 30 degrees with respect to the vertical). This image sequence was selected for further analysis because its Doppler angle was about 60 degrees, the errors in the estimating Doppler angles or phase noises was less likely to affect the measurement. Comparing M-mode and M-phase images extracted from the selected image sequence (Figures 6.7A and 6.7B), we found that there was no blood flow through the OFT for approximately half of the cardiac cycle. Blood flow started when the OFT walls started to expanding, and ended when the OFT fully contracted. Blood flow rose fast when the OFT opened half way and reached to peak when the OFT wall at its maximal expansion. No significant backflow was measured.

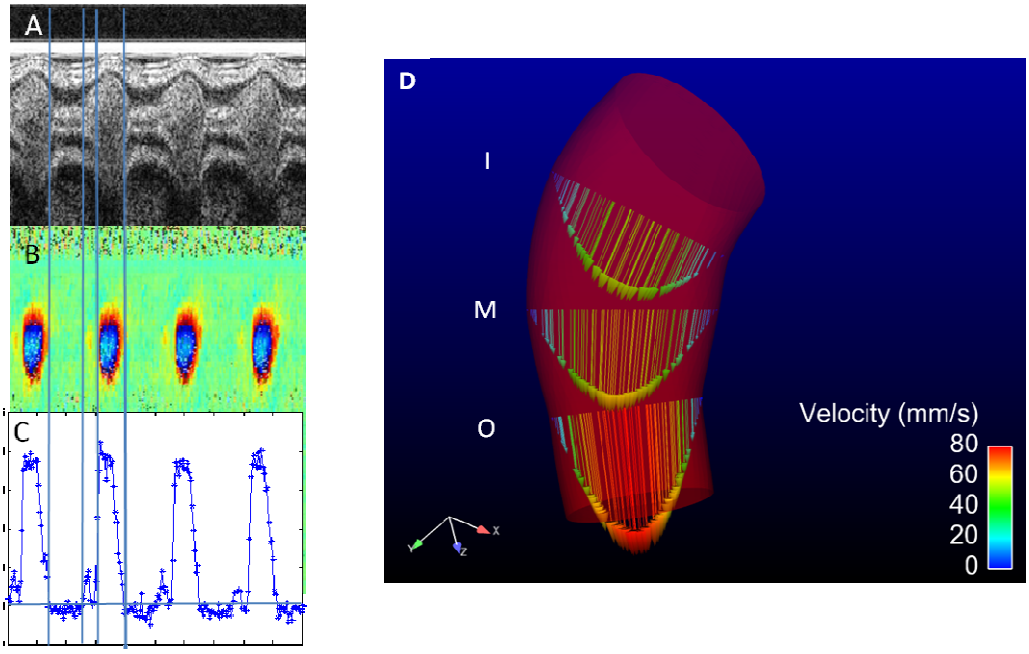


**Figure 6.7** Blood flow dynamics in the OFT. Temporal variation of blood velocity near OFT inlet (I), measured using Doppler OCT: (A) M-mode structural image, (B) M-phase image, (C) blood velocity trace over cardiac cycles, the velocity data were calculated using Eq 6.1 at the location of the horizontal dotted line overlaid on (A). Note that the perpendicular lines show the temporal relationship among the OFT wall motion, Doppler phase, and blood velocity, and the horizontal line overlaid on (C) indicates zero velocity. Spatial distribution of blood flow calculated using FE modeling: (D) blood flow profiles along the major axes of the elliptical cross-sections near the OFT inlet (I), middle (M) and outlet (O). Doppler flow data analysis was performed by Peng Lee.

#### 6.3.3.2 FE model

To further quantify the blood flow field, we generated subject-specific CFD models of the OFT from the representative embryo (see Supplemental Video 6.2). Because flow only occurs during 50% of the cardiac cycle, we used the CFD model to compute flow from 0.43T to 0.93T when the entire OFT lumen is open (refer to Figure 6.5C). Obtained peak velocities along the OFT were consistent with Doppler ultrasound measurements reported previously,[173] and with our Doppler OCT measurement (Figure 6.7C).

In general, we found that computed blood flow through the OFT was laminar, and did not present re-circulation regions. We found that, since the OFT is a tapered tube, during ventricular ejection, maximal velocities occurred at the distal region of the OFT (Figure 6.7D). The OFT wall motion affected flow during phases in which the OFT walls were either expanding or contracting (see Supplemental Figure 6.3), but not significantly during peak flow. Because of the curvature of the OFT, computed blood flow velocities slightly skewed towards the OFT inner curvature (Figure 6.7D). Further, the presence of cushions, which rendered an elliptical lumen cross-section, resulted in a non-uniform flow distribution: with maximum velocity around the center of the elliptical section, but maximum gradients of velocity towards the direction of the cushion (see Supplemental Video 6.3).

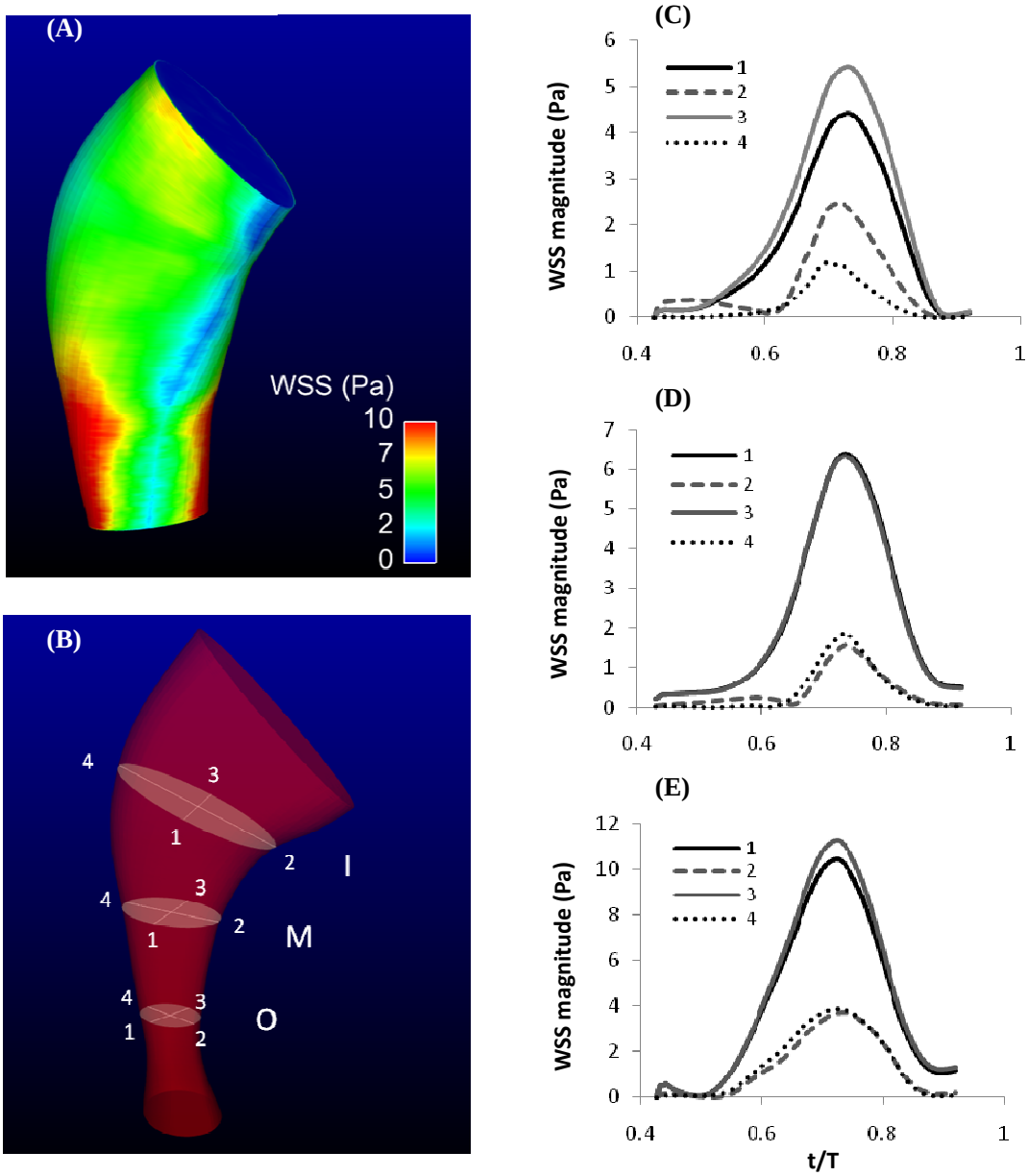


**Figure 6.8** Temporal and spatial distribution of wall shear stress (WSS) magnitude on the OFT lumen surface. (A) Spatial distribution of maximal WSS magnitude on the OFT lumen surface when the OFT is fully expanded; (B) OFT lumen surface showing 4 selected locations (1-4) at three cross-sections near the OFT inlet (I), middle (M), and the outlet (O). Points 1 and 3 are along the minor axis of the elliptical cross-section, representing the cushion region; points 2 and 4 are along major axis, represent the region without cushion. (C-E) Temporal variations of WSS at the 4 selected locations at cross-sections I, M, and O, respectively.

The described distribution of flow within the OFT resulted in a heterogeneous distribution of WSS on the OFT endocardium. Figure 6.8A shows that the largest WSS occurs at the distal portion of the OFT during the OFT maximal expansion. Temporal variation of WSS was analyzed at 3 luminal cross-sections near the OFT inlet, middle, and outlet (see Figure 6.8B). At each elliptical cross-section, 4 representative locations, with 1 and 3 at the minor axis of the ellipse representing the regions on the cushion surface, and with 2 and 4 at the major axis representing the region without cushion. In addition, location 2 further represent the region towards the OFT inner curvature, and 4 the region towards the outer curvature. We found that WSS on the cushion surface is larger than the regions without cushion, consistently at the 3 selected cross-sections (Figures 6.8C-E). We also observed that near the OFT inlet WSS in the OFT inner curvature is larger than the regions towards the outer curvature (Figure 6.8C).

## 6.4 Discussion

During early development, the OFT acts as a primitive valve: it allows blood ejection from the ventricle to the arterial system during ventricular systole, and prevents backflow during ventricular diastole. Proper function of the OFT is thus critical for cardiac function and further cardiac development. The biomechanical environment to which the OFT cells are subjected, determines the fate of the intraventricular septum and semilunar valves, which develop from the OFT after stage HH24. Therefore it is important to quantify this biomechanical environment during the cardiac cycle. In this paper, we focused on characterizing the *in vivo* cyclic motion of the OFT walls and blood flow dynamics within the OFT of chicken embryos at HH18.

Analyses of 4D OCT images allowed us to quantify the details of the *in vivo* motion of the OFT walls and their interaction with blood flow. To characterize blood flow dynamics within the OFT *in vivo*, we used Doppler OCT and CFD modeling. Phase measurements from Doppler OCT allowed correlation between cardiac wall motion and blood flow within the OFT. To further characterize detailed blood flow dynamics in the OFT we employed a subject-specific CFD model of the chick OFT. This CFD model allowed quantification of the details of blood flow within the OFT as well as quantification of the WSS exerted by blood flow on the walls of the OFT. In what follows, we will discuss each of these measurements/methods and their limitations, and how they contribute to our understanding of the OFT mechanics at HH18.

### 6.4.1 Limitations and assumptions of our analyses

4D OCT images were analyzed to characterize OFT motion during the cardiac cycle. In general, variations in imaging results came from three main sources: (1) biological variations of the embryos, (2) experimental conditions, and (3) image quality and image processing procedures, including 4D image reconstruction and image segmentation. Biological variations of embryos are inevitable, and our analyses aim to characterize variations in cardiac OFT function among 7 normal embryos. Efforts have been made to minimize variations in experimental conditions: i) we tightly controlled temperature (within 1° C) during image acquisition, which resulted in changes of cardiac period during acquisition of only up to 7%; and ii) we carefully examine the status of embryos prior to and after image acquisition; embryos showing any signs of bleeding or abnormal wall motion were excluded from the analysis. To ensure the accuracy of the 4D image

reconstruction, we compared OFT wall dynamics from longitudinal OCT images extracted from the reconstructed images with those from direct OCT imaging. Phase errors in the 4D reconstructed images were estimated to be 0.04±0.02T. We also estimated errors in image segmentation by comparing results from the employed automatic segmentation procedure against manual segmentation. We found that maximum differences in calculated areas as well as peak contraction strains were about 10% and occurred in the middle region of the OFT (L3). OCT image quality (signal to noise ratio) deteriorated with increased penetration depth, and thus affected image and image segmentation of the distal portion of the OFT (L4 and L5, see Figures 6.1M and N), which also explains the large variations observed in this region (see Table 6.1). Overall, errors were small, and 4D OCT imaging allowed us to accurately study the motion of the chick heart OFT wall.

To simplify the analysis of the 4D reconstructed images, we analyzed 2D image sequences from 5 locations along the OFT (L1 to L5, Figure 6.1C). For these locations, image planes were fixed in space and were perpendicular to the OFT centerline when the OFT was most constricted. During the cardiac cycle, the motion of the heart slightly changes the position of the OFT centerline. This shift in the centerline direction, however, was calculated to be small (within 10 degrees) at any of the chosen planes, so that the analyzed 2D planes were approximately perpendicular to the OFT centerline during the whole cardiac cycle. More importantly, by fixing the imaging planes in space, the image sequences showed the combined effect of OFT expansion and contraction in both radial and longitudinal directions. We observed that the longitudinal motion of the OFT wall decreased distally towards the aortic sac, which seems to be tethered.

Proximally, however, the contraction and expansion of the ventricle imposed a noticeable motion on the OFT inlet. By tracking an anatomical landmark of the OFT, namely the sharp curve that the cardiac wall forms at the intersection between the OFT and the ventricle (Figure 6.1C, the yellow point), we found the OFT wall moved longitudinally (approximately along the centerline direction) about 140 μm over the cardiac cycle (see Supplemental Video 6.4). This motion is significant considering that the length of the OFT is about 600 μm. To more closely examine the effects of this longitudinal motion, we extracted cross-sectional images near the OFT planes L1 and L2, but so that the planes of these cross-sectional images approximately followed the OFT longitudinal motion, estimated from the motion of the OFT landmark (see Supplemental Figure 6.4). We found that the effects of longitudinal motion were mainly confined to the proximal region of the OFT (the OFT inlet). Without correcting for the longitudinal motion, our analysis slightly overestimated the amplitude of the OFT wall motion (within 10%) with largest deviations occurring during maximal OFT expansion. While specific values varied, general trends in the motion of the OFT were not affected.

This simplified analysis also affected strain calculations. The strains were analyzed over cross-sections that were fixed in space, rather than moving with the cardiac tissue. Further, our approach could not resolve the residual strains (or morphogenetic strains) that arise during cardiac development due to tissue growth. [175] The strains quantified here, however, give a good estimation of changes in strains imposed on cardiac cells during the cardiac cycle

A dynamic CFD model of the OFT was used to quantify blood flow dynamics

within the OFT and the distribution of WSS in the endocardium. For this CFD model, the motion of the cardiac walls was quantified from lumen-wall segmentations of selected cross-sections (L1-L5) from a representative embryo heart OFT. While lumen cross-sections were assumed to be elliptical in the CFD model, this assumption should not significantly affect results, as blood flow occurs when the OFT walls are open, and lumen cross-sections most closely resemble the shape of an ellipse (see Supplemental Figure 6.2). Our models, further, were restricted to the time span during which blood flow could be measured within the OFT (~0.5T). Inaccuracies in flow calculations will thus be more important in the initial and final portions of the calculated flow time frame within the cardiac cycle. Even though wall motions were extracted from OCT images of a single embryo, and thus were subject-specific, blood pressure measurements were obtained from another embryo. This is because of limitations in performing both imaging and pressure measurements procedures in the same embryos. A more detailed, sensitivity analysis of the effects of small changes in blood pressure and wall motion on blood flow dynamics were performed in Chapter 4 and Chapter 5 (refer to Section 4.4.2, Section 4.4.3, and Section 5.7). Given these limitations, our CFD model of the OFT, provided valuable insights into the dynamics of blood flow in the OFT and estimations of the temporal and spatial variations of WSS on the OFT endocardium.

### 6.4.2 OFT function is regulated by the interaction between the cardiac wall and blood flow

OFT function is determined by the interaction of the cardiac wall layers (myocardium, cardiac jelly and endocardium) with the flowing blood. 4D images of the chick heart OFT

at HH18 showed a peristaltic-like motion, in which the OFT lumen closes with a phase lag proximally to distally, in agreement with previous works.[51] Our analyses of 4D OCT images of the *in vivo* heart OFT allowed us to visualize and quantify for the first time the detailed motion of each layer of the HH18 OFT wall and their interaction with blood flow.

#### 6.4.2.1 Myocardium

In the embryonic heart, the myocardium actively contracts during the cardiac cycle to pump blood through the heart. In the OFT, the myocardial wall exhibited different behavior proximally (inlet) and distally (outlet). Myocardial contraction rates and the amplitude of myocardial wall motion ($\Delta R$) decreased distally, resulting in circumferential strains and contraction strain rates that were significantly lower at the distal OFT than at the proximal region. The different proximal/distal behaviors of the OFT myocardium layer observed from OCT images suggested that the distal OFT wall may not actively contract, but may simply expand and contract following intracardiac pressure changes (Figs 6.5F and 6.6). Two possibilities may explain a lack or reduced active contraction of the OFT wall: (1) the OFT wall consists of proximal myocardium and distal non-myocardium components; and (2) the myocardium at the distal OFT is not fully functional. Recently, immunofluorescent staining showed that the entire OFT external layer exhibited myocardial phenotype at HH18; non-myocardium appears at the arterial pole at HH24 (24 hrs later).[176] Further, from stage HH14 to HH20, the OFT lengthens, [177] cells migrate from the secondary heart field to the OFT from the arterial pole, and are then induced to differentiate into OFT myocardium.[178] Therefore, although the distal

myocardium exhibits myocardial phenotype, the newly added myocardium may not be fully functional because active contraction of the myocardium requires assembling and organization of myofibrils.[15] Immature myocardium has fewer and/or less-oriented myofibrils that are incapable of coordinated contraction.[179] Taken together, our results suggest, along the cardiac OFT wall, the myocardium is at different levels of development, with mature myocardium at the proximal region and relatively more immature myocardium at the distal region.

Contraction and expansion of the OFT myocardium occurred both in the circumferential direction (changes in radius that lead to changes in myocardium perimeter and thickness) and longitudinal direction (changes in axial length). From the most constricted to the most expanded configurations, the myocardium stretches between 20 and 40% in the circumferential direction, and about 20% in the longitudinal direction. Our estimation for the peak longitudinal stretch of the OFT myocardium agrees well with reported peak longitudinal strain of the primitive ventricle (0.13-0.16) at HH18.[180] Further, our calculated circumferential strains were in agreement with reported circumferential fractional shortening of sarcomere spacing (0.40 ±0.04) along the inner ventricular myocardium of HH23 chick embryos.[181]

While we could quantify circumferential stretches, and their variation along the OFT wall (e.g., peak compression strains were lower distally than proximally), we assumed that longitudinal stretches were uniform. If this assumption is true, then, peak circumferential strains at the proximal OFT (L1-L4) are larger than peak longitudinal strains, indicating that the OFT is contracting primarily in the circumferential direction.

This is in agreement with the preferential circumferential orientation of the myocardium fibrils found in the OFT.[182] In contrast, the distal OFT (L5) has a more isotropic strain pattern, with similar circumferential and longitudinal strains, suggesting a less organized myocardium fibril network. Due to the cyclic expansion and compression of the myocardium wall, and the incompressibility of the myocardium, its thickness changes by about 10%. Therefore, during the cardiac cycle myocytes are subjected to large cyclic strains. These strains likely affect myocyte function and proliferation.

The cyclic motion of the OFT wall and its interaction with blood flow generates cyclic wall stresses in the myocardium. In the vasculature, circumferential wall stresses are generally uniform along the radial direction, and are larger than radial stresses. Frequently, vascular circumferential wall stresses are estimated using the Laplace law.[183] [184] The Laplace law, however, was derived assuming a thin cylindrical structure that is loaded with an internal pressure, under steady-state conditions. Although this is not true in the developing heart, if we neglect stresses in the cardiac jelly and assume that the myocardium bears the stress in the OFT wall, and since the structure of the OFT myocardium resembles a cylinder, Laplace law can be used to estimate the magnitude of wall stresses, and the magnitude of wall stress changes over the cardiac cycle. More accurate quantifications of wall stresses will require more detailed models that are outside the scope of this paper. Our results showed that wall stress in the OFT myocardium increases towards the distal region of the OFT. This remained true even if the phase between wall motion and blood pressure (which is an uncertainty of our models) was allowed to change (see Supplemental Figure 6.5). This is because blood pressures along the OFT decrease only slightly, while the myocardium layer tapered and its thickness

decreased distally, resulting in larger distal wall stresses. While this result will need further confirmation, it suggests that, during normal development, the OFT wall is subjected to a spatial (proximal to distal) gradient of wall stresses. Because wall stress has been proposed to be a critical biomechanical factor regulating myocardium proliferation in the embryonic heart,[15, 185] this finding could have implications for normal cardiac development.

#### 6.4.2.2 Cardiac jelly

Consistent with previous studies,[56] we have observed evidence of two pairs of cardiac cushions spirally distributed along the OFT (Figures 6.1E-I). The proximal cushions had the largest cardiac jelly mass, especially near the OFT inlet (Figure 6.6A). Over the cross-section, cardiac jelly motion is constrained by molecular tethers between the endocardium and myocardium layers, typically located at regions of lower cardiac jelly thickness, and that separate the cardiac jelly mass into two opposite cardiac cushions.[71, 134] Our OCT images showed folding of the endocardium that was consistent with tethering regions (points in the OCT image cross-sections). OCT images further showed that the spatial distribution of cardiac jelly (and thus cardiac cushions) was associated with the eccentric deformation of the myocardium and the shape of the lumen (Figure 6.1). The uneven distribution of cardiac jelly, forming opposing cardiac cushions facilitates lumen closure during OFT myocardial contraction, and thus presumably enabled the OFT to function as an effective primitive valve.

Over the cardiac cycle, the area of cardiac jelly (a measure of cardiac jelly mass) at any given cross-section changed by about 30% (see Table 6.1). This change in cardiac jelly

area was about the same for all the cross-sections analyzed (L1 to L5) even though cardiac jelly area, and thus cardiac jelly mass, decreased distally (from L1 to L5). Thus, changes in cardiac jelly mass seem to occur locally, with cardiac jelly mass displacing only relatively short distances in the longitudinal (axial) OFT direction. OCT images of the OFT further revealed a wave-like change of cardiac jelly mass along the OFT (see Supplemental Video 6.5), similar to that observed in the AV canal of HH17 chick embryos. [186] These variations in cardiac jelly mass over time are likely due to two factors: (1) lateral motions of cardiac jelly due to hemodynamic forces (blood pressure and shear stress); and (2) the longitudinal cyclic stretch of the myocardium, which also stretches the jelly longitudinally. Lateral motions of the cardiac jelly due to hemodynamic forces, were consistent with the characteristics and material properties of the cardiac jelly at early developmental stages. At HH18, the cardiac jelly in the OFT is mainly composed of glycosaminoglycans,[187] which makes it very soft and easy to deform.[186] [188] Thus lateral motion of the cardiac jelly is feasible under the action of biomechanical forces. Larger cardiac jelly areas mainly correlated with a closed lumen (see Figures 6.5B-F), when blood pressure from the ventricle was low (Figure 6.6A). There was however a slight increase in cardiac jelly area when the myocardium started to relax, which might indicate lateral motion of the cardiac jelly. This motion allowed the lumen to remain closed even after myocardium relaxation started. The smallest cardiac jelly area correlated with maximal lumen expansion, when blood pressure and WSS were high (Figure 6.6A). Thus it is plausible that pressures and wall shear stresses produced some longitudinal motion of cardiac jelly mass. The large area changes exhibited by the cardiac jelly can also be partially explained by the longitudinal deformation of the OFT. Upon OFT expansion the

myocardium stretches about 20% in the longitudinal direction, cardiac jelly had to distribute along the stretched OFT length, producing a decrease in the area of the cardiac jelly at a given cross-section (which is fixed in space). OCT images revealed that this longitudinal expansion occurred approximately in phase with radial OFT expansion, and thus minimum cardiac jelly area would occur during maximal myocardium expansion and maximal cardiac jelly areas during OFT wall contraction, as shown in Figures 6.5B-F. The longitudinal stretch of the myocardium could account for about 20% variation in cardiac jelly at a given cross section, and thus could account for most of the changes in cardiac jelly observed, with lateral (axial) motion of cardiac cushions perhaps accounting for the remaining 10% change, although this is probably an overestimation, as errors in cardiac jelly area quantification can be as high as 0.005 $mm^2$ (about 50% of cardiac jelly area at distal OFT). Our results suggest that lateral motion of the cardiac cushions in response to hemodynamic forces is relatively small.

#### 6.4.2.3 Endocardium

The circumferential strain in the endocardium was larger than that in the myocardium, especially at the middle region of the OFT (Figure 6.3C). Compared to the myocardium, the lumen undergoes larger cyclic area changes (Figures 6.2A and 6.4A), attributed to the soft cardiac jelly in between the myocardium and lumen. To avoid overstretch, during maximal contraction, the endocardium folds with an irregular shape to reduce the cyclic change in its perimeter (Figure 6.1). This phenomenon has also been noticed.[189]

#### 6.4.2.4 Lumen

The OFT lumen exhibits large changes in area from complete closure to maximal wall

expansion. A large lumen area allows blood to pass through the OFT during ventricular blood ejection; while lumen closure prevents backflow during ventricular diastole. Locally (at each cross-section analyzed) the lumen was fully closed for up to 0.3T, with largest closure time found at the middle region of the OFT, L3 (Figure 6.5D). However, due to the peristaltic motion of the OFT walls, the OFT was closed for about 0.5T, consistent with the ~0.5T duration of zero blood flow in the OFT measured using Doppler Ultrasound[190] and Doppler OCT. The long closure time of the OFT lumen suggests that the OFT functions as an effective valve, which ensures sufficient ventricular filling time while preventing backflow.

The uneven distribution of cardiac jelly around the myocardium layer renders an approximately elliptical lumen shape. Over the cardiac cycle, the shape ratio of the ellipse changes (see Table 6.1), so that upon maximal wall expansion the OFT lumen resembles a circle. Elliptical shape of lumen cross-section has been shown to be more biomechanically efficient than a circular lumen cross-section both to pump blood and to achieve full lumen closure.[189] The interaction between the cardiac jelly and lumen is important for the OFT to function as an effective valve.

The mechanical behavior of the lumen reflects the interaction between blood flow dynamics and the OFT wall. The peristaltic-like active contraction of the myocardium not only lengthens the closure time of the OFT lumen to ~0.5T, but because the proximal myocardium contracted before the blood fully passed through the OFT, the OFT active wall contraction transmitted momentum to the blood flowing through the OFT, facilitating blood flow through the OFT (see Supplemental Figure 6.3). On the other

hand, blood flow within the lumen affects the behavior of the OFT wall. When blood exits the ventricle, the high pressure in the blood likely contributes to the fast expansion of the OFT wall.

### 6.4.3 Blood flow dynamics results in a non-uniform distribution of wall shear stresses in the OFT endocardium.

Our CFD model of the OFT revealed the details of the blood flow velocity profile within the OFT and the distribution of WSS. Maximum Reynolds number in the OFT (a measure of the ratio of inertial to viscous forces) was about 5, and thus blood flow inertia and the effect of OFT wall motion on blood flow within the OFT could not be completely neglected. This can be seen by comparing results obtained from CFD models in which inertial effects are fully considered, versus results obtained under 'quasi steady-state' conditions, when the wall moves but inertial effects are neglected (see Supplemental Figure 6.3). This shows that while CFD models with static geometries can estimate blood flow velocities and WSS during the ejection phase, a dynamic CFD model that accounts for heart wall motion is needed to get more precise quantifications of WSS and its changes during the cardiac cycle.

Our CFD models revealed a heterogeneous distribution of WSS in the embryonic OFT. Calculated WSS were higher at the cushion surfaces, and at the inner curvature and narrow regions (see also in Chapter 4 and Chapter 5). The distribution of high WSS correlated well in locations with shear responsive genes (e.g., KLF2 and eNOS) which preferentially expressed at high shear stress regions at the inner curvature and narrowest part of the OFT.[24]

*In vitro* studies have shown that endothelial cells can sense WSS as low as 0.1 Pa within milliseconds. [35, 36] ECs then convert mechanical stimuli into intracellular signals that affect cellular gene expression and in turn cellular functions, e.g., proliferation, apoptosis, migration, permeability and remodeling. Thus, in the embryonic heart, ECs can sense and respond to variations in WSS within the cardiac cycle. [21, 191]

Our results showed that cardiac cells in the OFT are subjected to a combinations of biomechanical stimuli (stress and strain). Further the biomechanical environment to which cells are subjected vary in time over the cardiac cycle and along the spatial location in the OFT wall. This non-uniform distribution of WSS, strains and wall stress in the OFT wall likely generate regional-specific cellular responses within the OFT, and thus could contribute to the extensive remodeling and morphogenetic events that occur later in the OFT.

## 6.5 Data supplement

*Supplemental Videos:*

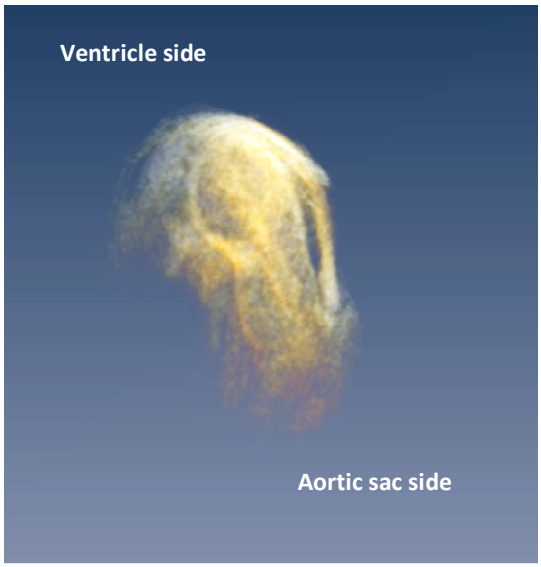


**Supplemental Video 6.1** 4D geometry of the OFT of a HH18 chick embryo, reconstructed from the 4D OCT image data.

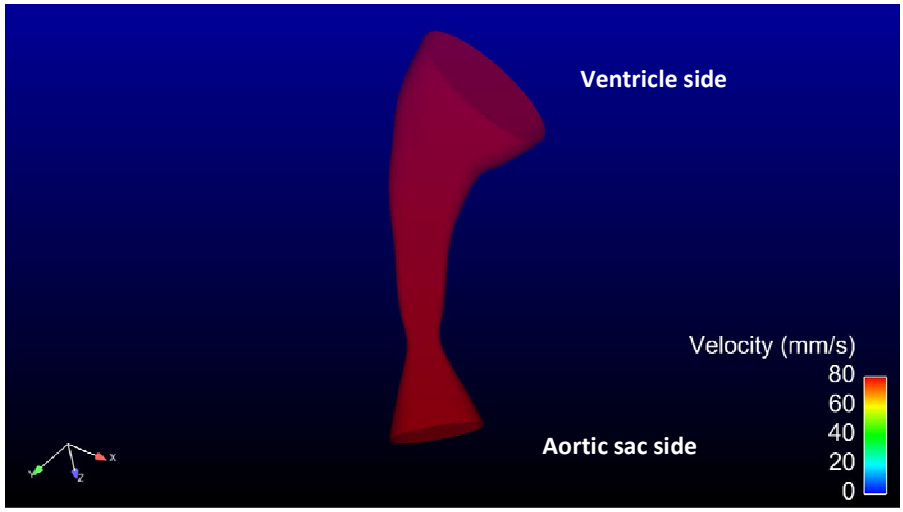


**Supplemental Video 6.2** Tempo-spatial distribution of blood flow field in the OFT of a HH18 chick embryo. The blood flow field was predicted with the 3D dynamic FE model of the OFT. For simplicity, blood flow profiles were depicted along the major axis of the elliptical cross-sections near the OFT inlet (I), middle (M), and the outlet (O).

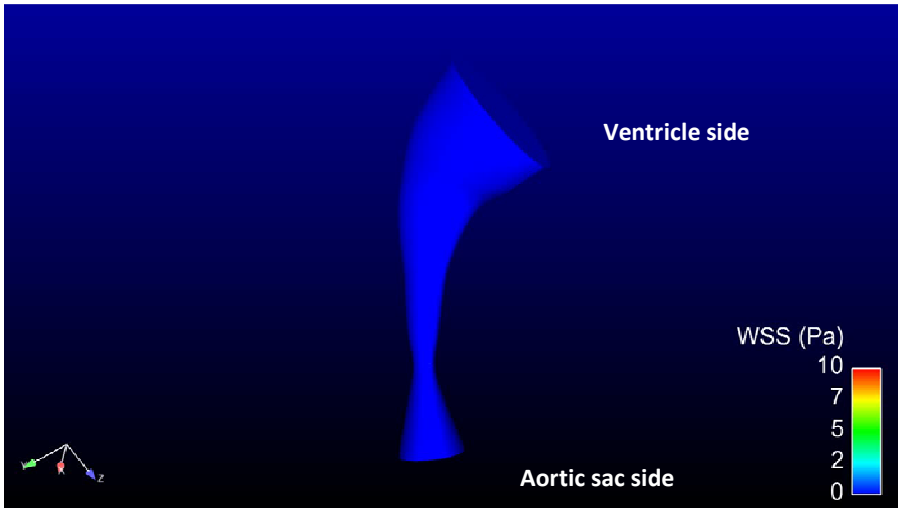


**Supplemental Video 6.3** Tempo-spatial variation of wall shear stress (WSS) on the OFT endocardium of a HH18 chick embryo. WSS was predicted with the 3D dynamic FE model of the OFT.

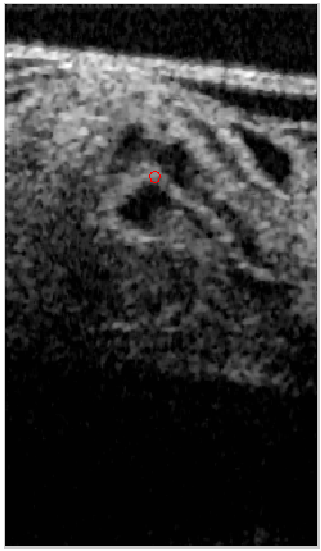

**Supplemental Video 6.4** OCT images of a OFT longitudinal section of a HH18 chick embryo. A landmark point (red point) shows the longitudinal motion of the OFT over the cardiac cycle.

**Supplemental Video 6.5** OCT images of an OFT longitudinal section of a HH18 chick embryo, showing the wave-like motion of the cardiac jelly along the OFT.

*Supplemental Figures*

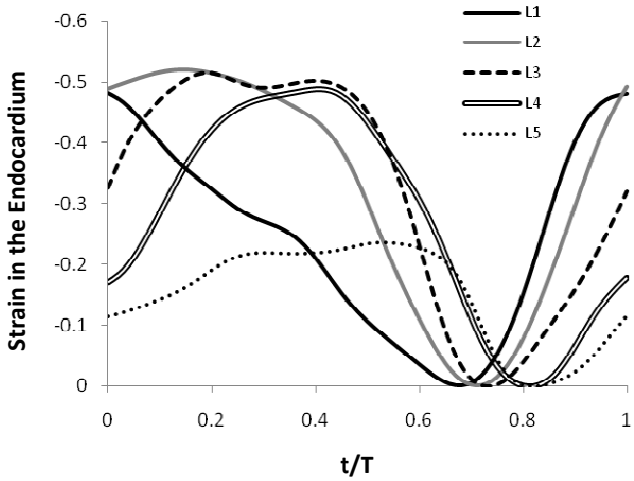


**Supplemental Figure 6.1** Temporal variation of circumferential strains in the endocardium at 5 selected OFT cross-sections.

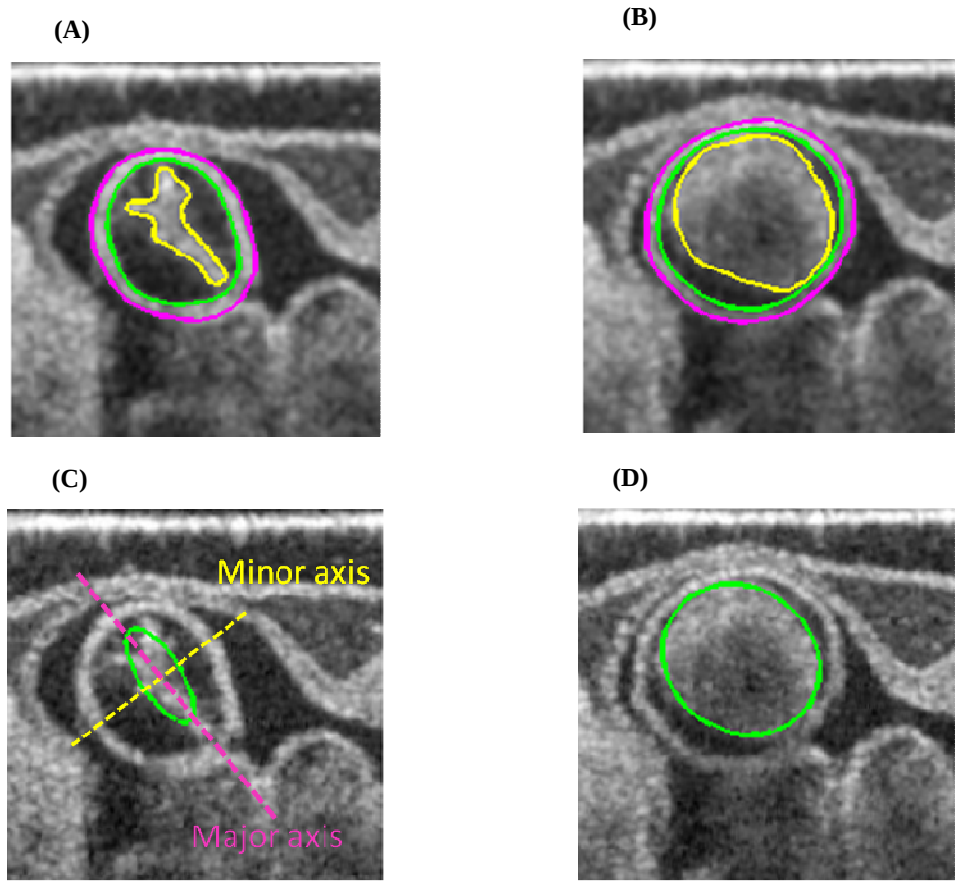


**Supplemental Figure 6.2** Illustration of image processing on OCT images of the OFT. Segmented contours of the OFT lumen (yellow), the interior boundary (green) and the exterior boundary (purple) of the myocardium are overlaid on cross-sectional OCT images, when the OFT is fully (A) contracted and (B) expanded. An elliptical model (the green curve) that fit the lumen is overlaid on the OCT images of the same OFT cross-section, when the OFT is fully (C) contracted and (D) expanded.

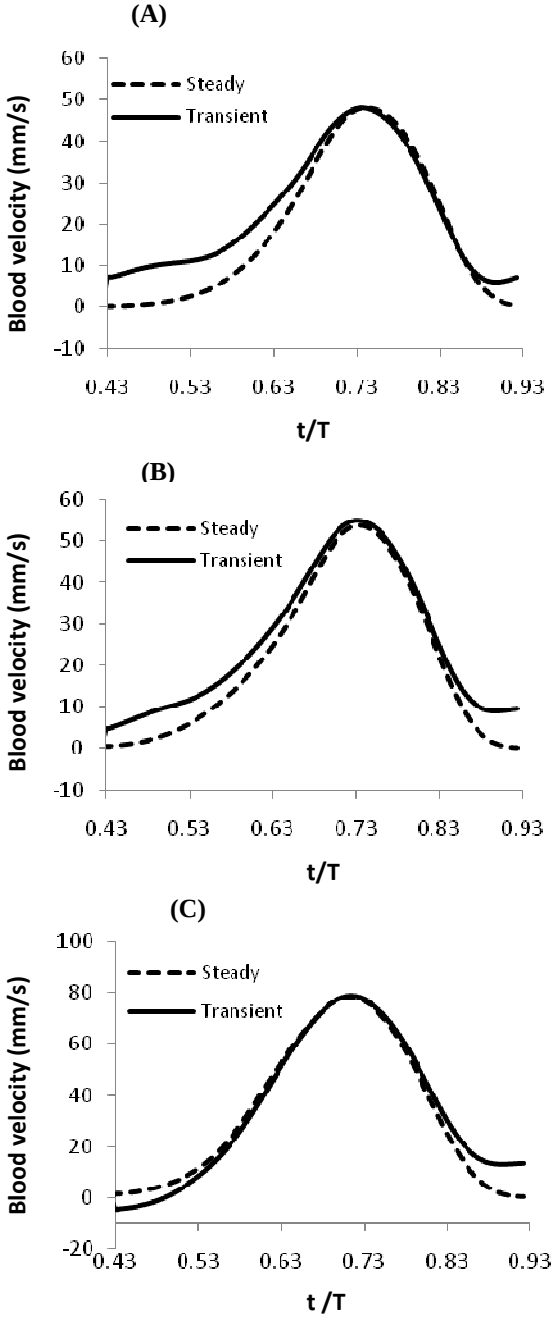


**Supplemental Figure 6.3** Comparisons of predicted centerline velocity profiles between the assumptions of a transient flow and a quasi-steady flow in FE modeling of the OFT: (A) near the inlet, (B) middle, and (C) outlet. The locations correspond to L2, L3 and L4 in image analysis,

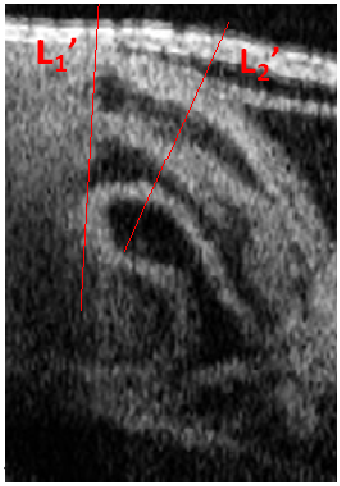


**Supplemental Figure 6.4** OCT image of a longitudinal section of the OFT, showing the locations of two cross-sections L1' and L2' to estimate the effects of longitudinal motion on image analysis. The two cross-sections are extracted from the 4D OCT image data that are perpendicular to the OFT axial centerline and move with the OFT longitudinally over the cardiac cycle.

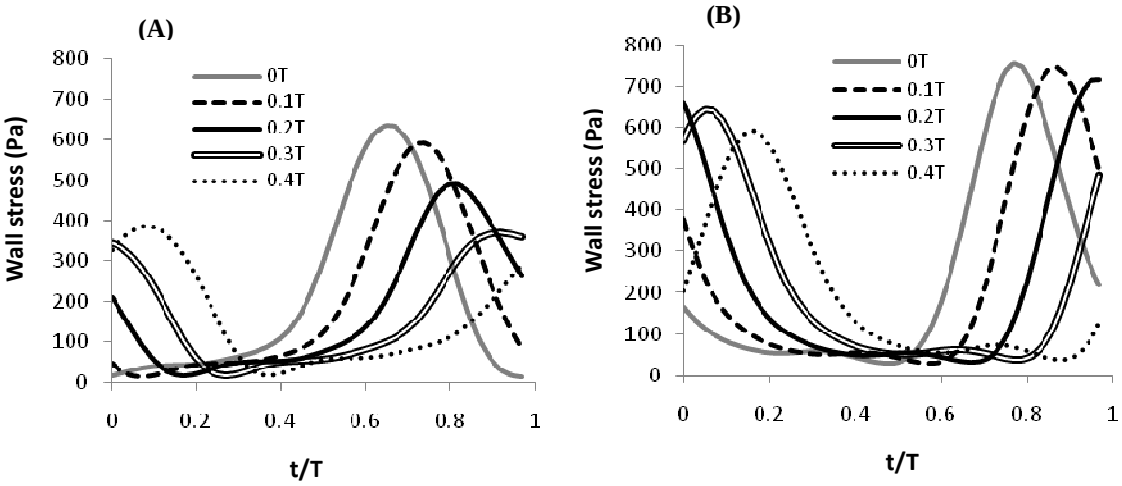


**Supplemental Figure 6.5** Effects of phase relationship between $P_V$ and R on the wall stress in the myocardium at (A) the OFT inlet and (B) the outlet. 0T, 0.1T, 0.2T, 0.3T, and 0.4T are conjectured phase lags of peak $P_V$ with respect to peak R. $P_V$, the ventricular pressure; R, effective radius of the myocardium; T, the cardiac cycle.

# Chapter 7: Changes in wall dynamics and biomechanical environment in the heart outflow tract after one hour banding in chicken embryos

## 7.1 Introduction

Cardiac development is governed by the dynamic interaction of genetic program and environmental factors. Disturbances in environmental factors may alter genetic expression and lead to congenital heart diseases. Congenital heart diseases affect about 1% live births, and are responsible for about 10% stillbirths, and possibly up to 20% of spontaneous miscarriages in the US.[136] Environmental factors include the biomechanical environment (i.e., biomechanical stresses and strains), which cardiac cells can sense and respond with a cascade of genetic pathways, regulating cellular behaviors and genetic expression.[29, 42, 47, 192, 193] Studies on animal models have shown that *in vivo* disturbances in wall dynamics or blood flow dynamics affect heart development and reproduced heart defects similar to human congenital heart diseases.[11, 14, 58, 194, 195] However, how cellular adaptations that occur in response to deviations from normal biomechanical environment affect heart development remain unclear, partly due to paucity of knowledge on the biomechanical environment which cardiac cells experience *in vivo*.

To study the roles of biomechanical factors in early heart development, we used chick embryos as the animal model, which have the advantages of fast development and easy access. At an early stage of HH18, the chick heart is a looped S-shape heart tube with five distinguishable heart segments: the sinus venosus, primitive atrium, primitive

ventricle, and outflow tract (OFT) connected in series.[50] The tubular heart has been dynamically contracting and pumping blood flow to supply embryo development.[49] The heart tube has no valves; blood flow from the ventricle to the arterial system is regulated through the cardiac cushions and dynamic wall motion of the heart OFT.[51, 171, 196] The OFT, the distal region of the heart where future semi-lunar valves develop, undergoes intensive morphogenetic remodeling.[55, 56] The morphogenesis of the OFT is sensitive to perturbations in the biomechanical environment and prone to heart defects.[11] In this thesis, we focused on the chick heart OFT to study the roles of the biomechanical environment in early heart development.

Outflow tract banding (OTB) is a surgical procedure frequently used to alter blood flow dynamics through the heart at early developmental stages.[12, 15, 59] In OTB, the OFT is tied with a suture that restricts the OFT luminal area at the banding site, increasing ventricular blood pressure and perturbing blood flow pattern within the OFT lumen.[15, 59] OTB leads to a spectrum of cardiac defects associated with the OFT, including ventricular septum defects, double outlet right ventricle, and persistent truncus arteriosus.[25] However, how OTB affect wall dynamics and hemodynamics in the OFT remain under-characterized. We focus here on biomechanical changes in the OFT wall motion and hemodynamics that occur right after OTB, before cardiac cells have time to biologically adapt to them.

Our objective in this chapter was to quantify the changes in the biomechanical environment introduced by OTB in HH18 chick embryos. Using optical coherence tomography (OCT), we acquired 4D images of the chick OFT *in vivo* and quantified the

changes in wall dynamics of the OFT over the cardiac cycle. To characterize the changes in hemodynamics in the OFT, we measured *in vivo* the ventricular pressures and blood flow patterns in the OFT. Based on the images and physiological pressure measurements, we estimated the changes in the biomechanical strains and stresses which the cardiac cells in the OFT wall are subjected to *in vivo*. Our findings allow us to understand whether and how early changes in biomechanical stimuli determine the fate of the heart.

## 7.2 Methods

### 7.2.1 Chick embryo preparation

Fertilized white Leghorn eggs were incubated at 38 ℃ and 80% humidity for approximately 72 hours to Hamilton-Hamburg (HH) stage 18 (embryo staging followed standard procedures[48]). Right before imaging or pressure measurement, a small window was opened on the egg shell and the underlying membrane was removed to expose the embryo heart. Since temperature affects cardiac function, during data acquisition the temperature of the chick embryo was maintained at $37.5 \pm 0.5$ ℃ within a warming chamber or a heat lamp using a temperature controller.

Two groups of chick embryos were studied: (1) a normal control group (n = 7) and (2) an OTB group (n = 5). For the normal control group, no further procedures were performed. For the OTB group, the stage HH18 chick embryonic hearts were tied with a 10-0 nylon suture at the OFT inlet region which partially constricted the luminal area at the banding site. Immediately after OTB, the egg shell was resealed with a parafilm and re-incubated for an hour before imaging and pressure measurement were performed.

### 7.2.2 4D imaging using OCT

We used a spectral-domain OCT customized to image the structure of the chick OFT in *ovo*.[60] The OCT system yielded an axial spatial resolution of 10 μm and a lateral spatial resolution of 16 μm. Using this system we acquired Images of 512 × 256 pixels (256 A-scans) at 140 frames per second. To capture the dynamics of the fast beating embryonic heart (typical heart rate is 2.5 Hz at HH18), we used a 4D imaging strategy and synchronization procedure to acquire and reconstruct 4D imaging data sets of the chick OFT (see details in Chapter 2). 4D image data sets of the OFT were visualized using the software Amira 5.2.2.

### 7.2.3 Image processing

To extract dynamic geometric information of the OFT from the 4D OCT images, we developed a set of image-analysis algorithms using Matlab (Mathworks, details see Chapter 3). We first segmented the lumen-wall interface of the OFT from a 3D-image dataset at a phase when the OFT was most constricted and then calculated the centerline along the axis of the OFT (details see Chapter 3). From the 4D reconstruction, we extracted 2D image sequences at 5 evenly spaced cross-sections perpendicular to the centerline near the OFT inlet, middle upstream, middle, middle downstream, and the outlet (L1-L5, see Figure 7.1). From the extracted image sequences, we delineated the boundaries of the OFT myocardium and lumen frame-by-frame during the cardiac cycle, and calculated the areas and perimeters of the OFT for further analysis.

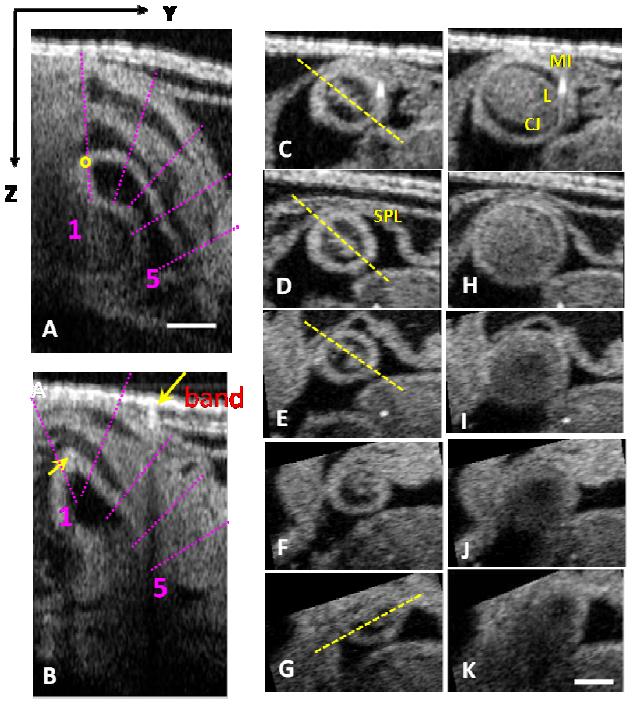


**Figure 7.1** OCT images of the heart OFT. (A) A longitudinal section of a normal OFT when the OFT is constricted, overlaid lines showing the locations where 5 cross-sections were extracted from the 4D OCT images of the OFT. (B) A longitudinal cross-section of a banded OFT, arrows showing the band. The cross-sections at locations 1-5 (C-G) at OFT maximal contracted state, and (H-L) at OFT maximal expansion state. The yellow lines in (C, D, E, and G) show the changes in the orientation of the OFT lumen along the OFT. M, myocardium; L, lumen; CJ, cardiac jelly; SPL, splanchnopleure membrane. Scar bar = 200 µm.

### 7.2.4 Metrics for geometry and wall dynamics

To quantify the OFT dynamic geometry and identify its changes due to OTB, we defined metrics based on the areas of the lumen ($A_L$) and interior of the myocardium ($A_{MI}$), calculated from the segmented contours of the myocardium and lumen. The dimensional changes were characterized by the internal radius of the myocardium$R = \sqrt{A_{MI}/\pi}$, $A_L$, and the area of cardiac jelly ($A_{CJ}$) over the cardiac cycle; $A_{CJ}$ was calculated as the difference in areas between $A_{MI}$ and $A_L$. The wall thickness of the myocardium was extracted as the difference between the exterior and interior contours of the myocardium.

To study the wall dynamics of the OFT myocardium, we defined amplitude of the wall motion ($\Delta R = R_{max} - R_{min}$), and radial velocity of the wall ($V_w$ = dR/dt). The

deformation patterns of the OFT wall were characterized with circumferential and radial strains. The radial strain in the myocardium was defined as

$$\varepsilon_r = (h - h_{max})/h_{max} \tag{7.1}$$

where h is the average thickness of myocardium at the OFT cross-section considered, calculated from images. The circumferential strain in the myocardium or endocardium was estimated by:

$$\varepsilon_\theta = (C - C_{max})/C_{max} \tag{7.2}$$

where C is the perimeter of the interior boundary of the myocardium or exterior boundary of the lumen, calculated from image segmentation. The circumferential strain rate was defined as $d\varepsilon_\theta/dt$.

To quantify the valve-like behavior of the OFT, from the extracted OFT cross-sections, we also extracted M-mode images along a line perpendicular to the slit-like lumen when the OFT is most constricted (refer to Figures 7.11 C and 7.11D). From these M-mode images, we identified and quantified the temporal durations of luminal expansion ($T_e$=$t_2$-$t_1$), contraction ($T_c$=$t_3$-$t_2$), and closure ($T_{closure}$=T-$T_e$-$T_c$), where $t_1$ is the onset of expansion defined as the point that the two sides of the lumen diverge in the M-mode image, $t_2$ is the onset of contraction defined at the maximal luminal expansion, and $t_3$ is the onset of closure defined at the point that the two sides of the lumen converge. The closures of the entire OFT were calculated from the difference in $t_3$ at positions L1 and L5.

### 7.2.5 Pressure measurement

We used a servo-null micro-pressure system (Model 5A-LN, Instrumentation for Physiology and Medicine, San Diego, CA) to measure blood pressures in normal (n = 29) and OTB (n = 6) chick embryonic hearts at HH18. Pressure measurement followed standard procedures. [165] Briefly, pressure traces were sampled at 100 Hz over at least 10 cardiac cycles in the primitive right ventricular region, which is immediately upstream the OFT. We used minimal pressures as zero pressure. Following Hu and colleagues' definitions,[138] end-systole pressure ($P_{es}$) was defined as the pressure at the maximal rate of pressure decreasing (minimal dP/dt). Here, we approximated end-diastole pressure ($P_{ed}$) with the pressure with the maximal rate of pressure increasing (maximal dP/dt).

We assumed that the OFT was a pressurized cylinder with thin wall. The circumferential wall stress $\sigma_\theta$ in the myocardium was estimated using Laplace law:

$$\sigma_\theta = PR/h \tag{7.3}$$

where P is the intracardiac pressure, R is the interior radius of the myocardium, and h is the averaged wall thickness of the cross-section considered.

### 7.2.6 Doppler ultrasound flow measurement

We used a Vevo 2100 ultrasound imaging system equipped with a MS-550S transducer (VisualSonics, Inc., Toronto, Canada) to measure the blood flow in the OFT of normal (n = 11) and banded (n = 10) chick embryos at HH18. Doppler ultrasound imaging was performed in pulsed-wave Doppler mode as previously described.[165, 197] Centerline blood flow velocity was acquired at 3 locations along the heart OFT, near the OFT inlet (the

banding site), middle, and outlet. The 3 locations were chosen roughly corresponding to positions L2, L3 and L4 in the 4D OCT images (refer to Figure 7.1). At each selected location of the OFT (inlet, middle and outlet), peak velocities were averaged over three consecutive cardiac cycles and among at least 10 chick embryos.

### 7.2.7 Statistical analysis

Image data, pressure data and velocities data were analyzed between the normal and OTB groups using Student's t-test, with statistically significance defined as a p valve <0.05. Values were represented as mean ±STD.

## 7.3 Results

### 7.3.1 Changes in OFT geometry and wall dynamics

#### 7.3.1.1 Myocardium

Compared to the normal group, the dimensions of the myocardium (both $R_{max}$ and $R_{min}$) did not change significantly, except that the minimal radius at L5 significantly reduced (Figure 7.2). The amplitude of wall motion reduced immediately after the banding site (i.e., L3, Figure 7.2). We used the maximal expansive radial velocity $V^{e}_{w\,max}$ during OFT expansion and maximal contractive radial velocity $V^{c}_{w\,max}$ during OFT contraction to characterize the dynamics of the OFT myocardium. $V^{e}_{w\,max}$ of the myocardium was not affected (Figure 7.3). $V^{c}_{w\,max}$ of the myocardium declined prior to the band (L1), whereas at and after the band, changes in $V^{c}_{w\,max}$ was not found significant.

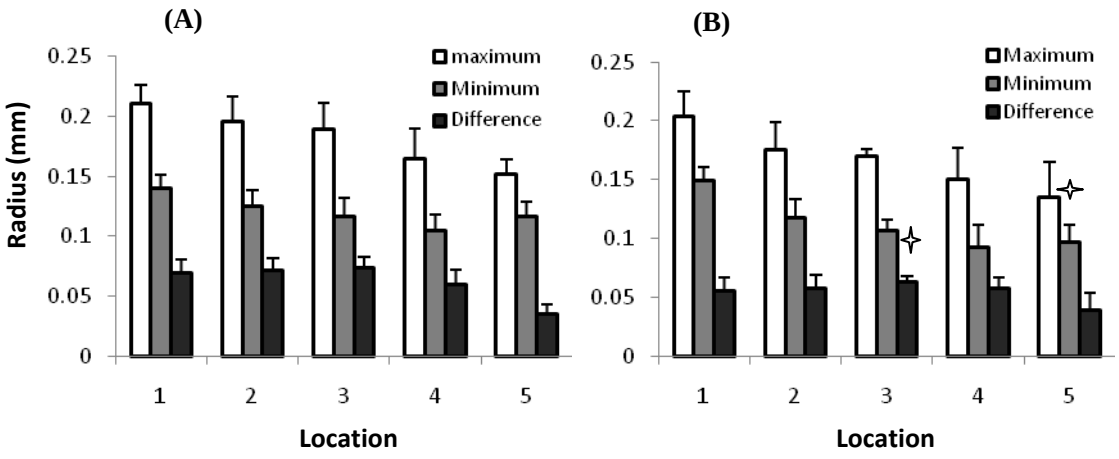


**Figure 7.2** Comparison of the maximal, minimal, and cyclic changes in the radium of the interior myocardium at the 5 selected OFT cross-sections between (A) normal and (B) OTB chick embryonic hearts. * indicates significantly different from normal ($p<0.05$).

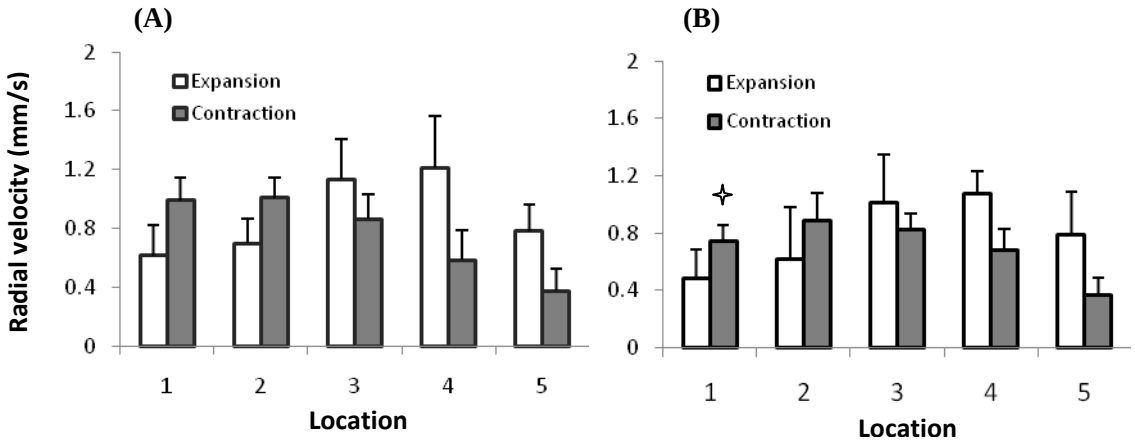


**Figure 7.3** Maximal expansion and contraction radial velocities of the myocardium at the 5 selected OFT cross-sections of (A) normal and (B) OTB chick embryonic hearts. * indicates significantly different from normal ($p<0.05$).

A noteworthy change was the peristaltic motion of the myocardium, manifested as a sequential appearance of $R_{max}$ from the OFT inlet (L1) to the outlet (L5) (see Figure 7.4A). In normal embryos, a phase lag in $R_{max}$ between the OFT inlet and outlet was estimated about 0.13T± 0.03T. Out of the five OTB chick embryos studied here, two embryos exhibited altered peristaltic motion, and among the OTB chicks, two opposite phenotypes were observed: (1) an increase in phase lag in $R_{max}$ (0.29T) and (2) a decrease

in phase lag in $R_{max}$ (0.03T) between the OFT inlet and outlet. The latter response was depicted in Figure 7.4B, showing that $R_{max}$ of the myocardium occurred almost simultaneously along the OFT.

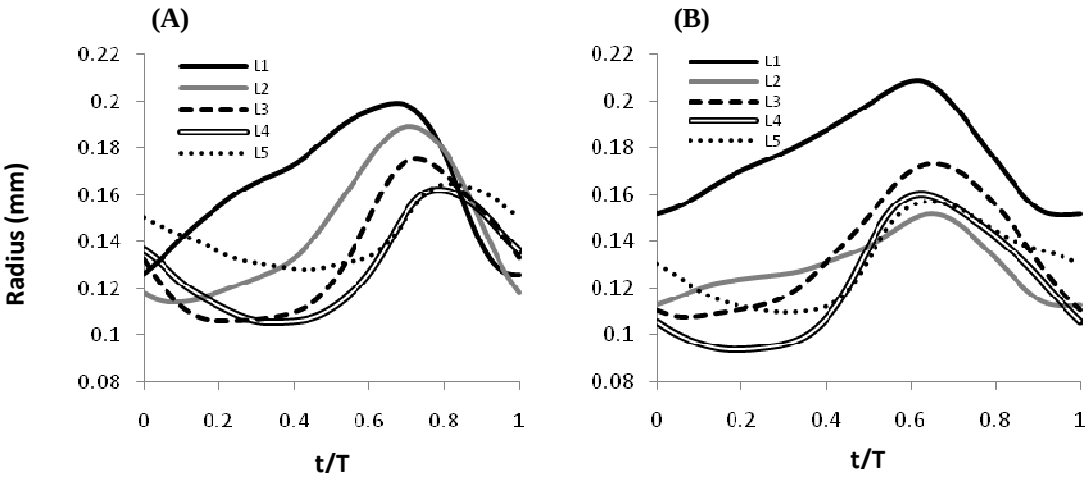


**Figure 7.4** Temporal variation of the interior radium of the OFT myocardium over a cardiac cycle at 5 selected OFT cross-sections of (A) a representative normal and (B) a typical OTB chick embryo.

### 7.3.1.2 Cardiac jelly

Similar to the control, along the OFT the OTB embryos had more cardiac jelly (maximal and minimal cardiac jelly areas in Figure 7.5) distributed proximately (L1-L2) than at the distal region; cardiac jelly reduced fast at L2 and L3, and remained almost constant at L4 and L5. Consistent with the distribution of cardiac jelly, the proximal region had the largest cyclic changes (the difference in maximal and minimal areas in Figure 7.5 and Figure 7.6). We did not find the reduction in cardiac jelly areas and the cyclic area changes due to OTB significant in any of the 5 locations of OTB embryos (Figure 7.5). In the particular OTB embryo shown in Figure 7.6, we noticed that dynamics of cardiac jelly was distinctly different from that of the normal embryo: (1) the maximal area of the cardiac jelly at L1 occurred right before maximal myocardium expansion (refer to Figure

7.4B), later in the cardiac cycle than its normal control, which occurred at initial expansion phase of the myocardium (refer to Figure 7.4A); (2) the area changes of the cardiac jelly reduced at and immediately after the band (L2-L3); (3) peristaltic occurrence of maximal jelly area along the OFT was disturbed. The changes in the dynamics of the cardiac jelly were best visualized in a longitudinal view and a frontal view simultaneously (see Supplemental Videos 7.1 and 7.2).

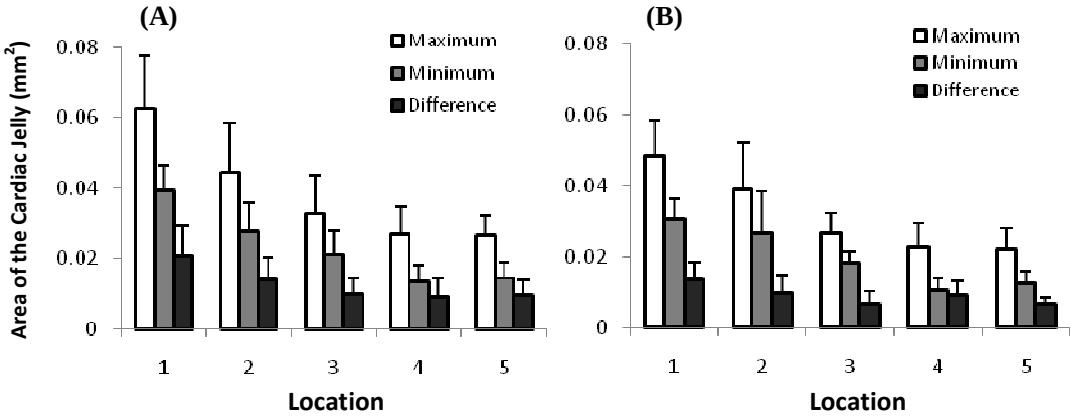


**Figure 7.5** Comparison of the maximal, minimal areas and cyclic area changes of the cardiac jelly at the 5 selected OFT cross-sections between (A) normal and (B) OTB chick embryonic hearts.

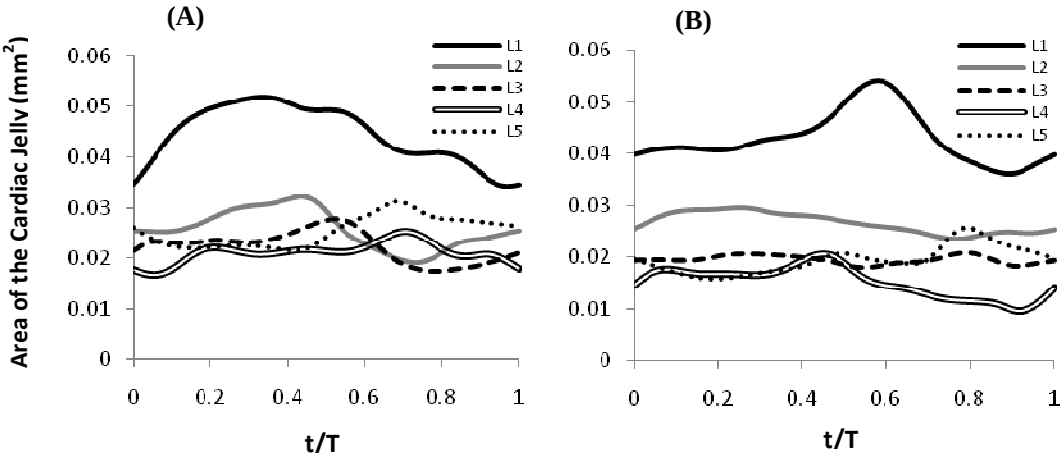


**Figure 7.6** Temporal variation in the areas of the cardiac jelly at the 5 selected OFT cross-sections of (A) a representative normal and (B) a representative OTB chick embryonic heart.

### 7.3.1.3 Lumen

The effects of OTB were apparent in luminal areas. Comparing to the control, the maximal luminal area and cyclic area change noticeably reduced at and immediately after the band (i.e., L2-L3, see Figure 7.7 and Figure 7.8). The minimal luminal area increased prior to the band (L1), whereas the minimal area at L5 was seen significantly decreased (see Figure 7.7 and Figure 7.8). The increase in minimal area at L1 was partly attributed to inability to empty the blood prior to the band due to increased afterload; detainment of blood in the OFT lumen at maximal constricted was observed in 2 out of 5 OTB chicks. The increase in minimal area at L1 was also partly attribute to the increase of endocardium area at L1 (3/5 OTB chicks), seen as more endocardial branches towards the myocardium (see Supplemental Figure 7.1). The decreases in L5 luminal areas observed in OTB was because the lumen at L5 was closed in 4 out of 5 OTB embryos, whereas in normal embryos, the lumen was not fully closed at L5 (6/7 embryos, refer to Chapter 6 Section 6.3.13).

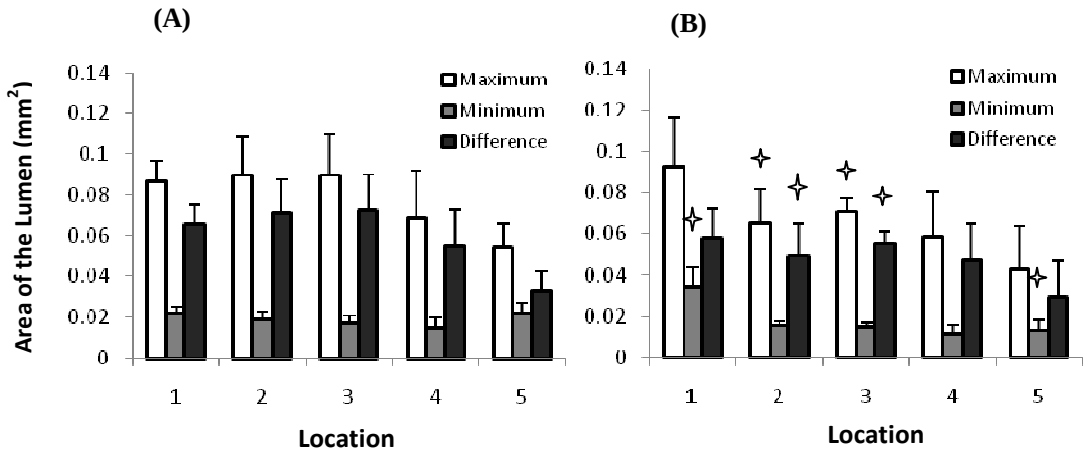


**Figure 7.7** Comparison of the areas and area changes of the lumen at the 5 selected OFT cross-sections between (A) normal and (B) OTB chick embryonic hearts. * indicates significantly different from normal ($p<0.05$).

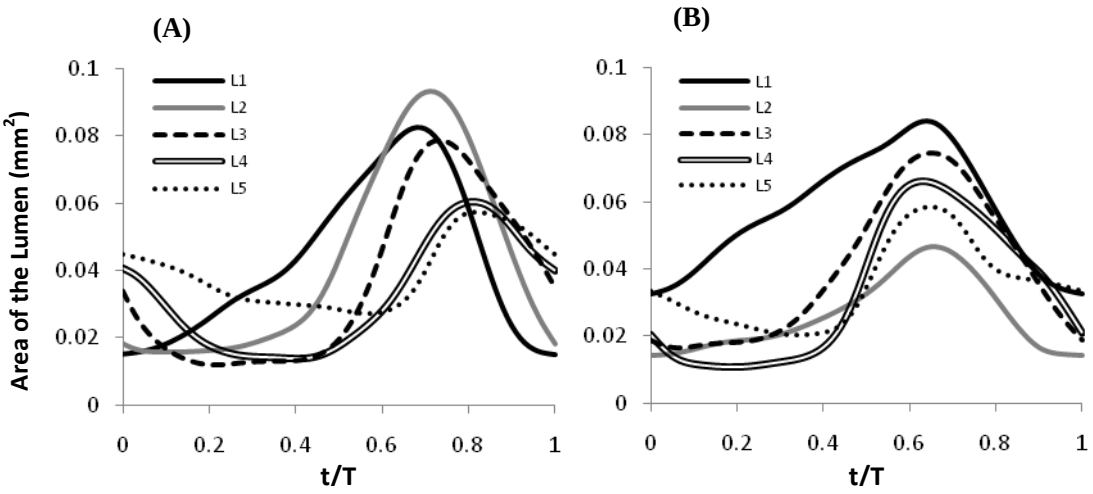


**Figure 7.8** Temporal variation of luminal areas at 5 selected OFT cross-sections of (A) a representative normal and (B) a representative OTB chick embryonic heart.

To reveal time spans for luminal expansion ($T_e$), closing ($T_c$), and closure ($T_{closure}$) within the cardiac cycle, we analyzed M-mode images at the 5 selected OFT cross-sections (see Figures 7.9C and 7.9D). In OTB embryos, $T_e$ and $T_c$ had an opposite trend with $T_e$ gradually decreasing and $T_c$ increasing towards distal OFT, similar as normal embryos (Figures 7.9A and 7.9B). In addition, we found that $T_e$ at L4 and $T_c$ at L5 significantly reduced and that $T_{closure}$ at L2, L4 and L5 significantly increased in the OTB embryos. However, the closure time of the entire OFT remained unchanged.

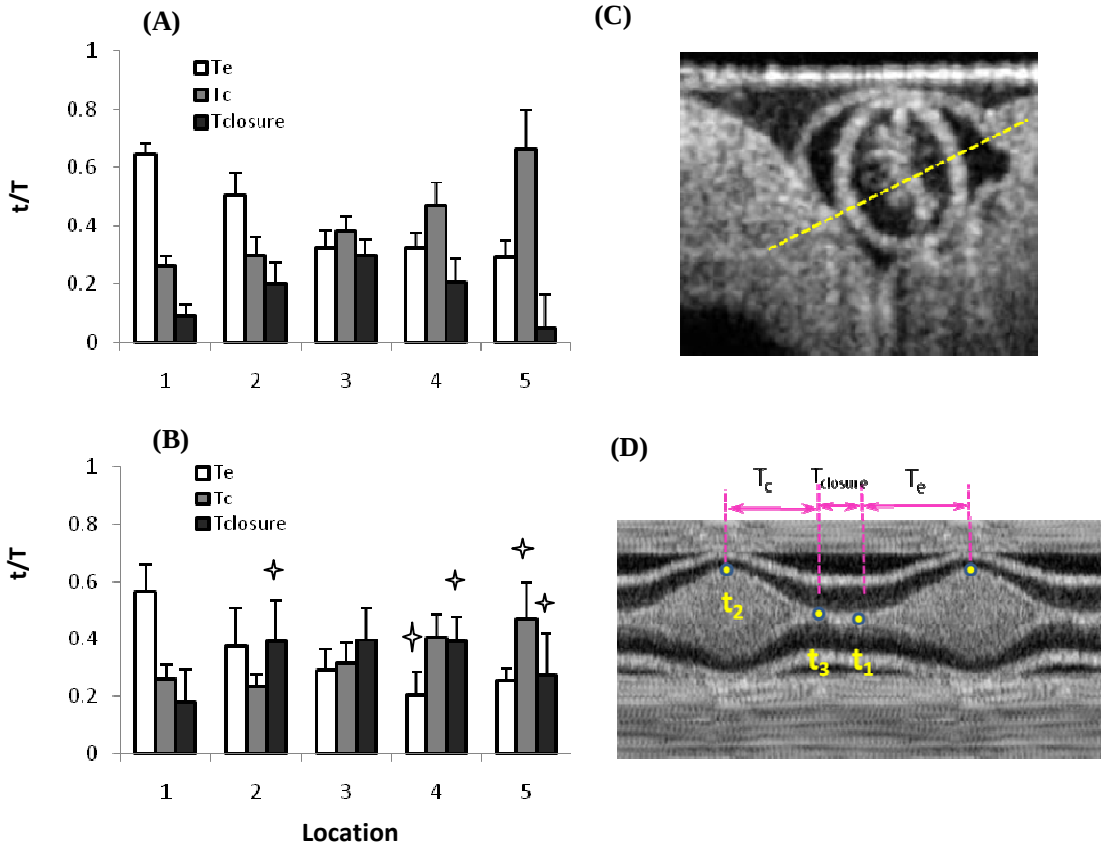


**Figure 7.9** Temporal behaviors of the lumen at the 5 selected OFT cross-sections of (A) normal and (B) OTB chick embryonic hearts. (C) A cross-sectional OCT image and (D) an M-mode OCT image extracted from the yellow line in (C) to illustrate the metrics for temporal behaviors of the lumen. $T_e$, time span for luminal expansion; $T_c$, time span for luminal closing, and $T_{closure}$, time span for luminal closure. * indicates significantly different from normal ($p<0.05$).

### 7.3.2 Changes in circumferential and radial strains

Figure 7.10 compares temporal variations of circumferential strains in the myocardium as well as the endocardium at the 5 selected OFT cross-sections in a normal embryo and an OTB embryo (the same embryo in Figures 7.4B, 7.6B, and 7.8B). The circumferential strain was estimated using Eq. 7.2, which used the maximal expansion of the OFT as the reference (zero strain), thus the circumferential strains were compressive (negative values) and reflected the contraction of the myocardium.

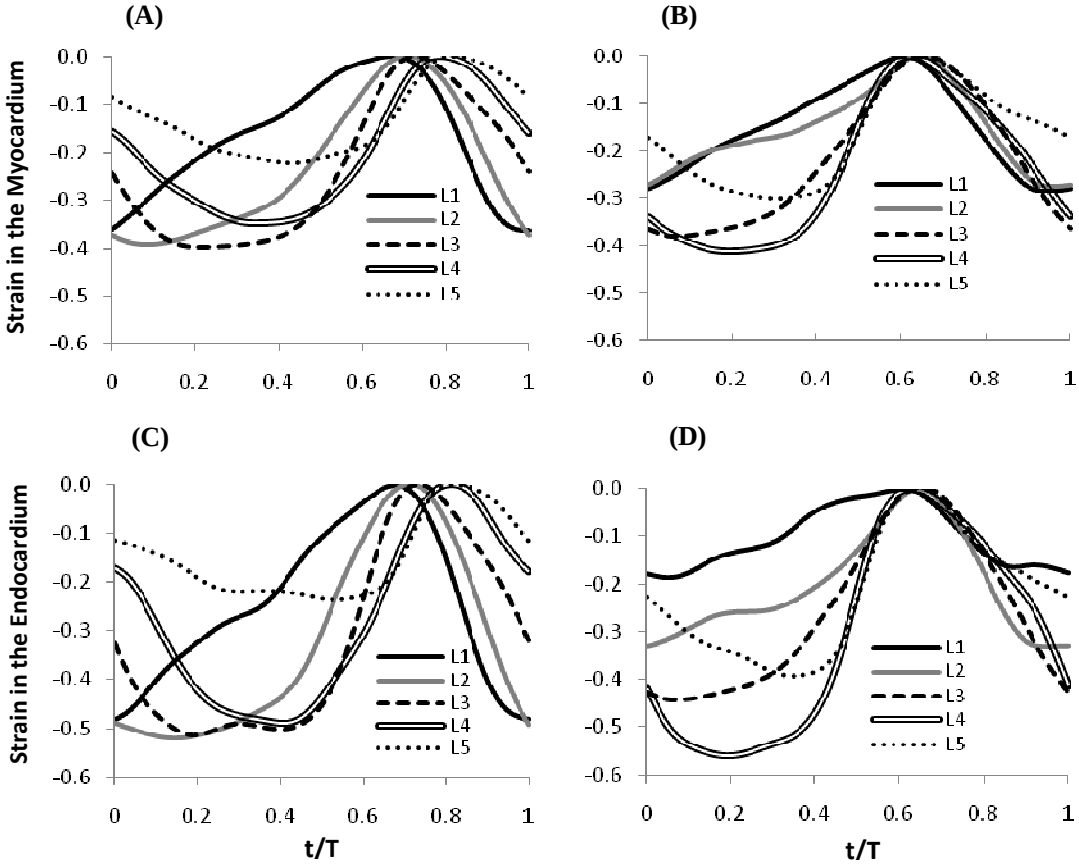


**Figure 7.10** Temporal variations of circumferential strains at the 5 selected OFT cross-sections in a representative normal and an OTB chick embryonic hearts. Circumferential strain in the myocardium: (A) normal and (B) OTB; circumferential strain in the endocardium: (C) normal and (D) OTB.

Similar to the normal embryo, circumferential strains in the myocardium of OTB embryo varied markedly over the cardiac cycle and along the OFT, following a similar temporal variation as the areas of the myocardium (refer to Figure 7.4). The largest compressive circumferential strain occurred at the maximal contraction of the OFT. The circumferential strain in the endocardium was larger than that in the myocardium at corresponding locations (see Figures 7.10 and 7.11). Compared to the control, the circumferential strain significantly decreased in the myocardium and the endocardium prior to the band at L1 in OTB embryos (see Figures 7.11). The contractive

circumferential strain rate decreased prior to the band at L1 and noticeable increased after the band at L4, whereas the changes in expansive strain rate were not found significant after one hour of banding (Figure 7.12).

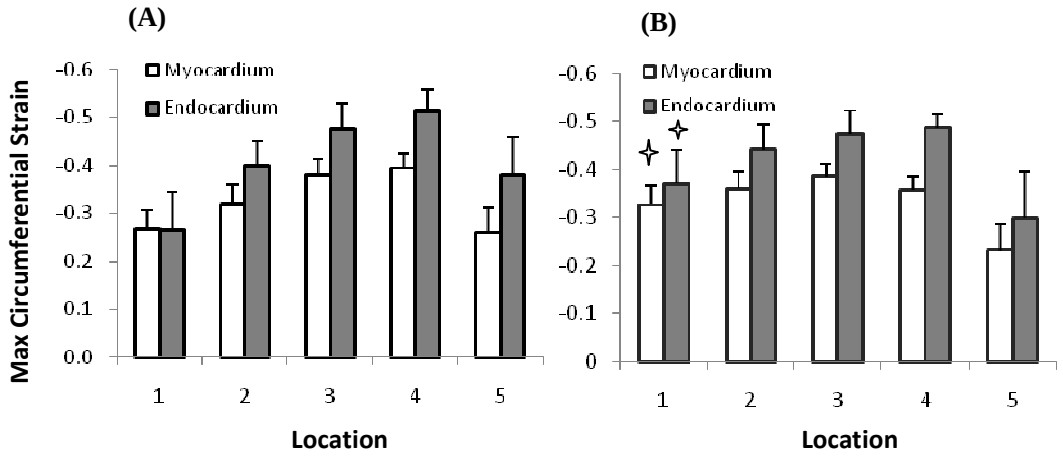


**Figure 7.11** Peak circumferential strains in the myocardium and the endocardium over a cardiac cycle at the 5 selected OFT cross-sections of (A) normal and (B) OTB chick embryonic hearts. * indicates significantly different from normal ($p<0.05$).

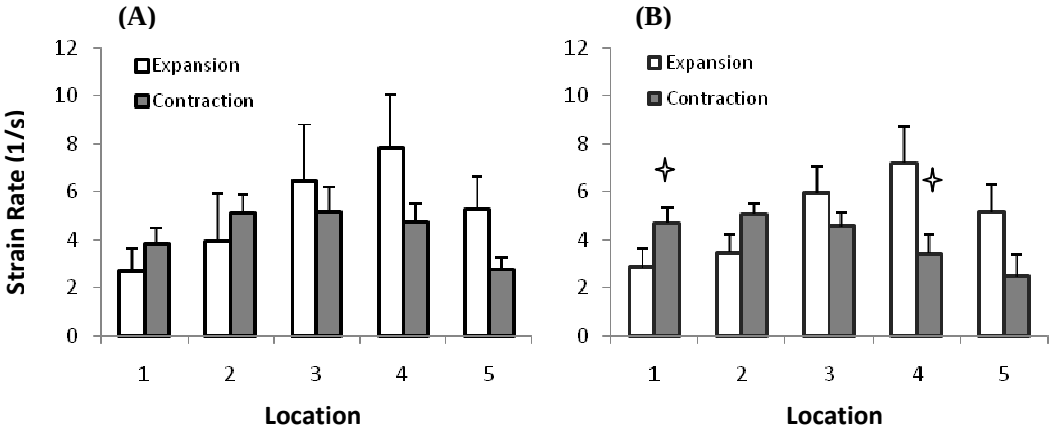


**Figure 7.12** Peak expansive and contractive circumferential strain rates in the myocardium over a cardiac cycle at the 5 selected OFT cross-sections of (A) normal and (B) OTB chick embryonic hearts. * indicates significantly different from normal ($p<0.05$).

To analyze changes in wall thickness of the myocardium during the cardiac cycle, radial strains at the 5 cross-sections were analyzed over the cardiac cycle from the OCT images of representative normal and OTB embryos (Figure 7.13). At each cross-section, the radial strain was the averaged strain over the cross-section; the local variations in radial stain over the cross-section were not reported. The spatial pattern of radial strain along the OFT was distinctly different between normal and OTB embryos. Here we used the peak radial strain to demonstrate the spatial variation in radial strain. In normal embryo, the peak radial strain had the maximum at the OFT inlet (L1), reduced to the minimum at the middle (L3), and increased again towards the OFT outlet. In the OTB embryo, the radial strain reduced prior and at the band (L1-L2) with a 50% reduction at the banding site (L2), whereas, immediately after the band (L3), the peak radial strain increased. Consequently, the OTB embryo had the largest peak radial strain at the middle region (L3) and the minimal peak strain at the band (L2).

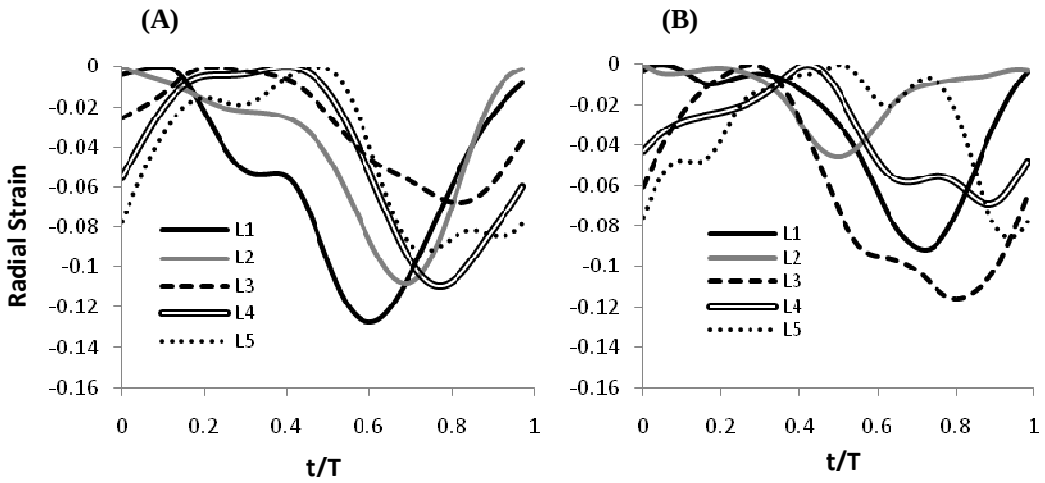


**Figure 7.13** Comparison of radial strain in the myocardium between normal and OTB embryos. Time variations of the radial strains in (A) a representative normal and (B) a representative OTB embryo at the 5 selected locations along the OFT (L1-L5) over a cardiac cycle.

### 7.3. 3 Changes in ventricular pressures

Ventricular pressures were compared between normal (n = 29) and OTB (n = 6) embryos with representative ventricular pressure traces depicted in Figure 7.14. Although the shape of ventricular pressure of the OTB chick was similar as that of the control, the ventricular pressure increased in OTB chick embryos after one hour of banding, consistent with the statement that one of rapid compensatory responses to OTB is an increase in ventricular pressure.[15] The peak systolic pressure, end-diastolic pressure, and maximal rate of ventricular pressure change (maximal dP/dt and minimal dP/dt) were compared between normal and OTB embryo groups (in Table 7.1). The peak systolic and end diastolic pressures were significantly higher than those of normal embryos, consistent with the trend reported in HH21 OTB embryos.[15, 59, 80] Pressure changes did not found significantly increased in the OTB embryos.

**Table 7.1** Comparison of ventricular pressures in normal and OTB HH18 chicken embryos

| | Control (n=20) | OTB (n=5) |
|---|---|---|
| $P_{PS}$ (mmHg) | 1.47(0.28) | 2.30(0.66)* |
| $P_{ED}$ (mmHg) | 0.72(0.23) | 1.19(0.39)* |
| max (dP/dt) (mmHg/s) | 15.2(4.7) | 25.6(12.8) |
| min (dP/dt) (mmHg/s) | 14.4(3.9) | 26.3(15.6) |

Data are presented as mean (standard deviation). * indicates significantly different from normal ($p<0.05$). $P_{ED}$; end diastolic pressure. $P_{PS}$, peak systolic pressure; Pressure measurement was performed by Aaron Troyer.

### 7.3.4 Changes in the wall stress in the myocardium

The wall stress in the myocardium was estimated over a cardiac cycle near the OFT inlet (L1, prior to the band) using Laplace law (Eq. 7.3). Both the wall thickness and internal radius of the myocardium were estimated from representative normal and OTB embryos (see Figure 7.14). We used representative ventricular pressures to approximate the pressures at the OFT inlet, and we assumed the phase relations between the pressure and geometry did not change in OTB embryos. Similar to the normal embryo, the wall stress in the myocardium at the OFT inlet varied markedly over the cardiac cycle with the minimum occurring during myocardium relaxation and maximal during myocardium contraction slightly before peak pressure (Figure 7.14). Both the peak wall stress (883 Pa OTB versus 436 Pa Control) and end-diastole wall stress (598 Pa OTB versus 367 Pa control) dramatically increased in the OTB embryo.

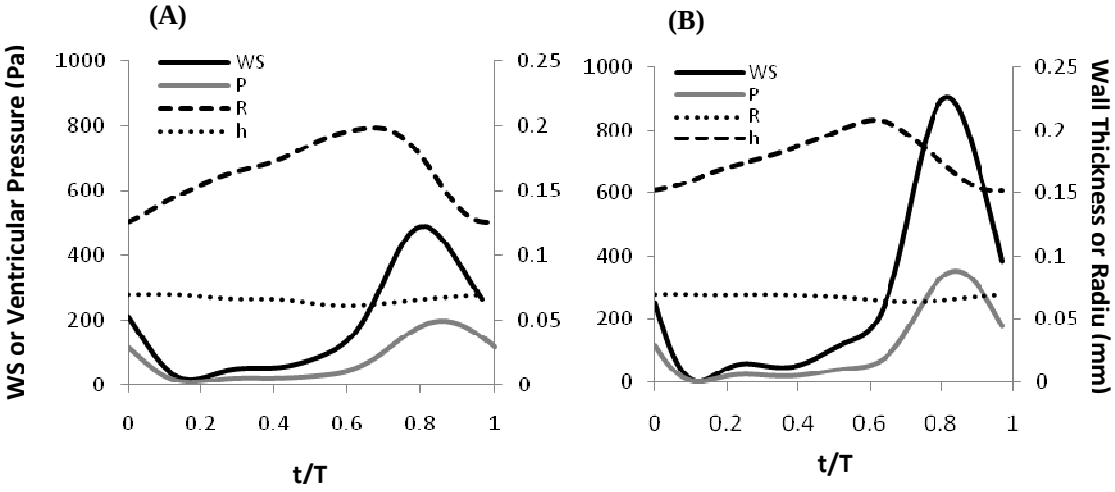


**Figure 7.14** Comparison of wall stress in the myocardium between normal and OTB chick embryos. Time variations of the wall stress (WS), ventricular pressure (P), wall thickness (h), and internal radium of the myocardium in: (A) a representative normal embryo and (B) a representative OTB embryo near the OFT inlet (prior to the band) over a cardiac cycle.

### 7.3.5 Changes in blood flow dynamics

We measured centerline velocities at the OFT inlet, middle, and outlet (approximately corresponding to positions L2, L3 and L4 in Figure 7.1, L2 is closest to the band) in normal and OTB embryos using Doppler ultrasound (Figure 7.15). We found that OTB affected blood flow differently along the OFT. The salient feature of blood flow in the OTB embryos was a dramatic increase of blood velocity at the banding site (~4 fold) than the normal control. Blood velocity after the band was higher than the control and recovered to normal near the OFT outlet.

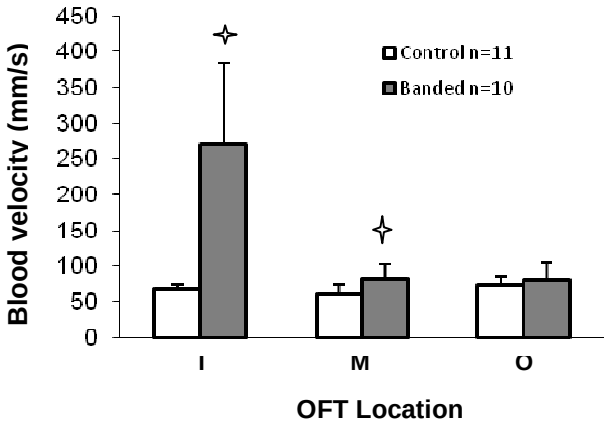


**Figure 7.15** Comparison of peak velocities near the OFT inlet, middle and outlet between normal and banded chick embryos.* indicates significantly different from normal ($p<0.05$). Doppler flow measurement was performed by Andrew Nickerson.

Besides large changes in magnitude, OTB also altered temporal features of the centerline velocity profiles along the OFT (Figure 7.16). Comparing to centerline velocities at corresponding locations between normal and OTB embryos, we noticed that (1) across the band, centerline blood velocity rose much sharply to the peak flow and immediately after the peak followed a transient backflow, rather than a shoulder as observed in normal embryos; (2) at the OFT middle region, more embryos showed

backflow before the peak velocity (5/10 OTB versus 1/11 Control); (3) near the OFT outlet, few embryos showed backflow before the peak (4/10 OTB versus 9/11 Control), and the shoulder after the peak reduced in magnitude and duration.

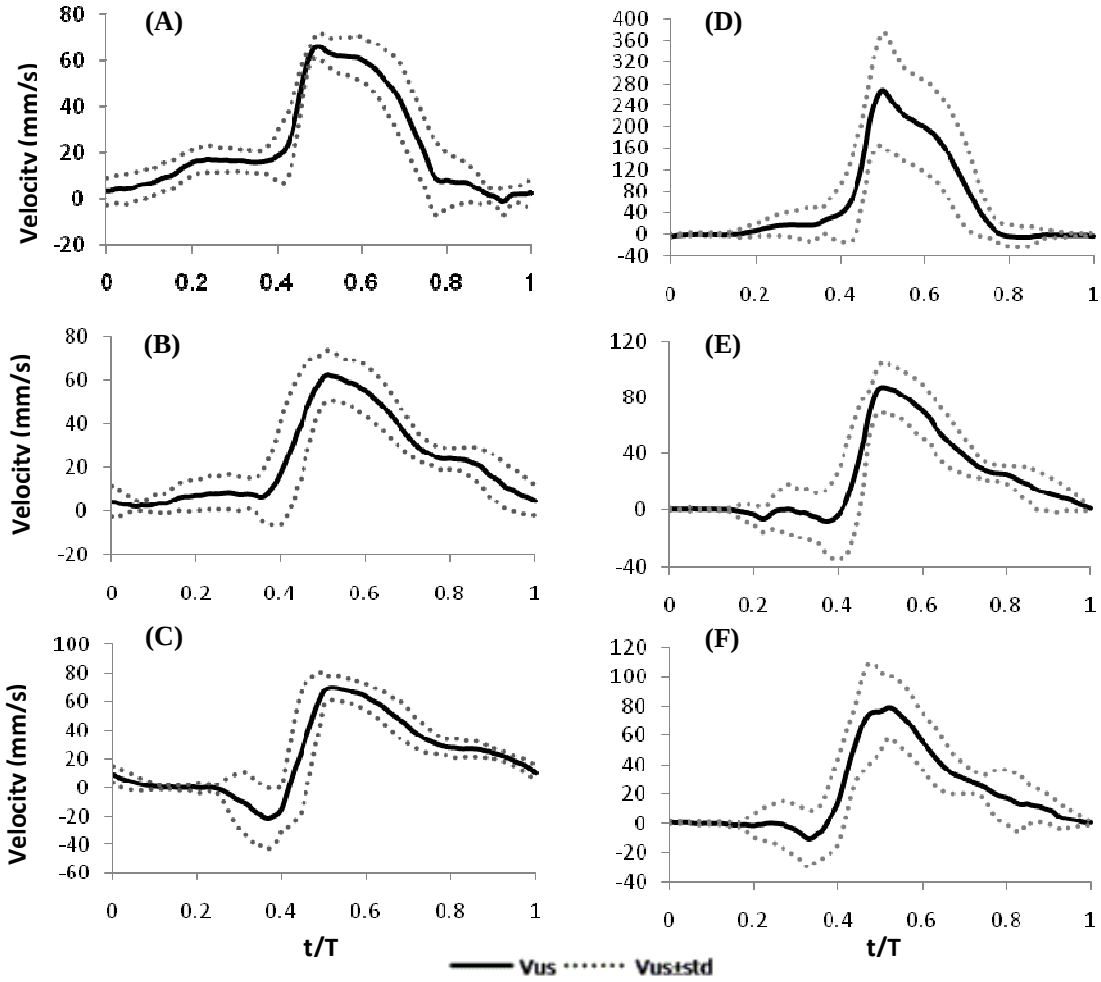


**Figure 7.16** Comparison of centerline velocities near the OFT inlet (I), middle (M), and outlet (O) between: (A-C) normal and (D-E) OTB chick embryos measured with Doppler Ultrasound. Note that the velocities were acquired sequentially at different OFT regions and were not synchronized in a normalized cardiac cycle. Vus, mean velocity measured using Doppler ultrasound; Vus±std, velocity varied with a standard deviation. Doppler flow measurement was performed by Andrew Nickerson.

## 7.4 Discussion

OTB is a useful model to study the changes in the biomechanical environment that may lead to heart malformations associated with the OFT region.[12, 25] We focused here on the effects of OTB on the mechanical behavior of the OFT wall and hemodynamics in the heart OFT of HH18 chick embryos. In the OTB group, the band partially occluded the OFT lumen, resulting about 60% constriction at the banding site. Ventricular pressures increased dramatically as soon as 1 hour after banding (see Figure 7.14 and Table 7.1). Both the physical constriction of the band and the increase in the ventricular pressure influence the behaviors of the OFT and hemodynamics. Because we imaged the OFT 1 hour after performing the OTB procedure, we expect that changes in OFT behaviors were mainly due to mechanical adaptations of the chick cardiovascular system to OTB, and not remodeling of the cardiovascular system, which would probably require more time to happen.

### 7.4.1 Study limitations

The variations in the results were mainly from three sources: 1) biological variations of the embryos, 2) variations in experimental procedures (OTB), and 3) limitations of the methods that we used to explore the biomechanical environment in living embryonic hearts, including imaging and image analysis procedures, pressure and flow measurement, and those simplifications made in calculating stresses and strains. Limitations and sources of errors in the methods should be noted when interpreting our data.

We have discussed errors associated with blood pressure measurements and Doppler

ultrasound flow measurements, which involve the uncertainties in the placement of the pressure probe in the embryonic heart and in the estimation of the Doppler angle in Chapter 5. We have discussed the errors resulting from the imaging and image analysis (image reconstruction and segmentation) in Chapter 6. We have also shown that the longitudinal motion of the OFT in the normal embryos compounds the comparison near the OFT inlet. Image reconstruction resulted in a phase error of 0.04 ± 0.02T. The segmentation procedure on the OCT images resulted in errors of about 0.002 $mm^2$, 0.0025 $mm^2$, and 0.005 $mm^2$ in the estimated areas for the interior myocardium, lumen, and cardiac jelly, respectively. Further, the segmentation resulted in an error of 0.02-0.04 in estimating the peak circumferential strain.

Another major limitation in methods was that we could not perform imaging, pressure and Doppler flow measurements simultaneously and within the same embryo, due to technical difficulties. The uncertainties would directly affect the calculation of the wall stress in the myocardium, which is a function of the pressure, inner radius and wall thickness of the myocardium according to Laplace law. We estimated the phase relationships between the ventricular pressure, OFT geometry, and blood flow within the OFT in normal chick embryos.[173] We then assumed that the phase relationships did not change in OTB embryos. Although we consider that the estimated phase relations are a good approximation for normal embryos, it is likely that the phase relationships between the pressure and wall motion change in response to OTB. To estimate the effects of phase relations on wall stress, we calculated wall stresses at different phase relationships (see Supplemental Figure 7.2). We found that despite the values of wall stress change with phase relations, the general trend in wall stress between the normal and OTB remains the

same.

The simplifications made in the definition of the strains and stresses are also worthy of noticing when comparing to other relevant work. In this thesis, we adopted the simplest form of strain definition, engineering strain, to estimate the averaged deformation over a cross-section. Therefore, we were not able to detect the local strain variations over the cross-section. In addition, we neglected the residue strain generated by differential growth.[175] The simplest form of strain provides us insight into the changes in deformation pattern along the OFT wall in OTB embryos with respect to normal embryos over the cardiac cycle.

We used Laplace law to estimate the averaged wall stress in the myocardium under a assumption that is $h/R<0.1$ with h denoting the wall thickness and r the internal radius of the myocardium. However, the OFT has an h/R ratio about 0.3-0.5. The violation of thin wall assumption means that the regional gradient of wall stress across the wall thickness is not negligible. The transmural distribution of wall stress may be important for remodeling of the myocardium, and will be interesting to study in our future work. In this thesis, the averaged wall stresses provides us insight on how markedly large changes in wall stress in the myocardium over a cardiac cycle as well as between the normal and OTB embryos.

### 7.4.2 Changes in wall dynamics

#### 7.4.2.1 Myocardium

After one hour banding, we did not observe significant changes in the dimension of the myocardium with respective to normal HH18 chick embryos, except that the minimal

radius at L5 significantly decreased (Figure 7.2). The band exerted physical constraint on the wall motion near the band (i.e., L1-L3 in Figure. 7.2); the amplitude of wall motion significantly reduced distal to the band at L3. Prior to the band at L1, the contractive radial velocity reduced (Figure 7.3), suggesting that the contractility of the myocardium was compromised prior to the band. Interestingly, we did not observed any significant changes at L2 (closest to the band) due to large variations resulting from difficulties in controlling exact locations and tightness of the band.

A most noticeable change was the motion pattern along the OFT. From the OTB embryo depicted in Figure 7.4, the entire wall opens almost simultaneously, distinct from the normal embryos. The changes in wall motion pattern affect the luminal area changes (Figure 7.8) and thus the blood flow pattern in the lumen, [163] as well as the cyclic circumferential strain over the cardiac cycle (Figures 7.10). Among other OTB embryos, another phenotype of wall motion was also observed such that the OFT exhibited a slower peristaltic motion than normal embryos (refer to Supplemental Figure 7.3). We cannot explain the diverse behaviors in wall motion in OTB embryos with such a limited sample size and the methodology used in this study. The motion pattern may be affected by a lot of factors including the conductance velocity of the electric impulse along the OFT wall, material properties of the myocardium, and the dynamic interaction between the wall and blood flow in the lumen. The different responses observed in this study may be associated with variations in the degree of tightness and placement of the band. More studies based on a large number of OTB embryos with a grade of tightness and locations, combined with investigation on responses at the cellular and molecular level, are necessary to understand the roles of biomechanical factors on motion patterns of the

myocardium. Collectively, our findings suggest that the motion pattern of the OFT myocardium is susceptible to changes and that the changes of the OFT motion pattern is a fast and sensitive adaptive mechanism to altered pressure loads and/or external constraints (e.g., the band). The wall motion pattern may be potentially a good and sensitive index for evaluating the OFT functionality.

#### 7.4.2.2 Cardiac jelly

In the OTB embryos, we did not observe significant changes in cardiac jelly areas (Figure 7.5). However, the motion dynamics of the cardiac jelly apparently changed over time and along the OFT (Figure 7.6, also see Supplemental Videos 7.1 and 7.2). Cyclic changes in cardiac jelly were presumably affected by three factors: (1) biomechanical forces exerted by the blood flow and contraction of the myocardium; (2) the physical constraint of the band; and (3) the longitudinal stretching of the OFT wall. At early stages (i.e., HH18), the major component of cardiac jelly is glycosaminoglycans,[187] which is very soft and easy to deform like a viscoelastic material.[186, 188] The biomechanical forces such as the blood pressure in the OFT lumen and contraction forces from the myocardium may induce local lateral motion of the cardiac jelly along the OFT. We found a temporal correlation among the area changes in the cardiac jelly, the lumen, and the myocardium. The area of the cardiac jelly was larger when the OFT lumen was closed (low blood pressure) and the myocardium was relaxed (low contraction force); and the area of the cardiac jelly became smaller during the maximal expansion of the OFT lumen (large blood pressure) and fast contraction of the myocardium (large contraction force, refer to Supplemental Figure 7.4). In the OTB embryos, both the physical band and changes in

biomechanical forces, including increased blood pressures (Figure 7.14 and Table 7.1) and altered myocardium contraction (Figure 7.4), may affect the lateral motion of the cardiac jelly and thus the cyclic changes in the cardiac jelly. In addition, when the OFT expanded circumferentially, the OFT stretched longitudinal towards the ventricle. As a result, the area of cardiac jelly reduced at any given cross-section, seen as thinning of cardiac jelly layer (see examples in Figures 7.1 D and 7.1I). In the OTB embryos, however, longitudinal deformation of the OFT was restricted (refer to Supplemental Videos 7.1 and 7.2), which may also contribute to the dynamic changes in the cardiac jelly. To further understand the mechanical factors responsible for dynamics motion of the cardiac jelly, a biomechanical model of the OFT that incorporates the dynamic motions of the three-layered OFT wall and fluid-structure interaction is necessary to identify the roles of the OFT longitudinal deformation and biomechanical forces imposed on the cardiac jelly.

#### 7.4.2.3 Lumen

The effects of OTB on the OFT lumen behaviors were apparently different prior to and after the band along the OFT (Figure 7.7). Prior to the band (L1), the minimal area increased, which is a sign of dilation due to blood detainment in some embryos. Chronic OTB is known to induce mild and moderate ventricular dilation (prior to the band) after 24 hour banding.[25] The minimal area at L5 reduced mainly as a result of increasing contractility of the myocardium at distal OFT (refer to the discussion in Section 7.4.3.1). The maximal luminal area and cyclic area change significantly reduced at and immediately after the band due to the physical constraint of the band (L2 and L3 in

Figure 7.7).

Noticeably, the closure time of the lumen increased particular at and after the band, as a result of reduced blood filling time ($T_e$) or myocardium contraction time ($T_c$) (see Figures 7.9A and 7.9B). The increase in luminal closure time ($T_{closure}$) ensures the entire OFT to close up to 0.5T, which may be a compensatory response to the changes in the peristaltic motion of the myocardium or cardiac jelly motion.

### 7.4.3 Changes in the biomechanical environment

#### 7.4.3.1 Strains in the myocardium and endocardium

After one hour of OTB, circumferential strains in the myocardium and the endocardium significantly reduced prior to the band at L1 (Figure 7.11). The observations of an increase in minimal area of the lumen (Figure 7.7) and a decrease in circumferential contractive strain rate at L1 (Figure 7.12) suggest that the reduction in the circumferential strain is mainly due to a reduction in contractility of the OFT myocardium prior to the band. In contrast, the contractive strain rate increased away from the band at L4 (Figure 7.12), suggesting an increase in myocardium contractility after the band. There were no obvious changes in the expansive strain rate (Figure 7.12), which suggest passive material properties of the myocardium do not change as an acute response to increased blood pressures. An increase in the myocardium stiffness was reported 24 hours after OTB. [16, 198]

Because the myocardium is non-compressible, both the circumferential stretch and longitudinal stretch change the wall thickness of the myocardium. The radial strain is an indicator of this cyclic change in wall thickness. The longitudinal stretch of the OFT

myocardium reduced to 0.07 (about 50% less than normal embryos[180]), estimated from a typical OTB embryo; the circumferential stretch was also constrained near the band (L1-L3). The combined effects resulted in a general reduction in radial strain in the OFT wall in the OTB embryo (Figure 7.13). We also noticed a change in radial strain pattern along the OFT. The radial strain reduced prior and at the band (L1 and L2), and increased immediately after the band at L3 (Figure 7.13). Since the trend was observed in a typical OTB embryo, more embryos need to be studied in order to confirm the spatial variation of the radial strain in the myocardium.

#### 7.4.3.2 Wall stress in the myocardium

OTB is an often used model to study the effects of increased afterload on the morphologic changes and growth of the ventricle, and an increased (end-systolic) wall stress in the ventricular myocardium has been correlated with an enhanced maturation in ventricular myocardium.[15] However, no study has been carried out to show the changes in the wall stress in the OFT myocardium, and its effects on the OFT growth and morphology. Here we estimated the wall stress in the myocardium near the OFT inlet prior to the band over a cardiac cycle, using Laplace law. We found both end-diastolic and end-systolic wall stresses in the OFT wall prior to the band increased, mainly as a response to the increased ventricular pressures (Figure 7.14). The increases in wall stress prior to the band correlated in space with the reduction in radial contractive velocity (Figure 7.3) and circumferential contractive strain rate at L1 (Figure 7.12), suggesting that increased wall stresses affect the contractility of the OFT (OFT function) before extensive remodeling events occur. As we know, the mature myocardium responds to

increased wall stresses by wall thickening or dilation.[199] In OTB embryos, both myocardium wall thickening and dilation prior to the band have been reported at later developmental stages.[25] Our findings on the OFT wall stress further confirm the view that the increases of end-systolic wall stress is associated with radial growth of the myocardium and end-diastolic wall stress with circumferential growth in embryonic myocardium development.[185, 189, 200, 201]

#### 7.4.3.3 Blood flow dynamics and wall shear stress

The most noticeable observation on blood flow dynamic was a dramatic increase of peak velocity across and immediately after the band (Figure 7.15), mainly as a synergic effect of the decreased OFT luminal areas and increased ventricular pressures. The large variations observed in the flow measurement at the banding site among OTB chicks were largely due to technical difficulties in rigorously controlling the tightness and biological responses to the band.

Although the time course of the centerline velocities in the OTB embryos exhibited similar trend as that in the normal embryos, some changes in temporal variation in blood flow dynamics reflected the changes in the OFT wall dynamics and blood pressures (Figure 7.16). In the OTB embryos, due to the restriction of the band, we did not observed the shoulder region before peak flow in the centerline velocity near the OFT inlet as often observed in normal embryos. Instead, we observed a small transient backflow across the band (5/10 OTB versus 1/11 control), which might result from the transient local negative pressure gradient due to large pressures drop across the band. Large backflow across the band has been reported after the intensive remodeling and

adaption has occurred in the OTB embryos.[202] The centerline velocities in normal embryos also exhibited a shoulder region (secondary peak) after the primary peak, driven by the additional momentum from the contraction of the OFT upstream region; towards the OFT outlet, the shoulder region increased in magnitude and duration (Figures 7.16A-C). In OTB embryos, however, the magnitude and duration of the shoulder region at the distal region decreased (Figure 7.16F), which was consistent with the reduced wall dynamics upstream in OTB (a reduced radial contractile velocity in L1-L3 see Figure 7.3).

The changes in flow dynamics are sensed by the endothelial cells on the OFT lumen surface in form of wall shear stress. The wall shear stress exerted by the blood flow on the OFT endocardium was estimated using the Hagen-Poiseuille law: $\tau = \frac{2\mu V_{max}}{R}$, where $\tau$ is the shear stress, $\mu$ the viscosity, $V_{max}$ maximal centerline velocity, and R the lumen radius. We found that the wall shear stress dramatically increased near the band region as a result of the reduced luminal area and increased blood velocity (Figures 7.7 and 7.15). The abnormal high magnitude of wall shear stress may up-regulate expression of eNOs[24, 203] and thus release of NO, which may be responsible for later vasodilatation in the myocardium before and after the band.[25] The pronounced changes in wall shear stress occurred at the proximal OFT, a region that is susceptible for emerging malformations in the OTB chicks, such as ventricular septal defects.

## 7.5 Conclusions

Our study examined for the first time the acute changes in the biomechanical environment within a cardiac cycle in the OFT in the OTB embryos. To maintain the

OFT function in regulating the blood flow from the ventricle to the arterial circulation, the OFT shows early signs of compensational changes in the wall dynamics of the myocardium and cardiac jelly, and the interaction between the wall and blood flow dynamics after one hour of OTB. As a consequence, the spatial distribution of biomechanical stresses and strains deviates from the normal pattern, especially near the band. The changes in the biomechanical environment at cellular level may pre-dispose the functional and structural abnormalities in the banded OFT at later developmental stages.

## 7.6 Data supplement

*Supplemental Videos:*

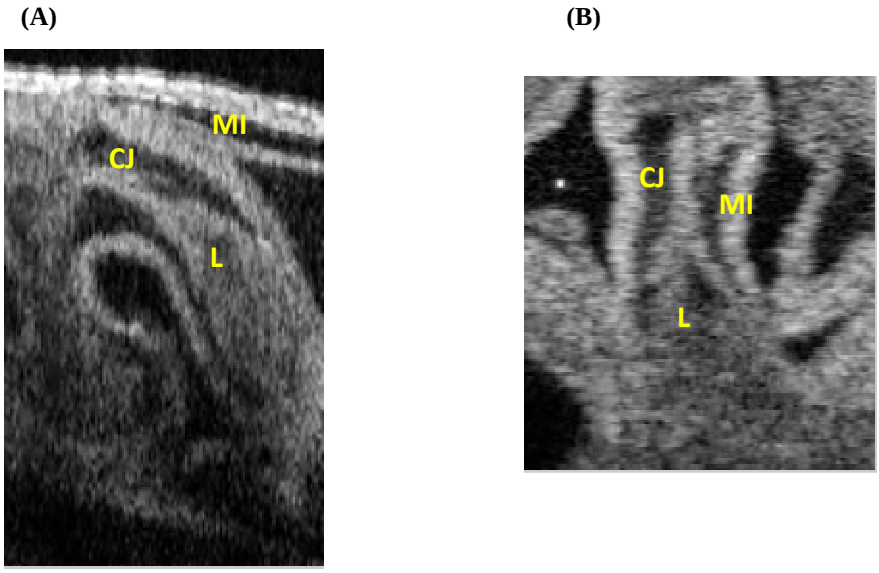


**Supplemental Video 7.1** Longitudinal (A) and frontal views (B) of the OFT of a representative HH18 chick embryo. Frontal view depicts a curve plane approximately along the axial centerline of the OFT in (A). Note the wave-like motion of the cardiac jelly. MI, myocardium; L, lumen; CJ, cardiac jelly.

**(A)** **(B)**

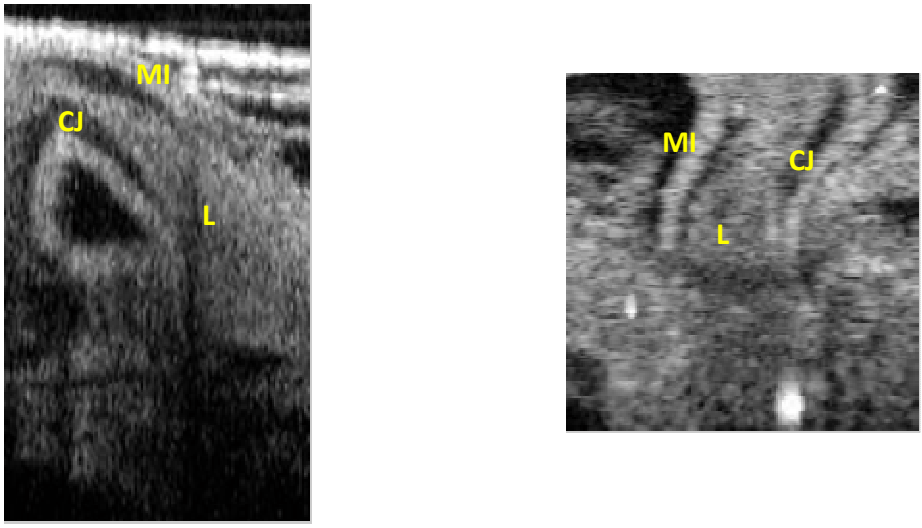


**Supplemental Video 7.2** Longitudinal (A) and frontal (B) views of the OFT of an OTB chick embryo. Frontal view depicts a curve plane approximately along the axial centerline of the OFT in (B). Note that the longitudinal motion of the OFT is dramatically reduced and that the wavelike-motion of the cardiac jelly is disrupted by OTB.

*Supplemental Figures:*

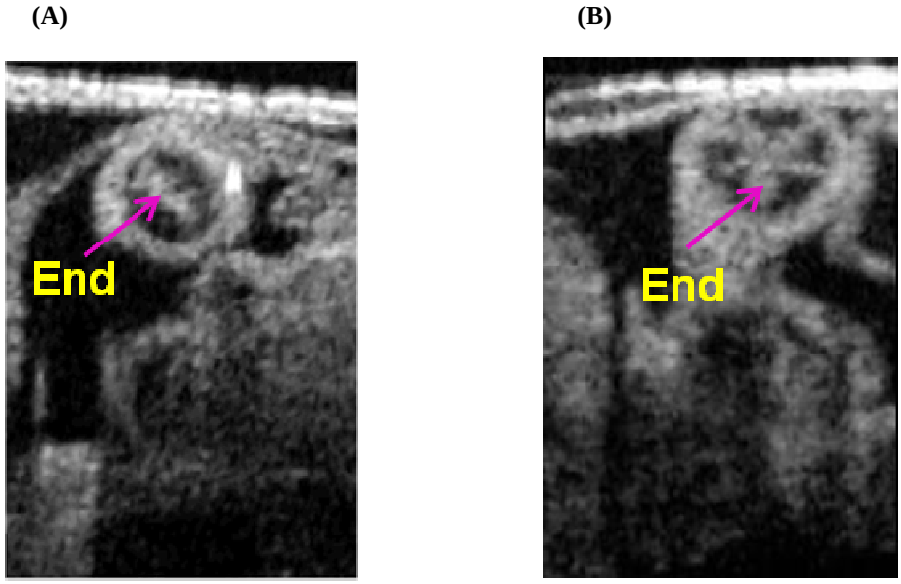


**Supplemental Figure 7.1** OCT cross-sectional image of the OFT inlet of (A) a representative normal embryo and (B) a typical OTB embryo when the OFT is fully closed. Note those extensive branches of the endocardium (End) towards the myocardium in the OTB embryo.

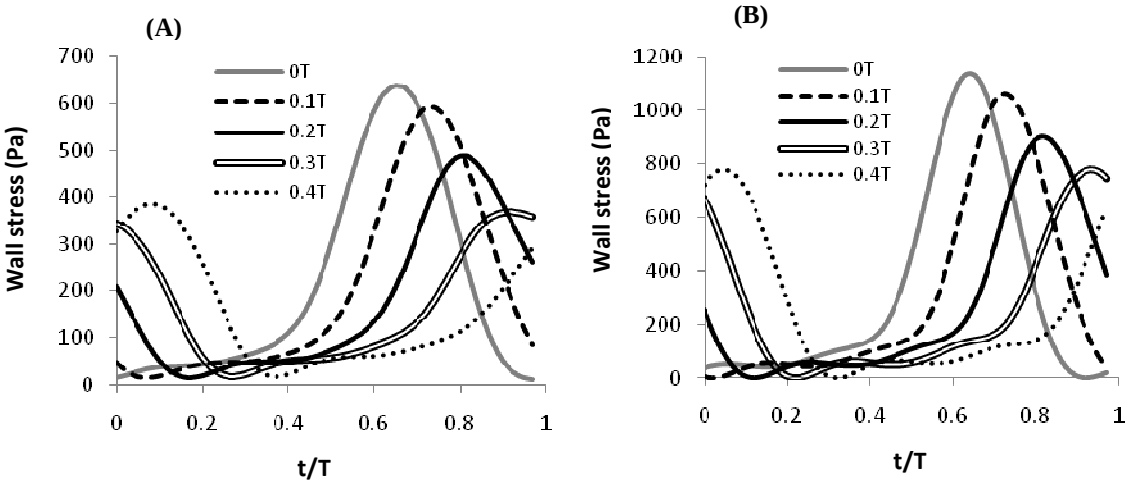


**Supplemental Figure 7.2** Comparison of wall stress in the myocardium at the OFT inlet between (A) a normal chick embryo and (B) an OTB embryo under different combinations of phase relations between $P_V$ and R. 0T, 0.1T,0.2T, and 0.4T are conjectured phase lags of peak $P_V$ with respect to peak R at the OFT inlet. $P_V$, the ventricular pressure; R, effective radius of the myocardium; T, a cardiac cycle.

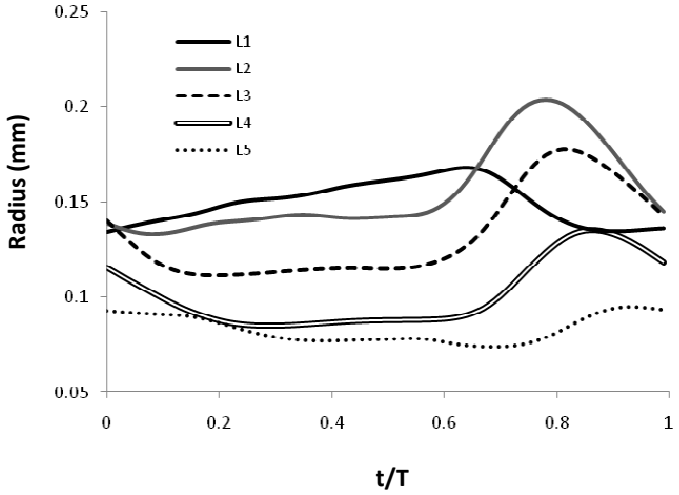


**Supplemental Figure 7.3** Temporal variation of the interior radius of the myocardium at 5 selected OFT cross-sections. This is another typical response to OTB, showing a slower peristaltic motion than normal HH18 chick embryos.

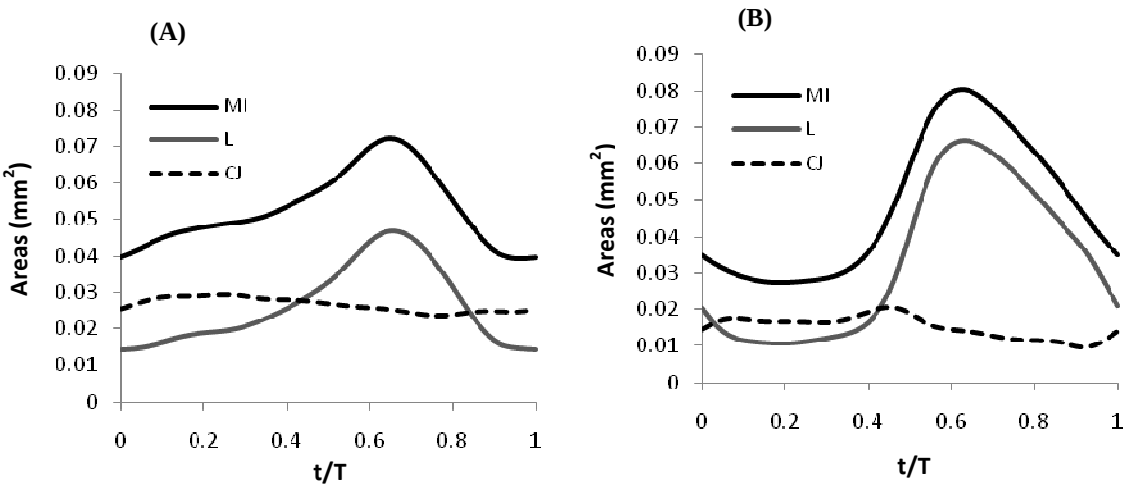


**Supplemental Figure 7.4** Temporal relationship between the areas of the OFT myocardium (MI), cardiac jelly (CJ), and lumen (L) at two locations: (A) L2 and (B) L4 in a typical OTB embryo. Large area of the cardiac jelly usually occurs during early myocardium relaxation and before fast increase of luminal area, or when the OFT is fully closed. The area of the cardiac jelly is small when the OFT is fully expanded or during fast myocardium contraction.

# Chapter 8: Summary and future work

## 8.1 Summary

The objective of this thesis was to develop a methodology to quantify the dynamical biomechanical environments in the early embryonic heart *in vivo* and non-invasively. The methodology enabled us to characterize the physiological biomechanical environment (biomechanical stresses and strains) that embryonic cardiac cells experience *in vivo*, and pathological changes in the biomechanical environment that may lead to heart defects. In this thesis, we used chicken embryonic hearts as the model system and focused on the chicken heart OFT, which provide us insight into the biomechanical environment that embryonic heart cells are exposed *in vivo*. In addition, we used an interventional experiment OTB to simulate disturbances in the biomechanical environment during heart development; OTB model has been reported to reproduce heart diseases associated with the OFT region.[25]

First, we developed a novel methodology that combines 4D imaging, image analysis, physiological measurement, and CFD modeling to quantify non-invasively the wall dynamics and blood flow dynamics within the chicken embryonic heart OFT *in vivo* for the first time. Specifically, we employed a high resolution, non-invasive imaging technique, OCT, and developed an image synchronization strategy to visualize *in vivo* the dynamics of the OFT of chicken embryonic hearts at an early stage (HH18). To extract dynamic geometric information from the 4D images of the embryonic heart, we developed a set of image analysis algorithms that enabled us to analyze the wall dynamics and biomechanical strains of the OFT wall within the cardiac cycle. To reveal

the blood flow dynamics in the OFT, we generated 3D dynamic FE models of the OFT based on the dynamic geometry of the OFT extracted from the 4D image data and *in vivo* pressure measurements. In contrast to previous studies,[21, 91, 139, 162] our FE models were capable of quantifying the blood flow dynamics and variations of WSS over the cardiac cycle.

Second, we characterized the biomechanical environment in the heart OFT of normal chicken embryos and acute changes in the biomechanical environment in the OFT in OTB embryos. Specifically, by employing the methodology we developed, we quantified the wall dynamics and blood flow dynamics within the OFT, and we revealed a heterogeneous distribution of biomechanical stresses and strains in the OFT wall that vary dramatically over the cardiac cycle. The heterogeneous and dynamic biomechanical environment, which embryonic cardiac cells are subjected to *in vivo*, may be associated with the complex morphogenetic events occur in the OFT (such as semi-lunar valves and septa development). Further, to understand what changes in the biomechanical environment that lead to heart defects, we focused on the changes in the wall dynamics and blood flow dynamics in the OFT, and the alterations in the distribution of biomechanical stresses and strains in the OTB embryos before extensive remodeling events initiate.

Collectively, the methodology that I developed in this thesis provided a way to investigate the dynamic biomechanical environment of embryonic heart development for the first time. The knowledge of the *in vivo* biomechanical environment as well as its changes will contribute towards understanding the mechanisms by which the

biomechanical factors affect heart development.

## 8.2 Major contributions

The major contributions of this thesis are:

1. I developed a 4D imaging strategy and an image post-synchronization algorithm that enabled us to visualize and quantify 4D geometry of the OFT *in vivo* with OCT. Our 4D synchronization algorithm is fast and accurately captures the dynamics of the OFT *in vivo*.

2. I developed a set of image analysis algorithms for 4D OCT images of the OFT. Specifically, the segmentation algorithm enabled us to delineate the 3D surfaces of the OFT myocardium and lumen at any given cardiac phase, and to demarcate the OFT wall from 2D time series of OCT images over a cardiac cycle. Algorithms developed to analyze the segmentation results allowed us to extract the cyclic strains from the OCT images. Further with pressure measurement data, we were able to estimate wall stress in the myocardium of the OFT.

3. I developed 3D dynamic FE models of the chick heart OFT. The FE models were based on 4D OCT image data and pressure data measured *in vivo*. The image-based FE models of the OFT enabled us to quantify the blood flow pattern within the OFT lumen and blood-flow induced WSS on the OFT wall. Moreover, we investigated the effects of biomechanical factors, such as blood pressures, wall motion pattern, and the geometry of the OFT on the blood flow dynamics and tempo-spatial distribution of WSS.

4. I, for the first time, elucidated the biomechanical environment in the heart OFT of normal HH18 chick embryos. The most important findings were: (1) the OFT function was regulated by the interaction of the wall dynamics and blood flow dynamics; (2) the wall dynamics and blood flow dynamics in the OFT established a unique biomechanical environment which embryonic cardiac cells on the OFT wall are subjected to; and (3) the biomechanical environment dynamically varied over the cardiac cycle and spatial locations of the OFT.
5. We, for the first time, characterized in detail acute changes in wall dynamics and hemodynamics in the heart OFT of OTB chick embryos. The notable findings were: (1) the OFT showed compensatory changes in the wall dynamics and blood flow dynamics after one hour of OTB; and (2) the biomechanical environment (stresses and strains) that the cardiac cells on the OFT wall experience was altered, especially near the banding site.

## 8.3 Future work

Current work is a preliminary step towards our goal to understand the roles of biomechanics factors in heart development. We could extend this work in the following directions:

### 8.3.1 Longitudinal study of the chick outflow tract

The OFT is a transient cardiac segment that undergoes intensive morphogenetic remodeling and functional evolution during heart development. The cardiac cells on the OFT wall are exposed to a constantly changing biomechanical environment.

Disturbances in the normal evolution of the biomechanical environment may impose the OFT to various forms of malformation. We envision that the knowledge of the normal changes in the biomechanical environment will be critical to understand how the biomechanical factors affect cellular behaviors and gene expression in the OFT at different developmental stages.

This thesis has provided a methodology to quantify the wall dynamics and flow dynamics of the developing OFT *in vivo*. We have studies the biomechanical environment of an important early stage of development when the morphogenesis of the OFT is sensitive to the biomechanical changes. It is feasible to apply the current methodology to follow the structural and functional development of the OFT across different stages. By doing so, we will reveal the complex morphogenetic events occurs in the OFT, and developmental changes in the wall dynamics and blood flow pattern. Further we will characterize the evolution of the biomechanical environment in the OFT, which will provide insight into the roles of the biomechanical factors in normal heart development, and will establish the baseline for investigating the changes in the biomechanical environment in our intervention models such as OTB or vitelline vein ligation.

### 8.3.2 OCT imaging and image analysis

#### 8.3.2.1 Blood flow measurement using OCT

One unique advantage of OCT is its capability to image the microstructure and blood flow simultaneously. In this thesis, we used OCT mainly for visualizing and quantifying the dynamics structure of the OFT. We encountered two major obstacles in flow

measurement in the OFT using Doppler OCT. First, the maximal flow velocity in the OFT was out of the measurement range of the current OCT system, which is constrained by the integration time of the CCD camera in the OCT system. When the blood flow velocity in the OFT is beyond the maximal velocity of the OCT system, the measured flow signal becomes phase-wrapped. Second, only the velocity component along the laser beam was detectable. Drs. Ma Zhenhe and Li Peng in Dr. Ruikang Wang's lab have made great strides in developing the unwrapping algorithm and estimating the absolute velocity, which extend OCT to quantify the blood flow in the OFT *in vivo*.[204] It will be also valuable to directly measure the absolute blood flow velocity *in vivo* by configuring the OCT image system and developing new signal processing algorithms. With the knowledge of absolute flow velocities in the OFT, WSS exerted by the blood flow will be directly derived. In addition, Doppler OCT will allow us to validate our subjective-specific FE model of the OFT with the blood flow measured in the same chick embryo.

#### 8.3.2.2 OCT image analysis

In this thesis, we have developed a 3D segmentation algorithm to delineate the OFT wall from an image sequence over time or a 3D volume image dataset. We applied the segmentation algorithm to OCT image sequences of several cross-sections that evenly span along the OFT. Our finding that the wall dynamics and biomechanical strains in the OFT wall change along the OFT and over the cardiac cycle suggests that a 4D segmentation algorithm will be a critical extension to study the biomechanics of the OFT. Dr. Yin Xin has made a huge progress in developing a robust 4D image segmentation

algorithm that allows us to better visualize and quantify the morphology and wall dynamics of the OFT within the cardiac cycle (Figure 8.1). We will apply the 4D segmentation algorithm to all the 4D image datasets of the OFT in normal and OTB chick embryos that we have acquired to study biological variations and OTB induced changes in the wall dynamics of the entire OFT. Furthermore, the biomechanical strains at each material point on the OFT wall will be extracted from the 4D segmentation.

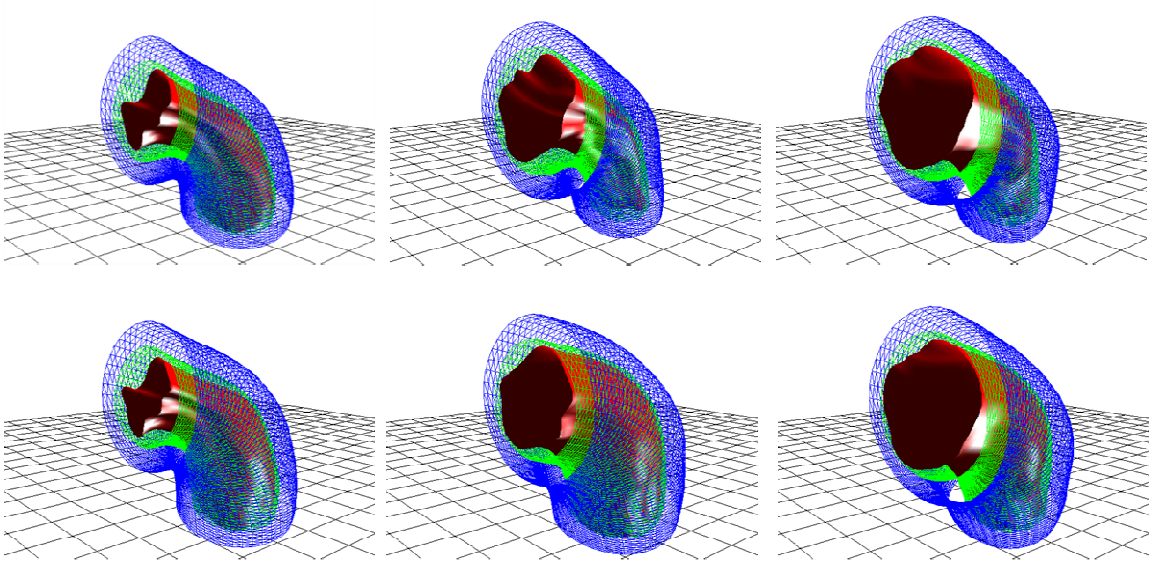

**Figure 8.1** Temporal variation of the OFT surfaces extracted from 4D OCT images of the OFT with a 4D segmentation algorithm. Blue and green surfaces are the external and the interior surfaces of the myocardium, respectively. Red surface is the OFT lumen. 4D segmentation on the OFT were performed by Dr. Xin Yin (Image courtesy of Dr. Yin Xin)

### 8.3.3 Finite element modeling

In this thesis, we have developed a subject-specific FE model of the OFT in a representative HH18 chick embryo. The FE model reveals a distinct blood flow pattern and heterogeneous distribution of flow-induced WSS on the OFT wall. A FE model of the heart OFT of OTB embryos will be important to quantify the changes in blood flow

dynamics and WSS in the OFT due to OTB. However, we have encountered some technical challenges in acquiring boundary conditions important for accurately modeling the OFT of OTB embryos: namely the aortic sac pressure data and phase relationships between the pressures and dynamic geometry of the OFT of OTB embryos. Dr. Shi Liang has made great advances and will continue to resolve the problems. Specifically, we will employ the OCT system to enhance the visualization of the pressure probe in the tiny beating embryonic chick heart. We will employ ECG signals to synchronize phase relationships between pressures and the dynamic geometry of the OFT. After successfully tackling these issues, we will generate FE models to quantity in details the changes of blood flow and WSS in the OFT of OTB embryos.

Further, to extend the quantitative powers of FE modeling in embryonic heart research, in particular the OFT, several improvements are recommended:

1. Use realistic subject-specific geometry of the OFT lumen. With the 4D segmentation algorithm that developed by Dr. Yin Xin, no assumptions on the OFT lumen geometry and wall motion are necessary.
2. Use realistic boundary conditions with blood pressures and geometric data synchronized within the cardiac cycle based on the simultaneous ECG signals acquired with pressure measurement and imaging.
3. Incorporate flow-structure interaction in modeling of the OFT. The FE model couples the interaction of the blood flow dynamics and wall dynamics of the OFT, which will provide us insight into regulatory mechanisms of the embryonic heart.

4. Use OCT Doppler flow measurement to improve model validation. Both the blood flow used for validation and the geometry used in the FE model will be acquired simultaneously from the same chick embryo.

### 8.3.4 Correlation with the gene expression pattern

This thesis has provided quantitative knowledge of biomechanical environment that the cardiac cells on the OFT wall are subjected *in vivo* in HH18 chick embryos, as well as a methodology that enables us to carry out longitudinal investigation into the changes in biomechanical environment with development . In Dr. Thornburg's lab, exciting research has been carried out in measuring gene expression level of biomechanical sensitive genes in chick embryos using microarray and real time (RT)-Polymerase Chain Reaction (PCR), and localizing gene expression using in situ hybridization (ISH) and immunohistochemistry (IHC). After ISH or IHC, the OFT was imaged using confocal microscopy and the gene expression pattern on the OFT wall was visualized using Amira 5.2.2 (see an example in Figure 8.2).

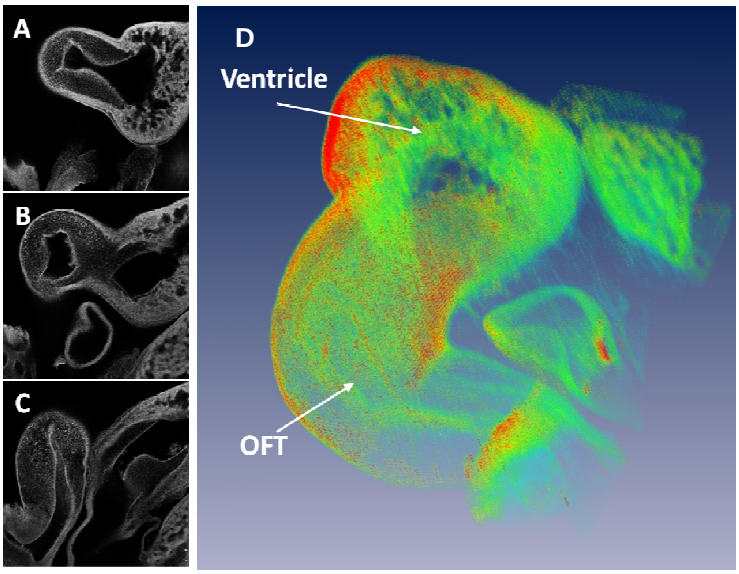


**Figure 8.2** Level and spatial distribution of gene expression of integrin-α4 in a normal HH24 chick embryo. (A-C) Examples of confocal microscopy images along the depth of the embryonic heart, with image intensity indicating the level of gene expression. (D) 3D voxel view of the gene expression of integrin-α4 (the red color), showing a strong express in the compact ventricular myocardium, and a mild express in the OFT myocardium and trabeculae. The 3D voxel view was reconstructed from the confocal image dataset in (A-C) using Amira 5.2.2. Confocal imaging was performed by Dr. Carley Shaut.

To determine the relationship between changes in biomechanical factors and associated changes in expression of biomechanical sensitive genes that modulate OFT morphogenesis, we will first correlate the spatial distribution of biomechanical indices (e.g., maximal circumferential strains, wall stress, and WSS) with spatial distribution of expression levels of candidate genes such as collagen α1 (XIV) and Integrin subunits α4 on the OFT wall of normal embryos from HH18 to HH24. The genes are selected from our microarray data whose transcriptions have been up-regulation as a response to OTB. We will also correlate the alterations in the biomechanical indices to the changes in gene expression levels and localizations on the OFT wall in OTB embryos from HH18 to HH24.

To understand the underlying regulatory mechanisms of biomechanical factors, we will characterize the features of the biomechanical factors at specific regions of interest such as the proximal and distal cardiac cushions as well as the inner curvature of the OFT, where differential morphological events occur later during development. We will design *in vitro* experiments with well controlled biomechanical environment (such as a flow chamber) that mimics the features of the *in vivo* biomechanical environment in order to differentiate the roles of individual biomechanical factor and a combination of biomechanical factors in OFT valve and septa development.

# References


**1.** Moorman AFM, Christoffels VM. Cardiac chamber formation: development, genes, and evolution. *Physiol. Rev.* Oct 2003;83(4):1223-1267.

**2.** Brand T. Heart development: molecular insights into cardiac specification and early morphogenesis. *Dev. Biol.* Jun 2003;258(1):1-19.

**3.** Srivastava D, Olson EN. A genetic blueprint for cardiac development. *Nature.* Sep 2000;407(6801):221-226.

**4.** Bruneau BG. The developing heart and congenital heart defects: a make or break situation. *Clin. Genet.* Apr 2003;63(4):252-261.

**5.** Olson EN. A decade of discoveries in cardiac biology. *Nat. Med.* 2004;10(5):467-474.

**6.** Srivastava D. Genetic regulation of cardiogenesis and congenital heart disease. *Annu. Rev. Pathol. Mech. Dis.* 2006;1:199-213.

**7.** Franco D, Lamers WH, Moorman AFM. Patterns of expression in the developing myocardium: towards a morphologically integrated transcriptional model. *Cardiovasc. Res.* 1998;38(1):25-53.

**8.** Cruz MVdl, Campillo-Sainz C, Munoz-Armas S. Congenital heart defects in chick embryos subjected to temperature variations. *Circ. Res.* 1966;18(3):257-262.

**9.** Zhang L. Prenatal hypoxia and cardiac programming. *J.Soc.Gynecol. Invest.* 2005;12(1):116-120.

**10.** Sharma S, Lucitti J, Nordman C, Tinney J, Tobita K, Keller B. Impact of hypoxia

on early chick embryo growth and cardiovascular function. *Pediatr. Res.* 2006;59(1):116-120.

**11.** Hogers B, DeRuiter MC, GittenbergerdeGroot AC, Poelmam RE. Unilateral vitelline vein ligation alters intracardiac blood flow patterns and morphogenesis in the chick embryo. *Circ. Res.* Apr 1997;80(4):473-481.

**12.** Clark EB, Rosenquist GC. Spectrum of cardiovascular anomalies following cardiac loop constriction in the chick embryo. *Birth Defects Orig. Artic. Ser.* 1978;14(7):431-442.

**13.** Hogers B, DeRuiter MC, Gittenberger-de Groot AC, Poelmann RE. Extraembryonic venous obstructions lead to cardiovascular malformations and can be embryolethal. *Cardiovasc. Res.* 1999;41(1):87-99.

**14.** Hove JR, Koster RW, Forouhar AS, Acevedo-Bolton G, Fraser SE, Gharib M. Intracardiac fluid forces are an essential epigenetic factor for embryonic cardiogenesis. *Nature.* Jan 2003;421(6919):172-177.

**15.** Clark EB, Hu N, Frommelt P, Vandekieft Gk, Dummett JL, Tomanek RJ. Effect of increased pressure on ventricular growth in stage 21 chick embryos. *Am. J. Physiol. Heart Circ. Physiol.* 1989;26:H55-H61.

**16.** Miller CE, Wong CL, Sedmera D. Pressure overload alters stress-strain properties of the developing chick heart. *Am. J. Physiol. Heart Circ. Physiol.* Nov 2003;285(5):H1849-H1856.

**17.** Taber LA. Mechanical aspects of cardiac development. *Progress in Biophysics and Molecular Biology.* 1998;69(2-3):237-255.

**18.** Bartman T, Hove J. Mechanics and function in heart morphogenesis. *Dev. Dyn.*

Jun 2005;233(2):373-381.

**19.** Thom T, Haase N, Rosamond W, Howard VJ, Rumsfeld J, Manolio T, Zheng ZJ, Flegal K, O'Donnell C, Kittner S, Lloyd-Jones D, Goff DC, Hong YL, Adams R, Friday G, Furie K, Gorelick P, Kissela B, Marler J, Meigs J, Roger V, Sidney S, Sorlie P, Steinberger J, Wasserthiel-Smoller S, Wilson M, Wolf P. Heart disease and stroke statistics - 2006 update - A report from the American Heart Association Statistics Committee and Stroke Statistics Subcommittee. *Circ. Res.* Feb 2006;113(6):E85-E151.

**20.** Hoffman JIE, Kaplan S. The incidence of congenital heart disease. *J. Am. Coll. Cardiol.* 2002;39(12):1890-1900.

**21.** Groenendijk BCW, Hierck BP, Vrolijk J, Baiker M, Pourquie M, Gittenberger-de Groot AC, Poelmann RE. Changes in shear stress-related gene expression after experimentally altered venous return in the chicken embryo. *Circ. Res.* Jun 2005;96(12):1291-1298.

**22.** Hove JR. Quantifying cardiovascular flow dynamics during early development. *Pediatr. Res.* 2006;60:6-13.

**23.** Tobita K, Keller BB. Right and left ventricular wall deformation patterns in normal and left heart hypoplasia chick embryos. *Am. J. Physiol. Heart Circ. Physiol.* September 1, 2000 2000;279(3):H959-H969.

**24.** Groenendijk BCW, Hierck BP, Gittenberger-de Groot AC, Poelmann RE. Development-related changes in the expression of shear stress responsive genes KLF-2, ET-1, and NOS-3 in the developing cardiovascular system of chicken embryos. *Dev. Dyn.* May 2004;230(1):57-68.

**25.** Sedmera D, Pexieder T, Rychterova V, Hu N, Clark EB. Remodeling of chick embryonic ventricular myoarchitecture under experimentally changed loading conditions. *Anat. Rec.* 1999;254(2):238-252.

**26.** Ohno M, Cooke JP, Dzau VJ, Gibbons GH. Fluid shear stress induces endothelial transforming growth factor beta-1 transcription and production. Modulation by potassium channel blockade. *J. Clin. Invest.* 1995;95(3):1363-1369.

**27.** Person AD, Klewer SE, Runyan RB. Cell biology of cardiac cushion development. *Int. Rev. Cytol.* 2005;243:287-335.

**28.** Li Y-SJ, Haga JH, Chien S. Molecular basis of the effects of shear stress on vascular endothelial cells. *J. Biomech.* 2005;38(10):1949-1971.

**29.** Davies PF. Flow-mediated endothelial mechanotransduction. *Physiol. Rev.* July 1, 1995 1995;75(3):519-560.

**30.** Chien S, Li S, Shyy JYJ. Effects of mechanical forces on signal transduction and gene expression in endothelial cells. *Hypertension.* 1998;31(1 II SUPPL.):162-169.

**31.** Mitsumata M, Fishel RS, Nerem RM, Alexander RW, Berk BC. Fluid shear stress stimulates platelet-derived growth factor expression in endothelial cells. *Am. J. Physiol. Heart Circ. Physiol.* 1993;265(1 34-1):H3-H8.

**32.** Resnick N, Collins T, Atkinson W, Bonthron DT, Dewey Jr CF, Gimbrone Jr MA. Platelet-derived growth factor B chain promoter contains a cis-acting fluid shear-stress-responsive element. *Proc. Natl. Acad. Sci. U. S. A.* 1993;90(10):4591-4595.

**33.** Corson MA, James NL, Latta SE, Nerem RM, Berk BC, Harrison DG.

Phosphorylation of endothelial nitric oxide synthase in response to fluid shear stress. *Circ. Res.* 1996;79(5):984-991.

**34.** Hsieh PCH, Davis ME, Lisowski LK, Lee RT. Endothelial-cardiomyocyte interactions in cardiac development and repair. *Annu. Rev. Physiol.* 2006;68:51-66.

**35.** Barakat AI, Lieu DK. Differential responsiveness of vascular endothelial cells to different types of fluid mechanical shear stress. *Cell Biochem. Biophys.* 2003;38(3):323-343.

**36.** Barakat AI, Lieu DK, Gojova A. Secrets of the code: Do vascular endothelial cells use ion channels to decipher complex flow signals? *Biomaterials.* 2006;27(5):671-678.

**37.** Lansman JB, Hallam TJ, Rink TJ. Single stretch-activated ion channels in vascular endothelial cells as mechanotransducers? *Nature.* 1987;325(6107):811-813.

**38.** Naruse K, Sokabe M. Involvement of stretch-activated ion channels in Ca2+ mobilization to mechanical stretch in endothelial cells. *Am. J. Physiol., Cell Physiol.* April 1, 1993 1993;264(4):C1037-C1044.

**39.** Hishikawa K, LÃ¼scher TF. Pulsatile stretch stimulates superoxide production in human aortic endothelial cells. *Circulation.* 1997;96(10):3610-3616.

**40.** Zheng W, Christensen LP, Tomanek RJ. Stretch induces upregulation of key tyrosine kinase receptors in microvascular endothelial cells. *Am. J. Physiol. Heart Circ. Physiol.* 2004;287(6 56-6):H2739-H2745.

**41.** Zhao S, Suciu A, Ziegler T, Moore Jr JE, Burki E, Meister JJ, Brunner HR.

Synergistic effects of fluid shear stress and cyclic circumferential stretch on vascular endothelial cell morphology and cytoskeleton. *Arterioscler. Thromb. Vasc. Biol.* 1995;15(10):1781-1786.

**42.** Lammerding J, Kamm RD, Lee RT. Mechanotransduction in cardiac myocytes. *Cardiac Engineering: from Genes and Cells to Structure and Function.* Vol 1015. New York: New York Acad Sciences; 2004:53-70.

**43.** Tobita K, Garrison JB, Liu LJ, Tinney JP, Keller BB. Three-dimensional myofiber architecture of the embryonic left ventricle during normal development and altered mechanical loads. *Anat. Rec. A Discov. Mol. Cell. Evol. Biol.* 2005;283A(1):193-201.

**44.** Holmes JW. Candidate mechanical stimuli for hypertrophy during volume overload. *J. Appl. Physiol.* Oct 2004;97(4):1453-1460.

**45.** Miller CE, Donlon KJ, Toia L, Wong CL, Chess PR. Cyclic strain induces proliferation of cultured embryonic heart cells. *In Vitro Cell. Dev. Biol.-Anim.* Nov-Dec 2000;36(10):633-639.

**46.** Vemuri R, Lankford EB, Poetter K, Hassanzadeh S, Takeda K, Yu ZX, Ferrans VJ, Epstein ND. The stretch-activation response may be critical to the proper functioning of the mammalian heart. *Proc. Natl. Acad. Sci. U. S. A.* 1999;96(3):1048-1053.

**47.** Groenendijk BCW, Van der Heiden K, Hierck BP, Poelmann RE. The role of shear stress on ET-1, KLF2, and NOS-3 expression in the developing cardiovascular system of chicken embryos in a venous ligation model. *Physiology.* December 1, 2007 2007;22(6):380-389.

**48.** Hamburger V, Hamilton HL. A series of normal stages in the development of the chick embryo. *J. Morphol.* 1951;88(1):49-92.

**49.** Martinsen BJ. Reference guide to the stages of chick heart embryology. *Dev. Dyn.* Aug 2005;233(4):1217-1237.

**50.** Männer J. Cardiac looping in the chick embryo: A morphological review with special reference to terminological and biomechanical aspects of the looping process. *Anat. Rec.* Jul 2000;259(3):248-262.

**51.** De Jong F, Opthof T, Wilde AAM, Janse MJ, Charles R, Lamers WH, Moorman AFM. Persisting zones of slow impulse conduction in developing chicken hearts. *Circ. Res.* 1992;71(2):240-250.

**52.** Keller BB, ed. *Embryonic cardiovascular function, coupling, and maturation: a species view*. New York: Cambridge University Press; 1996. Burggren WW, Keller BB, eds. Development of Cardiovascular Systems: Molecules to Organisms.

**53.** Gittenberger-de Groot AC, Bartelings MM, Deruiter MC, Poelmann RE. Basics of cardiac development for the understanding of congenital heart malformations. *Pediatric Research.* Feb 2005;57(2):169-176.

**54.** Keller BB, Hu N, Clark EB. Correlation of ventricular area, perimeter, and conotruncal diameter with ventricular mass and function in the chick embryo from stages 12 to 24. *Circ. Res.* 1990;66:109-114.

**55.** Rothenberg F, Fisher SA, Watanabe M. Sculpting the cardiac outflow tract. *Birth Defects Res. C Embryo Today.* 2003;69(1):38-45.

**56.** Qayyum SR, Webb S, Anderson RH, Verbeek FJ, Brown NA, Richardson MK.

Septation and valvar formation in the outflow tract of the embryonic chick heart. *Anat. Rec.* Nov 2001;264(3):273-283.

**57.** Soufan AT, Berg GVD, Moerland PD, Massink MMG, Hoff MJBVD, Moorman AFM, Ruijter JM. Three-dimensional measurement and visualization of morphogenesis applied to cardiac embryology. *J. Microsc.* 2007;225(3):269–274

**58.** Bartman T, Walsh EC, Wen KK, McKane M, Ren JH, Alexander J, Rubenstein PA, Stainier DYR. Early myocardial function affects endocardial cushion development in zebrafish. *PLoS. Biol.* May 2004;2(5):673-681.

**59.** Keller BB, Yoshigi M, Tinney JP. Ventricular-vascular uncoupling by acute conotruncal occlusion in the stage 21 chick embryo. *Am. J. Physiol. Heart Circ. Physiol.* December 1, 1997 1997;273(6):H2861-2866.

**60.** Rugonyi S, Shaut C, Liu A, Thornburg K, Wang RK. Changes in wall motion and blood flow in the outflow tract of chick embryonic hearts observed with optical coherence tomography after outflow tract banding and vitelline-vein ligation. *Phys. Med. Biol.* 2008;53(18):5077-5091.

**61.** Schmitt JM. Optical coherence tomography (OCT): a review. *IEEE J. Sel. Top. Quantum Electron.* Jul-Aug 1999;5(4):1205-1215.

**62.** Fujimoto JG. Optical coherence tomography for ultrahigh resolution in vivo imaging. *Nat. Biotechnol.* Nov 2003;21(11):1361-1367.

**63.** Boppart SA. Optical coherence tomography - principles applications and advances. *Minerva Biotechnol.* Dec 2004;16(4):211-237.

**64.** Tomlins PH, Wang RK. Theory, developments and applications of optical coherence tomography. *J. Phys. D-Appl. Phys.* Aug 2005;38(15):2519-2535.

**65.** Liebling M, Forouhar AS, Gharib M, Fraser SE, Dickinson ME. Wavelet-based synchronization of nongated confocal microscopy data for 4D imaging of the embryonic heart. Paper presented at: Proceedings of SPIE - The International Society for Optical Engineering, 2005; San Diego, CA.

**66.** Phoon CKL. Imaging tools for the developmental biologist: Ultrasound biomicroscopy of mouse embryonic development. *Pediatr. Res.* Jul 2006;60(1):14-21.

**67.** Boppart SA, Brezinski ME, Fujimoto JG. Optical coherence tomography imaging in developmental biology. *Methods Mol. Biol.* 2000;135:217-233.

**68.** Yelbuz TM, Choma MA, Thrane L, Kirby ML, Izatt JA. Optical coherence tomography - A new high-resolution imaging technology to study cardiac development in chick embryos. *Circulation.* Nov 2002;106(22):2771-2774.

**69.** Tearney GJ, Bouma BE, Boppart SA, Golubovic B, Swanson EA, Fujimoto JG. Rapid acquisition of in vivo biological images by use of optical coherence tomography. *Opt. Lett.* 1996;21(17):1408-1410.

**70.** Jenkins MW, Rothenberg F, Roy D, Nikolski VP, Hu Z, Watanabe M, Wilson DL, Efimov IR, Rollins AM. 4D embryonic cardiography using gated optical coherence tomography. *Opt. Express.* 2006;14(2):736-748.

**71.** Männer J, Thrane L, Norozi K, Yelbuz TM. High-resolution in vivo imaging of the cross-sectional deformations of contracting embryonic heart loops using optical coherence tomography. *Dev. Dyn.* 2008;237(4):953-961.

**72.** Männer J, Thrane L, Norozi K, Yelbuz TM. In vivo imaging of the cyclic changes in cross-sectional shape of the ventricular segment of pulsating embryonic chick

hearts at stages 14 to 17: A contribution to the understanding of the ontogenesis of cardiac pumping function. *Dev. Dyn.* 2009;238(12):3273-3284.

**73.** Jenkins MW, Adler DC, Gargesha M, Huber R, Rothenberg F, Belding J, Watanabe M, Wilson DL, Fujimoto JG, Rollins AM. Ultrahigh-speed optical coherence tomography imaging and visualization of the embryonic avian heart using a buffered Fourier Domain Mode Locked laser. *Opt. Express.* 2007;15(10):6251-6267.

**74.** Phoon CKL, Turnbull DH. Ultrasound biomicroscopy-Doppler in mouse cardiovascular development. *Physiol. Genomics.* 2003;14:3-15.

**75.** Vennemann P, Kiger KT, Lindken R, Groenendijk BCW, Stekelenburg-de Vos S, ten Hagen TLM, Ursem NTC, Poelmann RE, Westerweel J, Hierck BP. In vivo micro particle image velocimetry measurements of blood-plasma in the embryonic avian heart. *J. Biomech.* 2006;39(7):1191-1200.

**76.** Davis A, Izatt J, Rothenberg F. Quantitative measurement of blood flow dynamics in embryonic vasculature using spectral Doppler velocimetry. *Anat. Rec. (Hoboken).* 2009;292(3):311-319.

**77.** Oosterbaan AM, Ursem NTC, Struijk PC, Bosch JG, Steen AFWvd, Steegers EAP. Doppler flow velocity waveforms in the embryonic chicken heart at developmental stages corresponding to 5-8 weeks of human gestation. *Ultrasound Obstet. Gynecol.* 2009;33(6):638-644.

**78.** Poelma C, Van der Heiden K, Hierck BP, Poelmann RE, Westerweel J. Measurements of the wall shear stress distribution in the outflow tract of an embryonic chicken heart. *J. R. Soc. Interface.* January 6, 2010 2010;7(42):91-103.

**79.** Phoon CKL, Turnbull DH. Ultrasound biomicroscopy-Doppler in mouse cardiovascular development. *Physiol. Genomics.* Jun 2003;14(1):3-15.

**80.** Stekelenburg-De Vos S, Steendijk P, Ursem NTC, Wladimiroff JW, Delfos R, Poelmann RE. Systolic and diastolic ventricular function assessed by pressure-volume loops in the stage 21 venous clipped chick embryo. *Pediatr. Res.* Jan 2005;57(1):16-21.

**81.** Hu N, Clark EB. Hemodynamics of the stage 12 to stage 29 chick embryo. *Circ. Res.* 1989;65:1665-1670.

**82.** Lucitti JL, Tobita K, Keller BB. Arterial hemodynamics and mechanical properties after circulatory intervention in the chick embryo. *J. Exp. Biol.* May 2005;208(10):1877-1885.

**83.** Bathe KJ. *Finite Element Procedure*. NJ: Prentice Hall; 1996.

**84.** Taylor CA, Draney MT. Experimental and computational methods in cardiovascular fluid mechanics. *Annu. Rev. Fluid Mech.* 2004;36:197-231.

**85.** Steinman DA, Taylor CA. Flow imaging and computing: Large artery hemodynamics. *Ann. Biomed. Eng.* Dec 2005;33(12):1704-1709.

**86.** Steinman DA. Image-based computational fluid dynamics modeling in realistic arterial geometries. *Ann. Biomed. Eng.* Apr 2002;30(4):483-497.

**87.** Buchanan JR, Kleinstreuer C, Hyun S, Truskey GA. Hemodynamics simulation and identification of susceptible sites of atherosclerotic lesion formation in a model abdominal aorta. *J. Biomech.* 2003;36(8):1185-1196.

**88.** Friedman MH, Giddens DP. Blood flow in major blood vessels-modeling and experiments. *Ann. Biomed. Eng.* Dec 2005;33(12):1710-1713.

**89.** Saber NR, Wood NB, Gosman AD, Merrifield RD, Yang GZ, Charrier CL, Gatehouse PD, Firmin DN. Progress towards patient-specific computational flow modeling of the left heart via combination of magnetic resonance imaging with computational fluid dynamics. *Ann. Biomed. Eng.* 2003;31(1):42-52.

**90.** Tang BT, Cheng CP, Draney MT, Wilson NM, Tsao PS, Herfkens RJ, Taylor CA. Abdominal aortic hemodynamics in young healthy adults at rest and during lower limb exercise: Quantification using image-based computer modeling. *Am. J. Physiol. Heart Circ. Physiol.* 2006;291(2):H668-H676.

**91.** DeGroff CG, Thornburg BL, Pentecost JO, Thornburg KL, Gharib M, Sahn DJ, Baptista A. Flow in the early embryonic human heart: a numerical study. *Pediatr. Cardiol.* 2003;24:375-380.

**92.** Liebling M, Forouhar AS, Wolleschensky R, Zimmermann B, Ankerhold R, Fraser SE, Gharib M, Dickinson ME. Rapid three-dimensional imaging and analysis of the beating embryonic heart reveals functional changes during development. *Dev. Dyn.* 2006;235(11):2940-2948.

**93.** Swanson EA, Hee MR, Tearney GJ, Boumar B, Boppart S, Izatt J, Brezinski ME, Schuman JS, Puliafito CA, eds. *Optical coherence tomography principles, instrumentation, and biological applications*: Springer; 1996. A.M. Verga Scheggi SM, Arthur N. Chester, R. Pratesi, ed. Biomedical Optical Instrumentation and Laser-Assisted Biotechnology; No. 325.

**94.** Yelin R, Yelin D, Oh W-Y, Yun SH, Boudoux C, Vakoc BJ, Bouma BE, Tearney GJ. Multimodality optical imaging of embryonic heart microstructure. *J. Biomed. Opt.* 2007;12(6):064021

**95.** Luo W, Marks DL, Ralston TS, Boppart SA. Three-dimensional optical coherence tomography of the embryonic murine cardiovascular system. *J. Biomed. Opt.* 2006;11(2):021014.

**96.** O'Dell WG, McCulloch AD. Imaging three-dimensional cardiac function. *Annu. Rev. Biomed. Eng.* 2000;2:431-456.

**97.** Jenkins MW, Chughtai OQ, Basavanhally AN, Watanabe M, Rollins AM. In vivo gated 4D imaging of the embryonic heart using optical coherence tomography. *J. Biomed. Opt.* 2007;12(3):030505.

**98.** Mariampillai A, Standish BA, Munce NR, Randall C, Liu G, Jiang JY, Cable AE, Vitkin IA, Yang VXD. Doppler optical cardiogram gated 2D color flow imaging at 1000 fps and 4D in vivo visualization of embryonic heart at 45 fps on a swept source OCT system. *Opt. Express.* 2007;15(4):1627-1638.

**99.** Liebling M, Forouhar A, Gharib M, Fraser S, Dickinson M. Four-dimensional cardiac imaging in living embryos via postacquisition synchronization of nongated slice sequences. *J. Biomed. Opt.* 2005;10(5):054001.

**100.** Carerj S, Micari A, Trono A, Giordano G, Cerrito M, Zito C, Luzza F, Coglitore S, Arrigo F, Oreto G. Anatomical M-Mode: An Old-New Technique. *Echocardiography.* 2003;20(4):357-361.

**101.** Ruijtenbeek K, De Mey JGR, Blanco CE. The chicken embryo in developmental physiology of the cardiovascular system: A traditional model with new possibilities. *Am. J. Physiol. Regul. Integr. Comp. Physiol.* Aug 2002;283(2):R549-R550.

**102.** Stellingwerf RF. Period determination using phase dispersion minimization.

*Astrophys. J.* 1978;224:953-960.

**103.** Dworetsky MM. A period-finding method for sparse randomly spaced observations or "How long is a piece of string?" *Mon. Not. R. Astron. Soc.* 1983;203:917-924.

**104.** Roberts DH, Lehar J, Dreher JW. Time Series Analysis with Clean. I. Derivation of a Spectrum. *Astron. J. (N. Y.).* 1987;93(4):968-989.

**105.** Horst R, Pardalos PM, Thoai NV. *Introduction to Global Optimization (Nonconvex Optimization and its Applications).* Vol 48. 2 ed. Dordrecht: Kluwer Academic Publishers; 2000.

**106.** Unser M. Splines: a perfect fit for signal and image processing *IEEE Signal Process. Mag.* 1999;16(6):22-38.

**107.** Meijering EHW, Niessen WJ, Viergever MA. Quantitative evaluation of convolution-based methods for medical image interpolation. *Med. Image Anal.* 2001;5:111-126.

**108.** Pagani M, Lombardi F, Guzzetti S, Rimoldi O, Furlan R, Pizzinelli P, Sandrone G, Malfatto G, Dell'Orto S, Piccaluga E. Power spectral analysis of heart rate and arterial pressure variabilities as a marker of sympatho-vagal interaction in man and conscious dog. *Circ. Res.* August 1, 1986 1986;59(2):178-193.

**109.** Wang Y, Bradley AB, Joseph AI, Tan O, Huang D. Retinal blood flow measurement by circumpapillary Fourier domain Doppler optical coherence tomography. *J. Biomed. Opt.* 2008;13(6):064003.

**110.** Fishman M, Chien K. Fashioning the vertebrate heart: earliest embryonic decisions. *Development.* 1997;124(11):2099-2117.

**111.** Taber LA, Zhang J, Perucchio R. Computational model for the transition from peristaltic to pulsatile flow in the embryonic heart tube. *J. Biomech. Eng.* 2007;129(3):441-449.

**112.** Forouhar AS, Liebling M, Hickerson A, Nasiraei-Moghaddam A, Tsai HJ, Hove JR, Fraser SE, Dickinson ME, Gharib M. The embryonic vertebrate heart tube is a dynamic suction pump. *Science.* May 2006;312(5774):751-753.

**113.** Leatherbury L, Connuck DM, Gauldin HE, Kirby ML. Hemodynamic changes and compensatory mechanisms during early cardiogenesis after neural crest ablation in chick embryos. *Pediatr. Res.* 1991;30(6):509-512.

**114.** Gasca F, Ramrath L, Huettmann G, Schweikard A. Automated segmentation of tissue structures in optical coherence tomography data. *J. Biomed. Opt.* 2009;14(3):034046.

**115.** Singh ASG, Kolbitsch C, Schmoll T, Leitgeb RA. Stable absolute flow estimation with Doppler OCT based on virtual circumpapillary scans. *Biomed. Opt. Express.*1(4):1047-1059.

**116.** Kass M, Witkin A, Terzopoulos D. Snakes: Active contour models *Int. J. Comput. Vis.* 1988;1(4):321-331.

**117.** Delingette H, Hebert M, Ikeuchi K. Shape representation and image segmentation using deformable surfaces. *Image Vis. Comput.* 1992;10(3):132-144.

**118.** McInerney T, Terzopoulos D. Deformable models in medical image analysis: a survey. *Med. Image Anal.* 1996;1(2):91-108.

**119.** Pham DL, Xu C, Prince JL. Current methods in medical image segmentation. *Annu. Rev. Biomed. Eng.* 2000;2(1):315-337.

**120.** Xu C, Pham DL, Prince JL. Medical Image Segmentation Using Deformable Models. In: Fitzpatrick JM, Sonka M, eds. *Handbook on Medical Imaging--Volume III: Medical Image Analysis* SPIE Press; 2000:129-168.

**121.** Montagnat J, Delingette H, Ayache N. A review of deformable surfaces: Topology, geometry and deformation. *Image Vis. Comput.* 2001;19(14):1023-1040.

**122.** Mikic I, Krucinski S, Thomas JD. Segmentation and tracking in echocardiographic sequences: Active contours guided by optical flow estimates. *IEEE Trans Med Imaging.* 1998;17(2):274-284.

**123.** Horn BKP, Shunck BG. Determining Optical Flow. *Artif. Intell.* 1981;17:185-203.

**124.** Bruhn A, Weickert J. Lucas/Kanade meets Horn/Schunck: combining local and global optic flow methods. *Int. J. Comput. Vis.* 2005;61(3):211-231.

**125.** Cohen LD, Cohen I. Finite-element methods for active contour models and balloons for 2-D and 3-D images. *IEEE Trans Pattern Anal Mach Intell.* 1993;15(11):1131-1147.

**126.** Bruhn A. *Variational optic flow computation, accurate modelling and efficient numerics*. SaarbrÄucken,Germany: Department of Mathematics and Computer Science, Saarland University; 2006.

**127.** Canny J. Computational approach to edge edge detection. *IEEE Trans Pattern Anal Mach Intell.* 1986;PAMI-8(6):679-698.

**128.** McInerney T, Terzopoulos D. A dynamic finite element surface model for segmentation and tracking in multidimensional medical images with application

to cardiac 4D image analysis. *Comput. Med. Imaging. Graph.* 1995;19(1):69-83.

**129.** Chen J, Foo SW. Dynamic directional gradient vector flow for snakes. *IEEE Trans. Image Proc.* 2006;15(6):1563-1571.

**130.** Park H, Schoepflin T, Kim Y. Active contour model with gradient directional information: directional snake. *IEEE Trans Circ Syst Vid.* 2001;11(2):252-256.

**131.** Zijdenbos AP, Dawant BM, Margolin RA, Palmer AC. Morphometric analysis of white matter lesions in MR images: method and validation. *IEEE Trans Med Imaging.* 1994;13(4):716-724.

**132.** Atkins SM, Mackiewich BT. Fully automatic segmentation of the brain in MRI. *IEEE Trans Med Imaging.* 1998;17(1):98-107.

**133.** Chalana V, Kim Y. A methodology for evaluation of boundary detection algorithms on medical images. *IEEE Trans Med Imaging.* 1997;16(5):642-652.

**134.** Garita B, Jenkins MW, Han M, Zhou C, VanAuker M, Rollins AM, Watanabe M, Fujimoto JG, Linask KK. Blood Flow Dynamics of One Cardiac Cycle and Relationship to Mechanotransduction and Trabeculation during Heart Looping. *Am. J. Physiol. Heart Circ. Physiol.* January 14, 2011.

**135.** Lee JS, Yu Q, Shin JT, Sebzda E, Bertozzi C, Chen M, Mericko P, Stadtfeld M, Zhou D, Cheng L, Graf T, MacRae CA, Lepore JJ, Lo CW, Kahn ML. Klf2 Is an Essential Regulator of Vascular Hemodynamic Forces In Vivo. *Dev. Cell.* 2006;11(6):845-857.

**136.** Hoffman JIE. Incidence of congenital heart disease. II. Prenatal incidence. *Pediatr. Cardiol.* 1995;16:155-165.

**137.** Fisher AB, Chien S, Barakat AI, Nerem RM. Endothelial cellular response to

altered shear stress. *Am. J. Physiol. Lung Cell Mol. Physiol.* Sep 2001;281(3):L529-L533.

**138.** Hu N, Keller BB. Relationship of simultaneous atrial and ventricular pressures in stage 16-27 chick embryos. Vol 269; 1995:H1359-1362.

**139.** Loots E, Hillen B, Veldman AEP. The role of hemodynamics in the development of the outflow tract of the heart. *J. Eng. Math.* 2003;45(1):91-104.

**140.** Clark EB, Hu N. Developmental hemodynamic changes in the chick embryo from stage 18 to 27. *Circ. Res.* 1982;51:810-815.

**141.** Clark EB. *Functional aspects of cardiac development. In: Zak R(ed) Growth of the Heart in Health and Disease.* New York: Raven Press; 1984.

**142.** Davies PF, Zilberberg J, Helmke BP. Spatial microstimuli in endothelial mechanosignaling. *Circ. Res.* Mar 2003;92(4):359-370.

**143.** White CR, Haidekker M, Bao X, Frangos JA. Temporal gradients in shear, but not spatial gradients, stimulate endothelial cell proliferation. *Circulation.* 2001;103(20):2508-2513.

**144.** Liu A, Rugonyi S, Pentecost JO, Thornburg KL. Finite element modeling of blood flow-induced mechanical forces in the outflow tract of chick embryonic hearts. *Comput. Struct.* 2007;85(11-14):727-738.

**145.** Wang RK, Ma Z. A practical approach to eliminate autocorrelation artefacts for volume-rate spectral domain optical coherence tomography. *Phys. Med. Biol.* 2006;51(12):3231-3239.

**146.** Wang RK, Ma ZH. Real time flow imaging by removing texture pattern artifacts in spectral domain optical Doppler tomography. *Opt. Lett.* 2006;31:3001-3003.

**147.** Wang RK. In vivo full range complex Fourier Domain optical coherence tomography. *Appl. Phys. Lett.* 2007;90:1-3.

**148.** Donea J. Arbitrary Lagrangian-Eulerian finite element methods. *Comput Methods for Transient Anal.* 1983:474-515.

**149.** Rugonyi S, Bathe KJ. On finite element analysis of fluid flows fully coupled with structural interactions. *CMES - Computer Modeling in Engineering and Sciences.* 2001;2(2):195-212.

**150.** Chadwick P. *Continuum Mechanics: Concise Theory and Problems.* New York: Dover Publications Inc.; 1976.

**151.** Hogers B, DeRuiter MC, Baasten AMJ, Gitternberger-de GAC, Poelmann RE. Intracardiac blood flow patterns related to the yolk sac circulation of the chick embryo. *Circ. Res.* 1995;76:871-877.

**152.** ADINA R&D, Inc. *Adina System Online Manuals*. Watertown, MA; 2009.

**153.** Bathe KJ, Zhang H. A flow-condition-based interpolation finite element procedure for incompressible fluid flows. *Comput. Struct.* 2002;80(14-15):1267-1277.

**154.** White FM. Viscous Fluid Flow. 3 ed: McGraw Hill; 2006:127-129.

**155.** Ku DN, Giddens DP, Zarins CK, Glagov S. Pulsatile flow and atherosclerosis in the human carotid bifurcation: positive correlation between the plaque location and low oscillating shear stress. *Arteriosclerosis.* 1985;5:293-302.

**156.** Poelmann R, Gittenberger-de Groot A, Hierck B. The development of the heart and microcirculation: role of shear stress. *Med. Biol. Eng. Comput.* 2008;46(5):479-484.

**157.** Chien S. Effects of Disturbed Flow on Endothelial Cells. *Ann. Biomed. Eng.* 2008;36(4):554-562.

**158.** Antin PB, Fallon JF, Schoenwolf GC. The chick embryo rules (still)! *Dev. Dyn.* Mar 2004;229(3):413-413.

**159.** Qayyum SR, Webb S, Anderson RH, Verbeek FJ, Brown NA, Richardson MK. Septation and valvar formation in the outflow tract of the embryonic chick heart. *Anat. Rec.* 2001;264(3):273-283.

**160.** Patten BM, Kramer TC, Barry A. Valvular action in the embryonic chick heart by localized apposition of endocardial masses. *Anat. Rec.* 1948;102(3):299-311.

**161.** Bradley MP, Theodore CK. The initiation of contraction in the embryonic chick heart. *Am. J. Anat.* 1933;53(3):349-375.

**162.** Santhanakrishnan A, Nguyen N, Cox JG, Miller LA. Flow within models of the vertebrate embryonic heart. *J. Theor. Biol.* 2009;259(3):449-461.

**163.** Liu A, Wang R, Thornburg K, Rugonyi S. Dynamic variation of hemodynamic shear stress on the walls of developing chick hearts: computational models of the heart outflow tract. *Eng. Comput.* 2009;25(1):73-86.

**164.** Liu A, Wang R, Thornburg KL, Rugonyi S. Efficient postacquisition synchronization of 4-D nongated cardiac images obtained from optical coherence tomography: application to 4-D reconstruction of the chick embryonic heart. *J. Biomed. Opt.* 2009;14(4):044020.

**165.** Keller BB, Hu N, Serrino PJ, Clark EB. Ventricular pressure-area loop characteristics in the stage 16 to 24 chick embryo. *Circ. Res.* January 1, 1991 1991;68(1):226-231.

**166.** Johnston PM. Hematocrit values for the chick embryo at various ages. *Am. J. Physiol.* 1954;180(2):361-362.

**167.** Chien S. Shear Dependence of Effective Cell Volume as a Determinant of Blood Viscosity. *Science.* May 22, 1970 1970;168(3934):977-979.

**168.** Hierck B, Van der Heiden K, Poelma C, Westerweel J, Poelmann R. Fluid shear stress and inner curvature remodeling of the embryonic heart. Choosing the right lane! *ScientificWorldJournal.* 2008;8(212-222).

**169.** Jenkins MW, Peterson L, Gu S, Gargesha M, Wilson DL, Watanabe M, Rollins AM. Measuring hemodynamics in the developing heart tube with four-dimensional gated Doppler optical coherence tomography. *J. Biomed. Opt.* 2010;15(6):066022.

**170.** Pexieder T. Embryonic blood flow patterns and heart development. *J. Fla. Med. Assoc.* 1970;57(1):46.

**171.** Patten BM, Kramer TC, Barry A. Valvular action in the embryonic chick heart by localized apposition of endocardial masses. *Anat. Rec.* 1948;102(3):299-311.

**172.** Pexieder T. The conotruncus and its septation at the advent of the molecular biology era In: Clark E, Markwald R, Takao A, eds. *Developmental Mechanisms of Heart Disease*. Armonk, NY Futura Publishing Co.; 1995:227–248.

**173.** Liu A, Nickerson A, Troyer A, Yin X, Cary R, Thornburg K, Wang R, Rugonyi S. Quantifying blood flow and wall shear stresses in the outflow tract of chick embryonic hearts. *Comput. Struct.* 2011;89(11-12):855-867.

**174.** Clark EB, Hu N, Dummett JL, Vandekieft GK, Olson C, Tomanek R. Ventricular function and morphology in chick embryo from stages 18 to 29. *Am. J. Physiol.*

*Heart Circ. Physiol.* March 1, 1986 1986;250(3):H407-413.

**175.** Taber LA, Hu N, Pexieder T, Clark EB, Keller BB. Residual strain in the ventricle of the stage 16-24 chick embryo. *Circ. Res.* February 1, 1993 1993;72(2):455-462.

**176.** Rana MS, Horsten NCA, Tesink-Taekema S, Lamers WH, Moorman AFM, van den Hoff MJB. Trabeculated Right Ventricular Free Wall in the Chicken Heart Forms by Ventricularization of the Myocardium Initially Forming the Outflow Tract. *Circ. Res.* April 13, 2007 2007;100(7):1000-1007.

**177.** Waldo KL, Hutson MR, Ward CC, Zdanowicz M, Stadt HA, Kumiski D, Abu-Issa R, Kirby ML. Secondary heart field contributes myocardium and smooth muscle to the arterial pole of the developing heart. *Dev. Biol.* 2005;281(1):78-90.

**178.** Waldo KL, Kumiski DH, Wallis KT, Stadt HA, Hutson MR, Platt DH, Kirby ML. Conotruncal myocardium arises from a secondary heart field. *Development.* August 15, 2001 2001;128(16):3179-3188.

**179.** Markwald RR, Fitzharris TP, Manasek FJ. Structural development of endocardial cushions. *Am. J. Anat.* 1976;148:85-120.

**180.** Taber LA, Sun H, Clark EB, Keller BB. Epicardial strains in embryonic chick ventricle at stages 16 through 24. *Circ. Res.* November 1, 1994 1994;75(5):896-903.

**181.** Brooke J. Damon, Rémond MC, Bigelow MR, Trusk TC, Xie W, Perucchio R, Sedmera D, Denslow S, Thompson RP. Patterns of muscular strain in the embryonic heart wall. *Dev. Dyn.* 2009;238(6):1535-1546.

**182.** Sedmera D, McQuinn T. Embryogenesis of the Heart Muscle. *Heart Failure Clinics.* 2008;4(3):235-245.

**183.** Burton AC. On the physical equilibrium of small blood vessels. *Am. J. Physiol.* 1951;164:319-329.

**184.** Lee R, Kamm R. Vascular mechanics for the cardiologist. *J. Am. Coll. Cardiol.* 1994;23:1289-1295.

**185.** Lin IE, Taber LA. A model for stress-induced growth in the developing heart. *J. Biomech. Eng.* 1995;117(3):343-349.

**186.** Butcher JT, McQuinn TC, Sedmera D, Turner D, Markwald RR. Transitions in early embryonic atrioventricular valvular function correspond with changes in cushion biomechanics that are predictable by tissue composition. *Circ. Res.* May 25, 2007 2007;100(10):1503-1511.

**187.** Markwald RR, Fitzharris TP, Manasek FJ. Structural development of endocardial cushions. Vol 148; 1977:85-119.

**188.** Filas BA, Efimov IR, Taber LA. Optical coherence tomography as a tool for measuring morphogenetic deformation of the looping heart. *Anat. Rec. (Hoboken).* 2007;290(9):1057-1068.

**189.** Taber LA, Perucchio R. Modeling heart development. *J. Elast.* 2000;61(1-3):165-197.

**190.** Oosterbaan AM, Ursem NTC, Struijk PC, Bosch JG, van der Steen AFW, Steegers EAP. Doppler flow velocity waveforms in the embryonic chicken heart at developmental stages corresponding to 5–8 weeks of human gestation. *Ultrasound Obstet. Gynecol.* 2009;33(6):638-644.

**191.** Van der Heiden K, Groenendijk BCW, Hierck BP, Hogers B, Koerten HK, Mommaas AM, Gittenberger-de Groot AC, Poelmann RE. Monocilia on chicken embryonic endocardium in low shear stress areas. *Dev. Dyn.* 2006;235(1):19-28.

**192.** Sadoshima J, Izumo S. The cellular and moledcular response of cardiac myocytes to mechancial stress. *Annu. Rev. Physiol.* 1997;59(1):551-571.

**193.** Komuro I, Yazaki Y. Control of cardiac gene expression by mechanical stress. *Annu. Rev. Physiol.* 1993;55:55-75.

**194.** Gessner IH. Spectrum of Congenital Cardiac Anomalies Produced in Chick Embryos by Mechanical Interference with Cardiogenesis. *Circ. Res.* June 1, 1966 1966;18(6):625-633.

**195.** Harh JY, Paul MH, Gallen WJ, Friedberg DZ, Kaplan S. Experimental production of hypoplastic left heart syndrome in the chick embryo. *The American Journal of Cardiology.* 1973;31(1):51-56.

**196.** Ya J, Schilham MW, Clevers H, Moorman AFM, Lamers WH. Animal models of congenital defects in the ventriculoarterial connection of the heart. *J. Mol. Med.* Aug 1997;75(8):551-566.

**197.** Chabert S, Taber LA. Intramyocardial pressure measurements in the stage 18 embryonic chick heart. *Am. J. Physiol. Heart Circ. Physiol.* Apr 2002;282(4):H1248-H1254.

**198.** Tobita K, Schroder EA, Tinney JP, Garrison JB, Keller BB. Regional passive ventricular stress-strain relations during development of altered loads in chick embryo. *Am. J. Physiol. Heart Circ. Physiol.* Jun 2002;282(6):H2386-H2396.

**199.** Sasayama S, Ross J, Jr., Franklin D, Bloor CM, Bishop S, Dilley RB. Adaptations

of the left ventricle to chronic pressure overload. *Circ. Res.* March 1, 1976 1976;38(3):172-178.

**200.** Taber LA. Biomechanical Growth Laws for Muscle Tissue. *J. Theor. Biol.* 1998;193(2):201-213.

**201.** Taber LA. Biomechanics of cardiovascular development. *Annu. Rev. Biomed. Eng.* 2001;3:1-25.

**202.** McQuinn TC, Bratoeva M, DeAlmeida A, Remond M, Thompson RP, Sedmera D. High-frequency ultrasonographic imaging of avian cardiovascular development. *Dev. Dyn.* 2007;236(12):3503-3513.

**203.** Rubanyi GM, Romero JC, Vanhoutte PM. Flow-induced release of endothelium-derived relaxing factor. *Am. J. Physiol. Heart Circ. Physiol.* 1986;250(6).

**204.** Ma Z, Liu A, Yin X, Troyer A, Thornburg K, Wang R, Rugonyi S. Measurement of absolute blood flow velocity in outflow tract of HH18 chicken embryo based on 4D reconstruction using spectral domain optical coherence tomography. *Biomed Opt Express.* 2010;1(3):798-811.

# Biographical Note

Aiping Liu was born on January 30, 1977 in Guiyang, a beautify mountain city in Guizhou Province, China. She earned a Bachelor degree and Master degree in Process Equipment and Machinery at Zhejiang University (one of the top 3 Engineering schools in China), Hangzhou, China in 1999 and 2002, respectively. She was awarded first class scholarship each academic year, when she was in Zhejiang University, and was honored the outstanding graduate of Zhejiang Province in 1999.

She came to the USA in February 2002 for graduate study in the Department of Mechanical Engineering at Tennessee Technological University, Cookeville, TN. She worked with Dr. Ying Zhang in collaborative projects with Oakridge National Lab in predicting the material behaviors/phenomena in thermal barrier coatings for gas turbine Engine applications. In May 2004, she earned the second Master degree in Mechanical Engineering, with thesis titled “Numerical Modeling the Displacement Instability (Rumpling) due to Martensitic Phase Transformation in Platinum Aluminide Coatings”.

In August 2004, she started her PhD program in Department of Biomedical Engineering at Oregon Health and Science University (OHSU). She participated in a collaborative research project that aims to understand how hemodynamic forces affect cardiac development and the expression of cardiac genes in vivo, in chicken embryos. The goal is to elucidate the role of hemodynamic forces in cardiac development and ultimately contributing to the understanding the mechanisms of congenital heart diseases. Her PhD thesis research focused on developing a methodology to characterize the dynamic biomechanical environment of the heart outflow of chicken embryos under

normal and altered blood flow conditions. The multidisciplinary nature of her research project has provided her great opportunity to exciting discovery as well as extensive trainings in mathematical modeling, medical imaging, image processing, biology, and physiology. She was awarded an AHA predoctoral Fellowship for the years of 2008-2010, a NSF Fellowship in 2007 to attend the 6th International IEEE EMBS Summer School on Biocomplexity from System to Gene, Istanbul, Turkey, an Outstanding Trainee of the Year from the Heart Research Center of OHSU in 2008, and a Rose Award for recognizing outstanding service excellence at OHSU in 2008. In addition, she was reward a travel fellowship to attend 3rd USNCB Symposium on Frontiers in Biomechanics: Mechanics of Development in Farmington, PA, June 2011.

She is a student member of American Society of Mechanical Engineers (ASME) and Biomedical Engineering Society (BMES). To date she has published around 10 peer-reviewed journal papers and 10 conference papers or abstracts. A list of her publications is as follows:

**Peer-reviewed Journal Papers**

1. **Liu, A**, Yin X, Nickerson, A, Li P, Shi L, Thornburg K, Wang R, Rugonyi S (in preparation) Quantifying the Dynamic Biomechanical Environment in the Heart Outflow Tract of Chick Embryos.
2. **Liu, A**, Yin X, Nickerson, A, Li P, Shi L, Thornburg K, Wang R, Rugonyi S (in preparation) Characterization of the Acute Changes in the Dynamic Biomechanical Environment in the Heart Outflow Tract of Chick Embryos after Outflow Tract Banding.

3. Rugonyi S, **Liu A**, Yin X (2010) Imaging and Modeling of Blood Flow in the Developing Heart, *SPIE Newroom* (DOI: 10.1117/2.1201011.003365).
4. **Liu A**, Troyer A, Ma Z, Yin X, Cary P, Wang R, Thornburg KL, Rugonyi S **(in press)** Quantifying Blood Flow and Wall Shear Stress in the Outflow Tract of Chick Embryonic Hearts at Early Developmental Stages, *Computers and Structures.*
5. Ma Z, **Liu A**, Yin X, Troyer A, Thornburg, K, Wang, R, Rugonyi S (2010) Measurement of Absolute Blood Flow Velocity in Outflow Tract of HH18 Chicken Embryo based on 4D Reconstruction Using Spectral Domain Optical Coherence Tomography, *Biomedical Optics Express*, 1: 798-811.
6. **Liu A**, Wang R, Thornburg KL, Rugonyi S (2009) Efficient Post-acquisition Synchronization of 4-D Nongated Cardiac Images Obtained from Optical Coherence Tomography: Application to 4-D Reconstruction of the Chick Embryonic Heart, *Journal of Biomedical Optics*,14 (4): 044020 (also has been selected for the August 1, 2009 issue of *Virtual Journal of Biological Physics Research*)
7. **Liu A**, Wang R, Thornburg KL, and Rugonyi S (2009) Dynamic Variation of Hemodynamic Shear Stress on the Walls of Developing Chick Hearts: Computational Models of the Heart Outflow tract, *Engineering with Computers*, 25 (1): 73-86.
8. Rugonyi S, Shaut C, **Liu A**, Thornburg KL, Wang R (2008) Changes in Wall Motion and Blood Flow in the Outflow Tract of Chick Embryonic Hearts Observed with Optical Coherence Tomography after Outflow Tract Banding and Vitelline-vein Ligation, *Physics in Medicine and Biology*, 53:5077-5091.

9. **Liu A**, Rugonyi S, Pentecost JO, Thornburg KL (2007) Finite Element Modeling of Blood Flow-induced Mechanical Forces in the Outflow Tract of Chick Embryonic Hearts, *Computers and Structures*, 85 (11-14): 727-738.
10. Zhang Y, **Liu A**, Pint BA (2007) Interdiffusional Degradation of Oxidation-Resistant Aluminide Coatings on Fe-Base Alloys, Materials and Corrosion / Werkstoffe und Korrosion, 58: 751-761.
11. Zheng J, Sun G, Chen Z, Xu P, **Liu A**, Liu Y (2001) Unique Design of Junction Between Thick Pressure Vessel Shell and Thinner Hemispherical Head, Journal of Mechanical Engineering Science 215 Part C:1153-1158.
12. **Liu A**, Chen Z, Zheng J (2001) Design of Reinforcing Structure of Large Rectangular Opening, Pressure Vessel Technology, 18 (4): 46-49.

**Peer-reviewed Conference Publications**

1. **Liu A**, Yin X, Nickerson A, Shi L, Thornburg K, Wang R, Rugonyi S, "Quantifying the dynamic biomechanical environment in the heart outflow tract of early chick embryos", 3rd USNCB Symposium on Frontiers in Biomechanics: Mechanics of Development, Farmington, PA, June 2011.
2. **Liu A**, Thornburg K, Wang R, Rugonyi S, "Changes in Biomechanical Environment of Cardiac Cells in Chick embryos after Cardiac Outflow Tract Banding", ASME Summer Bioengineering Conference, Farmington, PA, June 2011.
3. **Liu A**, Troyer A, Yin X, Ma Z, Nickerson A, Wang R, Thornburg K, Rugonyi S, " Changes in Wall Shear Stress Generated by Outflow Tract Banding in the Hearts of Chick Embryos", Biomedical Engineering Society Annual Meeting, Austin, TX, October 2010.

4. **Liu A**, Wang R, Thornburg KL, Rugonyi S, "Wall Motion Influences Flow Pattern in the Outflow Tract of the Chick Embryonic Heart Tube", ASME Summer Bioengineering Conference, Naples, FL, June 2010.
5. Rugonyi S, **Liu A**, Wang R, Thornburg KL, "Integrative Computational Modeling and Imaging Approach to Study the Effects of Abnormal Hemodynamic Conditions on Cardiac Development", Weinstein Cardiovascular Development Conference, Amsterdam, The Netherlands, May 2010.
6. **Liu A**, Ma Z, Thornburg KL, Wang R, Rugonyi S, "4D Non-gated Chicken Embryo Heart Outflow Imaging Using Spectral Optical Coherence Tomography", SPIE photonic West, San Francisco, CA, Jan 2010.
7. Rugonyi S, **Liu A**, Troyer A, "Understanding the Influence of Embryonic Blood Flow on Cardiac Development", International Conference on Computational Methods for Coupled Problems in Science and Engineering, Ischia Island, Italy, June 2009.
8. **Liu A**, Wang R, Thornburg KL, Rugonyi S, "Efficient Synchronization and Reconstruction of 4D Non-Gated Cardiac Images of Chick Embryos Obtained from Optical Coherence Tomography", ASME Summer Bioengineering Conference, Lake Tahoe, CA, June 2009.
9. Rugonyi S, **Liu A**, Wang R, "Dynamic Variation of Shear Stresses in the Outflow Tract of the Chick Developing Heart", 9$^{th}$ US National Congress on Computational Mechanics, San Francisco, CA, July 2007.
10. **Liu A**, Wang R, Thornburg K, Rugonyi S, "Quantification of Blood Flow-induced Shear Stresses on the Heart Outflow Tract Wall in the Early Developing Chick Embryo", 2007 Northwest Biomechanics Symposium, Eugene, OR, May 2007.

**Other Talks and Seminars**

1. **Liu A**, Wang R, Thornburg K, Rugonyi S, “Wall Motion Influences Flow Pattern in the Outflow Tract of the Chick Embryonic Heart Tube”, Oregon Health & Science University, Heart Research Scientific Center Retreat, Portland, OR, May 2010.
2. **Liu A**, Rugonyi S, "Quantify Flow-induced Shear Stresses in the Cardiac Outflow Tract of Chick Embryos”, Oregon Health & Science University, Heart Research Center's "Try On For Size" (TOFS) Seminar Series, Portland OR, Nov 2009.
3. **Liu A**, Wang R, Thornburg K, Rugonyi S, “Segmentation of 3D Cardiac Images of a Chick Embryo Outflow Tract Obtained from Optical Coherence Tomography”, Oregon Health & Science University, Heart Research Center Scientific Retreat, Portland, OR, Feb 2009.
4. **Liu A**, Rugonyi S, "Quantifying Blood-flow Induced Shear Stress on the Wall of the OFT in the Developing Chick Heart", to college students of George Fox University, Portland, OR, Dec 2008.
5. **Liu A**, Rugonyi S, “Image-based Synchronization of OCT Images to Reconstruct 4D Images of the Chick Embryonic Heart”, Oregon Health & Science University, Biomedical Engineering Seminar, Portland, OR, Apr 2008.
6. **Liu A**, Wang R, Thornburg K, Rugonyi S, “Quantification of Wall Shear Stress in the Outflow Tract of the Embryonic Chick Heart”, Oregon Health & Science University, Heart Research Center Scientific Retreat, Portland, OR, Jan 2008.